Doctoral theses at NTNU, 2022:127

Filipe Borges

Quantitative Seismic Monitoring

Doctoral thesis

NTNU
Norwegian University of Science and Technology
Thesis for the Degree of
Philosophiae Doctor
Faculty of Engineering
Department of Geoscience and Petroleum

NTNU
Norwegian University of
Science and Technology

Filipe Borges

Quantitative Seismic Monitoring

Thesis for the Degree of Philosophiae Doctor

Trondheim, April 2022

Norwegian University of Science and Technology
Faculty of Engineering
Department of Geoscience and Petroleum

NTNU
Norwegian University of
Science and Technology

NTNU
Norwegian University of Science and Technology

Thesis for the Degree of Philosophiae Doctor

Faculty of Engineering
Department of Geoscience and Petroleum

ISBN 978-82-326-6251-7 (printed ver.)
ISBN 978-82-326-6876-2 (electronic ver.)
ISSN 1503-8181 (printed ver.)
ISSN 2703-8084 (online ver.)

Doctoral theses at NTNU, 2022:127

Printed by NTNU Grafisk senter

To my parents.

Acknowledgments

Completing this work would have been much more difficult - and less fun - without the people I had around me.

I cannot avoid starting by thanking my parents, Francisco Borges and Marta Souto. They provided all the support I needed for everything in my life, including the decisions they did not agree with. They have been the best teachers one could hope for, and after 34 years of lectures, I still have a lot to learn from them.

This Ph.D. was financed by Petróleo Brasileiro S/A (Petrobras), and I thank them for the financial and technical support during the project. I thank Paulo Johann and Edgar Thedy for supporting my Ph.D. project, Álvaro Martini for helping with data handling, and Alexandre Maul, André Bulcão, Bruno Pereira-Dias, Paulo Pires, and Roberto Dias for the technical discussions. I also thank all my other colleagues from Petrobras, who - despite the distance - helped me get through these past years. I extend my thanks to all my new friends here in Norway.

Daily life at IGP was much better in the companionship of the lovely and amazing people I met here, to whom I am very grateful. In particular, I thank Daniel Wehner, for a good deal of help with the research presented here, Marcin Duda, who shared the office with me, and Lucas Sevillano. I also thank the whole administrative and technical staff at the department: Sylvi Vefsnmo, Anne-Lise Brekken, Turid Uvsløkk, Madelein Wold, Lars Sandvik, and Knut Reitan Backe.

I'm deeply indebted to ConocoPhillips Skandinavia AS and the PL018 license partners (Total E&P Norge, Vår Energi, Equinor ASA and Petoro AS), and also to the Valhall Joint Venture companies, Aker BP ASA (operator) and Pandion Energy AS (partner), for kindly allowing me to use their data for this research, and for the permission to publish the results. I thank Per Gunnar Folstad for providing

information that was essential to some conclusions drawn in this research.

As the goal of the Ph.D. is to become a researcher, properly acknowledging the person in charge of guiding me is never enough. I'm lucky for being supervised by professor Martin Landrø, who did much more than I could ever expect from a supervisor. I hope we manage to continue to work together for the years to come, and that more fruitful work can emerge from it. I would also like to thank the other professors who helped me during those years at NTNU: Kenneth Duffaut, Rune Holt, Erling Fjær, Erik Skogen and Lasse Amundsen.

Finally, I thank NTNU and Norway for being the perfect home for the past years. Trondheim is the best city I have ever lived in, and I surely hope to be able to visit as often as possible.

Abstract

Seismic data is the main input for reservoir characterization in developing plays, when - in general - only conceptual geological models and few wells are available. When repeated over time, in a process called 4D seismic or time-lapse seismic, this type of geophysical measurement can become a powerful aid in reservoir monitoring and geomechanical risk assessment, since it is the only broad, spatially-continuous probing method for deep reservoir surveillance. The indirect nature of the seismic measurement, however, might make its interpretation ambiguous, particularly when we consider limitations caused by resolution, noise and inadequate acquisition geometry and processing. This uncertainty plays a more important role when time-lapse seismic measurements are used for quantitative estimations of changes in the reservoir or the overburden.

The main goal of this Ph.D. project was to develop and evaluate techniques for quantitative interpretation of time-lapse seismic data, as well as its associated uncertainties. In the first chapter of this thesis, we introduce some rock physics models, which are the essential link between seismic measurements and the subsurface properties. We discuss the seismic properties of brines, the most common fluid in subsurface, and how its salinity and temperature can affect the interpretation of 4D data. The same discussion is made for fluid mixing - another source of uncertainty in reservoir 4D seismic interpretation. The use of time-lapse anisotropy changes as source of information is also presented. These considerations are combined in various synthetic scenarios, which are used as examples to explore the uncertainties of quantitative interpretation of 4D seismic.

In the second chapter, the feasibility of near-well monitoring with tube waves is studied, and the analysis of several experiments with shallow well data acquisition is presented. The tube wave discussed here is the Stoneley mode, and its velo-

city and anelastic attenuation are connected to the shear modulus of the formation surrounding the well. Precise measurement of this wave mode can allow for monitoring the shear modulus of the nearby rock, and hence can be used as a time-lapse method. The acquisition and processing of data are detailed, and two modeled scenarios for monitoring are presented as feasibility studies.

The third chapter details a case study where time-lapse seismic is used for geomechanical monitoring in Ekofisk (southern North Sea). Due to a well collapse, water was injected into the overburden for over two years. The injection is thought to have caused a seismic event of moderate magnitude, together with sea bottom uplift. Seismic measurements, time-lapse bathymetry and forward geomechanical modeling are integrated to understand the effect of the water injection in the stress state of the field, which is also affected by the reservoir compaction caused by 4 decades of oil production.

The fourth chapter discusses the analysis of data recorded by the Valhall Life of Field Seismic (LoFS) system in 2014, during an ongoing acquisition in a nearby field. Several normal modes (harmonics) can be identified in the seismic data, despite the source-receiver offset being over 30 km. These harmonics can be used to monitor the shallow sediment layer, based on an analytical model. Low-frequency diving waves were also identified. A method to estimate the seafloor P-wave velocity based on passive measurements is suggested, evidencing how these unique acquisition geometries open the door for different monitoring methods.

The fifth and last chapter presents an analysis of the effects of water velocity variations and geometry repeatability in offshore seismic acquisitions. Elastic seismic modeling was performed, using high-resolution property models for two distinct survey dates. On each date, different water velocity profiles, measured in field experiments, are considered. To incorporate source and receiver non-repeatability, some differences in the acquisition geometries are also tested for each vintage. The synthetic data were compared in terms of time-lapse amplitudes, and repeatability was quantified via the normalized root mean squared attribute (NRMS). For the parameters considered in the study, the deterioration of NRMS seemed to be dominated by the non-repeatability of the receivers and by water velocity variations, with source non-repeatability having a lower contribution. The results can be used as a step towards a more robust methodology for time-lapse feasibility studies, which incorporates imaging uncertainties and allows us to understand the contribution of each element that could affect the 4D quality.

Contents

Introduction

One of the most widespread jokes about conceptual models is the *spherical chicken* metaphor: the brutal reduction in the complexity of real life problems, in an attempt to create models that can be handled analytically. Though sometimes mocked for providing results that deviate too much from reality, this is in fact a very powerful tool for tackling complicated problems - or, at least, for gaining intuitive comprehension about them.

Many such simplifications have been adopted when processing and interpreting seismic data. We can for example assume that the subsurface is formed by horizontal layers of constant properties (Thomson, 1950), which - albeit far from being true - gives reasonable results in regions of gentle dips and low velocity contrasts. More complex models include non-homogeneity of elastic properties and dipping layers (Ikelle and Amundsen, 2005). The natural path to a more trustworthy representation of the subsurface is currently being paved by meticulous imaging techniques such as anisotropic elastic full waveform inversion (Raknes and Arntsen, 2015) and least squares migration (Tarantola, 1986; Pereira-Dias et al., 2017).

The same increase in complexity is observed in rock physics models, which are also the subject of intense research (Mavko et al., 2009a). Evaluating the influence of pore fluid and effective stress in seismic wave propagation is an arduous task, as the degree of heterogeneity of rocks and fluids handled in the O&G industry is quite wide: a myriad of models aim at predicting how production and injection affect rock properties. For reservoir surveillance and optimization, a main interest in rock physics models is to establish a connection between the reservoir/overburden dynamic properties - such as pore pressure and fluid saturation - and seismic measurements, which are sensitive to elastic parameters like P- and S-wave velocities. For long-term field management, proper understanding of how the reservoir and

overburden respond to acute pressure changes might also be relevant to handle reservoir compaction/inflation, as well as its effects on the production facilities. Both reservoir management and geomechanical analysis usually rely on reservoir flow simulation to forecast the reservoir response during its production.

Flow models have hugely grown in complexity and precision in the last decades and, although flow simulation can be considered a forward modeling approach, the main goal - finding the correct representation of the reservoir properties - faces the same limitation of most inversion techniques: trying to solve an ill-posed problem, which admits several acceptable solutions. To constrain the ensemble of possible models, a broad set of boundary conditions is used, being the most common one the flow rate of producing wells (history matching). Apart from the production history, other inputs like Permanent Downhole Gauges (PDG) and formation tests can be integrated to improve the accuracy of the reservoir model. Most of these constrains, however, are usually limited to a narrow range of influence around the wells.

For areal reservoir characterization, seismic surveys have been the most common geophysical solution. In addition to that, the last 20 years have seen a boost in adoption of the seismic method as a reservoir surveillance practice (Landrø et al., 1999; Mitchell et al., 2009): by repeating several seismic surveys over the same region in different calendar times, one can obtain the elastic response of the reservoir under different states of pressure, temperature and fluid content. The technique is today broadly known as 4D seismic, or time-lapse seismic. The concept of reservoir surveillance can be extended to other geophysical methods: time-lapse gravimetric (Eiken et al., 2000) and electromagnetic (Orange et al., 2009) surveys have been successfully performed around the world. Nevertheless, seismic surveys are still the chief method employed by the O&G industry, both for characterization and monitoring purposes.

If the acquisition parameters of multiple seismic surveys are kept the same, the subtle differences observed in the resulting seismic images should arise solely from the changes in reservoir properties that influence the seismic wave propagation - namely, the elastic parameters, such as density, compressibility and shear modulus. When the detected changes can be converted into information about the reservoir dynamic properties like pore pressure and fluid saturation, these seismic-derived results become an important tool in the process of reservoir simulation and monitoring. Besides, as the seismic waves travel the whole path between surface and reservoir, time-lapse seismic measurements can also be used to study changes in the overburden, therefore supporting geomechanical modeling and interpretation.

As acquisition and processing techniques improve in quality, more detailed fea-

tures can be extracted from seismic data (Bunting et al., 2013; Tenghamn and Dhelie, 2009; Le Diagon et al., 2014). 3D seismic interpretation has hugely benefited from this, as interpreters became able to identify narrow channels, crevasses and other geological features made visible by higher signal-to-noise ratios (SNR) and broader frequency content. The benefits for 4D interpretation from these improvements are twofold: the increase in resolution allows for more precise mapping of water front advance/residual oil detection; and better SNR and repeatibility open the door for *quantitative* interpretation, i.e., numerically estimation of changes in pore pressure, fluid saturations and other dynamic reservoir properties from time-lapse data. On top of that, field instrumentation has made possible many novel acquisition configurations, such as permanent reservoir monitoring arrays (Bertrand et al., 2014; Kommedal et al., 2004) and fiber optics for well monitoring (Mateeva et al., 2013). These new data opens pave the way for innovative methods of interpretation, which could reveal more information about the subsurface.

The purpose of this PhD project was to study different techniques for quantitative interpretation of time-lapse seismic data. The thesis is divided in 5 chapters.

Chapter 1 offers a general introduction to the framework of time-lapse reservoir monitoring. We present some rock physics models, which establish how pressure and pore fluid saturation impact seismic measurements, and show how we can obtain the changes in dynamic properties from 4D seismic. The rock physics models are also used to interpret some 4D results in the rest of the thesis. To demonstrate the application of the reservoir monitoring techniques, some modeled scenarios are presented. In these scenarios, both hydrocarbon production and water injection are considered, as well as CO_2 sequestration. We discuss in particular the effect of brine temperature and salinity in 4D interpretation: brine properties are many times assumed as constant in time-lapse interpretation, but changes in these properties might compromise data interpretation. For the CO_2 sequestration example, the effect of an unknown fluid mixing law is investigated, since this is a point of uncertainty when mixing CO_2 and water. Using third-order elasticity (TOE), the time-lapse variation of seismic anisotropy is also examined.

Chapter 2 discusses a series of experiments performed in shallow wells in the basement of a laboratory in Trondheim. The experiments were aimed at measuring the velocity and absorption of the tube wave in the wells. The tube wave studied is the Stoneley mode, and its properties are connected to the shear modulus of the formation surrounding the well. Precise measurement of this wave mode can allow for monitoring the shear modulus of the nearby rock, and hence can be used as a time-lapse method. Because the low-frequency tube wave velocity is insensitive to the formation's density and bulk modulus, it can isolate non-fluid effects, providing

information that can be combined with other monitoring methods. The acquisition and processing of data is detailed, and some modeled scenarios for monitoring are presented.

Chapter 3 presents a case study where time-lapse seismic is used for geomechanical monitoring. Due to a well collapse, water was injected in the overburden of the Ekofisk field for over two years. The injection is thought to have caused a seismic event of moderate magnitude, as well as a sea bottom uplift. Time-shift seismic measurements, time-lapse bathymetry and forward geomechanical modelling are integrated to understand the effect of the water injection in the stress state of the field.

Chapter 4 discusses the analysis of data recorded by the Valhall Life of Field Seismic system (LoFS) in 2014, during an ongoing acquisition in a nearby field. The recorded data shows a clear arrival of at least four normal modes (harmonics), despite the distance of over 30 km between source and receivers. These harmonics can be used to monitor the shallow sediment layer, based on an analytical model. Low-frequency diving waves were also identified. Finite-differences modeling was used to reproduce the complex wave patterns detected in the data. A method to estimate the seafloor P-wave velocity based on passive measurements is suggested.

Chapter 5 presents the modeling and analysis of synthetic time-lapse data, using parameters similar to those of a Brazilian Pre-salt field. The effects of water velocity variations and geometry non-repeatability are investigated. The synthetic data (one for each calendar date studied) were compared in terms of time-lapse amplitudes, and repeatability was quantified via the normalized root mean squared attribute (NRMS). For the parameters considered in the study, the deterioration of NRMS seemed to be dominated by the non-repeatability of the receivers and by water velocity variations, with source non-repeatability having a lower contribution. The results can be used as a step towards a more robust methodology for time-lapse feasibility studies, which incorporates imaging uncertainties and allows us to understand the contribution of each element that could affect the 4D seismic image quality.

Publications

The following publications were derived from the work developed in this thesis:

Borges, F., and M. Landrø, 2017, Analysis of the influence of water salinity on time-lapse seismic response: Presented at the 79th EAGE Conference and Exhibition 2017

Borges, F., D. Wehner, and M. Landrø, 2018, Calculation of tube wave velocity in a shallow borehole using passive seismic recordings: Presented at the 80th EAGE Conference and Exhibition 2018

Wehner, D., F. Borges, and M. Landrø, 2018, Using well operation noise to estimate shear modulus changes from measured tube waves - a feasibility study: Presented at the Fifth CO_2 Geological Storage Workshop

Borges, F. and M. Landrø, 2018, Time-lapse separation of fluid and pressure effects with an arbitrary fluid mixing law: Presented at the Fifth CO_2 Geological Storage Workshop

Landrø, M., D. Wehner, and F. Borges, 2018, How variations of the formation shear modulus around boreholes could be estimated from the tube wave: AGU Fall Meeting Abstracts, S51F–0398

Borges, F., M. Landrø, and K. Duffaut, 2020, Time-lapse seismic analysis of overburden water injection at the ekofisk field, southern north sea: Geophysics, **85**, B9–B21

Wehner, D., F. Borges, and M. Landrø, 2021, Tube-wave monitoring as a method to detect shear modulus changes around boreholes: A case study: Geophysics, **86**, B193-B207

Borges, F. and M. Landrø, 2022, Far-offset detection of normal modes and diving waves: A case study from the Valhall Field, southern North Sea: Geophysics, **87**, B105-B115

Borges, F., M. Muzzette, L. E. Queiroz, B. Pereira-Dias, R. Dias, and A. Bulcão, 2022, Analysis of water velocity changes in time-lapse ocean bottom acquisitions-a synthetic 2d study in santos basin, offshore brazil: Journal of Applied Geophysics, **197**, 104521

A manuscript describing the analysis and interpretation of anelastic attenuation of tube waves (see **Chapter 2**) is currently being prepared for submission.

Other Contributions

In addition to the published work directly related to the main topic of the thesis, constant collaboration was kept with other professionals in the industry, leading to some publications that are not entirely related to seismic monitoring. They are summarized below:

Fonseca, J., L. Teixeira, A. Maul, P. Barros, F. Borges, J. Boechat, and M. González, 2018, Modelling geological layers into new velocity models for seismic migration process-a brazilian pre-salt case: Presented at the First EAGE/PESGB Workshop on Velocities

Teixeira, L., J. Nunes, A. Maul, J. Fonseca, P. Barros, and F. Borges, 2018, Seismic-based salt characterisation for geomechanical modelling of a presalt reservoir: Presented at the 80th EAGE Conference and Exhibition 2018

Dias, R., J. Fonseca, A. Bulcão, B. Dias, L. Teixeira, A. Maul, and F. Borges, 2019, Salt stratification and least square migration to improve pre-salt reservoir images: Santos basin, brazilian offshore example: Presented at the Second EAGE/PESGB Workshop on Velocities

Maul, A. R., M. A. C. Santos, C. G. Silva, M. d. L. Á. G. Farias, J. S. da Fonseca, F. A. de Souto Borges, and C. E. B. de Salles Abreu, 2019b, Evaporitic velocity modeling uncertainties and variabilities: Implications for pre-salt projects in the santos basin, brazil: Brazilian Journal of Geophysics, **37**, 175–186

Maul, A. R., M. A. C. Santos, C. G. Silva, L. M. T. da Silva, M. d. L. Á. G. Farias, J. S. da Fonseca, R. de Melo Dias, J. B. T. Boechat, F. A. de Souto Borges, L. F. Fernandes, et al., 2019a, Improving pre-salt reservoirs seismic images when considering the stratified evaporites insertion in the initial model for the velocity updating processes prior to the seismic migration: Brazilian Journal of Geophysics, **37**, 235–247

Dias, R., F. Borges, C. Ushirobira, C. Carbonari, B. P. Dias, and A. Bulcão, 2020, Seismic modeling to mitigate risk in well location-a case study in brazilian pre-salt: 82nd EAGE Annual Conference & Exhibition, European Association of Geoscientists & Engineers, 1–5

Maul, A., A. Bulcão, R. Dias, B. Pereira-Dias, L. Teixeira, F. Borges, M. González, C. Guizan, and M. Cetale, 2021, Benefits of inserting salt stratification to detail velocity model prior to least-squares reverse-time migration: Journal of Applied Geophysics, 104469

Chapter 1

Fluid and Pressure Effects on 4D Seismic Data

In this chapter, some rock physics and fluid models are discussed. We introduce Biot's poroelastic model, from which Gassmann's equations can be derived; the Hertz-Mindlin model, which is a grain contact theory for modeling the dependence of elastic modulus with pressure; and the third-order elasticity model (TOE), which leads to a more complex relation between elastic properties and strain. We then discuss some fluid properties (like brine salinity) in the context of reservoir monitoring and talk about different ways in which fluids can mix in the pore space. Both the rock physics models and the Gassmann equation are used in other parts of the thesis, so this Chapter lays some foundations to be used further in the work.

In addition to the theoretical introduction, four modeled scenarios for reservoir monitoring are presented. These scenarios combine different assumptions on pore pressure and fluid content in distinct calendar dates. The main goal of these scenarios is to quantify the contribution of different brine salinities, brine temperatures, and fluid mixing law to 4D seismic interpretation. Inversion methods based on time-lapse measurements are proposed to invert the modeled reflectivity changes back to the reservoir properties. The uncertainties of the results are also estimated and discussed.

Some of the results presented in this chapter have been published in two conference papers:

Borges, F., and M. Landrø, 2017, Analysis of the influence of water salinity on time-lapse seismic response: Presented at the 79th EAGE Conference and Exhibition 2017

Borges, F. and M. Landrø, 2018, Time-lapse separation of fluid and pressure effects with an arbitrary fluid mixing law: Presented at the Fifth CO_2 Geological Storage Workshop

In addition to the published results (which are detailed in more depth here), this chapter presents a discussion about the use of anisotropy as a source of information for quantitative time-lapse interpretation (Section 1.4). The complete equations for the uncertainty estimation in the scenario of water injection with different salinity can be found in Appendix B, and an introduction to Decision Trees and Random Forest, one of the methods used for inversion, can be found in Appendix C.

1.1 Rock Physics Models

1.1.1 Biot's Poroelastic Model

The most common model for understanding the behavior of fluid-filled rocks under different stresses is Biot's poroelastic model (Biot, 1941). Briefly, Biot's assumptions are that rocks are porous and permeable (allowing for fluid movement and pressure equalization), linearly elastic, homogeneous, and isotropic - the model was later extended to handle anisotropy as well (Biot and Willis, 1957).

Biot's results can be used to calculate the compressibility of the rock under different fluid contents. This result, known as the Biot-Gassmann equation (Gassmann, 1951), is expressed in Equation 1.1. Through it, one can obtain the velocity of propagation of the compressional modes (P-waves) for different pore fluid properties. In order to do so, it is necessary to know the density (ρ) of the the system, the rock porosity (φ), the bulk modulus of the rock matrix (K_{ma}), the bulk modulus of the rock frame (which is the bulk modulus of the rock without any fluid in its pores - K_{dry}), the bulk modulus of the fluid in the pore space (K_f) and the shear modulus of the rock frame (μ).

$$V_p^2 = \frac{1}{\rho}\left\{ K_{dry} + \frac{4}{3}\mu + \frac{(K_{ma} - K_{dry})^2}{K_{ma}\left(1 - \varphi + \varphi\frac{K_{ma}}{K_f} - \frac{K_{dry}}{K_{ma}}\right)} \right\} \tag{1.1}$$

The rock properties to be used in Equation 1.1 are usually obtained from well logs, calibrated by laboratory ultrasonic tests and analysis of rock mineralogy - this process in itself is rather uncertain, and might introduce significant uncertainty in 4D seismic interpretation. The fluid properties can be obtained either analytically (for fluids of known composition) or via Pressure-Volume-Temperature (PVT) analysis. The density is obtained by averaging the densities of the rock matrix (ρ_{ma}) and fluid, weighted by the porosity. In the case where several fluids are present in

the pore space, each with saturation S_i and density ρ_i, the density is given by

$$\rho = (1-\varphi)\rho_{ma} + \varphi \sum_i S_i \rho_i, \qquad \sum_i S_i = 1. \tag{1.2}$$

Equations 1.1 and 1.2 show that the effect of fluid on the P-wave velocity is included via two proxies: density and fluid bulk modulus.

The bulk modulus of the fluid can be difficult to estimate when there is a fluid mixture - the way the fluids behave when under compression will be different according to the way they are mixed, and this is a topic that will be further discussed in this chapter. For now, we can consider that the mixture is homogeneous, and that an effective bulk modulus for the fluid mixture can be obtained by Wood's law, or Reuss average (Reuss, 1929) of the bulk moduli K_i of all fluids in the pore space:

$$\frac{1}{K_f} = \sum_i \frac{S_i}{K_i}. \tag{1.3}$$

In Biot-Gassmann's model, the shear modulus μ of the rock is not a function of fluid properties. The S-wave V_s velocity is given by

$$V_s = \sqrt{\frac{\mu}{\rho}}, \tag{1.4}$$

from where we can see that the only influence of pore fluid in the S-wave velocity comes from changes in density.

It is important to highlight that, in this model, there is no effect of the pore fluid on the dry rock properties (K_{dry}, μ and φ). That means that we disregard, for example, chemical interactions between rock and fluid that could weaken the rock frame. It is also assumed that porosity is constant, and that dry rock properties do not change within the temperature range considered.

1.1.2 Hertz-Mindlin Model

Several models attempt to describe the behavior of the rock frame (namely, the bulk modulus K and the shear modulus μ) under different effective stresses. The values of K_{dry} and μ can, as many other rock properties, be represented as a function of the effective stress σ_{eff} to which the rock is subjected (Mavko et al., 2009a). The effective stress is given by

$$\sigma_{eff} = \sigma_c - nP_P, \tag{1.5}$$

where σ_c is the confining stress and P_P is the pore pressure. The parameter n is labeled *effective stress coefficient*, and its determination is also a matter of debate in the literature (Müller and Sahay, 2016). As a simplification, $n = 1$ is assumed in this chapter - in that case, the resulting effective stress is also called *net stress* (σ_{net}).

One of the simplest models for stress-dependence of elastic moduli is the Hertz - Mindling model (Mindlin, 1949), which results in an exponential relation between the elastic moduli and the confining stress. Assuming a collection of unconsolidated, random-sized spherical grains, the model derives the following relation for bulk and shear modulus at different effective stresses σ (Bjorlykke, 2010, Chapter 19):

$$\frac{K}{K_0} = \left(\frac{\sigma}{\sigma_0}\right)^{(1/3)} \qquad \text{and} \qquad \frac{\mu}{\mu_0} = \left(\frac{\sigma}{\sigma_0}\right)^{(1/3)} \tag{1.6}$$

Using equations 1.6 and 1.1, the pressure and fluid effects can be easily modeled, which is usually done to support interpretation of field measurements. It is also a way of performing a prompt feasibility study in exploration plays, since limited information is necessary as input. One way of adding more information to Hertz-Mindlin's model is to tweak the coefficient of the power law, to fit different dependence of elastic moduli/seismic velocities with stress. Traditionally, however, it is more usual to obtain such relations from lab tests of plugs and core samples.

1.1.3 Third-Order Elasticity (TOE)

Linear elasticity deals with phenomena in which the deformations that a material undergoes are infinitesimal, and hence can be approximated by a linear relation with stress. This is the domain of Hooke's law, and is generally valid when studying the strain caused by a seismic wave. The linear elasticity model states that

$$\sigma_{ij} = C_{ijkl}\mathcal{E}_{ij}, \tag{1.7}$$

where the strain $\mathcal{E}_{ij}$ is connected to the stress σ_{ij} via the stifness tensor C_{ijkl}. In the range where linear elasticity is valid, C_{ijkl} is constant, and the strain is linearly proportional to the stress.

When a reservoir is strongly depleted or subjected to acute injection, however, it is not rare to find changes in pore pressures of several megaPascals. These massive changes can lead to significant variation in the effective stress, causing the reservoir to compact or to arch, depending on the resulting stress regime. This is then a situation where linear elasticity is no longer a suitable model to properly describe the rock behavior: the rock strain is now finite, and the relation between stress and strain becomes nonlinear.

To represent this effect, we use an expansion of the linear concept, which is the equivalent to adding an extra power of the Taylor series in the representation of the energy as a function of strain. The elastic energy U of the system is written as

$$U = \frac{1}{2} C_{ijkl} \mathcal{E}_{ij} \mathcal{E}_{kl} + \frac{1}{6} A_{ijklmn} \mathcal{E}_{ij} \mathcal{E}_{kl} \mathcal{E}_{mn} \tag{1.8}$$

From the expression above, one can see the origin of the therm *third-order elasticity:* the energy is a function of the third power of the components of the strain. This is the model used by Rasolofosaon (1998) and Prioul and Lebrat (2004). The linear Hooke model (equation 1.7) leads to a energy function of second order in the strain tensor, being then called *second-order elasticity* (SOE).

Equation 1.8 can be interpreted in terms of an effective stiffness tensor C^{eff}_{ijkl}, which is a function of the strain:

$$C^{\text{eff}}_{ijkl} = C^{0}_{ijkl} + A_{ijklmn} \mathcal{E}_{mn} \tag{1.9}$$

The tensor C^{0}_{ijkl} is the stiffness of the rock in a given reference state (not necessarily in absence of stress), and the term $A_{ijklmn}\mathcal{E}_{mn}$ accounts for the extra contribution due to the strain the system experiences, when compared to the reference state in which C^{0}_{ijkl} is measured.

The sixth-order tensor A_{ijklmn} can lead to a huge increase in the complexity of the system: it is a 729 terms-tensor that, in a general/triclinic medium, can be reduced to 56 independent terms - a staggering number, notwithstanding. However, experimental data (Prioul et al., 2004) document that this tensor can typically be considered isotropic, leading us to a palatable set of three independent variables.

Using Voigt notation and assuming an isotropic A_{ijklmn}, equation 1.9 for a medium with vertical transverse isotropy (VTI) can be written as

$$\begin{aligned}
C^{\text{eff}}_{11} &\approx C^{0}_{11} + A_{111}\mathcal{E}_{11} + A_{112}(\mathcal{E}_{22} + \mathcal{E}_{33}) \\
C^{\text{eff}}_{22} &\approx C^{0}_{11} + A_{111}\mathcal{E}_{22} + A_{112}(\mathcal{E}_{11} + \mathcal{E}_{33}) \\
C^{\text{eff}}_{33} &\approx C^{0}_{33} + A_{111}\mathcal{E}_{33} + A_{112}(\mathcal{E}_{11} + \mathcal{E}_{22}) \\
C^{\text{eff}}_{12} &\approx C^{0}_{12} + A_{123}\mathcal{E}_{33} + A_{112}(\mathcal{E}_{11} + \mathcal{E}_{22}) \\
C^{\text{eff}}_{13} &\approx C^{0}_{13} + A_{123}\mathcal{E}_{22} + A_{112}(\mathcal{E}_{11} + \mathcal{E}_{33}) \\
C^{\text{eff}}_{23} &\approx C^{0}_{13} + A_{123}\mathcal{E}_{11} + A_{112}(\mathcal{E}_{22} + \mathcal{E}_{33}) \\
C^{\text{eff}}_{44} &\approx C^{0}_{44} + A_{144}\mathcal{E}_{11} + A_{155}(\mathcal{E}_{22} + \mathcal{E}_{33}) \\
C^{\text{eff}}_{55} &\approx C^{0}_{44} + A_{144}\mathcal{E}_{22} + A_{155}(\mathcal{E}_{11} + \mathcal{E}_{33}) \\
C^{\text{eff}}_{66} &\approx C^{0}_{66} + A_{144}\mathcal{E}_{33} + A_{155}(\mathcal{E}_{11} + \mathcal{E}_{22})
\end{aligned} \tag{1.10}$$

Selecting as independent values A_{111}, A_{112} and A_{113}, we have $A_{144} = (A_{112} - A_{123})/2$ and $A_{155} = (A_{111} - A_{112})/4$. The three independent parameters can be measured in ultrasonic tests, and allow for the calculation of the changes in the effective stiffness tensor when the rock is under influence of a static stress different from the stress in the reference state C^0_{IJ}.

1.1.4 Fluid Properties

The elastic properties of fluids in the pore space do not fall into the "rock physics" label, but they play an important role in time-lapse seismic interpretation. In one of the most cited works in applied geophysics, Batzle and Wang (1992) presented results that allow for calculation of density and bulk modulus of hydrocarbons and brines under different salinities, temperatures, pore pressures and gas content. In this thesis, Batzle & Wang's equations were used to estimate the properties of brine and oil. When CO_2 properties were also necessary for modeling, we employed the results made available by Mavko et al. (2009b), last accessed in July 19 2017.

1.2 The Effects of Brine Salinity and Temperature

In offshore fields, the most cheap and convenient source of water for injection is seawater. Still, its use for injection may pose some challenges, ranging from operational ones, like corrosion of pipelines (Roche et al., 2007), to changes in the rock frame itself - the brine *in situ* will likely have a different composition, which may lead to the weakening of the rock matrix due to dissolution (Vanorio et al., 2011a) or loss of injectivity, caused by precipitation of salts. To mitigate such problems, the injected water usually goes through several treatment steps, like the use of a biocide, filtering for suspended solids, and desulfation (Pedenaud et al., 2012).

Despite going through the aforementioned processes, the salinity of the treated water is mostly unchanged, remaining around 35,000 ppm and usually contrasting with the formation water of deep reservoirs, which can run from a few thousand ppm above that (Bjørlykke and Gran, 1994) to over 100,000 ppm or more (Batzle and Wang, 1992). Figure 1.1 shows a collection of brine salinity and fluid temperature values sampled in several reservoirs in the world, both onshore and offshore. The orange dots come from a database provided by C&C Reservoirs (2020), and the green ones belong to an operating E&P company. The geothermal gradient (Fridleifsson et al., 2008), drawn as a blue line in panel **(b)** appears as a clear trend of increasing *in situ* fluid temperatures for deeper reservoirs and is similar to the best fit line (in black), which has a gradient of 21 °C/km. As for brine salinity, there is no clear correlation with depth of burial - the composition of the dissolved salts

depends on the depositional environment and hydrothermal/diagenetic processes, and polynomial fits of higher-order or power laws fail to reach a determinations coefficient $R^2 > 0.03$.

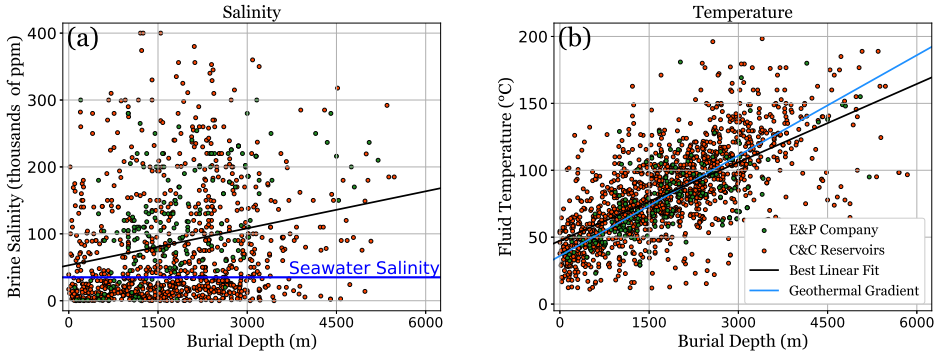

Figure 1.1: Brine salinity **(a)** and fluid temperature **(b)** for several hydrocarbon fields, from two different databases. Thick blue line on left plot represents the seawater salinity, of 35,000 ppm. Black lines are the best linear fits.

The salinity of injection water has also sparked interest as an EOR method: several different studies (Webb et al., 2003; Skrettingland et al., 2011) point to the injection of low-salinity water (LSW) as a means to achieve a higher recovery factor, though the mechanism by which this effect occurs is still a matter of debate (see Sheng (2014) for a thorough review on the subject).

The concentration of dissolved salts in the brine has a significant impact on its density and compressibility. A sharp contrast in salinity between the injected water and the formation water can therefore be used as a way to monitor the advance of the water injection front. To study the time-lapse effect of injection of water of different salinities, two different production scenarios were modeled: injection of water with different salinity below the free water level (scenario **1A**), and a water-displacing-oil, or water sweep case (scenario **1B**). Table 1.1 shows some information regarding each of these scenarios. In both scenarios, a single well injects seawater in a 100m-thick homogeneous, radially unbounded, isotropic sand layer which originally contains brine (**1A**) or oil + connate water (**1B**) as pore fluid.

	Pore Fluid (Baseline)	Pore Fluid (Monitor)	Fluid Temperature
Scenario 1A	Brine	Brine + Seawater	Variable
Scenario 1B	Brine + Oil	Brine + Residual Oil + Seawater	Constant

Table 1.1: Two scenarios were modeled. **1A** Injection below the free water level. **1B** Injection in the oil zone.

A simple reservoir model provides pressure, saturation, salinity, and temperature for different calendar times. Those are combined with a rock physics model and Gassmann's equations to create values of density and P- and S-wave velocities, from which synthetic reflectivity is calculated via Zoeppritz's equations (Zoeppritz, 1919). The reflectivity is then convolved with a wavelet, and white Gaussian noise is added to the synthetic data. The noisy data is used as input for an inversion algorithm, and the outputs are compared with the modeled values.

For this model, a logarithmic dependence of bulk and shear moduli with effective stress was assumed. The motivation behind this choice lies in the studies performed with rock samples analog to a reservoir whose analysis was planned at the beginning of the work plan. The expressions for K_{dry} and μ as functions of stress can be found in Appendix A.1.

No gas was assumed to be dissolved in the brine - although the amount of gas that can go into solution in brines is significantly less than the expected numbers for light oils, it can still have some impact on brine properties. It is worth mentioning that the expressions used for modeling the data hold for sodium chloride solutions - the most common salt in brines - and are very likely not valid when there are considerable amounts of other salts (Zarembo and Fedorov, 1975).

1.2.1 Scenario 1A - Injection Below Free Water Level

In this first modeled scenario, the only fluid in the pore space is brine. We consider the injection of seawater, which has a lower salinity (35,000 ppm) and lower temperature (20 °C) than the fluid originally in the formation (120,000 ppm and 80 °C, respectively). Besides, the injection makes the pore pressure increase with time, hence resulting in smaller effective stress.

Figure 1.2 shows the modeled effect of different salinities (we will use the symbol η for salinity), temperatures (T), and pore pressures (P_P) on the elastic properties of a rock. The full lines represent the values calculated using the empirical rock physics model (See Appendix A.1), Biot-Gassmann's equation (Equation 1.1) and Batzle & Wang's relations, while the circles represent a polynomial least-squares fit (1st and 2nd orders - Equations 1.11, 1.12 and 1.13) of the change of each elastic property according to the underlying reservoir parameter.

The approximations employed to fit the theoretical curves are very similar to the ones presented by Landro (2001):

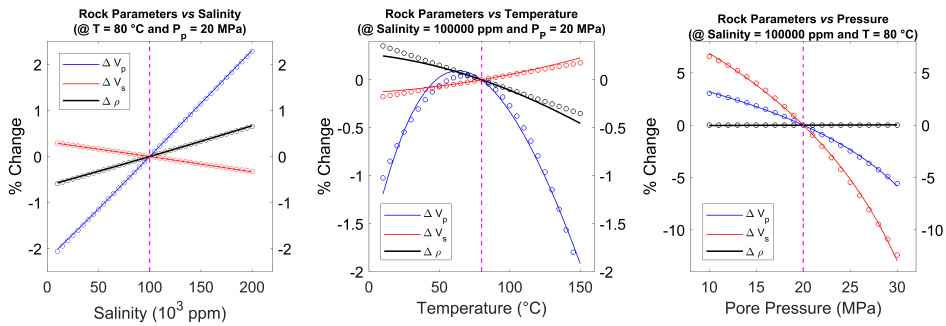

Figure 1.2: Relative changes in P-wave velocity (V_p - Blue), S-wave velocity (V_s - Red) and Density (ρ - Black) as a function of different reservoir properties. **Left** As a function of salinity (ppm), for a reference salinity - dashed in magenta - of 100,000 ppm. Fitted values using equation 1.11 are displayed in circles. **Center** Same, but for temperature (°C), with a reference temperature of 80°C. Fitted values obtained with equation 1.12. **Right** Same, but for pore pressure (MPa), with a reference value of 20 MPa. Fitted values obtained with equation 1.13.

- Elastic Properties *versus* Salinity (η)

$$\frac{\Delta V_p^{(\eta)}}{V_p} = f_\alpha \Delta\eta$$

$$\frac{\Delta V_s^{(\eta)}}{V_s} = f_\beta \Delta\eta \tag{1.11}$$

$$\frac{\Delta \rho^{(\eta)}}{\rho} = f_\rho \Delta\eta$$

- Elastic Properties *versus* Temperature (T)

$$\frac{\Delta V_p^{(T)}}{V_p} = q_\alpha \Delta T + r_\alpha (\Delta T)^2$$

$$\frac{\Delta V_s^{(T)}}{V_s} = q_\beta \Delta T \tag{1.12}$$

$$\frac{\Delta \rho^{(T)}}{\rho} = q_\rho \Delta T$$

- Elastic Properties *versus* Pore Pressure (P_P)

$$\frac{\Delta V_p^{(P_P)}}{V_p} = l_\alpha \Delta P_P + m_\alpha (\Delta P_P)^2$$

$$\frac{\Delta V_s^{(P_P)}}{V_s} = l_\beta \Delta P_P + m_\beta (\Delta P_P)^2 \tag{1.13}$$

$$\frac{\Delta \rho^{(P_P)}}{\rho} = 0$$

The constants in equations 1.11, 1.12 and 1.13 can be obtained from laboratory tests on core samples and plugs, or from calibrated well log data. Once they are known, a system of equations can be solved for obtaining the changes in pressure, salinity, and temperature (this step will be detailed later in this chapter). The input information to obtain those changes are the measured changes in the elastic properties of the reservoir - namely, density, P-wave velocity, and S-wave velocity.

One of the ways of obtaining these changes is by measuring the change in the reflectivity coefficient at a given interface for two different calendar dates. The forward problem - of finding reflectivity coefficients for a set of elastic parameters - is trivial, but the inverse one is not: directly obtaining the earth properties solely from the seismic response is an ill-posed problem (Tikhonov et al., 1998), a challenging task in several fields (Bertero and Boccacci, 1998).

Several approximations for Zoeppritz's equations are available in the literature. The most widely-adopted ones are Aki-Richards (Aki and Richards, 2002), Smith-Gidlow (Smith and Gidlow, 1987), and Fatti (Fatti et al., 1994b). These approximations allow us to have a more clear and intuitive understanding of the impact of each elastic parameter on the amount of energy that is reflected at an interface. They form the basis for AVO analysis - the study of the variation of reflected energy with the angle of incidence.

Originally a technique used for reservoir characterization (Ostrander, 1984), Landro (2001) has proposed the use of the changes in the AVO between time-lapse surveys as a source of information about the changes in the reservoir rock properties. The Smith and Gidlow (1987) approximation for the P-wave reflectivity, for example,

reads

$$R(\theta) = \frac{1}{2}\left(\frac{\Delta\rho}{\rho} + \frac{\Delta V_p}{V_p}\right) - 2\frac{V_s^2}{V_p^2}\left(\frac{\Delta\rho}{\rho} + 2\frac{\Delta V_s}{V_s}\right)\sin^2\theta + \frac{1}{2}\frac{\Delta V_p}{V_p}\tan^2\theta \tag{1.14}$$

In the expression above, the Δ symbol means the contrast of a certain parameter across a given interface between layers 1 and 2: $\Delta\rho = \rho_2 - \rho_1$. Following the same notation, $\rho = (\rho_2 + \rho_1)/2$.

In a first-order approximation, we can represent the change in reflection coefficient between two seismic surveys $R^{(t_1)}(\theta)$ e $R^{(t_2)}(\theta)$ as a function of the 4D relative changes in the elastic parameters:

$$\begin{aligned}\Delta R^{(4D)}(\theta) &= R^{(t_2)}(\theta) - R^{(t_1)}(\theta) \\ &\approx \frac{1}{2}\left(\frac{\Delta\rho^{(4D)}}{\rho} + \frac{\Delta V_p^{(4D)}}{V_p}\right) - 2\frac{V_s^2}{V_p^2}\left(\frac{\Delta\rho^{(4D)}}{\rho} + 2\frac{\Delta V_s^{(4D)}}{V_s}\right)\sin^2\theta \\ &+ \frac{1}{2}\frac{\Delta V_p^{(4D)}}{V_p}\tan^2\theta\end{aligned} \tag{1.15}$$

The index $4D$ on equation 1.15 means the difference in a given property between the calendar times t_1 and t_2. Making use of the Taylor expansion for trigonometric functions, and assuming small angles, $\tan^2\theta \approx \sin^2\theta + \mathcal{O}(\theta^4)$. We then have a expression similar to the one proposed by Shuey (1985):

$$\begin{aligned}\Delta R^{(4D)}(\theta) \approx \frac{1}{2}\left(\frac{\Delta\rho^{(4D)}}{\rho} + \frac{\Delta V_p^{(4D)}}{V_p}\right) + \Bigg[\frac{1}{2}\frac{\Delta V_p^{(4D)}}{V_p} \\ -2\frac{V_s^2}{V_p^2}\left(\frac{\Delta\rho^{(4D)}}{\rho} + 2\frac{\Delta V_s^{(4D)}}{V_s}\right)\Bigg]\sin^2\theta + \mathcal{O}(\theta^4)\end{aligned} \tag{1.16}$$

This equation can be written in a more compact form:

$$\Delta R^{(4D)}(\theta) = \Delta R(0) + \Delta G \times \sin^2\theta + \mathcal{O}(\theta^4) \tag{1.17}$$

We will use the expression above to fit the change in the reflection coefficient as a function of $\sin^2\theta$.

In many seismic acquisitions with the reflection method, the "usable" offsets comprise angles of incidence up to 30°. For such value, $\theta^4 \approx 0.075$. Besides, larger

offsets - for a given target depth - mean a larger effect of geometric spreading and, hence, less energy is being registered by the receivers: the large offset portion of the seismic signal usually displays lower SNR, which implies that the terms of high-order in θ for these approximations not only contribute less to the total reflectivity but also have higher uncertainty. Only $\Delta R(0)$ and ΔG, then, will be used in our analysis. These terms read

$$\Delta R(0) = \frac{1}{2}\left(\frac{\Delta\rho^{(4D)}}{\rho} + \frac{\Delta V_p^{(4D)}}{V_p}\right) \tag{1.18}$$

and

$$\Delta G = \frac{1}{2}\frac{\Delta V_p^{(4D)}}{V_p} - 2\frac{V_s^2}{V_p^2}\left(\frac{\Delta\rho^{(4D)}}{\rho} + 2\frac{\Delta V_s^{(4D)}}{V_s}\right). \tag{1.19}$$

Another common source of information that can be extracted from seismic data is the *travel time* τ in a given layer. Considering a layer of thickness h with a P-wave velocity V_p, the two-way travel time for normal incidence is

$$\tau = \frac{2h}{V_p}. \tag{1.20}$$

If we assume that the layer thickness is unchanged between two seismic surveys (this hypothesis should be verified by geomechanical analysis), we can write

$$\begin{aligned}
\Delta\tau &\approx \frac{\partial\tau}{\partial V_p}\Delta V_p^{(4D)} + \frac{1}{2!}\frac{\partial^2\tau}{\partial V_p^2}^2 \\
&= -\frac{1}{V_p}\overbrace{\frac{2h}{V_p}}^{\tau}\Delta V_p^{(4D)} + \frac{1}{V_p^2}\overbrace{\frac{2h}{V_p}}^{\tau}(\Delta V_p^{(4D)})^2 \\
&\left(\frac{\Delta V_p^{(4D)}}{V_p}\right)^2 - \left(\frac{\Delta V_p^{(4D)}}{V_p}\right) - \frac{\Delta\tau}{\tau} = 0.
\end{aligned} \tag{1.21}$$

We now employ these approximations to obtain expressions for the changes in salinity, pressure and temperature. Solving equation (1.21), we have

$$\frac{\Delta V_p^{(4D)}}{V_p} = \frac{1 \pm \sqrt{1 + 4\dfrac{\Delta\tau}{\tau}}}{2}.$$

The physical insight demands that we adopt the solution which implies zero changes in velocity when $\Delta\tau = 0$. That means

$$\frac{\Delta V_p^{(4D)}}{V_p} = \frac{1 - \sqrt{1 + 4\dfrac{\Delta\tau}{\tau}}}{2} \tag{1.22}$$

Using equation (1.18), we can isolate the change in density as a function of $\Delta R(0)$ and change in P-wave velocity:

$$\frac{\Delta\rho^{(4D)}}{\rho} = 2\Delta R(0) - \frac{\Delta V_p^{(4D)}}{V_p} \tag{1.23}$$

We re-write (1.19) as

$$\frac{\Delta\rho^{(4D)}}{\rho} + 2\frac{\Delta V_s^{(4D)}}{V_s} = \frac{V_p^2}{4V_s^2}\left(\frac{\Delta V_p^{(4D)}}{V_p} - 2\Delta G\right) \tag{1.24}$$

A key point here is the fact that the pore fluid content does not impact the rock shear modulus - this is an assumption from Biot-Gassmann's model, and can be seen from equation 1.4:

$$\begin{aligned}
\Delta V_s &\approx \frac{\partial V_s}{\partial\rho}\Delta\rho + \frac{\partial V_s}{\partial\mu}\cancelto{0}{\Delta\mu} \\
&= -\frac{1}{2\rho}\underbrace{\sqrt{\frac{\mu}{\rho}}}_{V_s}\Delta\rho \\
\frac{\Delta V_s}{V_s} &= -\frac{1}{2}\frac{\Delta\rho}{\rho}
\end{aligned} \tag{1.25}$$

The result above, combined with equations 1.11 and 1.12, implies that $f_\rho = -2f_\beta$ and $q_\rho = -2q_\beta$.

If we replace the left side of equation (1.24) with the approximations obtained in (1.11), (1.12) and (1.13), only the pressure term is non-zero. As for the right side of the equation, ΔG is measured in the seismic, and the change in P-wave velocity was obtained in (1.22), while the ratio between P-wave and S-wave velocities comes from the initial state of the reservoir. We then have

$$l_\beta\Delta P + m_\beta(\Delta P)^2 = \frac{V_p^2}{8V_s^2}\left(\frac{1 - \sqrt{1 + 4\dfrac{\Delta\tau}{\tau}}}{2} - 2\Delta G\right)$$

Re-arranging, we finally get

$$(\Delta P)^2 + b_P(\Delta P) + c_P = 0, \tag{1.26}$$

with

$$b_P = \frac{l_\beta}{m_\beta} \tag{1.27}$$

and

$$c_P = \frac{V_p^2}{8 m_\beta V_s^2}\left(2\Delta G - \frac{1-\sqrt{1+4\dfrac{\Delta\tau}{\tau}}}{2}\right) \tag{1.28}$$

Now, we will sum up the density and P-wave contributions of (1.11), (1.12) and (1.13). We get

$$\begin{aligned}\frac{\Delta V_p^{(4D)}}{V_p} &= l_\alpha \Delta P + m_\alpha (\Delta P)^2 + f_\alpha \Delta\eta + q_\alpha \Delta T \\ &\quad + r_\alpha (\Delta T)^2 \qquad \text{and} \\ \frac{\Delta\rho^{(4D)}}{\rho} &= f_\rho \Delta\eta + q_\rho \Delta T\end{aligned}$$

From the second expression, we can isolate $\Delta\eta$ and substitute in the first one:

$$\begin{aligned}\Delta\eta &= \frac{1}{f_\rho}\left(\frac{\Delta\rho^{(4D)}}{\rho} - q_\rho \Delta T\right) \\ \frac{\Delta V_p^{(4D)}}{V_p} &= l_\alpha \Delta P + m_\alpha (\Delta P)^2 + r_\alpha (\Delta T)^2 \\ &\quad + \frac{f_\alpha}{f_\rho}\left(\frac{\Delta\rho^{(4D)}}{\rho} - q_\rho \Delta T\right) + q_\alpha \Delta T\end{aligned} \tag{1.29}$$

Now, all we have to do is re-arrange this result and use the previously obtained expressions for density (1.23) and P-wave velocity (1.22). We then get

$$(\Delta T)^2 + b_T(\Delta T) + c_T = 0, \tag{1.30}$$

with

$$b_T = \frac{q_\alpha - \dfrac{f_\alpha}{f_\rho} q_\rho}{r_\alpha}$$

and

$$c_T = \frac{1}{r_\alpha}\left\{2\Delta R(0)\frac{f_\alpha}{f_\rho} + l_\alpha \Delta P + m_\alpha(\Delta P)^2 - \frac{1-\sqrt{1+4\dfrac{\Delta\tau}{\tau}}}{2}\left(1+\frac{f_\alpha}{f_\rho}\right)\right\}$$

Once the temperature value is calculated, we input it in (1.29) and use (1.23) for the density. We get then

$$\begin{aligned}\Delta\eta &= \frac{1}{f_\rho}\left(\frac{\Delta\rho^{(4D)}}{\rho} - q_\rho \Delta T\right)\\ &= \frac{1}{f_\rho}\left(2\Delta R(0) - \frac{1-\sqrt{1+4\dfrac{\Delta\tau}{\tau}}}{2} - q_\rho\Delta T\right)\end{aligned}$$

In a more compact form, we can write

$$\Delta P_P = \frac{-b_P + \mathrm{sgn}(b_P)\sqrt{b_P^2 - 4c_P}}{2} \tag{1.31}$$

$$\Delta T = \frac{-b_T + \mathrm{sgn}(b_T)\sqrt{b_T^2 - 4c_T}}{2} \tag{1.32}$$

$$\Delta\eta = \frac{1}{f_\rho}\left[2\Delta R(0) - \frac{1-\sqrt{1+4\dfrac{\Delta\tau}{\tau}}}{2} - q_\rho\Delta T\right] \tag{1.33}$$

In equations 1.31 and 1.32, the effect of the seismic measurements (reflectivity and traveltime) is contained in the parameter c. If the seismic remains unchanged, $c = 0$. That's the reason why we use the signal function $\mathrm{sgn}(b)$ in the solution: there are two mathematically possible solutions, but only one will be zero when the seismic response is null.

Uncertainty Estimation

The results displayed previously are an attempt to simplify the relations between reservoir properties and time-lapse seismic response, which are highly non-linear. Even though we were able to find some 2$^{\text{nd}}$-order analytic solutions, we still face

the non-linearity dependence between variables. That can be a complication when we try to propagate the error of our measurements since most of the exact solutions for error propagation hold only for functions that are linear combinations of their variables.

What we will do here is use a first-order approximation for the error propagation (Ku, 1966). The linearization of functions for this purpose is common practice in engineering since many techniques - such as Kalman filter (Emerick and Reynolds, 2012) - are optimal when dealing with linear inputs.

For a function $f(\mathbf{x}) = f(x_1, x_2, ..., x_n)$, the variance in f will depend on the Jacobian matrix of f - which reduces to the gradient vector, since our function is scalar - and the variance-covariance matrix Σ^x, which contains the uncertainty in the input variables. The variance σ_f^2 is given by

$$\sigma_f^2 = \begin{bmatrix} \frac{\partial f}{\partial x_1} & \frac{\partial f}{\partial x_2} & \cdots & \frac{\partial f}{\partial x_n} \end{bmatrix} \begin{bmatrix} \sigma_1^2 & \sigma_{12} & \sigma_{13} & \cdots \\ \sigma_{21} & \sigma_2^2 & \sigma_{23} & \cdots \\ \sigma_{31} & \sigma_{32} & \sigma_3^2 & \cdots \\ \cdots & \cdots & \cdots & \ddots \end{bmatrix} \begin{bmatrix} \frac{\partial f}{\partial x_1} \\ \frac{\partial f}{\partial x_2} \\ \vdots \\ \frac{\partial f}{\partial x_n} \end{bmatrix},$$

or, more compactly,

$$\sigma_f^2 = (\boldsymbol{\nabla} f)\Sigma^x(\boldsymbol{\nabla} f)^\top, \tag{1.34}$$

where $\sigma_{ij} = \text{cov}(x_i, x_j) = \text{E}[(x_i - \bar{x_i})(x_j - \bar{x_j})]$ is the covariance between variables x_i and x_j.

In our case, the functions f will be the estimated changes in pore pressure, temperature and salinity. The variables $\mathbf{x}$ are the seismic measurements ($\Delta R(0)$, ΔG, $\Delta\tau/\tau$) and the constants used to fit the elastic parameters of the formation as a function of reservoir properties (l_α, m_α, l_β, m_β, q_α, r_α, q_ρ, f_α, f_ρ), amounting to 12 variables, and a total of 144 elements in the variance-covariance matrix.

The variance σ_i^2 of each variable can be obtained from the measured data. The co-variance, however, might be a bit more challenging to evaluate: in principle, there should be no correlation between, for example, laboratory measurements of S-wave velocity and seismic measurements of two-way traveltime. We assumed no correlation between the measurements of rock physics and seismic data.

The rock physics parameters were modeled according to a normal distribution.

Mean value ψ_i was set as the correct value of each of them, and standard deviation σ_i to 20% of the mean value. The correlation coefficients ϱ_{ij} was generated randomly, in the interval $[-0.4,\ 0.4]$. The index i and j range from 1 to 9, representing the constants used for least-square fit in equations 1.11, 1.12 and 1.13. Then a set of values was calculated using a multivariate normal distribution, with mean $\Psi = \{\psi_i\}$ and variance-covariance Υ. The set of points has a probability density function D given by

$$D(\mathbf{y}) = \frac{\exp\left[-\frac{1}{2}\left(\mathbf{y}-\Psi\right)^{\top}\Upsilon^{-1}\left(\mathbf{y}-\Psi\right)\right]}{(2\pi)^{6}\sqrt{|\Upsilon|}}, \tag{1.35}$$

with $\mathbf{y} = (\Delta R(0),\ \Delta G,\ \Delta\tau/\tau,\ l_\alpha,\ m_\alpha,\ l_\beta,\ m_\beta,\ q_\alpha,\ r_\alpha,\ q_\rho, f_\alpha,\ f_\rho)$.

From the set of values described by D, the variance-covariance matrix Σ is computed. An example can be checked in Figure 1.3, for noisy seismic data. Notice that there is no correlation between the pairs of variables seismic-rock physics. For displaying, all the variables have been standardized, being transformed to distributions with mean 0 and standard deviation equal to 1.

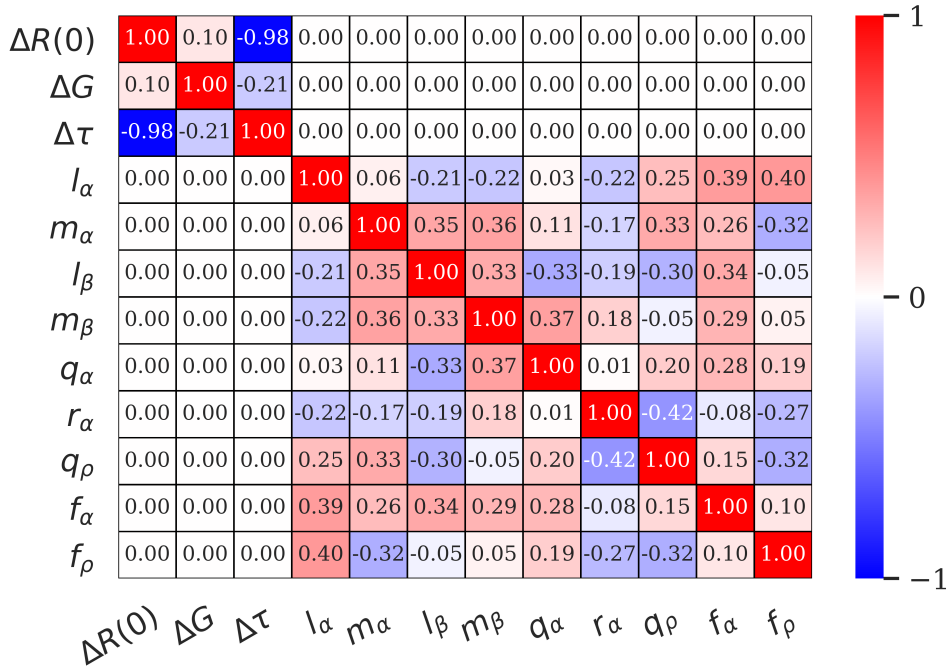

Figure 1.3: Variance-Covariance matrix Σ for standardized variables.

There are situations in which a correlation between rock physics parameters and seismic measurements might arise. In field data, seismic will be available at every point of the seismic grid (or other upscaled/downscaled grid used for inversion). Ideally, rock physics parameters should be represented in the same grid. The number of rock samples taken for studies, however, is often very limited, and this "hard" data will be restricted to a few wells.

Representation of rock data in the whole area of study is usually done using geostatistics (Matheron, 1963; Coburn, 2000), being *kriging* a widely employed method (Cressie, 1990). Kriging can be improved by using a regional variable as a trend, in a technique called kriging with external drift (Pebesma, 2006). For this, the variables must correlate, like in the use of acoustic impedance as drift for creating porosity volumes. If a similar method is employed to estimate the rock physics constants in the inversion grid, with seismic-derived attributes being used as trends, a non-zero covariance component between seismic measurements and rock parameters may appear.

In the particular case when we disregard all the covariance terms and consider only the variance of $\mathbf{x}$, the standard deviation of f becomes

$$\sigma_f = \sqrt{\left|\frac{\partial f}{\partial x_1}\right|^2 \sigma_1^2 + \left|\frac{\partial f}{\partial x_2}\right|^2 \sigma_2^2 + \cdots + \left|\frac{\partial f}{\partial x_n}\right|^2 \sigma_n^2}$$

The analytic expression for partial derivatives of each variable (pressure, temperature, and salinity) are calculated in Appendix B.

Results

The modeled distributions of pore pressure and brine salinity for this scenario can be verified in Figure 1.4 for a given time step.

In Figure 1.2 it is possible to see how the reservoir dynamic properties affect the elastic properties, one reservoir parameter at a time. In the reservoir model, however, all properties are changing simultaneously, at different rates. Figure 1.5 shows how each of them contributes to the total change in the P-wave velocity and density. It can be seen that the sum of the effects of each parameter is not exactly equal to the total change of all parameters combined. This happens because of the non-linearity of the Batzle-Wang equations. Still, the approximation is quite reasonable.

The inverted changes in pore pressure, brine salinity and brine temperature, obtained using equations (1.31), (1.32) and (1.33), are displayed in Figures 1.6, 1.7 and 1.8.

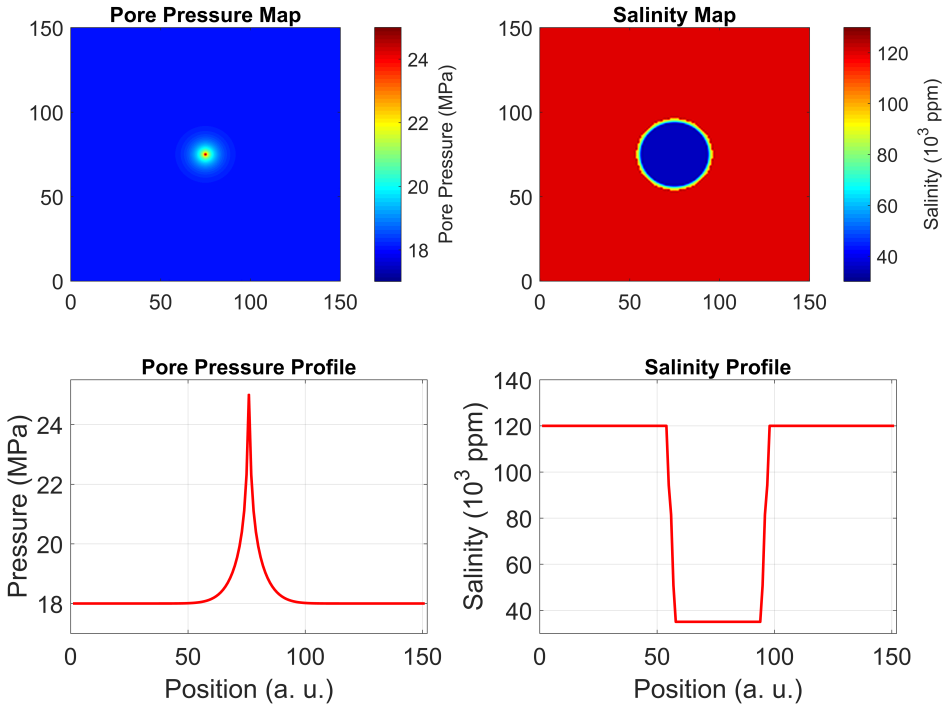

Figure 1.4: Top Areal distributions of pore pressure (left) and brine salinity (right). **Bottom** Distributions of pore pressure and salinity along a E-W or N-S section through the well.

The obtained result for the pressure is a good example of the influence of salinity on time-lapse seismic interpretation. If we disregard the salinity and temperature contrasts and interpret the whole 4D signal as being caused by the effects of change in pore pressure, we obtain the green curve in Figure 1.6. This curve is an overestimation of the correct result, and one can see that it has a sharp interface, resembling a water injection front: that is a warning that this effect is likely to be caused by fluid displacement, not pressure.

The results for brine salinity (Figure 1.7) and temperature (Figure 1.8) are a bit less encouraging. As it can be seen, the predicted salinity close to the well is actually below the injected water salinity (35,000 ppm), which is not physically possible. These results arise from the extremely high sensitivity that temperature has to the measured seismic parameters.

Checking Figure 1.9, we can see that we are in the range of values close to the maximum of the function $\Delta V_p/V_p = f(T)$, which means that the derivative is

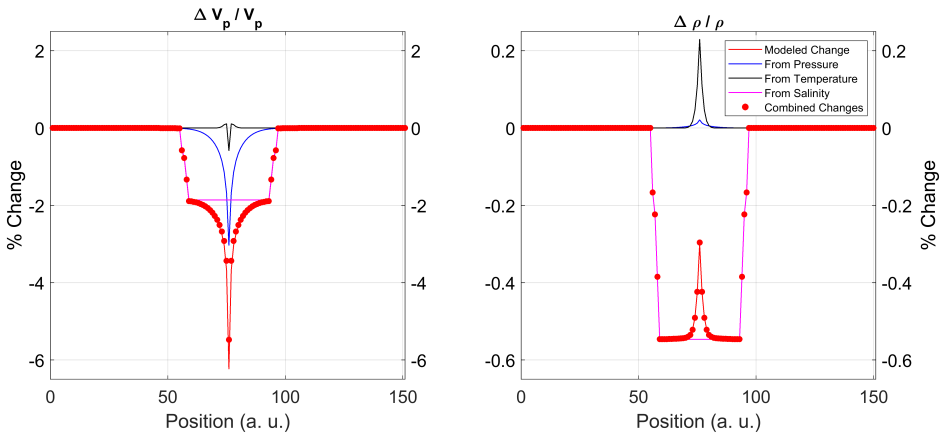

Figure 1.5: Relative Changes in P-wave velocity (**left**) and density (**right**) caused by changes in pore pressure (blue), temperature (black) and brine salinity (magenta). The red line represents the exact change in the reservoir. The red circles represent the sum of the isolated effect of each parameter.

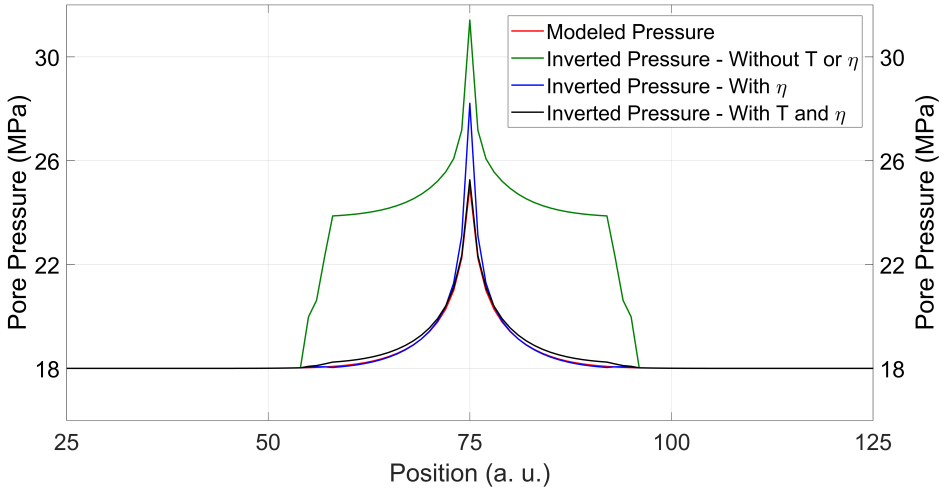

Figure 1.6: Inverted pore pressure, obtained from 1.31 and noise-free synthetic data. The Red line is modeled data, green is the result obtained without considering the effects of temperature or salinity, blue is the result considering only the effect of salinity, and black is the result obtained considering all the parameters.

close to zero, and the velocity changes slowly, even with large temperature variations. We can also see that by plotting $\Delta T = f^{-1}(\Delta V_p/V_p)$ (rightmost plot in Figure 1.9).

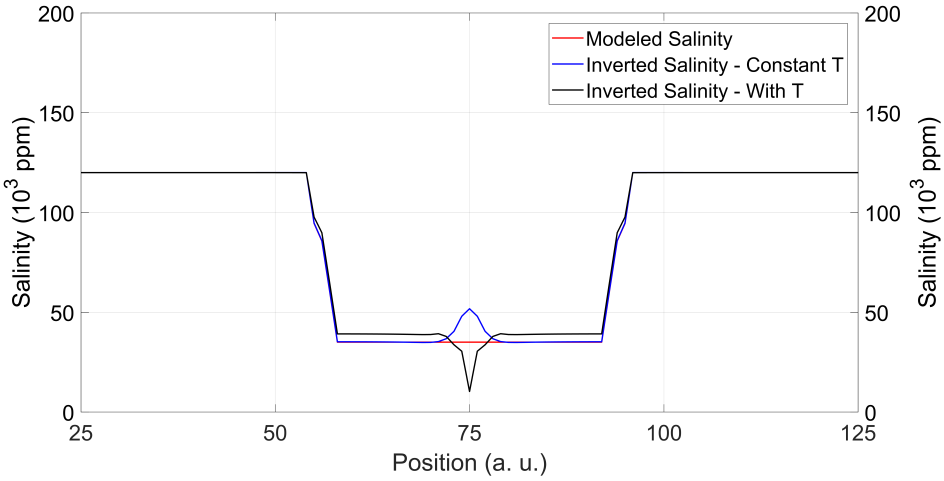

Figure 1.7: Inverted brine salinity, obtained from 1.33 and noise-free synthetic data. Red line is modeled data, blue is the result obtained without considering the effect of temperature, and black is the result obtained considering all the parameters.

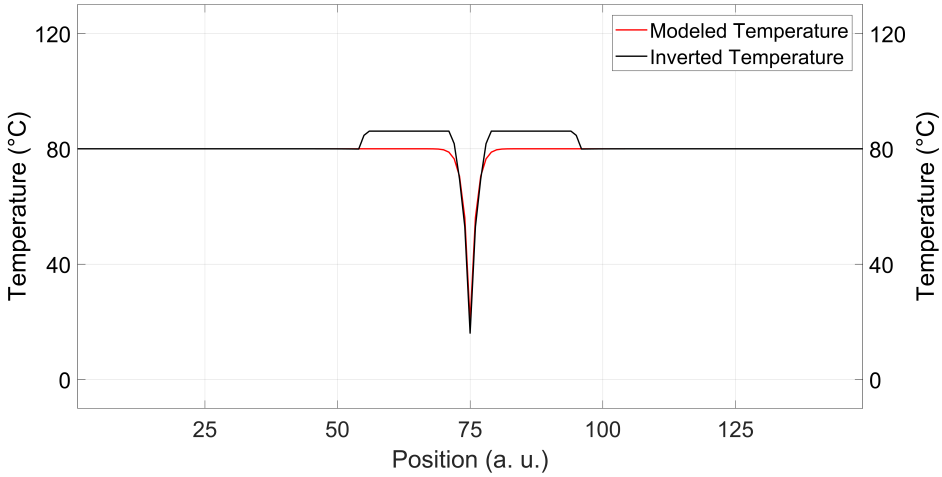

Figure 1.8: Inverted brine temperature, obtained from 1.32 and noise-free synthetic data. Red line is modeled data, and black is the result from inversion.

It can be seen that, in the range of values that we are studying, a 0.5% change in P-wave velocity would mean a drop of around 54 °C in brine temperature, while a 1% change means 66 °C drop. This is why even a minor misfit in the data (which happens when we use linear and quadratic approximations) can result in a substantial mistake in the estimated temperature. The mistake "propagates" to the

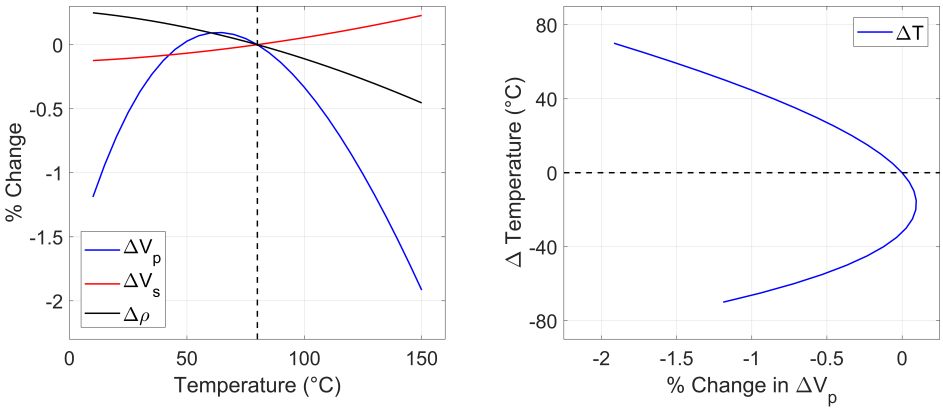

Figure 1.9: Left Variation of rock properties with temperature (reference value is 80 °C). Same as central plot in Figure 1.2. **Right** Inverse function of blue curve on the left, or P-wave velocity variation as function of temperature changes, when all other parameters are held constant. Black dotted line is a reference for $\Delta T = 0$.

calculation of salinity since the two are obtained simultaneously.

Figures 1.10, 1.11 and 1.12 show some results for the the calculations in the presence of white Gaussian noise. It can be seen in Figure 1.10 that the uncertainty in the estimated pressure is fairly low, while those for salinity and temperature are much higher. This is a hint that even for very high-quality seismic data, these estimates should be interpreted with prudence.

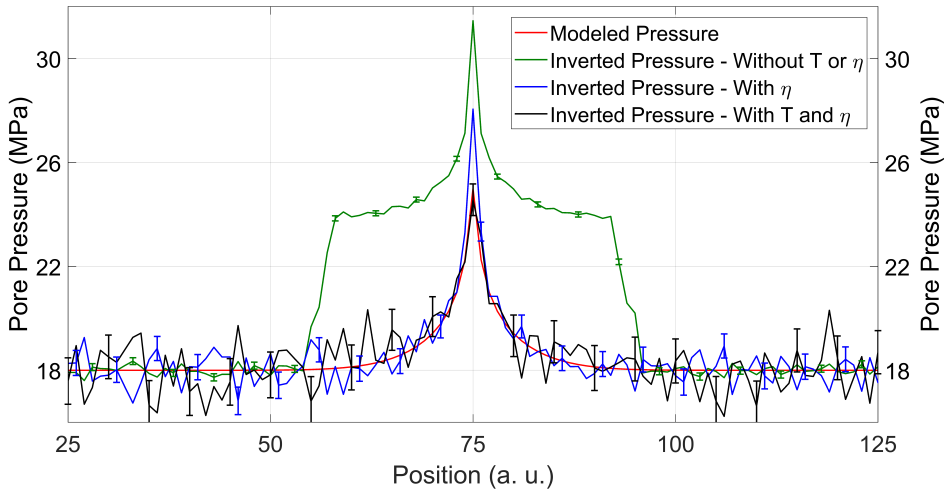

Figure 1.10: Inverted pore pressure, obtained from 1.31 and noisy synthetic data. The Red line is modeled data, green is the result obtained without considering the effects of temperature or salinity, blue is the result considering only the effect of salinity, and black is the result obtained considering all the parameters. Error bar represents one standard deviation, calculated using 1.34.

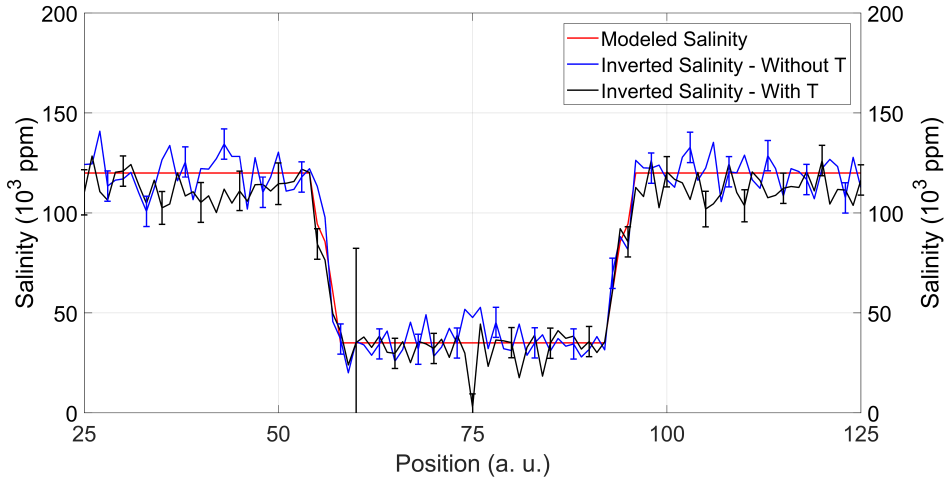

Figure 1.11: Inverted brine salinity, obtained from 1.33 and noise-free synthetic data. Red line is modeled data, blue is the result obtained without considering the effect of temperature, and black is the result obtained considering all the parameters. Error bar represents one standard deviation, calculated using 1.34.

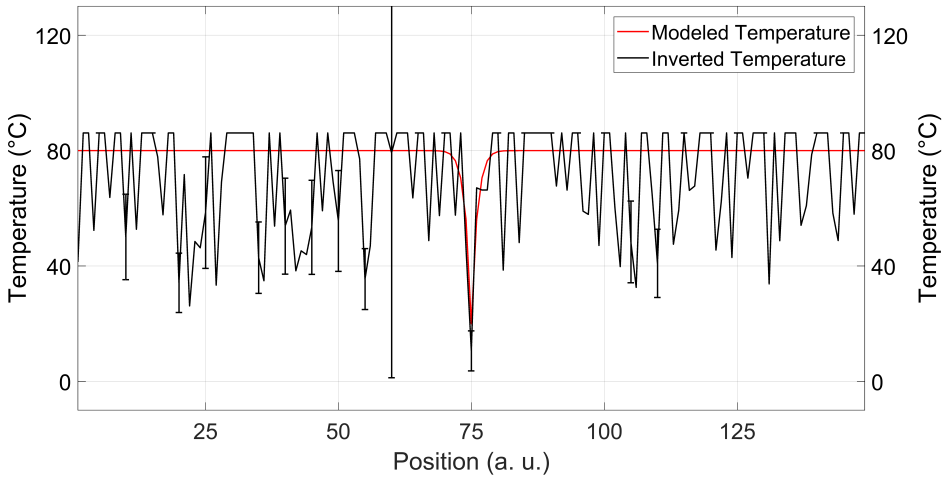

Figure 1.12: Inverted brine temperature, obtained from 1.32 and noise-free synthetic data. Red line is modeled data, and black is the result from inversion. Error bar represents one standard deviation, calculated using 1.34.

1.2.2 Scenario 1B - Water Sweep

Scenario **1B** simulates the injection of seawater in a initially oil-saturated reservoir. In this case, both the brine saturation and its salinity are changing simultaneously. The pore pressure is also increasing. Since the temperature behaviour of hydrocarbons is composition-dependent and complex, we decided to drop this effect here, as it is not the focus of the analysis.

Like in Scenario **1A**, a simple reservoir model is used to model a time series of pressure, salinity and saturation. Low salinity injection (2,000 ppm) is also investigated. The elastic changes are calculated and, using synthetic seismic data as input, we recover the changes in the dynamic reservoir parameters.

For time-dependent saturation, the linear approximations proposed in equations 1.11, 1.12 and 1.13 fail to represent the rock behaviour accurately. A non-linear least squares method is employed to achieve the best estimations of pressure, saturation and salinity. In order to obtain the uncertainty, we performed several realizations with random rock physics parameters and noise levels.

A time-lapse measurement $\mathbf{S}$ is a measure of the changes in the elastic properties of the rock - V_p, V_s and ρ. These changes depend on the changes in the reservoir parameters $\mathbf{R}$ - pore pressure (P_P), Water Saturation (S_w) and salinity (η). The quantities $\mathbf{S}$ and $\mathbf{R}$ are connect by a set of rock physics relations $\mathscr{P}$. We can write

$\mathbf{S} = \mathscr{P}\mathbf{R}$ or, identically,

$$\begin{bmatrix} \Delta V_p/V_p \\ \Delta V_s/V_s \\ \Delta \rho/\rho \end{bmatrix} = \begin{bmatrix} \\ \text{Rock Physics} \\ \\ \end{bmatrix} \begin{bmatrix} \Delta S_w \\ \Delta \eta \\ \Delta P_P \end{bmatrix}$$

Ideally, we would be able to invert the "Rock Physics" matrix and correctly obtain the reservoir parameters from the measured seismic data. The complexity of this matrix, however, prevents us from doing so point-blankly. We then resort to finding the values $\mathbf{R}^*$ which minimize the squared difference between the measured seismic and values generated by the rock physics model:

$$\mathbf{R}^* = \arg\min \left|\mathbf{S}(\mathbf{R}) - \mathbf{S}^{\text{obs}}\right|^2 \tag{1.36}$$

The algorithm used for the minimization was the one proposed by Levenberg (1944), also known as damped least-squares.

Uncertainty Estimation

The estimated error for scenario **1B** was calculated in a different fashion. Since it is difficult to obtain an explicit relation between the reservoir properties and the seismic measurements, we ran several different models considering different input parameters for our rock physics model, as well as different noise levels. The modeled data was always kept the same: the idea was to simulate the uncertain in the rock physics model used for the analysis.

The rock physics parameters were assumed as having a normal distribution, with mean value equal to the correct one (used for modeling the synthetic data) and standard deviation of 20% of the mean value.

Results

Figures 1.13, 1.14 and 1.15 show the results of the inversion for scenario **1B**. It is clear that, in the case where water is displacing oil, the influence of the salinity contrast is much less significant. This influence gets more expressive if the original hydrocarbon in the formation is heavy oil.

A scenario of low-salinity water injection (LSW) was also investigated, using a 2,000 ppm salinity for the injected water. The result for water saturation can be checked in figure 1.16. Once again, the impact of the salinity in this scenario is marginal, though it may be quantifiable in seismic data of very high SNR like those from permanent reservoir monitoring arrays (Thedy et al., 2015).

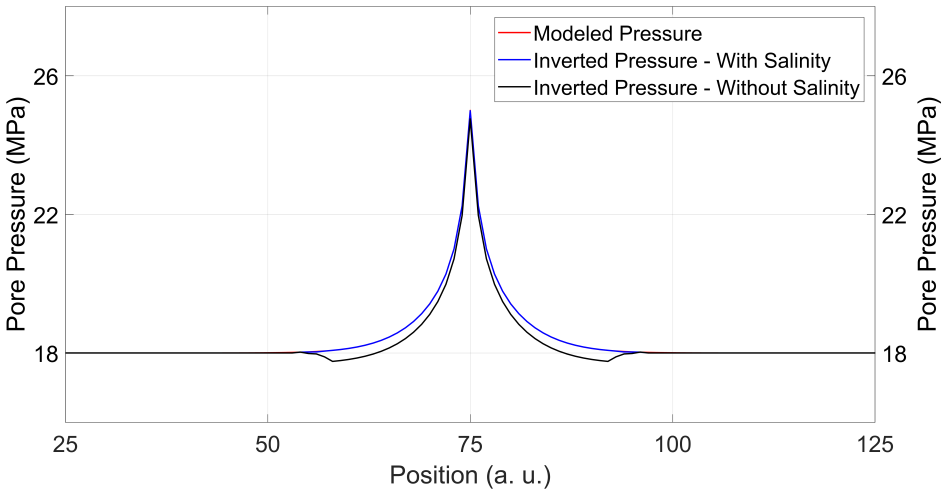

Figure 1.13: Inverted pore pressure, obtained from (1.36) and noise-free synthetic data. Red line is the modeled data, black line is the result obtained without considering the effect of salinity, and blue line is the result obtained considering all the parameters.

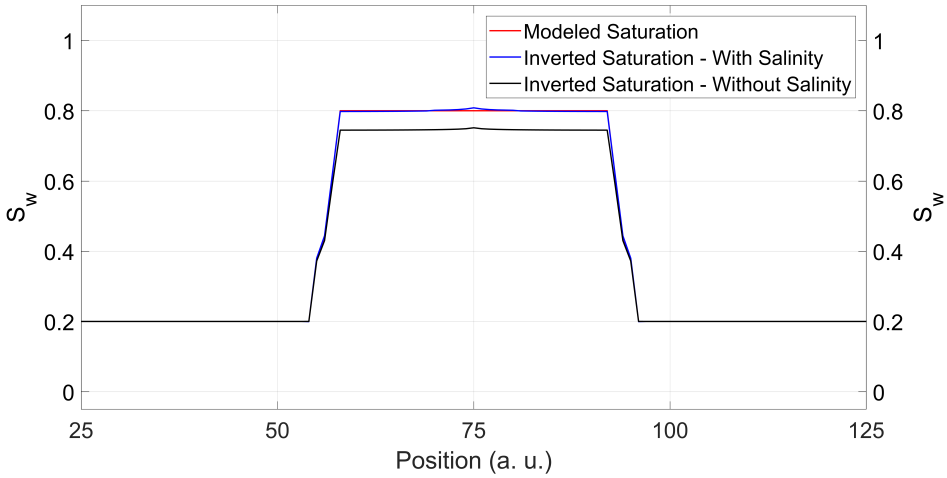

Figure 1.14: Inverted brine saturation, obtained from (1.36) and noise-free synthetic data. Red line is the modeled data, black line is the result obtained without considering the effect of salinity, and blue line is the result obtained considering all the parameters.

Figures 1.17, 1.18 and 1.19 display the results obtained when noise is added to the synthetic data, for the case of seawater injection. As in scenario **1A**, one can see that even low levels of noise, with low impact in pressure and saturation estimates, cause a substantial uncertainty in the calculated salinity.

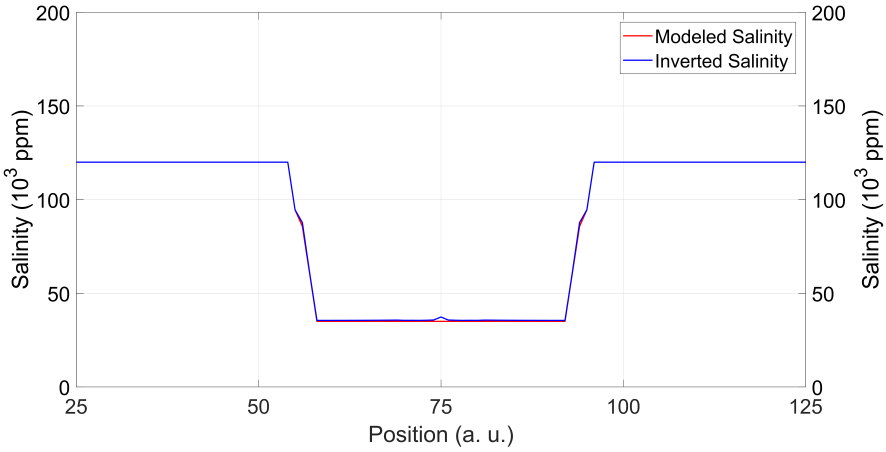

Figure 1.15: Inverted brine salinity, obtained from (1.36) and noise-free synthetic data. Red line is the modeled data, and blue line is inverted salinity.

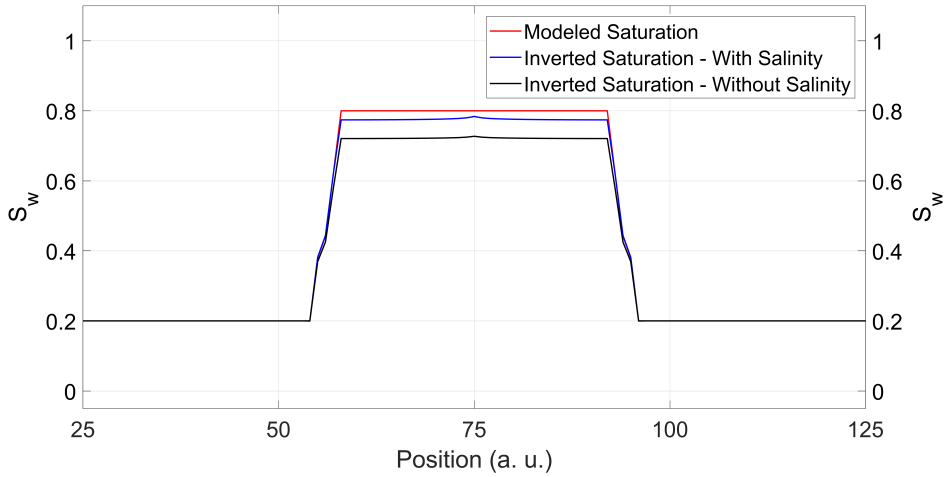

Figure 1.16: Inverted brine saturation, obtained from (1.36) and noise-free synthetic data for a low-salinity injection scenario. Red line is the modeled data, black line is the result obtained without considering the effect of salinity, and blue line is the result obtained considering all the parameters.

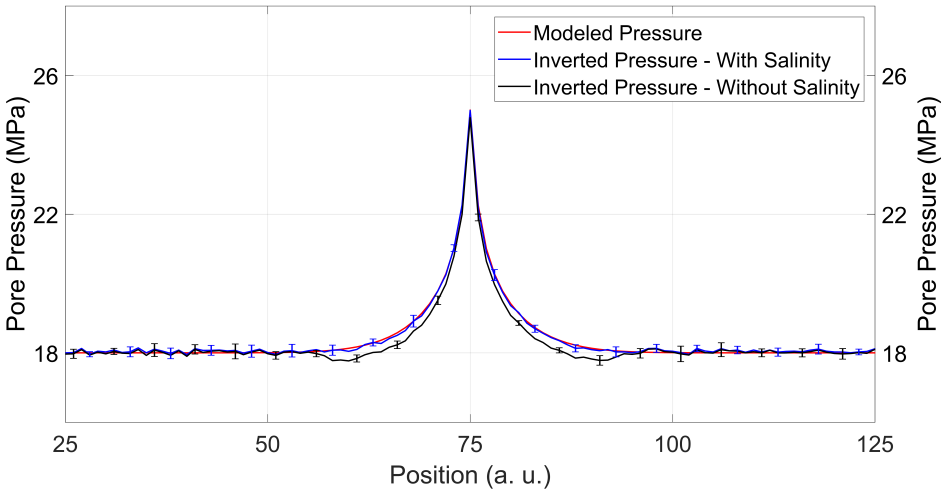

Figure 1.17: Inverted pore pressure, obtained from (1.36) and synthetic data with added noise. Red line is the modeled data, black line is the result obtained without considering the effect of salinity, and blue line is the result obtained considering all the parameters. Error bar represents one standard deviation in a normal distribution.

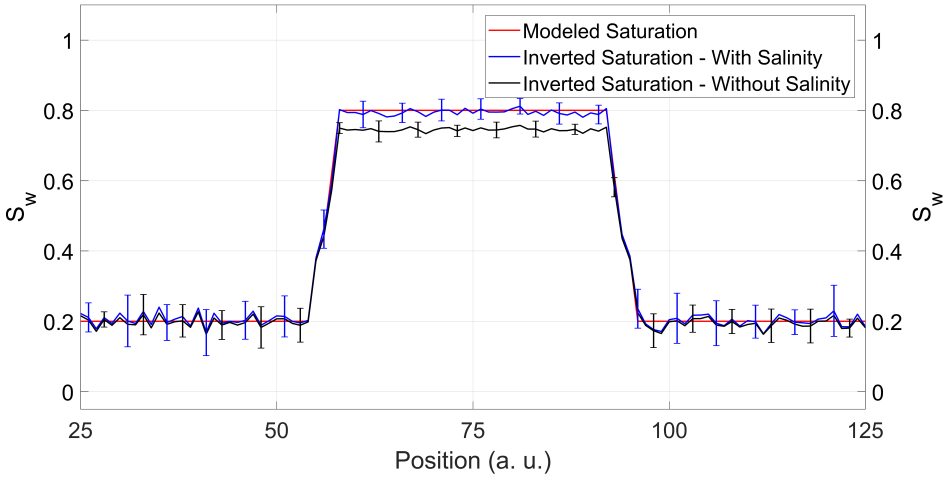

Figure 1.18: Inverted brine saturation, obtained from (1.36) and synthetic data with added noise. Red line is the modeled data, black line is the result obtained without considering the effect of salinity, and blue line is the result obtained considering all the parameters. Error bar represents one standard deviation in a normal distribution.

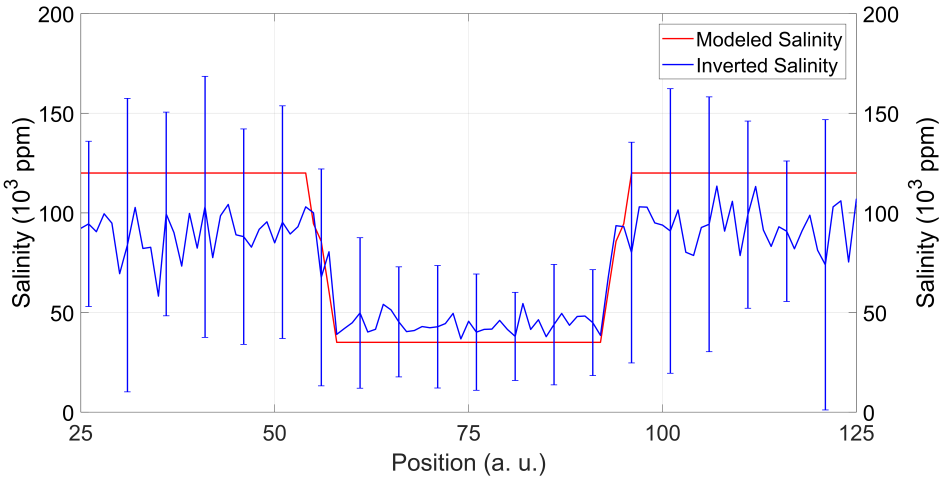

Figure 1.19: Inverted brine salinity, obtained from (1.36) and synthetic with data added noise. Red line is the modeled data, and blue line is inverted salinity. Error bar represents one standard deviation in a normal distribution.

1.2.3 Discussion

Injection of seawater as an IOR method can change the salinity of the reservoir brine. Modelling shows that this difference can be significant when dynamic reservoir properties are estimated from time-lapse seismic surveys. The estimation of salinity will likely show a high intrinsic uncertainty, but accounting for it can be important to obtain more accurate values of other properties of interest.

In the case of water injection in the aquifer, a significant contrast of salinity (about 100,000 ppm or more) between the injected water and the formation brine may have a non-negligible contribution to the total 4D signal. Hence, not taking the salinity into account as a degree of freedom can mislead the inversion for changes in pore pressure.

When the scenario of waterflood is evaluated, the salinity contrast seems to play a smaller role in time-lapse interpretation. The mismatch between blue and black lines in Figure 1.14 has the same order of magnitude of the uncertainty bars in Figure 1.18, prompting us to interpret that the correction due to the use of salinity will likely be below the expected accuracy of the seismic measurement.

Some premises assumed to develop this work may limit its applicability. Biot-Gassmann's equation assumes an isotropic reservoir, low frequencies and homogeneous composition of rock frame. These conditions are usually fulfilled in deep turbidite reservoirs. Also, it was assumed a homogeneous saturation when more

than one fluid was involved, which may not always hold true.

Data from amplitude and traveltime from the seismic experiment were also considered to be reliable, even if noisy. If the reservoir is below the tuning threshold, one can no longer trust the amplitude as a true representation of the Earth response. Time-shift measurements also become unreliable in this situation. The use of inverted data is advised.

The next step in this work is testing the method in field data. The ideal configuration would be monitoring the injection of low-salinity water in the aquifer, with a pressure similar to the formation's: we would be able to isolate the observed changes as salinity-dependent only.

1.3 Fluid-Pressure Discrimination with an Arbirtrary Fluid Mixing Law

The way the fluids mix in the pore space plays an important role in quantitative interpretation of time-lapse data. We have previously assumed that a mixture of fluids in the pore space could have its effective behaviour represented by the Reuss average of all the fluids. This is, however, only one of the many models for effective fluid properties under partial saturation. Among the several available models, we highlight here two particular cases:

Homogeneous Mixing When a pressure change is applied to a point in the fluid, it rapidly balances in all fluids and phases. Usually implies that the fluids are mixed on a finer scale. The effective fluid bulk modulus can be approximated by the Reuss average K_R (Equation 1.3).

Heterogeneous Mixing Large amounts of a single fluid/phase are clustered in areas of dimensions similar to the wavelength. Their local behavior can be reproduced by Gassmann's equation for a single fluid, but surrounding patches will have different bulk moduli. The effective fluid bulk modulus can be approximated by the Voigt average K_V.

Following a notation similar to 1.3, the effective fluid for the case of **heterogeneous mixing** can be written as

$$K_V = \sum_i S_i K_i \tag{1.37}$$

Pressure-fluid discrimination depends on the effective properties of the fluid mix, and understanding the mixing laws is important not only for surveillance of pro-

ducing hydrocarbon reservoirs: the massive increase in CCS projects in the last decade has led to a necessity of monitoring the proper storage of CO_2, so as to ensure that the injected gas remains stored in the target reservoir, and that there is no abnormal pore pressure build up. A very popular model for the effective properties of a mix between gas and fluids is the one proposed by Brie et al. (1995):

$$K_{Brie} = (K_{liquid} - K_{gas})(1 - S_{gas})^e + K_{gas} \tag{1.38}$$

In Brie's formula, K_{liquid} stands for the Reuss average of the liquid phase, and e is an empirical constant, often set to 3.

Since we usually do not know the actual mixing law in the pore space, the relation between effective fluid modulus and fluid saturation is no longer unique: one can not directly derive P-wave velocity from saturation alone. Hence, an assumption on fluid mixing is frequently made prior to interpretation.

Despite being frequently used to model the effective bulk modulus of partial saturations, Brie's formula is empirical, and can sometimes fall outside the "physical" bounds for a the fluid mixture. This can be seen in Figure 1.20, where Brie's average drops below the lower bound. Rock physics and fluid parameters for modeling can be checked in Appendix A.2.

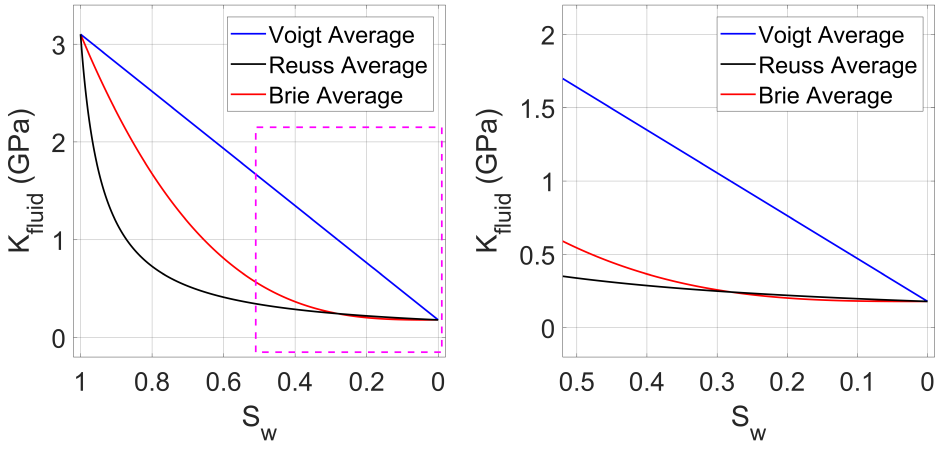

Figure 1.20: Left Upper (Voigt - blue) and Lower (Reuss - black) bounds for a CO_2-brine mixture, for different brine saturations S_w ($S_w + S_{CO_2} = 1$). Brie's relation with coefficient $e = 3$ is drawn in red. **Right** Zoom in the area marked by magenta square in left plot. Notice that Brie's average falls below the Reuss bound for some saturations.

Regardless of the real mixing law, Reuss and Voigt averages act respectively as lower and upper bounds for the effective modulus of the mixture. For any mixture,

an effective fluid modulus K_{fl} can always be written as

$$K_{fl} = fK_R + (1-f)K_V, \qquad 0 \leq f \leq 1 \tag{1.39}$$

We can then represent the effective fluid modulus as a two-variable function, depending both on the f number and the fluid saturation. Figure 1.21 (left) shows the bulk modulus of a mixture of water and CO_2, as a function of f and water saturation. In order to properly represent the effective fluid modulus in a 2D plot, we can project all the values in the K-S_w plane, as in Figure 1.21 (right).

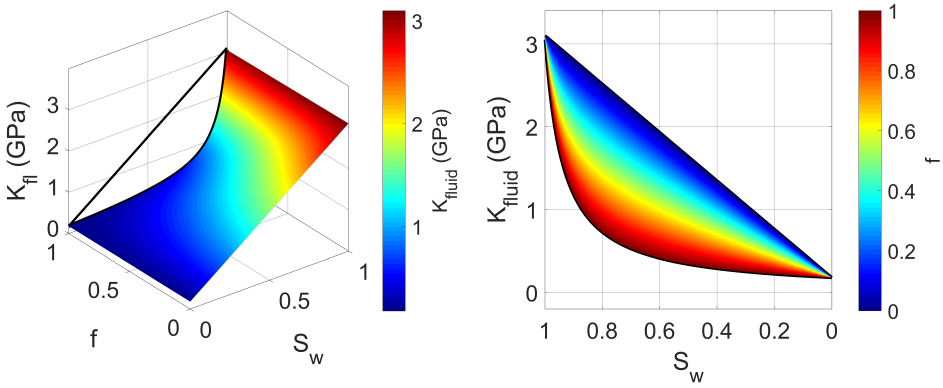

Figure 1.21: Left Fluid bulk modulus for a mixture of water and CO_2, as function of water saturation (S_w) and f value, as in equation 1.39. Full black lines are K_R and K_V, and color scale is K_{fl}. **Right** 2D projection of the left plot. Thick black lines are Reuss and Voigt averages. Color scale is f number.

As mentioned before, in most 4D seismic studies an assumption is made about the kind of fluid mixture law that better represent the fluid behavior in the reservoir, being the most common assumption that of homogeneous mixing. To study the effect of this choice in the predictions, we will make no such assumption, but rather set the fluid mixture law as a degree of freedom in an inversion for pore pressure, water saturation, and f number, hence making sure that we use a model that respects the physical bounds of the mixture, and also works with a linear relation for the mixture-dependent coefficient, instead of an exponential one like in equation 1.38.

1.3.1 Modelling

For this study, the reservoir scenario considered was injection of CO_2 in an homogeneous sandstone which initially was 100% saturated with brine. Temperature was held constant. We generated a time series of values of fluid saturation and pore

pressure, which we will try to recover using an inversion procedure based on measured reflectivity and time-shift - a similar workflow to that applied in section 1.2. We compare the results obtained with our method and when wrong assumptions are made about the fluid mixing law.

The modeled pressure and saturation values can be checked in Figure 1.22. The black lines are the general trend of the model: increase in pore pressure and decrease in water saturation, both caused by CO_2 injection. The red dots represent the calendar dates when the reservoir is sampled.

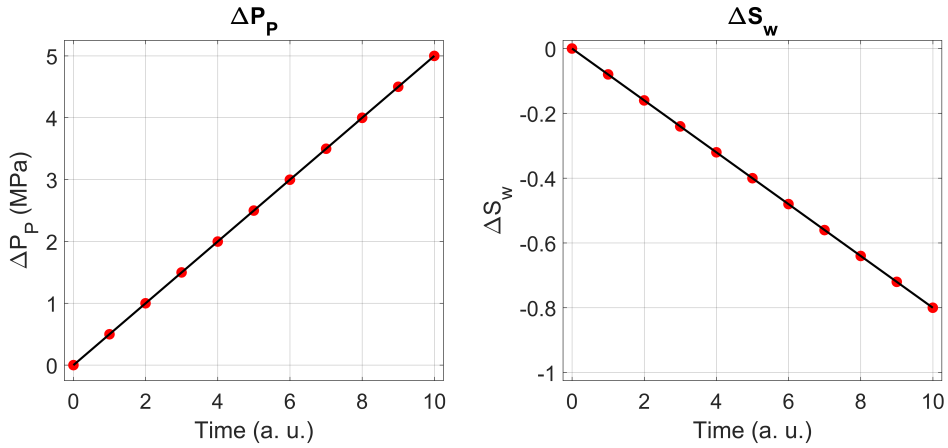

Figure 1.22: Reservoir modelling for CO_2 injection in a brine-saturated sandstone, showing increase in pore pressure (**Left**) and decrease in water saturation (**Right**). Black lines are the modelled values, and red dots represent the sampling points.

The reservoir rock is assumed to be homogeneous and isotropic, and the dependence between dry rock properties and effective stress was modeled using third-order elasticity (Section 1.8), with effective stress coefficient n being set as 1. Biot-Gassman's equation (1.1) was used to model the effect of fluid in the rock compressibility. As before, no interaction is assumed between fluid and rock matrix, so porosity and dry rock properties do not correlate with fluid saturation.

The effective fluid properties are modeled using Brie's formula, with coefficient set to 3. This is equivalent to a saturation-dependent f number:

$$f = \frac{K_V - K_{Brie}}{K_V - K_R}. \tag{1.40}$$

The synthetic data can be seen in Figure 1.23. Black wiggles are baseline, and red ones are monitor. It is clear that we have changes in amplitude on both top and base reflections, and also a change in traveltime inside the reservoir layer.

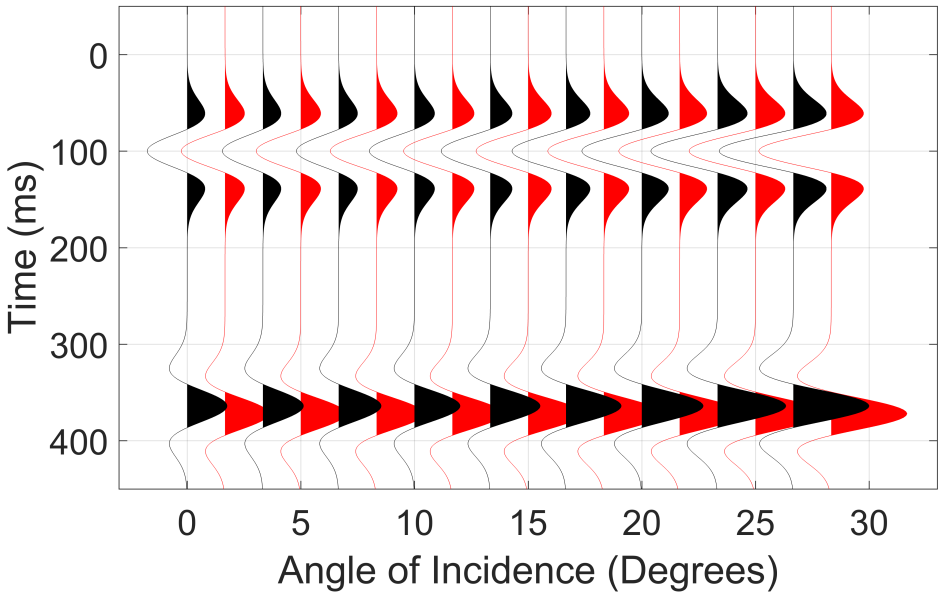

Figure 1.23: Modeled synthetic data for two different time steps: baseline (black) and monitor (red).

Figure 1.24 shows the same dataset, but with addition of white Gaussian noise. Notice that the main trend of amplitude increase and time-shifts can be detected, but correctly isolating these values becomes more challenging. Both noise-free and noisy synthetic data were inverted for reservoir properties.

1.3.2 Inversion

As it happened in section 1.2.2, the petroelastic models used to connect the reservoir changes and the seismic changes are too complicated to allow for a direct, analytic solution. We here employ two inversion algorithms for obtaining the desired reservoir parameters:

Deterministic Solution Use of polynomial equations (up to 2^{nd} order) to simplify the relation between reservoir parameters and elastic properties

Stochastic Solution Use of a stochastic random forest algorithm to classify the measured seismic data into clusters of previously modeled changes in reservoir parameters

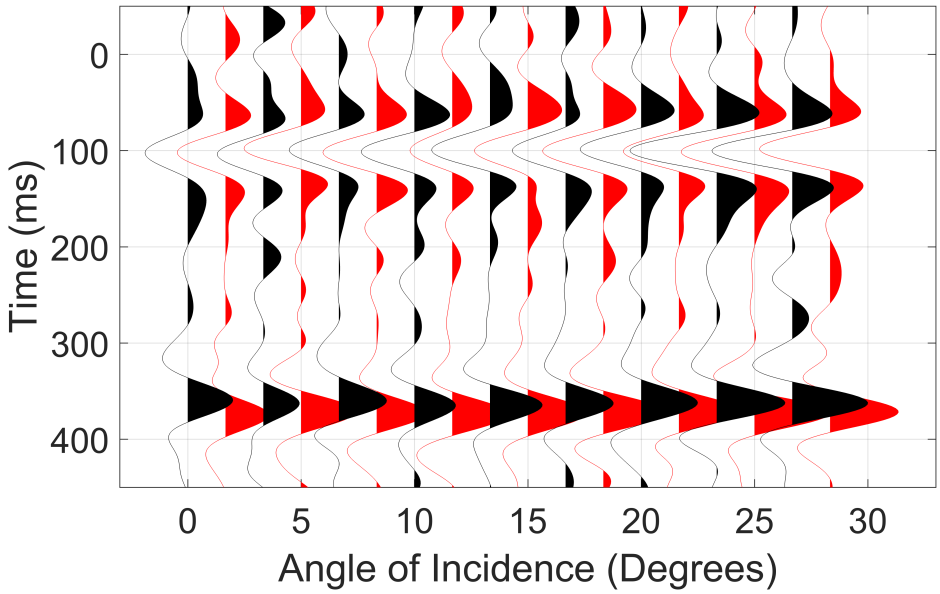

Figure 1.24: Modeled synthetic data + noise for two different time steps: baseline (black) and monitor (red).

Deterministic Solution

For the **Deterministic Solution**, we assume that the changes in every elastic property ($\Delta V_p/V_p$, ΔV_s, $\Delta\rho/\rho$) can be expressed as a multinomial combination of the reservoir parameters, up to second degree in the variables - and here we include the f value. This can be summarized in the multinomial expansion below:

$$\begin{aligned}
\frac{\Delta V_p}{V_p} &= \sum_{k_1+k_2+k_3=2} m_\alpha(k_1,k_2,k_3)\prod_{j=1}^{3} x_j^{k_j} \\
\frac{\Delta V_s}{V_s} &= \sum_{k_1+k_2+k_3=2} m_\beta(k_1,k_2,k_3)\prod_{j=1}^{3} x_j^{k_j}, \\
\frac{\Delta \rho}{\rho} &= \sum_{k_1+k_2+k_3=2} m_\rho(k_1,k_2,k_3)\prod_{j=1}^{3} x_j^{k_j}
\end{aligned} \tag{1.41}$$

with $(k_1,k_2,k_3) \in \mathbb{N}$ and $x_j = (\Delta P_P, \Delta S_w, f)$ for $i = (1,2,3)$, respectively.

The constants m can be obtained by least-square regression of experimental (or modeled, in our case) values of changes in velocities and density from the desired

rock physics model, for the expected range of reservoir parameters in the study. This range of values was the same used for the stochastic inversion.

Not all coefficients are relevant in a regression - the values of f, for example, do not impact the density or the S-wave velocity in our model. The method used to select the significant variables was backward elimination with adjusted R^2 as criteria. Despite much criticism towards step-wise regression methods (Flom and Cassell, 2007), we believe that in this case the approach is suitable, since we have prior knowledge about how the independent variables (reservoir parameters) affect the dependent variables (elastic properties).

Once the values of the constants m are obtained, we input the observed values $\mathbf{S}^{\text{obs}} = (\Delta V_p/V_p,\ \Delta V_s,\ \Delta\rho/\rho)^{\text{obs}}$ in the system of equations 1.41 and solve it for the reservoir variables $\mathbf{x} = (\Delta P_P, \Delta S_w, f)$. This is a non-linear system, and the solution can be obtained by reaching a minimum for the difference between observed and modeled values. The solution $\mathbf{x}^*$ is then

$$\mathbf{x}^* = \arg\min \left|\mathbf{S}(\mathbf{x}) - \mathbf{S}^{\text{obs}}\right|^2 \tag{1.42}$$

Even though global minimization may be difficult to assess, the algorithm always does converge because we limit the search space: there is no point in looking for solutions with negative pressure or with saturation outside the bound $[0, 1]$, for example. In this limited search space, the minimum was calculated with basin-hopping algorithm (Wales and Doye, 1997).

Stochastic Solution

For the **Stochastic Solution**, the chosen algorithm was *Random Forest* (Breiman, 2002). Random Forest is built upon the Regression Tree method, which is itself under a more general class of methods entitled Classification and Regression Trees (CART). It is a widely used method for several data mining activities, including very complex ones such as real-time human pose recognition (Shotton et al., 2011). More on this subject is available in Appendix C.

Starting from the same dataset generated for the multinomial fitting of the deterministic solution, a bootstrap sampling is performed, with a number of samples equal to the size of our dataset. This sample is then used as input for a decision tree regression, applying the mean squared error criteria. The process is repeated several times (1000 times, for our case), and the results of all decision trees are averaged, creating then the random forest regressor that we use for obtaining the reservoir parameters from measured seismic data. The main advantage of relying in random forest methods instead of pure decision tree is to avoid the "overfitting" problem, when the model is forced to predict very well the initial dataset but fails

to reproduce further results.

1.3.3 Results

The results of the inversion of noise-free data can be checked in Figure 1.25. Notice that when the arbitrary fluid mix law is accounted for (full lines), both inversion methods yield very similar results. If we make the wrong assumption of Reuss average for the fluid moduli (dotted lines), the results for pressure and saturation deteriorate.

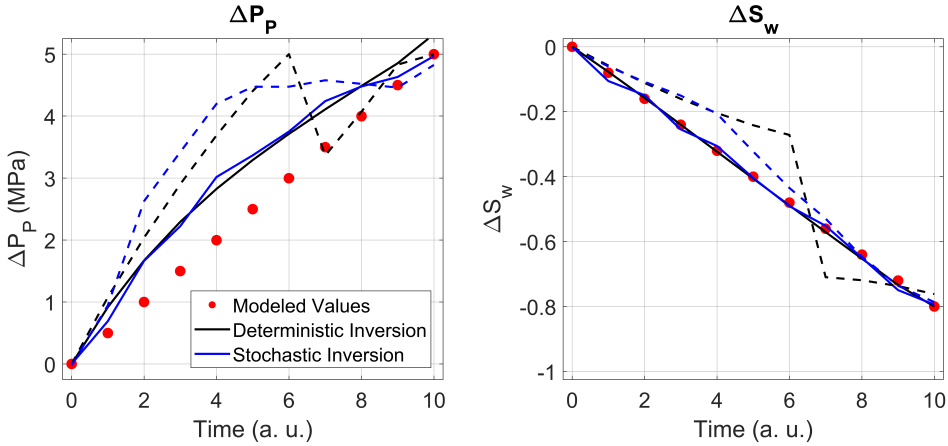

Figure 1.25: Inversion of noise-free synthetic data for changes in pore pressure (**Left**) and water saturation (**Right**). Red dots are modeled data, black full line is result of inversion with deterministic method, and blue full line is result of inversion with stochastic method. Dotted lines are inversion results when Reuss fluid average is assumed.

Addition of noise to the synthetic data has the expected effect of reducing the accuracy of the results (Figure 1.26), particularly for pressure estimation. Still, including the fluid mix law in the inversion procedure continues to yield better results. This does not hold true for very low SNR ratios (Figure 1.27), when the noise starts to play a more relevant role in the misfit between modeled and inverted reservoir parameters.

To check the effectiveness of the method for several levels of SNR, we calculated the mean square error (MSE) between the modeled and inverted values, both for pressure and for saturation. The results can be checked in Figure 1.28. It can be noticed that, in general, accounting for an arbitrary fluid mix law increases the accuracy of pore pressure and fluid saturation. For the conditions we modeled, this holds true when SNR is above 5.

Figure 1.29 shows the values of f for different levels of noise, as well as the MSE

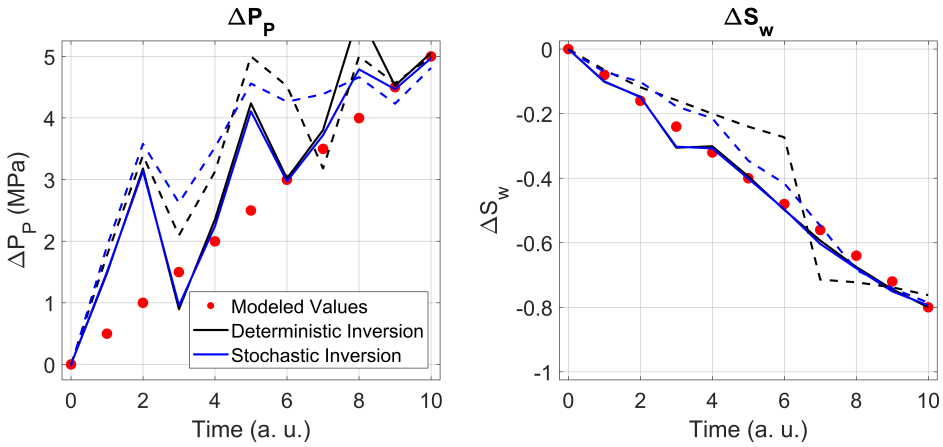

Figure 1.26: Inversion of synthetic data for changes in pore pressure (**Left**) and water saturation (**Right**), when noise is added (SNR = 5). Red dots are modeled data, black full line is result of inversion with deterministic method, and blue full line is result of inversion with stochastic method. Dotted lines are inversion results when Reuss fluid average is assumed.

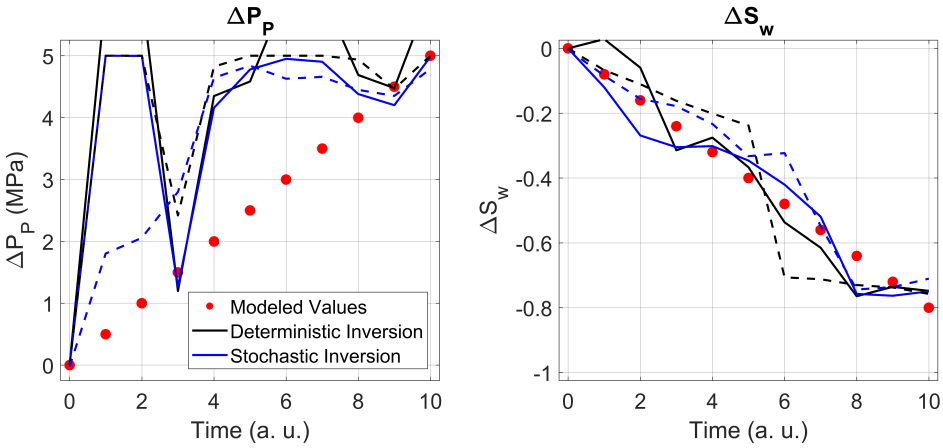

Figure 1.27: Inversion of synthetic data for changes in pore pressure (**Left**) and water saturation (**Right**), when noise levels are increased even further (SNR = 1). Red dots are modeled data, black full line is result of inversion with deterministic method, and blue full line is result of inversion with stochastic method. Dotted lines are inversion results when Reuss fluid average is assumed.

of the estimations. The results worsen very fast with increasing of noise levels.

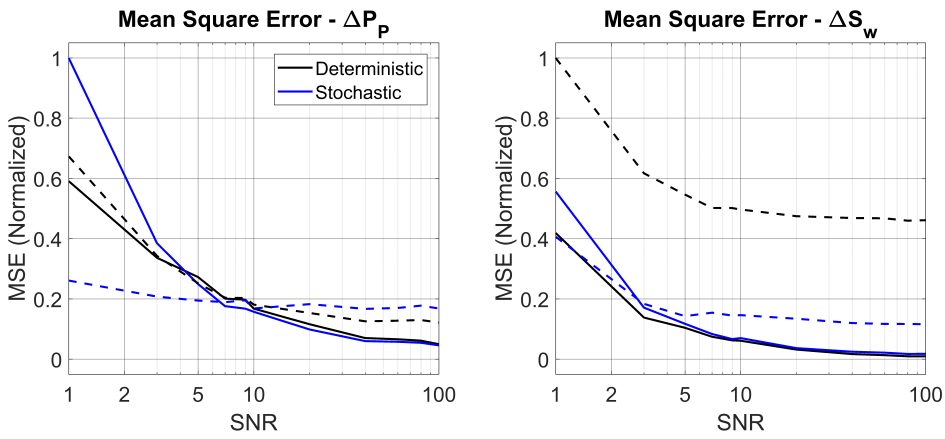

Figure 1.28: Normalized mean square error (MSE) between modeled and inverted values of pore pressure (**Left**) and water saturation (**Right**), for different noise levels. Black full line is result of inversion with deterministic method, and blue full line is result of inversion with stochastic method. Dotted lines are inversion results when Reuss fluid average is assumed.

1.3.4 Discussion

The results reveal that the impact of including an arbitrary fluid mixing law as a degree of freedom in the inversion allowed for obtaining better saturation and pore pressure estimations in the noise-free data, for both inversion algorithms evaluated. The improvement in saturation results is more significant than in pore pressure estimations.

When noise levels are higher, the impact of the method is less pronounced. For pressure estimations, the Reuss average hypothesis yielded a result closer to the modeled one. For water saturation, the deterministic method with the Reuss average hypothesis yields the worst result, while the three other combinations perform similarly.

We only considered here the mixing between two fluids, and the fluids were assumed to have no effect in the rock matrix. The CO_2 properties were kept constant: if the variations in pore pressure are too large, they can have a significant impact in the fluid properties as well.

Further studies in field data would allow for a better assessment, and are a clear next step.

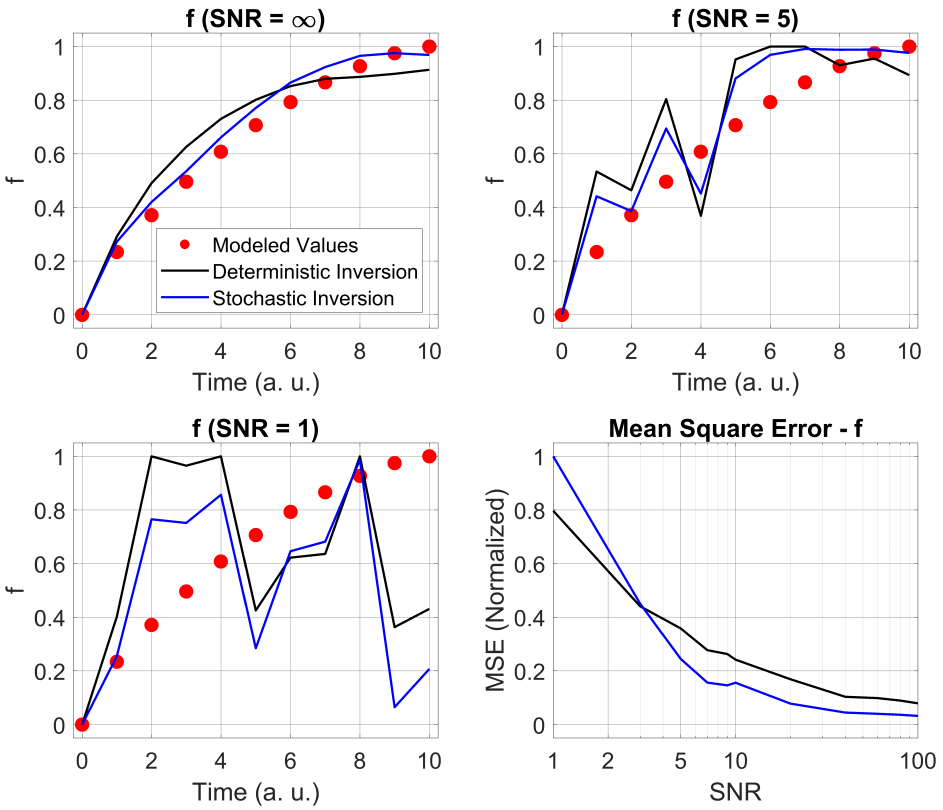

Figure 1.29: Inverted f number for different noise levels (**Top Left**, **Top Right** and **Bottom Left**) and normalized mean square error (MSE) for different noise levels (**Bottom Right**). Red dots are modeled data, black full line is result of inversion with deterministic method, and blue full line is result of inversion with stochastic method.

1.4 Anisotropy Changes: a Source of Information for Quantitative 4D Interpretation?

Anisotropy in the seismic scale can have a series of underlying sources, and is usually classified based of its main cause: inherent or induced (Casagrande, 1944). Inherent anisotropy arises as an effective medium behavior, due to the heterogeneity of the molecules and crystals or because of the geologic layering / preferential deposition direction (Bakulin and Grechka, 2003; Backus, 1962; Fjær et al., 2008). Induced anisotropy can be caused, for example, by a non-hydrostatic stress regime (Mavko et al., 2009a)

There are mainly three models that attempt to reproduce and explain the effect of

stress on seismic anisotropy: the ones based on contact models (Mindlin, 1949; Walton, 1987); the crack closure model (Sayers, 2002); and the non-linear elasticity models (Rasolofosaon, 1998; Prioul and Lebrat, 2004), presented previously in section 1.1.3, and that will be used in this section.

Pore pressure changes in a reservoir can cause a hydrostatic change in the effective stress, but the *strain* associated to this change is not necessarily equal in the three principal stress directions - after all, it is usual that a reservoir is subjected to a non-hydrostatic initial stress regime, being the most common case the normal stress regime, for which $S_V > S_H > S_h$ (Zoback, 1992; Anderson, 1951).

An anisotropic effective stress can lead to different rock strengths for each axis, and thus to different strains when the rock is exposed to hydrostatic stress changes. For our study, we will consider S_V as the principal stress, with $S_H \approx S_h$.

We will use third-order elasticity theory (TOE) to model the change in anisotropy parameters of a hydrocarbon reservoir with VTI anisotropy, subjected to water injection or to depletion. As in previous sections, we model the reflectivity on the top of the reservoir and use an AVO approximation to recover the changes in elastic parameters, which are used as input for a time-lapse inversion to estimate changes in pore pressure, fluid saturation, brine salinity, and fluid temperature.

1.4.1 Modelling

Equation 1.9 allows for the calculation of changes in the effective stiffness tensor when the rock is under influence of a static stress different from the one in the reference state C^0_{ijkl}.

In our model, the rock initially displays a VTI behavior. Because of that, any hydrostatic changes in effective stress will cause an strain such that $\mathcal{E}_{11} = \mathcal{E}_{22} \neq \mathcal{E}_{33}$. If we input this in equation 1.10, we can check that the resulting system will retain its azimuthal symmetry. This outcome is part of a more general behavior described by group theory (Curie, 1894).

We can then use equation 1.10 in combination with Thomsen parameters (Thomsen, 1986) to estimate how the anisotropy changes as a function of strain:

$$\begin{aligned} \varepsilon &= \frac{C_{11} - C_{33}}{2C_{33}} \\ \delta &= \frac{(C_{13} + C_{14})^2 - (C_{33} - C_{44})^2}{2C_{33}(C_{33} - C_{44})} \\ \gamma &= \frac{C_{66} - C_{44}}{2C_{44}} \end{aligned} \tag{1.43}$$

Prioul et al. (2004) propose a first-order approximation to obtain an explicit relation between Thomsen parameters and stress. This approximation leads to constant parameters when the medium is subjected to hydrostatic stress changes, even if the medium is originally anisotropic. Here, we will not rely on this approximation: instead, we use the definition of the Thomsen parameters to update the anisotropy according to the pore pressure changes - assuming that they are connected to the effective stress changes by an effective pressure coefficient of 1. The behavior of the Thomsen parameters can be checked in Figure 1.30.

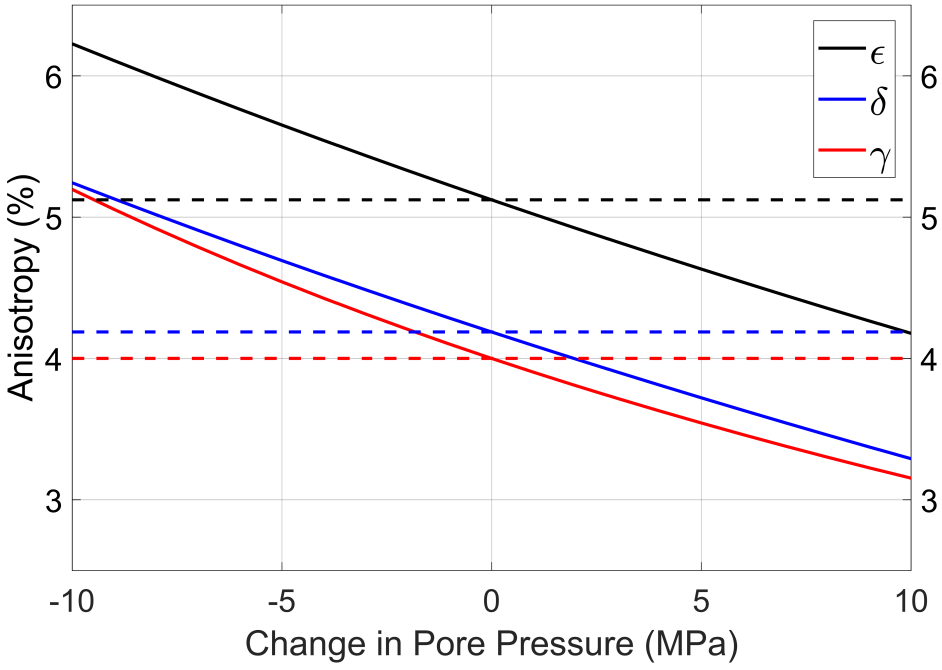

Figure 1.30: Comparison between anisotropy behavior predicted by TOE (full line) and first-order approximation proposed by Prioul et al. (2004) (dashed line) under hydrostatic stress changes.

For reservoir modelling, two different production scenarios were considered: **injection of seawater in the oil zone** (from now on, referred to as scenario **2A**) and **depletion with gas coming out of solution** (scenario **2B**). In the first scenario, we have a simultaneous change in pore pressure, fluid saturation, fluid temperature and brine salinity. In the second scenario, both the fluid temperature and the brine salinity are held constant.

As before, a time series of reservoir parameters is modeled and used as input to create synthetic seismic data. Brine and oil properties were calculated using the

equations proposed by Batzle and Wang (1992). Fluid mixture properties were obtained with the Reuss average. No effects of temperature or salinity on the rock matrix were considered - the rock frame properties depend only on the effective stress. Matrix density and rock porosity were assumed to be constant.

The contribution of the pore fluid to the elastic moduli of the rock was modeled with help of anisotropic Biot-Gassmann equation (Gassmann, 1951):

$$C_{ijkl}^{sat} = C_{ijkl}^{dry} + \frac{\left(K_0\delta_{ij} - \frac{C_{ijaa}^{dry}}{3}\right)\left(K_0\delta_{kl} - \frac{C_{bbkl}^{dry}}{3}\right)}{\varphi\frac{K_0}{K_{\text{fl}}}(K_0 - K_{\text{fl}}) + \left(K_0 - \frac{C_{ccdd}^{dry}}{9}\right)} \tag{1.44}$$

In equation 1.44, K_0 stands for the bulk modulus of the mineral (quartz, in our study), C_{ijkl}^{dry} is the stiffness tensor of the dry rock, K_{fl} is the effective bulk modulus of the fluid mixture and δ_{ij} is the Kronecker Delta. Einstein summation convention was used to make the formula more compact.

The dry moduli C_{ijkl}^{dry} are obtained from the set of initial values C_{ijkl}^{0}, and then updated according to (1.10). When both pore pressure and fluid properties are changing simultaneously, the steps chosen for updating the elastic moduli are

1. From the reference state (baseline vintage), use (1.44) to obtain the saturated moduli with the initial saturation
2. Calculate strain using

$$\mathcal{E}_{ij} = \left(C_{ijkl}^{sat}\right)^{-1}\sigma_{ij} \tag{1.45}$$

3. Update the dry moduli using (1.45) and (1.10)
4. Update saturated moduli using (1.44) with new fluid saturation

It is worth taking some lines do discuss the order in which these procedures are performed. We could, for example, begin by updating the saturated moduli with the new fluid properties, then proceeding to the calculation of strain and, from this, update the new dry moduli, which would be combined with the fluid properties using (1.44). It is equivalent to performing step 4 before step 1. This alternative workflow, albeit valid, yields slightly different results.

If we think of pore pressure (P_P), salinity (η), brine saturation (S_w) and temperature (T) as state variables, it is a bit surprising that two different paths, both with

equivalent initial and final states, produce different elastic moduli. The reason for that resides in the fact that pore pressure is not a state variable of the rock in this case, but *strain* is. The different paths actually mean different strains, ergo the difference in the final stiffness tensor. Nonetheless, in the range of values we studied this difference is quite small, so any sequence of steps is actually valid.

All values for the rock and fluid parameters can be found in Appendix A.

Reflectivity at the interface between two anisotropic rocks

The most common way of obtaining the reflectivity at an interface is by means of Zoeppritz equations, which we have employed in the previous sections. Zoeppritz's results are obtained from the continuity of stress and displacement at the interface, and they must be modified when any of the media is anisotropic.

We will use the results presented by Graebner (1992b), accounting for a correction of the factor of 2 in the equation for K_1, after equation 4 in his original paper. It is not to our knowledge if any corrections have already been published for these equations - if there is a correction, we apologize for the redundancy. Graebner's results allow us to obtain the exact value for the reflectivity at an interface. For this calculation, we introduce an overburden rock, whose elastic parameters can be verified in Appendix A.

Just as with Zoeppritz's equations, the exact expressions for reflectivity are difficult to analyze - it is not intuitive to isolate, for example, the effect of a change in P-wave velocity or density, since the calculations are based on the components of the stiffness tensor. To get better insight on the effect of each parameter on the reflectivity, we will resort to the results obtained by Ruger (1997) for the PP reflection coefficient R_{PP}, which are here presented in a way similar to the one used by Stovas and Landro (2002):

$$R_{\mathrm{PP}}(\theta) = \frac{1}{2}\frac{\Delta Z}{Z} + \frac{1}{2}\left[\frac{\Delta V_p}{V_p} - \left(\frac{2V_s}{V_p}\right)^2 \frac{\Delta\mu}{\mu}\right]\sin^2\theta + \frac{1}{2}\frac{\Delta V_p}{V_p}\sin^2\theta\tan^2\theta + \frac{1}{2}\Delta\delta\sin^2\theta + \frac{1}{2}\Delta\varepsilon\sin^2\theta\tan^2\theta \tag{1.46}$$

In equation 1.46, the Δ symbol means the contrast of a certain parameter across a given interface ($\Delta V_p = V_{p_2} - V_{p_1}$). Following the same notation, $V_p = (V_{p_2} + V_{p_1})/2$. $Z = \rho V_p$ stands for the acoustic impedance, and μ is the shear modulus.

Equation 1.46 resembles the reflectivity approximation proposed by Smith and Gidlow (1987), with the exception of the two last terms, which account for the contrast in anisotropy between the two media. We can then follow the same logic

applied in (1.15) and use this expression to estimate, in first order, how differences between the reflectivity in distinct calendar times t_1 and t_2 are linked to the changes in the elastic properties of the reservoir between these time frames:

$$\begin{aligned} R_{\text{PP}}^{(4D)}(\theta) &= R_{\text{PP}}^{(t_2)}(\theta) - R_{\text{PP}}^{(t_1)}(\theta) \\ &\approx \frac{1}{2}\frac{\Delta Z^{(4D)}}{Z} + \frac{1}{2}\left[\frac{\Delta V_p^{(4D)}}{V_p} - \left(\frac{2V_s}{V_p}\right)^2 \frac{\Delta \mu^{(4D)}}{\mu}\right] \sin^2\theta \\ &+ \frac{1}{2}\frac{\Delta V_p^{(4D)}}{V_p} \sin^2\theta \tan^2\theta + \frac{1}{2}\Delta\delta^{(4D)} \sin^2\theta + \frac{1}{2}\Delta\varepsilon^{(4D)} \sin^2\theta \tan^2\theta \end{aligned} \tag{1.47}$$

In equation 1.47, $\Delta^{(4D)}$ stands for the difference in a property between calendar times t_2 and t_1.

We can further simplify (1.47) by focusing on the particular cases when all the changes in anisotropy due to production are caused by pressure changes and can be modeled by TOE, with an isotropic third-order tensor A_{ijklmn}. If this is the case, we can approximate $\Delta\delta^{(4D)} \approx \Delta\varepsilon^{(4D)}$, and then get

$$\begin{aligned} \Delta R_{\text{PP}}^{(4D)}(\theta) \approx \frac{1}{2}\frac{\Delta Z^{(4D)}}{Z} - 2\frac{V_s^2}{V_p^2}\frac{\Delta \mu^{(4D)}}{\mu} \sin^2\theta \\ + \frac{1}{2}\left(\frac{\Delta V_p^{(4D)}}{V_p} + \Delta\varepsilon^{(4D)}\right) \tan^2\theta \end{aligned} \tag{1.48}$$

Equation 1.48 can be written in a more compact way by denoting the intercept, gradient and curvature AVO terms:

$$\Delta R_{\text{PP}}^{(4D)}(\theta) = \Delta R(0) + \Delta G \sin^2\theta + \Delta F \tan^2\theta \tag{1.49}$$

By combining equation 1.48 and the time-shift equation 1.22, we have four unknowns ($\Delta V_p/V_p$, $\Delta V_s/V_s$, $\Delta\rho/\rho$ and $\Delta\varepsilon$) and four seismic measurements ($\Delta R(0)$, ΔG, ΔF and $\Delta\tau/\tau$). If we obtain the former set from the later, we have the necessary input for estimating the changes in the reservoir properties.

The main challenge is to estimate the values of R, G and F from AVO. Figure 1.31 shows this with modeled data: The full circles in the left panel are the reflectivity calculated using equation 1.46, and they match the exact reflectivity (full line) to a very good degree. The open circles, representing Zoeppritz isotropic reflectivity, are a good fit for smaller angles, but start to deviate from the correct result above 25° - 30°. PS reflectivity is shown in red just out of completeness, and hasn't been

used for inversion. The plot on the right shows the relative difference between the correct and least-square fitted values of R, G and F, for different cut-off angles. The curvature term (F) is extremely sensitive and, since it is the only term that actually contains the changes in anisotropy, its use as input for quantitative 4D inversion becomes more arduous.

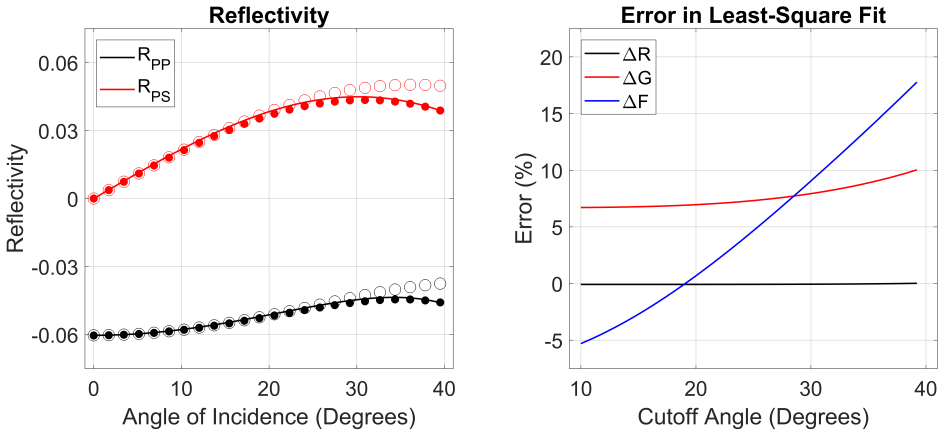

Figure 1.31: Left PP Reflectivity (Black) and PS Reflectivity (Red) for the interface between two VTI media. Full line is exact solution (Graebner, 1992b), full circles are approximation showed in equation 1.46, and open circles are Zoeppritz reflectivity for an isotropic medium. **Right** Error in least-square fit for R, G and F.

1.4.2 Inversion

The inversion methods employed in this study were the same ones used in section 1.3: deterministic and stochastic. The main difference arises from the extra dimension caused by the introduction of a new variable (ε). The multinomial expansion for the deterministic case becomes

$$\begin{aligned}
\frac{\Delta V_p}{V_p} &= \sum_{k_1+k_2+k_3+k_4=2} m_\alpha(k_1,k_2,k_3,k_4) \prod_{j=1}^{4} x_j^{k_j} \\
\frac{\Delta V_s}{V_s} &= \sum_{k_1+k_2+k_3+k_4=2} m_\beta(k_1,k_2,k_3,k_4) \prod_{j=1}^{4} x_j^{k_j} \\
\frac{\Delta \rho}{\rho} &= \sum_{k_1+k_2+k_3+k_4=2} m_\rho(k_1,k_2,k_3,k_4) \prod_{j=1}^{4} x_j^{k_j} \\
\Delta \varepsilon &= \sum_{k_1+k_2+k_3+k_4=2} m_\epsilon(k_1,k_2,k_3,k_4) \prod_{j=1}^{4} x_j^{k_j},
\end{aligned} \tag{1.50}$$

with $(k_1, k_2, k_3, k_4) \in \mathbb{N}$ and $x_j = (\Delta P_P, \Delta S_w, \Delta\eta, \Delta T)$ for $i = (1, 2, 3, 4)$, respectively. Choice of significant variables, objective-function minimization, and random forest parametrization were performed with the same methods used in section 1.3.

1.4.3 Results

The results for inversion of noise-free data in scenario **2A** can be seen in Figure 1.32. Pore pressure and water saturation are in good agreement, particularly for the stochastic method, but still far from being a perfect match. This is curious because, since noise-free modeled data was used, one would expect the inversion to recover the modeled reservoir parameters. The results for brine salinity and fluid temperature deviate significantly from the modeled values. Addition of noise to the data makes the match between modeled and inverted results decline even further (Figure 1.33).

The results for inversion of noise-free data in scenario **2B** can be seen in Figure 1.34. Since there are only two variables to invert for, the results are more stable, both for pore pressure and oil saturation changes. The inversion results for noisy data can be checked in Figure 1.35, and Figure 1.36 shows the normalized mean squared error for different noise levels.

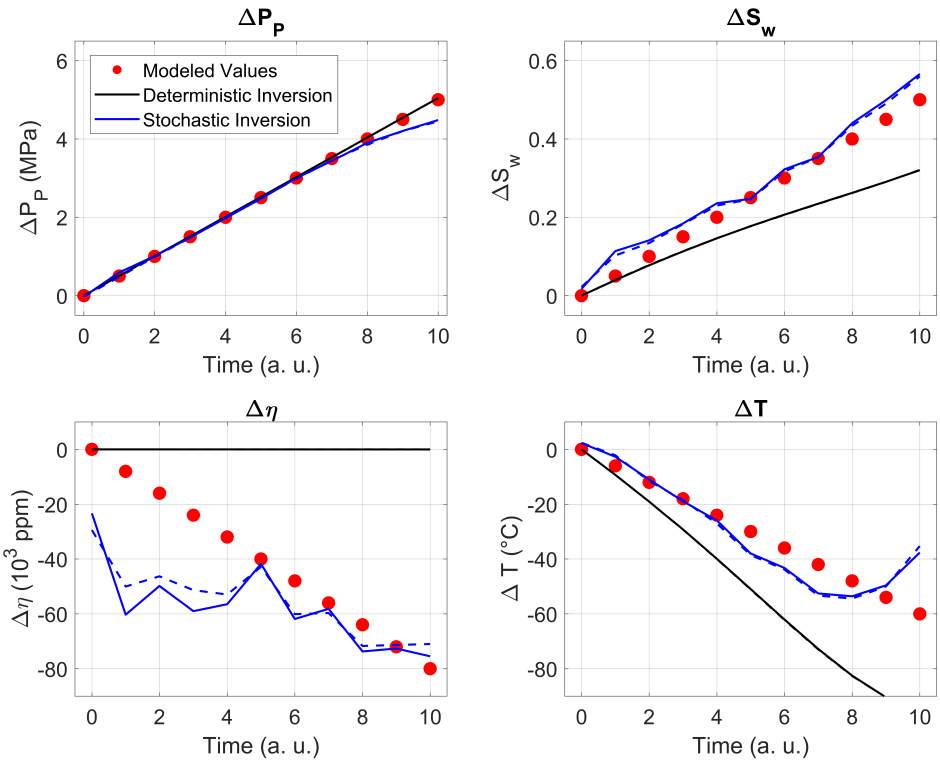

Figure 1.32: Results of inversion for changes in pore pressure (**Top Left**), water saturation (**Top Right**), brine salinity (**Bottom Left**), and fluid temperature (**Bottom Right**), for noise-free data. Red dots are modeled data, black full line is result of inversion with deterministic method, and blue full line is result of inversion with stochastic method. Dotted lines are inversion results when anisotropy is ignored.

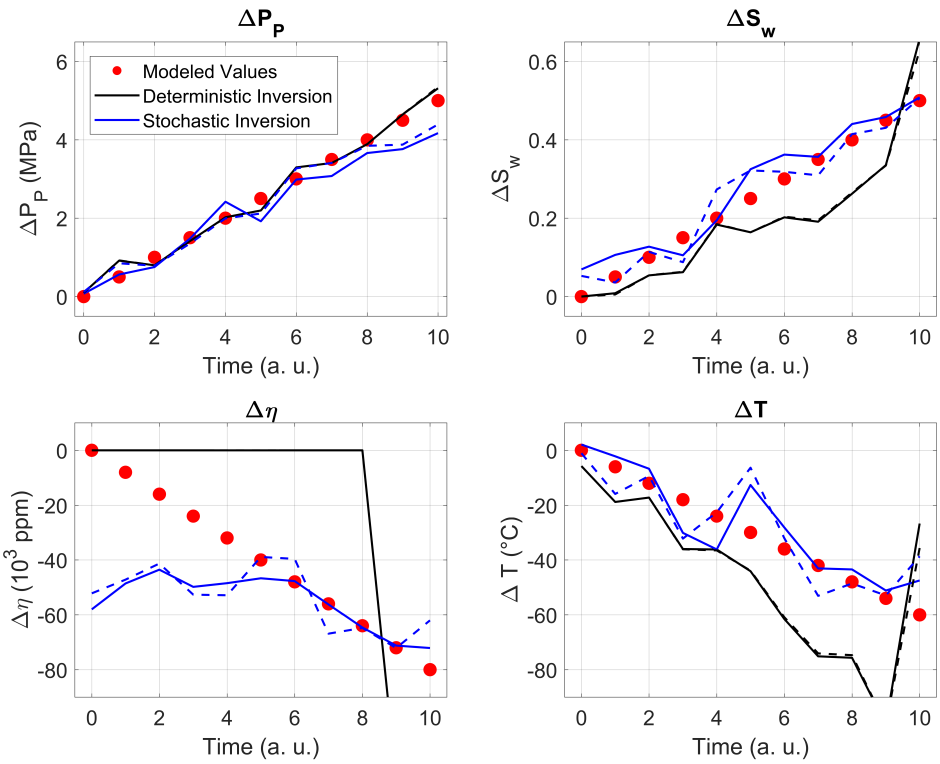

Figure 1.33: Results of inversion for changes in pore pressure (**Top Left**), water saturation (**Top Right**), brine salinity (**Bottom Left**), and fluid temperature (**Bottom Right**), for data with SNR = 10. Red dots are modeled data, black full line is result of inversion with deterministic method, and blue full line is result of inversion with stochastic method. Dotted lines are inversion results when anisotropy is ignored.

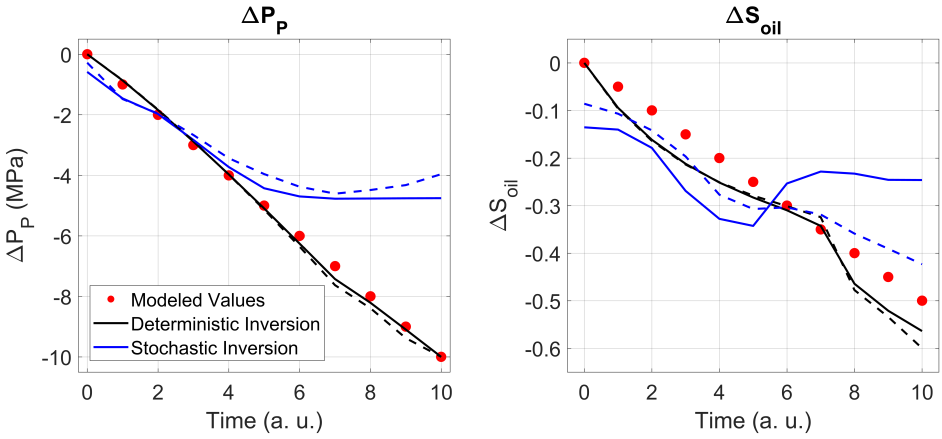

Figure 1.34: Results of inversion for changes in pore pressure (**Left**) and oil saturation (**Right**) for noise-free data. Red dots are modeled data, black full line is result of inversion with deterministic method, and blue full line is result of inversion with stochastic method. Dotted lines are inversion results when anisotropy is ignored.

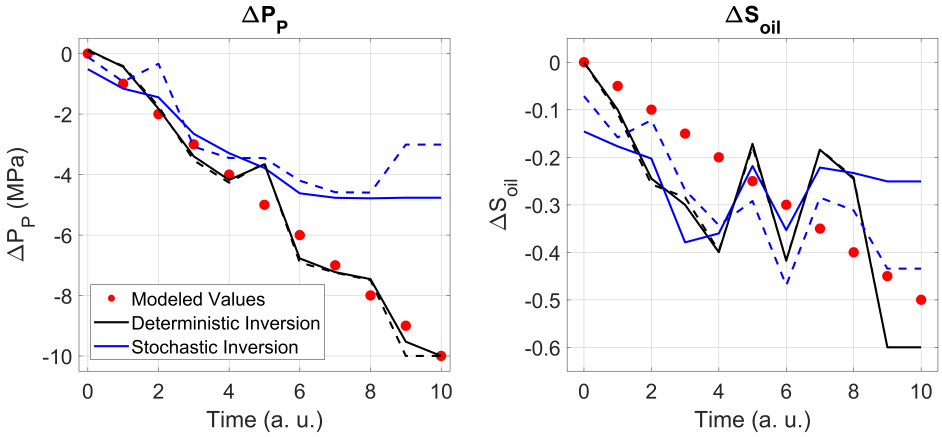

Figure 1.35: Results of inversion for changes in pore pressure (**Left**) and oil saturation (**Right**) for data with SNR = 10. Red dots are modeled data, black full line is result of inversion with deterministic method, and blue full line is result of inversion with stochastic method. Dotted lines are inversion results when anisotropy is ignored.

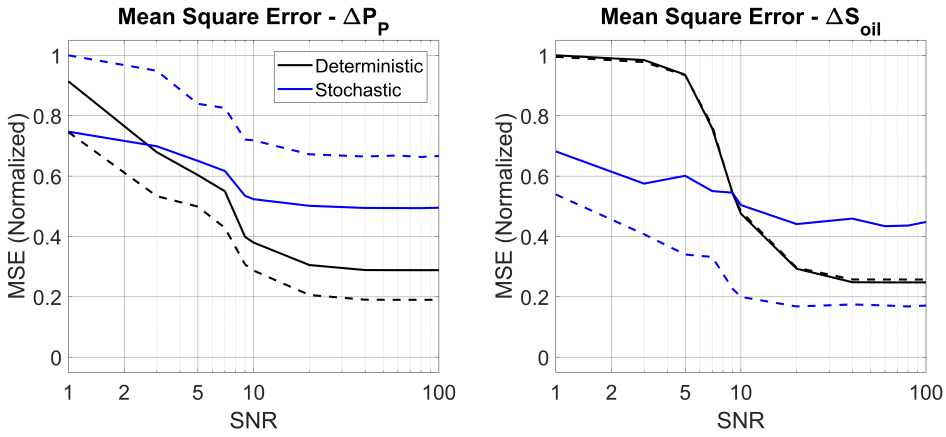

Figure 1.36: Normalized mean square error (MSE) between modeled and inverted values of pore pressure (**Left**) and oil saturation (**Right**) for different noise levels. Black full line is result of inversion with deterministic method, and blue full line is result of inversion with stochastic method. Dotted lines are inversion results when anisotropy is ignored.

1.4.4 Discussion

For scenario **2A**, it was expected that the inclusion of anisotropy as a source of information would be mandatory for a good result, since there are four unknowns (Pressure, Saturation, Brine Salinity and Fluid Temperature) and only three variables in the isotropic model: P- and S-wave velocities, and density.

Yet, the results reveal that the effect of including anisotropy was marginal: it did not allow for the quantification of brine salinity or fluid temperature, and only slightly improved the estimations of water saturation and pore pressure. This last result is in agreement with those presented in section 1.2.2: the effect of salinity is not of much impact in the pressure change estimations when brine saturation is also changing. This was observed for both inversion methods applied.

In scenario **2B**, the inclusion of anisotropy had basically no effect in the estimations performed with the deterministic method. The stochastic method results exhibited an improvement in the pore pressure estimations when anisotropy measurements were included, but a much worse oil saturation estimation was obtained in that case. For noise-free data, the deterministic method yielded better results.

For what we could verify, the modeled changes in anisotropy had little to no impact in the quantitative estimations of reservoir parameters change. Since these results were obtained under controlled, modeled scenarios, we expect that in field data the results would also not be very encouraging.

Only anisotropy changes caused by the effective pressure and modeled by TOE were considered. Further studies may reveal that other rock physics templates lead to a different contribution of anisotropy measurements to quantitative 4D interpretation. TOE was chosen due the fairly high number of laboratories with facilities to measure the rock physics properties necessary to build this kind of model.

One major assumption is that there is no creep or other time-dependent effects on the rock. If that is the case, the analysis performed here loses validity, since one no longer can directly associate the rock elastic properties uniquely with a reservoir configuration. Also, no changes in the overburden were considered.

VTI symmetry was picked out of simplicity. Other symmetries, like TTI or orthorhombic, can provide extra information (via AVAZ) that could be used to obtain better results. Scenarios with change in the model symmetry, such as the development of a horizontal fracture network, would require more careful evaluation.

The proper measurement of anisotropy changes is likely the most difficult practical challenge. AVO curvature is usually very noisy, and relying on it for estimating $\Delta\varepsilon$ will likely lead to poor results. Anisotropic time-lapse elastic FWI (Bergslid et al., 2015) can be an alternative source of 4D anisotropy changes.

1.5 Conclusions

The goals of this chapter were twofold. The first one was to present a literature review of some rock physics templates and fluid properties, which are useful for the interpretation of time-lapse seismic data. The second goal was to evaluate some second-order effects in the quantitative interpretation of time-lapse seismic data: brine salinity, brine temperature, and fluid mix. These effects are labeled "second-order" because they depend on fluid saturation, which is usually the protagonist in 4D seismic interpretation. Brine salinity and temperature, as well as fluid mixing, are generally taken into account in 4D seismic modeling and interpretation. However, they are usually assumed as static. In this chapter, we tried to obtain the changes in those parameters directly from time-lapse measurements, which is not a common practice in the industry.

To achieve the second goal, four production scenarios were studied. These scenarios were modeled using different rock physics models, from which elastic properties and synthetic seismic were generated. The synthetic data were then inverted for reservoir properties under different inversions schemes, and results were compared with the modeled values, both in the case of noisy and noise-free data.

In section 1.2, injection of seawater in reservoirs/aquifers of high salinity was considered. The results showed that the salinity contrast can compromise the estim-

ations of pore pressure changes when injecting into the aquifer. Since the effect of salinity is modulated by the fractional amount of brine in the pore space, the presence of other fluids renders this effect less significant.

In section 1.3, the effect of different fluid mixing laws was evaluated. The results showed that accounting for fluid mixing as a degree of freedom can have some impact on pressure and saturation discrimination for data with very high SNR, but the benefits are dwarfed by other sources of uncertainty for low-quality data.

In section 1.4, we studied how anisotropy changes during production, using an approach based on third-order elasticity. We discussed how a hydrostatic pore pressure change can lead to changes in anisotropy - given that the reservoir shows anisotropic behavior prior to production - and how this change can be measured with time-lapse AVO. Estimated changes in Thomson's ε were used as input for time-lapse inversion. The results showed little to no improvement in results when compared to the isotropic assumption, neither in the case of a complex system - with four variables changing simultaneously - nor for a simpler configuration, where only pore pressure and fluid saturation change with time. The causes behind these results were not entirely clear, and they were therefore not published.

Chapter 2

Near-Well Monitoring

This chapter describes a series of experiments performed in the basement of a building owned by SINTEF and NTNU, in Valgrinda (S. P. Andersens veg 15B, 7031 Trondheim). The basement houses a working hall for several professionals from NTNU and SINTEF, serving as a laboratory for experiments on different subjects. In this working area, two shallow wells were drilled: a 30m-deep well (from now on deemed **Well 1** or **Shallow Well**) and a 95m-deep one (**Well 2** or **Deep Well**). Those wells were drilled for different purposes, ranging from studies on drilling / cementation to the evaluation of the benefits of instrumented wells.

The lab also contains a water tank, often used to perform tests with seismic sources (airguns and water guns). Due to the limited size of the tank, however, having both a seismic source and sensors in the tank can compromise data acquisition. Because of that, some experiments - conducted by then Ph.D. candidate Daniel Wehner - involved the deployment of a hydrophone array in one of the water-filled wells, which lie a few meters away from the tank. Then, the seismic signature of the sources could be studied without contamination by the reverberations inside the water tank. Analysis of data recorded inside the well revealed a high-amplitude, non-dispersive event, which was interpreted as a tube wave.

Tube waves are a common subject in borehole geophysics, where they are usually recorded in open wells, with a controlled source (e.g. sonic logging tool). By studying their propagation, one can characterize - and perhaps monitor - the rock formation behind the well. For configurations of cased wells, without a controlled source, there are few cases presented in the literature. In this chapter, we present the analysis of tube waves in such configuration: cased wells, for acquisitions with sources with variable seismic signature.

A crucial step to using tube waves as a characterization or monitoring method is the precise measurement of their properties - namely, velocity and attenuation. These will be the focus of this chapter. In addition, two feasibility studies for monitoring have been modeled: one based on velocity measurements, and one based on attenuation measurements. The theory behind the modeling of those scenarios has mostly been described in Chapter 1, and we will refrain from doing it again here, where the main focus will be on the theory of tube waves and on the methodology employed to measure them.

This chapter would not exist without the collaboration of Dr. Daniel Wehner, who was responsible for data acquisition and shared the load of data processing and interpretation. Daniel was responsible for conceiving the experiment and setting up the acquisition equipment, and he published the results of the analysis of some of these data (Wehner et al., 2017). After this publication, we worked together in repeating the experiment several times (acquiring both active and passive data). Daniel was responsible for data processing using the line fit method presented in this chapter, while I proposed and implemented the Radon and Cepstrum methods, as well as the modeling of the synthetic data presented in the Discussion section. Daniel also contributed to the literature review in the analysis of the tube wave attenuation, and he participated actively in the interpretation of the results.

Daniel Wehner is the first author in two of the four publications derived so far from the work described in this Chapter:

Wehner, D., F. Borges, and M. Landrø, 2018, Using well operation noise to estimate shear modulus changes from measured tube waves - a feasibility study: Presented at the Fifth CO_2 Geological Storage Workshop

Borges, F. and M. Landrø, 2018, Time-lapse separation of fluid and pressure effects with an arbitrary fluid mixing law: Presented at the Fifth CO_2 Geological Storage Workshop

Landrø, M., D. Wehner, and F. Borges, 2018, How variations of the formation shear modulus around boreholes could be estimated from the tube wave: AGU Fall Meeting Abstracts, S51F–0398

Wehner, D., F. Borges, and M. Landrø, 2021, Tube-wave monitoring as a method to detect shear modulus changes around boreholes: A case study: Geophysics, **86**, B193-B207

Parts of the content presented in this chapter are also published in Daniel's Ph.D. thesis (Wehner, 2019). He has kindly authorized the use of the results as part of this thesis, and several figures are credited to him. In addition to what has been

published in the aforementioned papers, this chapter details the use of the cepstrum method for passive monitoring, a feasibility study for shallow monitoring, the analysis of some biases observed in the tube wave velocity estimation, and the theory and method for the tube wave attenuation study.

A manuscript describing the analysis and interpretation of anelastic attenuation of tube waves is currently being prepared for submission.

2.1 Experimental Setup

As mentioned in the introduction, the experiments presented in this chapter were conducted in two boreholes in the basement of a SINTEF building. A sketch with the setup is shown in Figure 2.1. The leftmost well on top of the figure is the deep well (95 m), and the rightmost is the shallow one (30 m). They are cased with the same material and have different diameters and casing thicknesses (parameters are summarized in Table 2.1). Both wells are filled with water.

For data recording, a 24-channels hydrophone array was used. Spacing between each receiver was 1 m. The radius r_{min} (Table 2.1) of the hydrophone array is estimated from the mean thickness of the individual hydrophones and the cable. The depths where the hydrophones are located are also illustrated in Figure 2.1, where H-24 is the shallowest receiver. As a source, a hand-held hammer is used to hit the concrete floor. The positions of the hammer source for different experiments are indicated by the stars in Figure 2.1.

A total of 14 data acquisitions were performed. Their parametrization can be checked in Table 2.2. Experiments labeled **Active S/D** employ the hammer as an active source, and the hydrophones are either deployed in the shallow (**S**) or the deep well (**D**). Passive recordings are based only on ambient noise, with exception of experiment **Passive S III**. For these recordings, while an experiment with an up-and downward rotating metal pipe was being performed in the deep well, the hydrophones were deployed in the shallow well and recorded data for a total of 320 seconds. The drill string was active for 76 seconds. The drill acts as an incoherent energy source and was classified as passive recording.

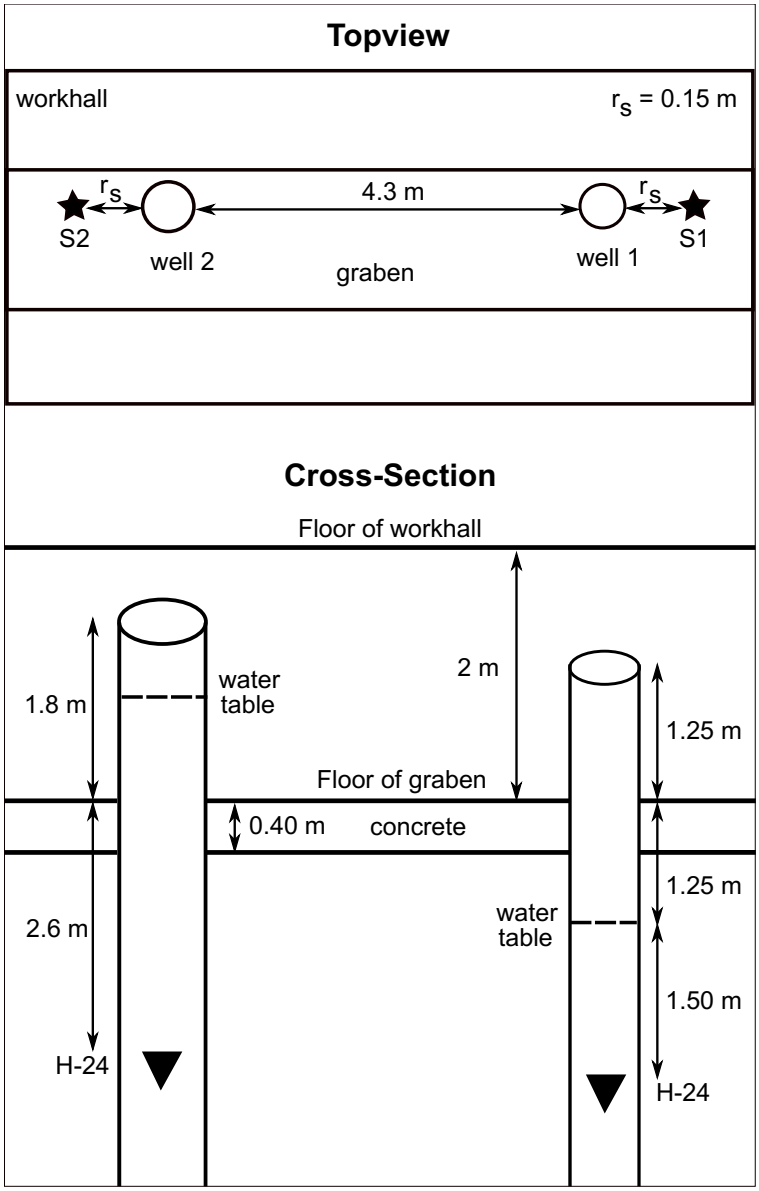

Figure 2.1: Experimental set up inside the workhall. The shallow (30 m) and deep (95 m) boreholes are shown on topview and cross-section. The stars indicate the positions of the hammer source with r_s = 0.15 m. The shallowest hydrophone is indicated by H-24, with a regular spacing of 1 m to the next receiver (Wehner et al., 2021).

Borehole	Well 1	Well 2
Borehole Parameters		
Radius (r_{max})	0.075 m	0.15 m
Depth (z_w)	30 m	95 m
Casing Parameters		
Thickness (d_c)	0.004 m	0.005 m
Poisson's Ratio (ν_c)	0.26	
Shear Modulus (μ_c)	78 GPa	
Fluid Parameters		
Density (ρ_f)	998.8 kg/m^3	999.2 kg/m^3
Bulk Modulus (K_f)	2.10 GPa	2.07 GPa
Temperature (T_w)	11°C	8 °C
Hydrophone Array Parameters		
Radius (r_{min})	0.013 m	
Shear Modulus (μ_t)	1.0 GPa	

Table 2.1: Some parameters for the experimental setup (Wehner et al., 2021).

	Well	# Traces	Source	Sampling (ms)	Trace Length (s)	Date
Active S I	Well 1	82	Hammer	0.25	1	28.09.2017
Active S II	Well 1	80	Hammer	0.25	1	19.10.2017
Active S III	Well 1	80	Hammer	0.25	1	15.11.2017
Active S IV	Well 1	80	Hammer	0.25	1	02.03.2018
Active S V	Well 1	80	Hammer	0.25	1	07.03.2018
Active S VI	Well 1	80	Hammer	0.25	1	08.03.2018
Active S VII	Well 1	80	Hammer	0.25	1	15.03.2018
Active S VIII	Well 1	80	Hammer	0.25	1	04.05.2018
Active D I	Well 2	78	Hammer	0.25	1	26.10.2017
Passive S I	Well 1	4500	Noise	1	16	12.09.2017
Passive S II	Well 1	3706	Noise	1	16	12.10.2017
Passive S III	Well 1	76	Drill	0.25	4	24.05.2018
Passive S IV	Well 1	7738	Noise	1	16	11.01.2019
Passive D I	Well 2	1800	Noise	1	16	27.10.2017

Table 2.2: Parameters for the different experiments performed. The labels **S** and **D** stand for shallow and deep well, respectively.

2.2 Theory

2.2.1 Tube Wave Velocity

A wave that propagates on the interface between two media is called an *interface* - or *surface* - wave. They are old acquaintances of geoscientists working with land seismic, where they are generally known as ground roll (Porsani et al., 2009; Karsli and Bayrak, 2008). Surface waves are labeled according to the interface where they propagate, as well as the propagation mode, e.g. Rayleigh waves in solid-vacuum interfaces (Rayleigh, 1885) and Scholte waves in solid-fluid interfaces (Scholte, 1942, 1947). Of particular interest for us in this chapter are Stoneley waves, which propagate in a solid-solid interface (Stoneley, 1924).

In the specific case of boreholes, Stoneley waves appear in the interface between casing and formation, being then called *tube waves* (Galperin, 1985). These waves are commonly recorded during borehole geophysical acquisitions such as Vertical Seismic Profiling (VSP) and acoustic logging, but are mostly treated as noise, and removed during processing. However, they do carry information about the formation behind the casing, and can then be used to study the shear modulus and attenuation of the rock (White, 1965).

A detailed explanation of the relation between tube wave velocity and formation shear modulus can be found in Marzetta and Schoenberg (1985). The dispersion

relation for surface modes propagating in a fluid-filled borehole is

$$f_1 k_r r_b J_1(k_r r_b) + f_2 \rho_f \omega^2 r_b J_0(k_r r_b) = 0, \tag{2.1}$$

where r_b is the inner radius of the borehole, ρ_f is the density of fluid inside the borehole, $k_r = (\omega^2/\alpha_f^2 - k_z^2)^{1/2}$ is the radial wavenumber, ω is the angular frequency, k_z is the axial wavenumber, α_f is the fluid P-wave velocity, and $J_n(x)$ is Bessel's function (first type) of order n. Expressions for f_1 and f_2 are available in Marzetta and Schoenberg (1985).

The result show in equation 2.1 can be simplified by using a low-frequency approximation. For a fluid-filled cased borehole with a tool inside, the tube wave velocity v_t is (Norris, 1990)

$$v_t = \left\{ \rho_f \left[\frac{1}{K_f} + \frac{\eta}{(1-\eta)\mu_t} + \frac{1}{(1-\eta)N} \right] \right\}^{-1/2}, \tag{2.2}$$

where K_f is the fluid bulk modulus, μ_t is the tool shear modulus, and $\eta = r_{\text{min}}/r_{\text{max}}$ is a geometric factor (see Figure 2.2). N is given by

$$N = \frac{2(1-\nu_c)\mu_s + (\mu_c - \mu_s)(1-a^2)(1-\zeta\nu_c^2)}{2(1-\nu_c) - (1-\mu_s/\mu_c)(1-2\nu_c+\zeta\nu_c^2)(1-a^2)},$$

where ν_c and μ_c are Poisson's ratio and shear modulus of casing, $a = (r_{\text{max}} - d_c)/r_{\text{max}}$ is another geometrical factor, μ_t is the shear modulus of the tool inside the borehole, μ_s is the formation's shear modulus, and ζ defines the coupling between the casing and formation: $\zeta = 1$ allows for movement of the casing in the axial direction relative to the formation, and $\zeta = 0$ restricts this movement.

Figure 2.3 shows the modeled dispersion relations for parameters similar to the ones we have in our experimental setup, both for an open and a cased borehole. For the low-frequency limit, we also plot the velocity obtained using the results presented in equation 2.2. The results are clearly in very good agreement, and no significant dispersion is expected in the range of frequency that was studied. The difference in phase velocity between the zero-frequency approximation and the Nyquist frequency of some of our data (2000 Hz) is less than 0.1%. Based on this result, from now on we will assume the tube wave is non-dispersive in our frequency range, and that its velocity is given by equation 2.2.

By measuring the tube wave velocity and using equation 2.2, one can obtain the shear modulus of the formation. The estimation of μ_s is very sensitive to all parameters, and a very accurate measurement of the tube wave velocity is necessary to

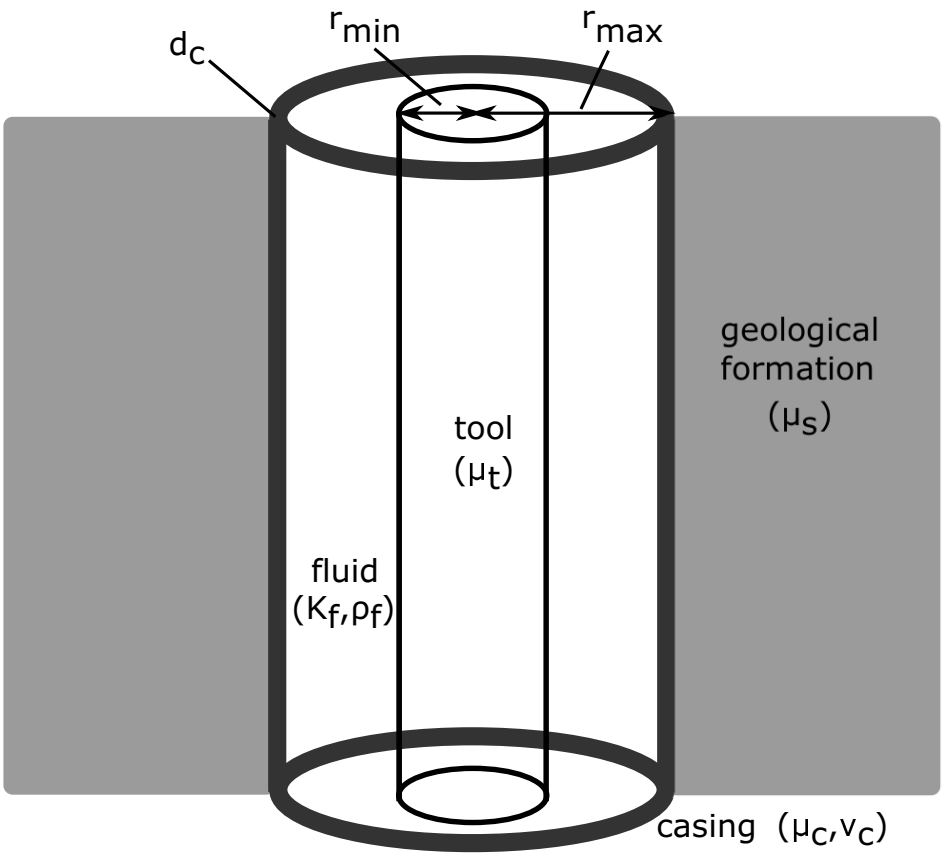

Figure 2.2: Borehole set up, with parameters for calculating tube wave velocity with equation 2.2 (Wehner et al., 2021).

get a good confidence interval, as can be checked in Figure 2.4. More details can be found in Wehner et al. (2021).

As seen in Figure 2.3, the modeled tube wave velocity for a configuration akin to ours is expected to be above 1000 m/s. This velocity is higher than the usual shear wave mode's in shallow formations, and measurements in a nearby test site (Long and Donohue, 2007) indicate a shear velocity v_s (or β) in the range of 120 m/s to 300 m/s, which is significantly lower than the modeled v_t. The propagation of a higher-velocity tube wave will then lead to the generation of *Mach waves* in the medium (Anderson Jr, 2010; Meredith et al., 1993).

Mach waves are very common in aerodynamics and fluid flow (Landau and Lifshitz, 1987). Pressure Mach waves appear when a body moves inside a fluid with a

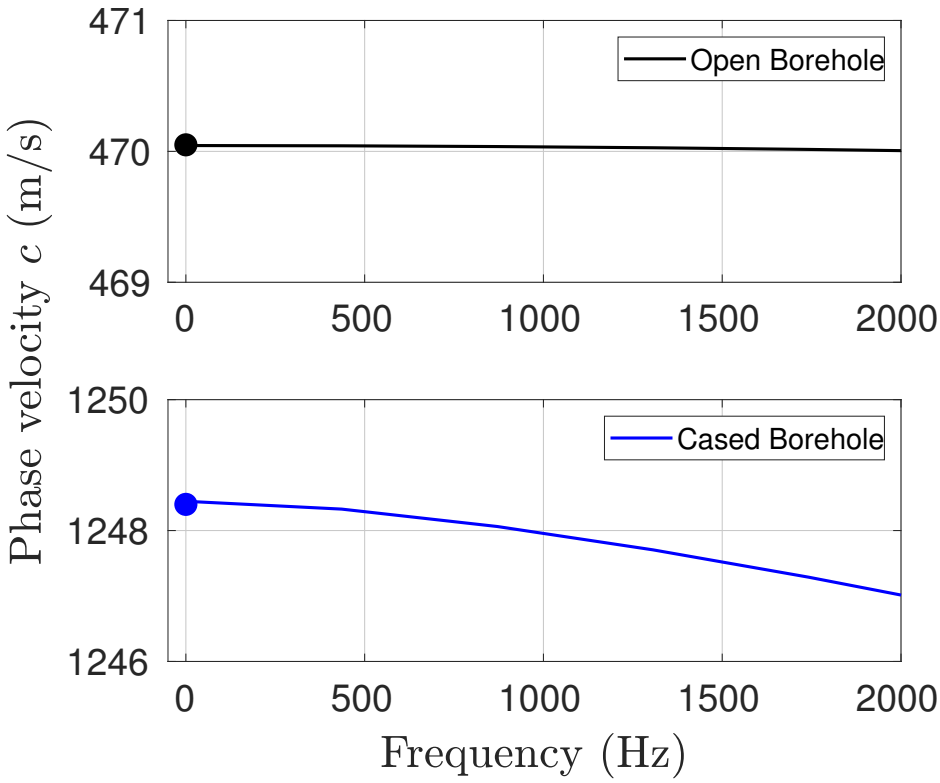

Figure 2.3: Modeled dispersion relations for tube wave phase velocity in an open (black) or cased (blue) borehole. Dots at zero frequency indicate low-frequency result published by Norris (1990).

velocity superior to the sound velocity in that medium. For a wave propagating in a tube, we can think in terms of Huygens' principle, and take every point in the tube wavefront as a new source: the wave propagating away from the well will form the characteristic Mach cone, with angle $\varphi = \sin^{-1}(1/M)$, where $M = v_t/\beta$ is the Mach number.

Figure 2.5 shows a sketch of how this Mach wave would propagate from one well to the other (left), and also shows a snapshot of a finite-difference modeling of the tube wave in a well, surrounded by a medium where $\beta < v_t$ (right). Tube wave velocity was modeled as 1100 m/s, and shear wave velocity was 500 m/s. Notice the cone propagating away from the well. If a series of receivers is put vertically in a nearby monitoring well, they will measure a linear event with velocity $v = 1100$ m/s, and tube waves in this second well will also be excited by the upgoing energy of the Mach cone. This will be further discussed in section 2.5.

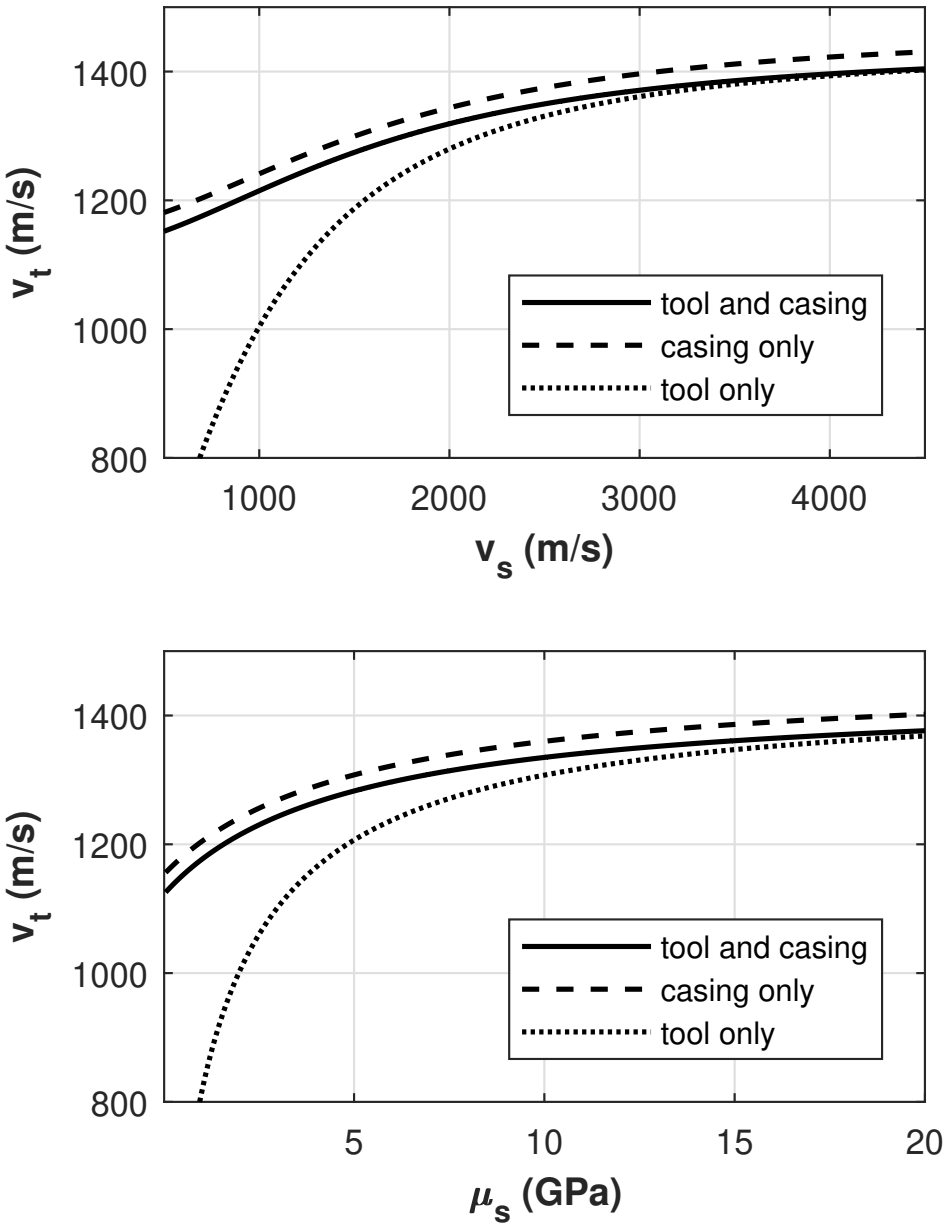

Figure 2.4: Relation between the tube wave velocity v_t and S-wave velocity v_s (**Top**) and shear modulus μ_s (**Bottom**) of the formation surrounding the well, for different setups (Wehner et al., 2021).

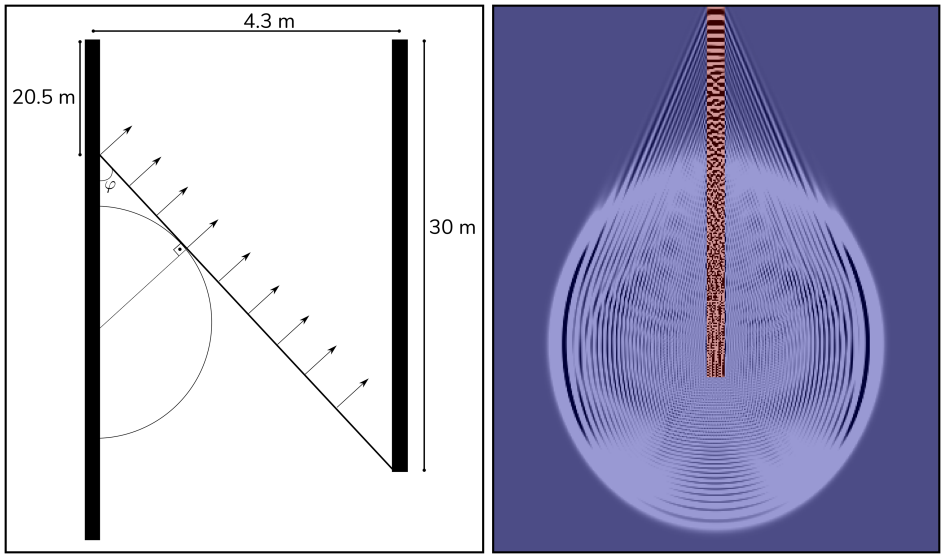

Figure 2.5: Left Sketch of depth section of experimental setup, showing angle or propagation of Mach wave ($\varphi \approx 24.5°$). **Right** Finite-difference modelling of source fired in the bottom of a well. Notice the Mach cone, propagating faster then the shear velocity in the medium. To ease visualization, distances are not in scale.

2.2.2 Tube Wave Attenuation

Seismic waves in real media are subject to attenuation - the decay of amplitude with distance (Müller et al., 2010). Attenuation can commonly be described as a combination of three general phenomena: **geometrical spreading**, **scattering**, and **anelastic attenuation**.

The two first phenomena involve conservation of energy: **geometrical spreading** is a natural consequence of the distribution of the wave energy over a larger surface, as the wave propagates - in the simple case of a spherical wavefront, the energy density decreases with the square of the sphere radius. Meanwhile, **scattering** is caused by heterogeneities in the medium, and its effect on the seismic wave depends on the scale of the spacing between these heterogeneities (Sayers, 1981; Wapenaar et al., 2013). The **anelastic attenuation** (or ***absorption***), on the other hand, is caused by the dissipation of energy during the propagation - usually in the form of heat and friction.

Tube waves, in particular, propagate in a confined space, being composed of a series of critical reflections and refractions within the well. Because of that, they do not suffer from geometrical spreading and can propagate over large distances

along the borehole (Ziatdinov et al., 2005). Besides, on our test site, there are no indications of strong scatterers in the frequency range of the recorded tube wave (Wehner et al., 2021; Long and Donohue, 2007): an X-Ray Diffraction (XRD) analysis of samples from the well drilling indicated that the soil is composed mostly (70%) of quartz, mica, and plagioclase. The composition is fairly uniform in the well depth range, with Gamma-ray log measurements indicating values around 60 (API units). The amplitude decay of the tube wave modes is assumed to be mainly caused by anelastic attenuation.

The anelastic attenuation is commonly modeled with the use of the quality factor Q, sometimes referred to as attenuation or absorption factor (Futterman, 1962). The parameter Q is a function of the fractional energy E dissipated per cycle (Sheriff and Geldart, 1995):

$$Q^{-1} = \frac{\Delta E_{\text{cycle}}}{2\pi E} \tag{2.3}$$

In a medium with constant Q, the effect of anelastic attenuation on the amplitude spectrum $A(f)$ can be written as

$$|A_t(f)| = |A_0(f)|e^{-\pi f(t-t_0)/Q}, \tag{2.4}$$

where $|A_0(f)|$ is the amplitude spectrum measured at an initial time t_0 and $|A_t(f)|$ is the spectrum measured at a later time t.

For a tube wave with phase velocity $c(f)$, the distance travelled in the borehole $\Delta z = z - z_0$ can be written as $\Delta z = c(f)(t - t_0)$. Under the hypothesis of non-dispersive tube wave in a limited frequency range, $c(f) = c$ is constant. Using the angular frequency $\omega = 2\pi f$, equation 2.4 can be rewritten as

$$|A_t(w)| = |A_0(w)|e^{-\gamma(\omega)z}, \tag{2.5}$$

where $\gamma(\omega) = \dfrac{\omega}{2cQ}$, which is the expression used by Stevens and Day (1986). By using a setup with an open well and no tool deployed inside the borehole, these authors presented the following expression for the factor $\gamma(\omega)$ (see equation 1 in their paper):

$$\gamma(\omega) = \frac{\omega}{2c}\left[\frac{\beta}{c}\frac{\partial c}{\partial \beta}\frac{1}{Q_\beta} + \frac{\alpha}{c}\frac{\partial c}{\partial \alpha}\frac{1}{Q_\alpha} + \frac{\alpha_f}{c}\frac{\partial c}{\partial \alpha_f}\frac{1}{Q_{\alpha_f}}\right] \tag{2.6}$$

In equation 2.6, α and β represent the compressional and shear velocities of the formation, with their respective absorption factors being Q_α and Q_β, respectively.

α_f stands for the compressional velocity of the borehole fluid, with fluid absorption being represented by Q_{α_f}. The coefficients multiplying each body wave absorption term are called **partition coefficients** (Cheng et al., 1982), and they weight the harmonic average used to calculate the contribution of each Q term.

Equation 2.6 is a special case of a more generic result for the contribution of each term to the total anelastic attenuation in a layered medium (Anderson and Archambeau, 1964). If we ignore terms of order $1/Q^2$, the total Q in a medium with n layers can be written as

$$\frac{1}{Q} = \sum_{i=1}^{n} \frac{v^{(i)}_{\alpha,\beta}}{c} \frac{\partial c}{\partial v^{(i)}_{\alpha,\beta}} \frac{1}{Q^{(i)}_{\alpha,\beta}}, \tag{2.7}$$

where c is the phase velocity, $v^{(i)}_{\alpha,\beta} = \alpha^{(i)},\ \beta^{(i)}$ are the compressional and shear wave velocities of the i-th layer, and $Q^{(i)}_{\alpha,\beta}$ are the respective quality factors. By using equation 2.7, the total Q can be measured and, if some of the elements on the right-hand side of the equation are known, the other elements can be inverted for. This is one of the goals of this chapter: to measure the tube wave absorption Q, and from it estimate the formation shear wave absorption Q_β.

By going back to the experimental setup shown in Figure 2.1, the setup can be interpreted as a four-layers cylindrical medium, with polar symmetry along the well axis. The “layers" are the hydrophone array (or tool), the borehole fluid, the well casing, and the geological formation. Because the shear velocity of the fluid is zero, these four layers, combined with equation 2.7, unfold in a total absorption Q depending on 7 seven terms:

$$\begin{aligned} Q^{-1} = &\overbrace{\frac{\alpha_t}{c}\frac{\partial c}{\partial \alpha_t}\frac{1}{Q_{\alpha_t}} + \frac{\beta_t}{c}\frac{\partial c}{\partial \beta_t}\frac{1}{Q_{\beta_t}}}^{\text{tool}} + \overbrace{\frac{\alpha_f}{c}\frac{\partial c}{\partial \alpha_f}\frac{1}{Q_f}}^{\text{fluid}} \\ &+ \underbrace{\frac{\alpha_c}{c}\frac{\partial c}{\partial \alpha_c}\frac{1}{Q_{\alpha_c}} + \frac{\beta_c}{c}\frac{\partial c}{\partial \beta_c}\frac{1}{Q_{\beta_c}}}_{\text{casing}} + \underbrace{\frac{\alpha}{c}\frac{\partial c}{\partial \alpha}\frac{1}{Q_\alpha} + \frac{\beta}{c}\frac{\partial c}{\partial \beta}\frac{1}{Q_\beta}}_{\text{formation}} \end{aligned} \tag{2.8}$$

Despite containing several terms, equation 2.8 can be made fairly simple by assuming some hypotheses, which we list below.

1. In the low-frequency approximation, the phase velocity is given by equation 2.2, depending neither on the P-wave velocity of the formation nor on the tool's. Therefore, the respective partial derivatives of the phase velocity with respect to these

velocities are zero, and the terms Q_{α_t} and Q_{α} do not contribute to the total absorption Q;

2. It was not possible to obtain the values of Q for the material used in the well casing (steel type S355J2H). Measurements of attenuation in aluminum and steel suggest that Q_{α_c} and Q_{β_c} can easily exceed 10^5 (Zemanek Jr and Rudnick, 1961; Wanniarachchi et al., 2017). These values by far exceed the usual values of rocks and soils (Batzle et al., 2005), and therefore their contribution to the total absorption is likely quite small. Still, since this contribution is weighted by the partition coefficient, the combined effect of these two numbers will be evaluated;

3. The fluid attenuation is often discussed in works about sonic logging (Stevens and Day, 1986; Cheng et al., 1982), which is justified by the fact that well logging usually happens with drilling fluid inside the well, not water: drilling fluids can easily show absorption three to four orders of magnitude higher than pure water (Motz et al., 1998). For water, the attenuation due to absorption in the frequency range studied here is about 0.1 dB/km (Fisher and Simmons, 1977; Ainslie and McColm, 1998), which translates into a Q_f above 10^5. Thus, as in the point made with the casing absorption, we might be able to disregard this term, depending on its partition coefficient;

4. Finally, one last term left to discuss is the shear absorption of the hydrophone tool (Q_{β_t}). This value is difficult to estimate because the tool is made of different materials (the hydrophone electronics, jacked in a PVC coating). The anelastic attenuation in minerals/solid materials is usually quite low (Toksöz et al., 1979). This is not the case for PVC: Favretto-Anres and Sessarego (1999) published values of shear wave attenuation for ultrasonic frequencies, indicating a high absorption (low Q). The values are in a higher frequency range but, by fitting a simple power-law (Kibblewhite, 1989), we can estimate the shear absorption at 1 kHz as being about 1 dB/m, which would mean $Q_{\beta_t} \approx 30$. We will use this value for some estimations in this paper, but a sensitivity analysis is also presented in the discussion section since this is a point of significant uncertainty in the study.

To weight the effect of each non-zero term in equation 2.8, it is necessary to compute also the partition coefficients. Figure 2.6 shows these coefficients for a range of formation shear velocities, using the parameters presented in Table 2.1 for the deep well (well 2). A total of four configurations are shown, considering both open and cased wells, with and without a measuring tool inside. It is clear that, by casing the well, the partition coefficient of the formation shear absorption (red lines in Figure 2.6) drops significantly, representing a smaller contribution of this parameter to the total absorption.

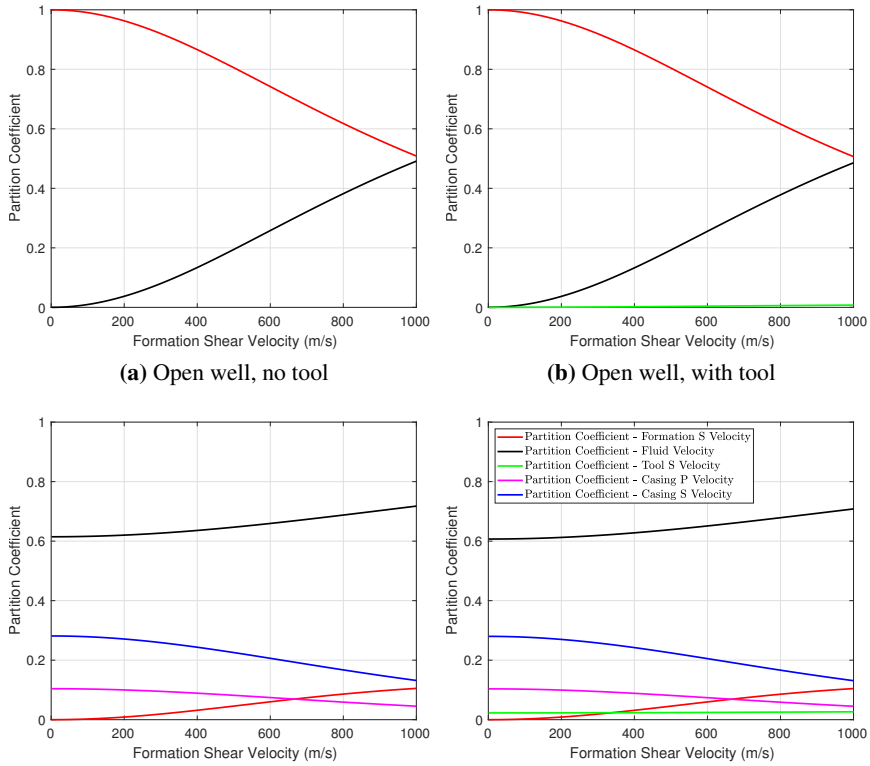

(a) Open well, no tool

(b) Open well, with tool

(c) Cased well, no tool

(d) Cased well, with tool

Figure 2.6: Partition coefficients for different experimental setups and formation shear velocities, using the parameters presented in Table 2.1 for the deep well (well 2). **(a)** Open well, without casing or tool inside. **(b)** Open well, with the measuring tool deployed. **(c)** Cased well, without the measuring tool. **(d)** Cased well, with tool inside. Scenario **(d)** is the one that represents our experiment. The legend shown in **(d)** is the same for all plots.

The estimated velocity in the formation surrounding the borehole in our experiment is 350 m/s, which makes the formation partition coefficient quite low when compared to other elements (Figure 2.6d). Tables 2.3 and 2.4 show the partition coefficients for this velocity in both wells, together with the product of partition coefficient and respective quality factor (Q_i).

The partition coefficients shown in Tables 2.3 and 2.4 indicate that the effect of the tool shear absorption is over two orders of magnitude stronger than that of fluid absorption and casing absorption. These values are dependent on the borehole geometry, casing material, and shear velocity of the formation, and the total absorption will have different sensitivities to these parameters under variable ex-

Table 2.3: Partition coefficients for formation shear velocity of 350 m/s in the shallow well (well 1). The value of 30 for the tool shear quality factor is only an estimation.

Parameter	Formation S	Fluid	Tool S	Casing P	Casing S
$\frac{v_{\alpha,\beta}^{(i)}}{c}\frac{\partial c}{\partial v_i}$	0.011	0.687	0.107	0.067	0.190
$Q^{(i)}$	Q_s	10^5	30	10^5	10^5
$\frac{v_{\alpha,\beta}^{(i)}}{c}\frac{\partial c}{\partial v_i}\frac{1}{Q_{\alpha,\beta}^{(i)}}$	$\frac{1}{90\,Q_s}$	6.9×10^{-6}	3.6×10^{-3}	6.7×10^{-7}	1.9×10^{-6}

Table 2.4: Partition coefficients for formation shear velocity of 350 m/s in the deep well (well 2). The value of 30 for the tool shear quality factor is only an estimation.

Parameter	Formation S	Fluid	Tool S	Casing P	Casing S
$\frac{v_{\alpha,\beta}^{(i)}}{c}\frac{\partial c}{\partial v_i}$	0.025	0.623	0.023	0.092	0.250
$Q^{(i)}$	Q_s	10^5	30	10^5	10^5
$\frac{v_{\alpha,\beta}^{(i)}}{c}\frac{\partial c}{\partial v_i}\frac{1}{Q_{\alpha,\beta}^{(i)}}$	$\frac{1}{40\,Q_s}$	6.2×10^{-6}	7.8×10^{-4}	9.2×10^{-7}	2.5×10^{-6}

perimental configurations. For this study, because of the much lower magnitude of these effects, we will drop the fluid and casing terms from equation 2.8, keeping only the tool and the formation's shear absorption contributions to the total Q.

In the next section, we will describe the data processing, where the values of velocity and attenuation are obtained from the experimental data.

2.3 Data Processing

A broad set of experiments was performed, resulting in the acquisition of a significant amount of data. Figure 2.7 displays raw data from three experiments: **Active S I**, **Active D I**, and **Passive D I** (See Table 2.2). In the active experiments, data has been shifted to ease display (the recording times are not synchronized with the source). Some coherent events can be identified, even before any processing.

Figure 2.8 shows the Fourier transform of the data displayed in Figure 2.7. The three experiments show a similar low-frequency content, but they start to deviate

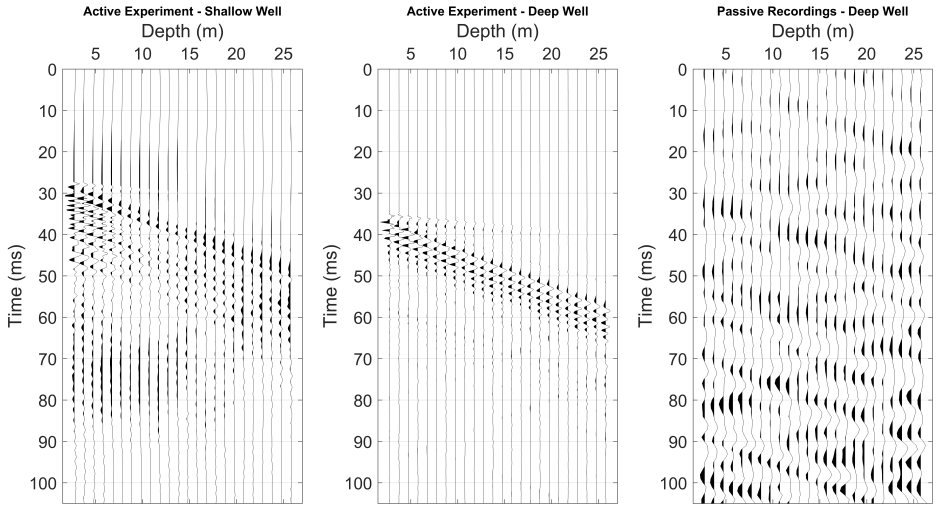

Figure 2.7: Example of seismic recordings for three different experiments: **Active S I** (**Left**), **Active D I** (**Center**), and **Passive D I** (**Right**). In the active experiments, data has been shifted in time to ease comparison and display.

when the frequency increases. To isolate the higher-frequency events in the active source experiments, a Butterworth bandpass filter (100 Hz - 450 Hz) of order 3 is applied to the data (Butterworth, 1930). The results can be checked in Figure 2.9.

Some interesting features can be noticed in the filtered data. First and foremost, the coherent events are now easier to spot. The strongest ones are clear downgoing waves (red arrows), and their velocity can be visually estimated as 1100 - 1200 m/s. A steeper event in the central panel, which fades away at about 20 m depth, has a velocity of almost 6000 m/s. The blue arrow in this same panel points to an *upgoing* wave, also with a velocity in the range 1100 - 1200 m/s.

As seen in section 2.2, the Stoneley mode shows little to no dispersion in configurations similar to our experiment's. We should then see these events as lines in the frequency-wavenumber domain. 2D Fourier transforms of the three examples (after bandpass filter) are displayed in Figure 2.10, where we indeed do see the expected linear pattern. In the center plot, three linear events can be seen: two downgoing (equivalent to the red arrows in the center plot of Figure 2.9) and one upgoing (blue arrow). The passive recordings (rightmost plot) also show the same pattern, but with the color, and scale tightened by two orders of magnitude.

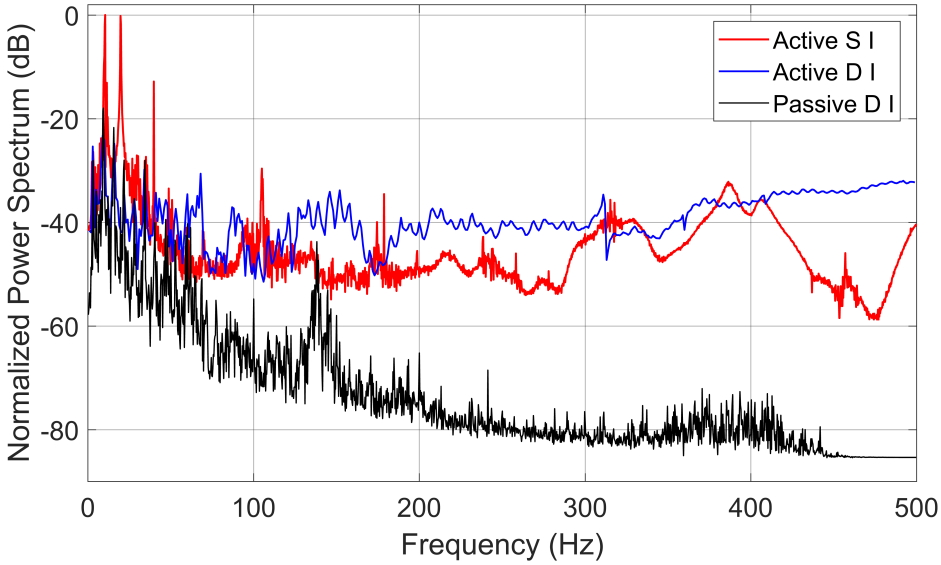

Figure 2.8: Power spectrum of data displayed in Figure 2.7.

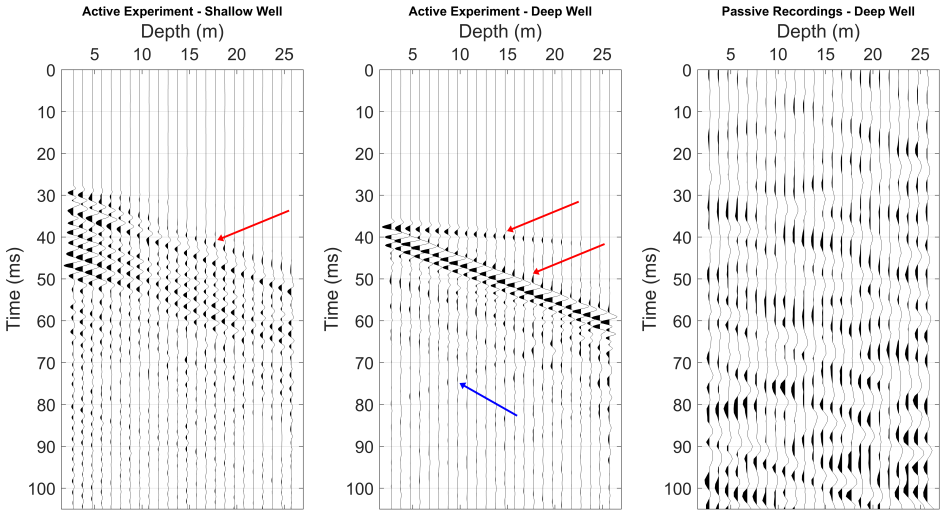

Figure 2.9: Same recordings of Figure 2.7, after bandpass filter (100 Hz - 450 Hz): **Active S I** (**Left**), **Active D I** (**Center**), and **Passive D I** (**Right**). Red arrows point some downgoing coherent events, and blue arrow points a possible upgoing event. In the active experiments, data has been shifted in time to ease comparison and display.

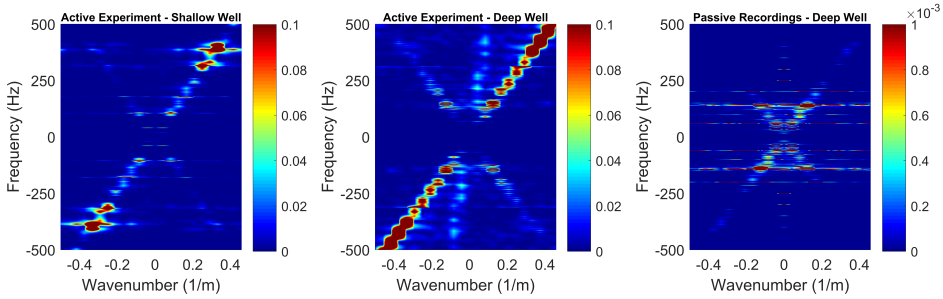

Figure 2.10: 2D Fourier transform of data shown in Figure 2.9: **Active S I** (**Left**), **Active D I** (**Center**), and **Passive D I** (**Right**). Data is normalized by the same factor, and color scale in rightmost figure is 100 times tighter.

The group velocity of an event can be calculated as the derivative of the frequency ω with respect to the wavenumber k. For a non-dispersive event, this derivative is simply the angular coefficient of the line in the 2D Fourier plot. We will now present two possible methods for obtaining the angular coefficient of this line, and one for the study of the passive recordings.

2.3.1 Velocity Estimation

Least-Square Line Fit

The first method used to calculate the velocity is a least-square line fit through the maxima in the frequency-wavenumber domain (Wehner et al., 2017). The core idea of the method is fairly intuitive: for every frequency f_i in the plots in Figure 2.10, the wavenumber $k_i^{\max}$ which gives maximum amplitude is picked. After that, the line going through the origin that has the smallest least-square difference to those points is selected as the best fit. Its angular coefficient α is calculated, and the result is interpreted as the velocity v_t of the non-dispersive event. Equation 2.9 represents this mathematically, and Figure 2.11 shows the result of this method applied to one of the experiments in the deep well.

$$v_t = \arg\min_{\alpha} \sum_i \left| f_i - \alpha k_i^{\max} \right|^2 \tag{2.9}$$

Figure 2.12 presents a sketch of a linear event observed in the f-k domain. Dark colors represent stronger amplitudes. The blue dots illustrate the maximum amplitudes that are picked, and the red y axis represents the best least-square fit to all points that goes through the origin. The tube-wave velocity is represented with the angular coefficient $\alpha = \tan\theta$. This figure also presents information about the Radon method, which will be introduced next.

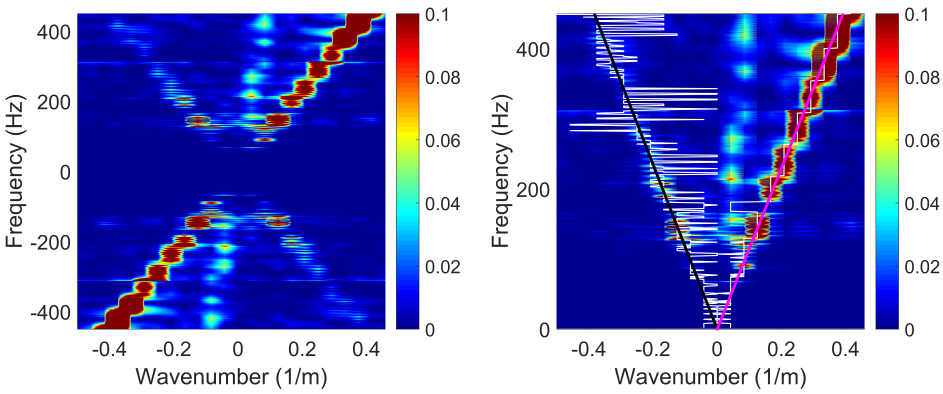

Figure 2.11: Left 2D Fourier transform of one recording from **Active D I**. **Right** Upper half of left plot, with white lines showing the amplitude maxima in each quadrant. Black line is the least-square fit of upgoing event ($v = 1175$ m/s), and magenta line is the fit of downgoing event ($v = 1146$ m/s).

Radon Transform

Given the linear nature of the events we are measuring, another method of particular interest is the *Radon transform* (Radon, 1986). The Radon transform $R(x', \psi)$ of a two-dimensional function $F(x, y) = F(\vec{r})$ is the line integral of F on the lines L, which can be written as

$$\begin{aligned} R(x', \psi) &= \int_L F(\vec{r})|d\vec{r}| \qquad \text{or} \\ &= \int_{-\infty}^{\infty} F(x' \cos\psi - y' \sin\psi, x' \sin\psi + y' \cos\psi) dy', \end{aligned} \tag{2.10}$$

where x' and y' are the rotated axis of the coordinate system and ψ is the rotation angle with respect to the f-k domain (see Figure 2.12). The Radon transform that we apply here is similar to the one used for *slant stacking*, or $\tau - p$ transform (Claerbout, 1985). Another common application of the transform is the parabolic Radon for multiple removal (Hampson, 1986; Foster and Mosher, 1992).

As we have seen in the previous section, the tube wave plots as a linear event in the f-k domain. By calculating the line integral for several angles in the 2D Fourier plot, the resulting transform would have its maximum in the angle that concentrates most of the energy. As in the line fit method, the tangent of this angle gives the velocity of a linear event.

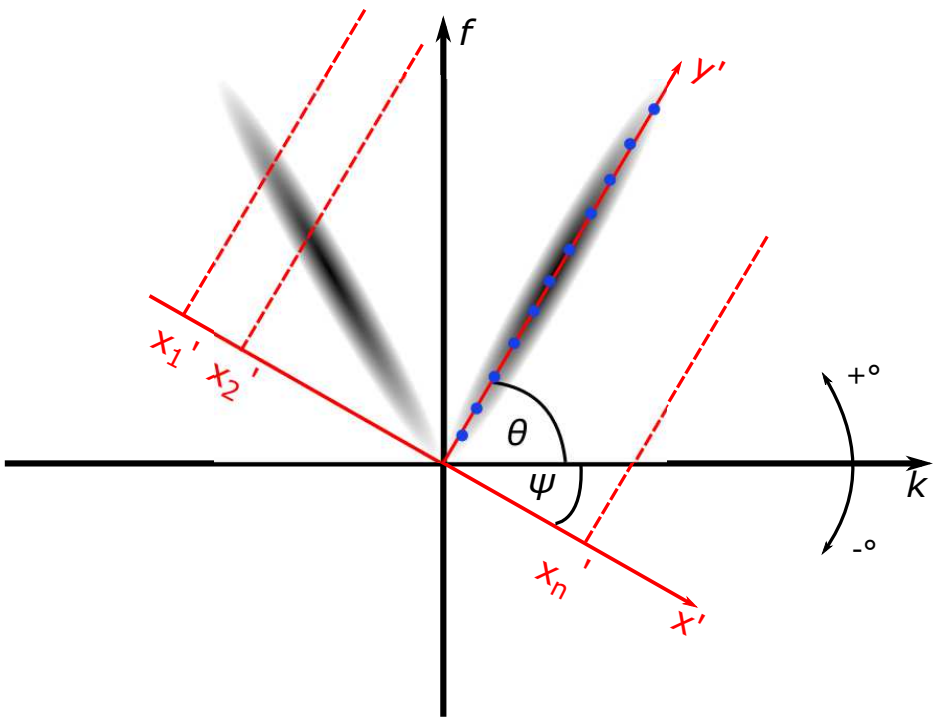

Figure 2.12: Sketch of a linear, symmetric event in the f-k domain. Dark colors represent stronger amplitudes. Blue dots denote maximum amplitudes picked for the line-fit, and θ is the angle between the fitted line and k axis. The red coordinate system represents the Radon transform rotated by an angle ψ. Dashed, red lines illustrate the series of line integrals performed parallel to the axis y'. The values of these integrals represent $R(x', \psi)$. Note that the angle θ is positive, while ψ is negative, as indicated by the black arrow (Wehner et al., 2021).

The geometry of Figure 2.12 shows that the focusing of the Radon integral occurs at an angle $\theta = \psi + 90°$. As the event goes through (0 m^{-1}, 0 Hz), the maximum for the example in Figure 2.12 appears at a displacement $x' = 0$ (the Radon transform is calculated assuming the f-k transform as an image, hence x' is dimensionless, being measured in pixels). We note that the Radon transform and line-fit method should theoretically lead to the same result for v_t.

To have the same basis for comparing the results, we also bandpass-filter the data (100 - 450 Hz) and apply a fan-filter to remove velocities below 300 m/s and above 6000 m/s. Figure 2.13 shows a f-k transform of the data in central panel of Figure 2.7, the resulting line fit, and its Radon transform.

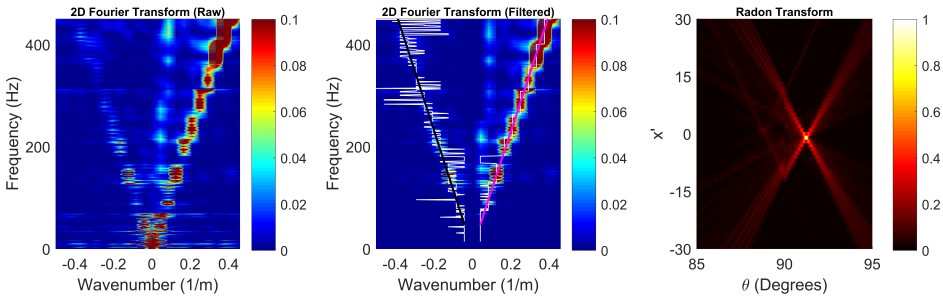

Figure 2.13: Left 2D Fourier transform of one recording from **Active D I** (only upper half of plot). **Center** Left plot after bandpass filter (100 Hz - 450 Hz) and fan filter (300 m/s - 6000 m/s), with white lines showing the amplitude maxima in each quadrant. Black line is the least-square fit of upgoing event ($v = 1162$ m/s), and magenta line is the fit of downgoing event ($v = 1146$ m/s). **Right** Normalized Radon transform of center plot. Maximum Radon amplitude indicates that both upgoing and downgoing velocities are $v = 1131$ m/s.

Cepstrum

The initial purpose of the passive recordings was to characterize the noise in our work environment and try to perform our acquisition experiments at times of the day when noise levels were the lowest. To do that, we calculated the *spectrogram* of the recordings, which is shown in Figure 2.14. Each vertical trace is the power spectrum of a 16-seconds trace from experiment **Passive D I**.

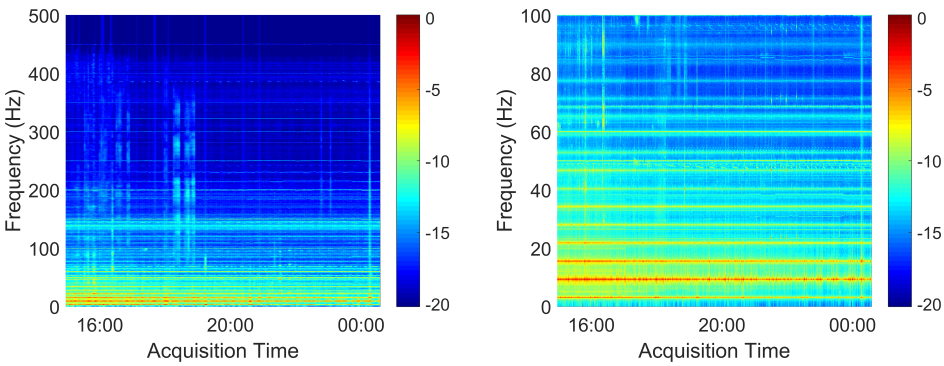

Figure 2.14: Left Normalized spectrogram of **Passive D I**. Color scale is decibels. **Right** Zoom on the left panel (frequencies up to 100 Hz) reveal a periodic pattern in the frequency peaks.

In the absence of an active seismic source, ambient noise is the only source of energy. Apart from some characteristic low-frequency noises (such as the ventilation

system and the normal modes of the building) and the power network frequency (50Hz), there was no reason to expect any coherency in the data. This does not hold, as can be noticed in Figures 2.10 (Right) and 2.14.

A series of periodic events in the frequency domain is usually related to harmonics, as these reinforce the amplitudes at certain frequencies. If the patterns had been identified in a time series, a simple Fourier transform would highlight the periodicity of the data. With the data already in the frequency domain, a Fourier transform would just bring us back to the recorded data, where no periodicity could be easily spotted (see Figure 2.7, rightmost panel). We need a tool that helps study periodic patterns in the frequency domain. This tool is called *cepstrum*, an anagram of the word spectrum (Bogert, 1963; Noll and Schroeder, 1964).

The cepstrum $c(q)$ of a time series $d(t)$ is calculated by taking the inverse Fourier transform of the logarithm of a signal's spectrum:

$$c(q) = \mathcal{F}^{-1}\left\{ \log\Big(\mathcal{F}\big\{d(t)\big\}\Big) \right\} \tag{2.11}$$

The resulting variable q of this inverse Fourier transform is labeled *quefrency* and has a dimension of time. A peak at a certain quefrency q_0 means that the frequency spectrum is periodic, with intervals of $1/q_0$.

Some good intuition about how the cepstrum can be used to find periodic events in the frequency domain is available in Oppenheim and Schafer (2004). As an example, we can think of a signal $x(t)$, which is the combination of a pulse $d(t)$ with its reflection delayed by a time τ, modulated by a reflection coefficient R:

$$x(t) = d(t) + Rd(t-\tau), \qquad |R| \leq 1. \tag{2.12}$$

Applying Fourier transform to both sides of the equality, we get

$$X(\omega) = D(\omega) + Re^{i\omega\tau}D(\omega).$$

The power spectrum of signal $x(t)$ is given by

$$|X(\omega)|^2 = |D(\omega)|^2[1 + R^2 + 2R\cos(\omega\tau)]$$

The presence of the delayed reflection creates an oscillatory modulation in the power spectrum, as is well known in the analysis of seismic data with "ghost"

(Rosa, 2018). To isolate this oscillatory term, we can calculate the logarithm of the power spectrum:

$$\begin{aligned} C(\omega) &= \log|X(\omega)|^2 \\ &= \log|D(\omega)|^2 + \log[1 + R^2 + 2R\cos(\omega\tau)] \end{aligned} \tag{2.13}$$

As in the Fourier analysis, the cepstrum of a signal has a real and a complex part. The inverse Fourier transform of function $C(\omega)$ in equation 2.13 is the *power cepstrum* of $x(t)$. Figure 2.15 shows the power cepstrum of the data from experiment **Passive D I**.

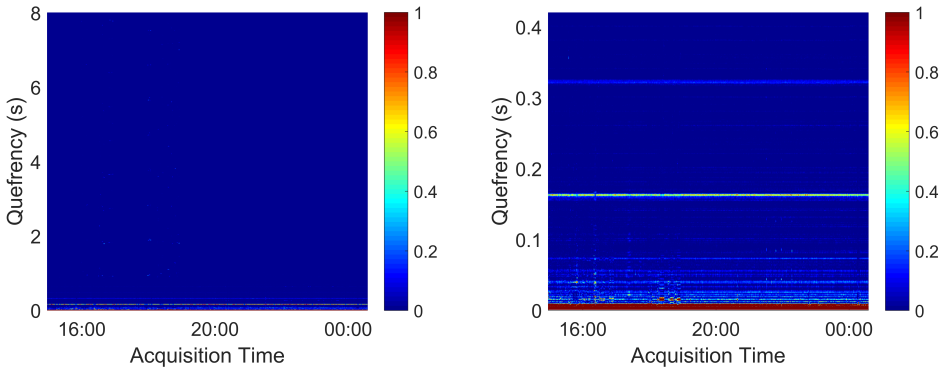

Figure 2.15: Left Power cepstrogram of experiment **Passive D I**. Color scale is intensity (arbitrary). **Right** Zoom on the left panel (quefrencies up to 0.4 s) reveals a peak around 0.163 s.

The right panel in Figure 2.15 shows a peak in cepstrum for quefrency $q_0 = 0.163$ s, which is associated with a spacing between frequency peaks of 6.135 Hz. We can interpret this spacing in terms of equation 2.12, and think of the delay τ as the time that an event takes to cover the distance from the hydrophone position until the extremity of the well, and then back to the sensor. If the depth of the well is h and the event propagates with velocity v, then $\tau = 2h/v$.

Because τ is given by the peak quefrency, we can calculate the velocity of the event as being $v = 2h/q_0$. If we compute the velocity with the average peak quefrency from Figure 2.15, we find $v = 1166$ m/s - compatible with the tube wave velocity measured using Radon transform and frequency-wavenumber line fit. This is a strong indication that the event is also detectable even in the absence of an active seismic source: most of the random noise created by several incoherent sources cancels out, but the frequencies associated with the well harmonics add up to stronger events, highlighting above the background noise level.

Because of the longer recording times necessary to calculate the velocity using cepstrum analysis, this method was only used to obtain the velocity from some passive recordings experiments. Also, to properly compare the results with the other methods, we removed velocities above 6000 m/s and below 300 m/s via *liftering* - the equivalent to filtering, but in the cepstrum domain.

Feasibility for Velocity Monitoring

To illustrate the feasibility of using tube wave measurements as a monitoring tool, a modeled scenario of shear modulus variation due to CO_2 injection is proposed.

As seen in Equation 2.2, the tube wave depends on changes in the shear modulus μ_s of the geological formation. Differences only due to density contrast between different fluids should not be noticeable from the measured tube wave velocity. Therefore, we focus on the mechanisms which change the shear modulus in geological formations. Chemical processes can lead to precipitation and dissolution effects, which have an impact on the shear modulus. These effects are experimentally investigated by Vanorio et al. (2011b) and Vialle and Vanorio (2011) for the case where CO_2 is injected into rock samples. The chemical effects are pronounced in carbonate rocks or brine-saturated sandstone. In carbonate rocks, a dissolution of the rock-forming minerals leads to a reduction of the shear modulus. In other formations, e.g. sandstones, a precipitation effect can be expected depending on the brine composition. The change of the shear modulus μ_s is caused by variations of the porosity due to precipitation and dissolution.

Another mechanism that could lead to changes in the shear modulus is a variation of the effective stress that can be caused by production or injection at reservoirs. For a collection of loose, uncemented grains in hydrostatic confining stress, it was shown in section 1.1.1 that the shear modulus $\mu_s(P)$ can be estimated as a function of the modulus $\mu_0(P_0)$ and the pressure ratio (P/P_0):

$$\mu_s(P) = \mu_0 \left(\frac{P}{P_0}\right)^{1/3}, \tag{2.14}$$

where μ_0 and P_0 are the shear modulus and pressure at time zero, before the injection. The effects that change the shear modulus are then variations of porosity due to precipitation or dissolution effects and changes in the effective stress.

We will assume that the well is drilled and completed in a sandstone formation, with a porosity of 30% at a depth of approximately 750 m. The initial confining pressure is 15 MPa, assuming a density of 2000 kg/m^3 for the overburden, and the initial pore pressure is 7.5 MPa, leading to an effective pressure of 7.5 MPa. In real applications, changes in the shear modulus due to pressure changes and pre-

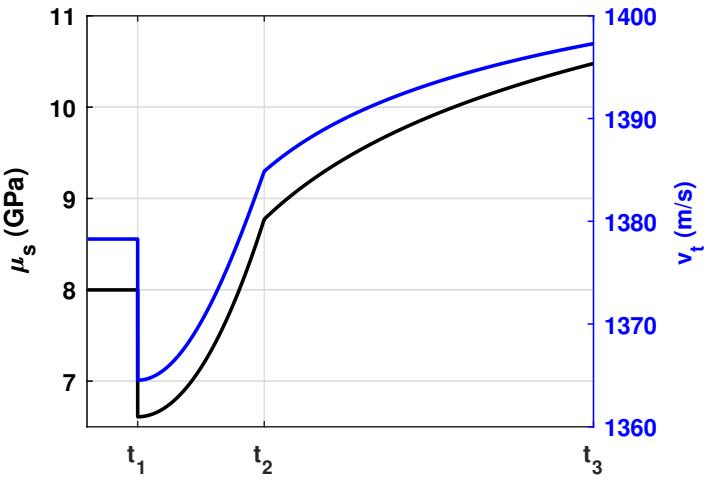

Figure 2.16: Modelled change of shear modulus μ_s (black, left axis) for a sandstone formation at approximately 750 m depth during CO_2 injection, together with corresponding change of the tube wave velocity v_t (blue, right axis). The injection starts at t_1 and ends at t_2. At t_3 the initial pore pressure is reached (Wehner, 2019).

cipitation/dissolution effects happen simultaneously, but on different time scales. While the pressure increase around the well occurs immediately after the injection has started, the chemical effects can take longer to manifest.

The time frame of the chemical processes is difficult to estimate. Recent studies illustrate that mineralization can happen faster than expected (Matter et al., 2016). In the modeled example we assume relative times, with injection beginning at t_1. The injection leads to a decrease in the shear modulus (Figure 2.16) due to increased pore pressure. It is assumed that the injected CO_2 increases the pore pressure by 2.5 MPa: an increase in pore pressure of up to 10 MPa due to injection is detected in different field sites (Duffaut and Landrø, 2007; Grude et al., 2014). After injection starts, we assume halite starts to deposit in the pore space, reducing the porosity to 27%, hence increasing the shear modulus. At t_2 the injection stops, and the pore pressure slowly decreases until it reaches its initial value at t_3. It is also assumed that the precipitation of halite minerals stops after t_2. If the chemical process continues after t_2, the shear modulus will increase even more.

The borehole in this example has a steel casing with a diameter of $18\frac{5}{8}$ in. (ca. 47.3 cm) and a thickness of 0.435 in. (ca. 1.1 cm), which is reasonable to assume for a depth of 750 m (Bourgoyne Jr. et al., 1986; Aadnøy, 2010). We assume a cylindrical tool inside the well (injection pipe and a hydrophone array). The diameter of the tool is 5.5 in. (ca. 14 cm), and it has a mean shear modulus of

50 GPa. The well is filled with water between the casing and the tool - the water has a temperature of 20 °C, following a geothermal gradient of 25 °C/km. This setup is used to model the changes of the tube wave velocity v_t according to the variations of the shear modulus (Figure 2.16, blue line). The modeled variations in shear modulus and tube wave velocity will be compared with the experimental uncertainty, to be presented in the Results section.

2.3.2 Attenuation Estimation

Calculation of Absorption from Experimental Data

The relation between total absorption Q of the tube wave and the shear absorption of the formation Q_β, keeping the two non-zero terms from equation 2.8, is

$$Q^{-1} = \frac{\beta_t}{c}\frac{\partial c}{\partial \beta_t}\frac{1}{Q_{\beta_t}} + \frac{\beta}{c}\frac{\partial c}{\partial \beta}\frac{1}{Q_\beta},$$

or

$$Q_\beta = \frac{\beta}{c}\frac{\partial c}{\partial \beta}\frac{Q}{1 - \frac{\beta_t}{c}\frac{\partial c}{\partial \beta_t}\frac{Q}{Q_{\beta_t}}} \tag{2.15}$$

To obtain the shear absorption using equation 2.15, it is necessary to estimate the total tube wave absorption from the experimental data. This estimation was calculated using the spectral ratio method (White, 1992). Going back to equation 2.4, the ratio between the amplitude spectra - or spectral ratio - in times t and t_0 is

$$|A_t(f)|/|A_0(f)| = e^{-\pi f(t-t_0)/Q}, \text{ or}$$

$$\ln(|A_t(f)|/|A_0(f)|) = -\pi f(t-t_0)/Q = -\psi f, \tag{2.16}$$

with $\psi = \pi(t-t_0)/Q$. The value of Q can be obtained from the slope of the best fit line (going through the origin) in the plot of the logarithm of the spectral ratio, as a function of frequency. The first step for this calculation, then, is obtaining the amplitude spectra for the receivers.

Before the calculation of the amplitude spectrum, a linear moveout (LMO) correction using the estimated tube wave velocity was applied to the data, to align the events. Figure 2.17 shows one recording before and after the application of LMO correction. Besides the tube waves, a wave in the well casing (interpreted as a P-wave, due to its velocity and the material properties) and the water P-wave can also be identified. Prior to the calculation of the power spectrum, an *f-k* filter

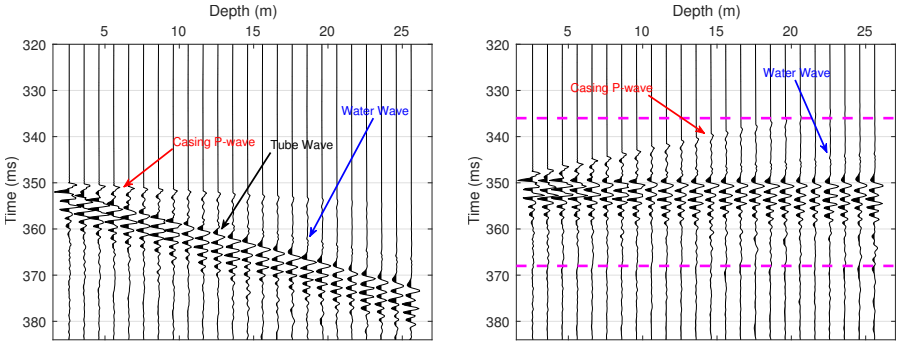

(a) Sample of experimental data.

(b) Data after linear moveout (LMO) correction.

Figure 2.17: Sample of data acquired in an experiment in well 2, before **(a)** and after **(b)** a linear moveout correction with the velocity of the tube wave ($v_t = 1137$ m/s). Red arrows point to the compressional body wave in the well casing (velocity of about 5000 m/s), the blue arrow points to the water wate (velocity of 1500 m/s), and the black arrow indicates the tube waves. The magenta dashed lines in Figure 2.17b show the 32 ms window that was selected for calculating the amplitude spectrum.

was applied to remove these two events, since they separate well in the frequency-wavenumber domain.

Figure 2.18a shows the amplitude spectrum of three receivers, for the same data shown in Figure 2.17b: the shallowest receiver (at about 2.6 m below the source position - see Figure 2.1), an intermediate receiver at 14.6 m, and a deep receiver (24.6 m below source position). The amplitude spectra (dashed lines in Figure 2.18a) are used to calculate an envelope (full, thick lines in the same Figure) - this is done to mitigate strong amplitude variations caused by the ghost effect (Cheng and Margrave, 2013). Figure 2.18b shows the plot of the logarithm of the spectral ratio, taking as reference the shallowest receiver. The dashed lines in Figure 2.18b are the best fit that goes through the origin. Because of the anomalous increase in the spectrum at high frequencies for the deepest receivers, we chose to fit the line only up to a frequency of 1500 Hz.

Using line fits as those shown in Figure 2.18b, the total tube wave absorption Q is estimated, and from it equation 2.15 is used to estimate the tool shear quality factor Q_{β_t} and the formation shear quality factor Q_β. In our estimations, which will be presented in the Results section, we take a fixed receiver as the reference for the calculation of the spectral ratio. That means that, when we plot the estimated Q_β for a certain depth, it represents the average Q_β from that point up to the depth of the reference receiver (z = 2.6 m for the shallowest receiver, for example).

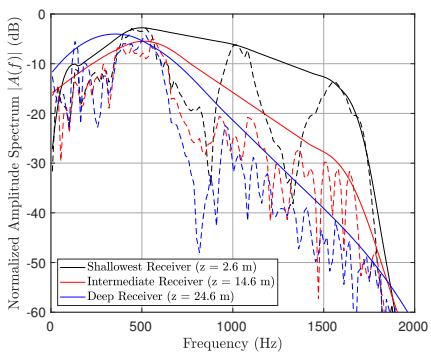

(a) Amplitude spectrum for some receivers (data from Figure 2.17a).

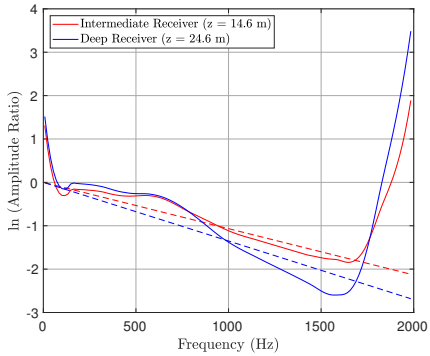

(b) Logarithm of amplitude ratios for data in Figure 2.18a, having the shallowest receiver as reference.

Figure 2.18: Amplitude spectra **(a)** and amplitude ratios **(b)** for some receivers in one experiment (data from Figure 2.17a). In panel **(a)**, dashed lines represent the amplitude spectrum, and full lines represented a smoothed envelope of this spectrum. In panel **(b)**, full lines show the logarithm of the amplitude ratio, and dashed lines show best least-square linear fit that goes through the origin.

Obtaining Q_{β_t} and Q_β

Because of the uncertainty about the shear quality factor of the hydrophone array (Q_{β_t}), we propose to use the measurements of the tube wave quality factor in the shallow well (Q^{sh}) and in the deep well (Q^{dp}) to invert for both properties. Assuming that the tool properties do not change between experiments, and that the rock formation properties are the same surrounding both wells (since these are less than five meters apart), we can use equation 2.8 (considering that only two elements are non-null) and write the following system of equations:

$$\begin{bmatrix} \frac{\beta_t}{c^{\text{sh}}}\frac{\partial c^{\text{sh}}}{\partial \beta_t} & \frac{\beta_t}{c^{\text{dp}}}\frac{\partial c^{\text{dp}}}{\partial \beta_t} \\ \frac{\beta}{c^{\text{sh}}}\frac{\partial c^{\text{sh}}}{\partial \beta} & \frac{\beta}{c^{\text{dp}}}\frac{\partial c^{\text{dp}}}{\partial \beta} \end{bmatrix} \begin{bmatrix} \frac{1}{Q_{\beta_t}} \\ \frac{1}{Q_\beta} \end{bmatrix} = \begin{bmatrix} \frac{1}{Q^{\text{sh}}} \\ \frac{1}{Q^{\text{dp}}} \end{bmatrix}, \quad \text{or} \tag{2.17}$$

$$\mathbf{M}\mathbf{x} = \mathbf{y} \tag{2.18}$$

The systems of equations shown in 2.17 in 2.18 can be solved using the well measurements, together with the partition coefficients presented in Tables 2.3 and 2.4. Since we have 23 depth measurements for each well (one receiver must be used as reference), we can solve the equation for Q in three ways:

i. **Hypothesis 1: Both Q_{β_t} and Q_β vary with depth.** In this hypothesis, equation 2.17 is solved independently for each of the 23 depth measurement. The system becomes determined, and the shear quality factors ($\mathbf{x}$) can be obtained as $\mathbf{x} = \mathbf{M^{-1}y}$ - or, using the values from Tables 2.3 and 2.4,

$$\begin{bmatrix} \dfrac{1}{Q_{\beta_t}} \\ \dfrac{1}{Q_\beta} \end{bmatrix} = \begin{bmatrix} 10.40 & -4.80 \\ -9.57 & 44.41 \end{bmatrix} \begin{bmatrix} \dfrac{1}{Q^{\text{sh}}} \\ \dfrac{1}{Q^{\text{dp}}} \end{bmatrix} \tag{2.19}$$

ii. **Hypothesis 2: Q_{β_t} is constant, and Q_β varies with depth.** If this hypothesis, the tool shear quality factor is constant, and the formation shear quality factor changes with depth. There are therefore 46 measurements (23 in each well), and 24 variables to invert for, leading to an over-determined system that can be posed as a least-squares problem, and solved with the conjugate gradient method (Berry et al., 1994).

iii. **Hypothesis 3: Both Q_{β_t} and Q_β are constant in the depth range investigated** In this third hypothesis, neither the tool nor the formation's shear quality factors change with depth. There are therefore 46 measurements (23 in each well) and 2 variables to invert for, leading again to an over-determined system, also solved as a least-squared problem.

The results of the three hypotheses mentioned above will be presented and discussed later in this work.

Feasibility for Q Monitoring

As there are several parameters involved in the estimation of the shear absorption of the formation, it might be difficult to estimate the absolute value of absorption, since the uncertainty in all those parameters will contribute to the computation of Q_β. Still, if the estimated values are precise and consistent, the measurements of tube wave attenuation could potentially be applied to detect variations in shear formation absorption, and therefore be employed as a surveillance method.

The shear absorption of a formation can be a function of dynamic parameters like temperature, effective pressure, and partial fluid saturation (Jones and Nur, 1983; Winkler and Nur, 1979). We can then estimate the feasibility of detection of formation shear absorption variation, using tube wave attenuation measurements.

Murphy III (1982) published the results of measurements of seismic attenuation in Massilon sandstones (23% porosity), under different saturation conditions. The

measurements were made in the range of hundreds of Hz, which seem adequate to use as an analog to our case since the absorption is frequency-dependent (Müller et al., 2010). The measurements indicated that the absorption on the samples was relatively constant for most water saturations, but changed considerably close to 100% saturation (see Figures 6 and 7 in his paper). This behavior was observed for different frequency ranges in the acoustic range. Assuming that the qualitative behavior of our formation is similar, a reduction of water saturation from 100% to 90% would indicate an increase in Q_β by about 50%-60%. This change is significant, and its implications for the total tube wave attenuation will be presented in the next section.

2.4 Results

2.4.1 Velocity Estimation

We now compare the results obtained for the different experiments and methods that have been discussed. We highlight here that, before the calculation of the 2D Fourier transforms, the data has been "padded" with zeros, so that the number of samples in both time and spatial domains is a power of 2 - this was done to optimize the Fast Fourier Transform algorithm (Cooley and Tukey, 1965). In the time domain, data was padded to a number of samples equal to the closest power of 2. In the spatial domain, data was padded to 64 samples.

Table 2.5 compiles the averages and standard deviations of the results obtained.

Line Fit and Radon

An example of velocity calculated using the Line Fit and Radon methods can be seen in Figure 2.19. Figure 2.20 compiles the results shown in Table 2.5 for the shallow well, and Figure 2.21 shows a crossplot of the experiments in this same well. Three biases can be observed in these Figures:

1. The Radon method is more consistent than the line fit (see error bars in Figure 2.20);
2. The upgoing Radon velocity is always faster than the equivalent line-fit one, while the opposite happens for the downgoing velocity
3. The upgoing Radon velocity is always faster than the downgoing Radon velocity, and the opposite happens for the line-fit velocity

These biases will be investigated in the Discussion section.

	Line Fit		Radon		Cepstrum
	Upgoing	Downgoing	Upgoing	Downgoing	-
Active S I	1204 ± 12.3	1208 ± 2.1	1214 ± 4.7	1198 ± 1.4	-
Active S II	1145 ± 24.5	1217 ± 1.9	1210 ± 1.5	1189 ± 0.1	-
Active S III	1099 ± 5	1206 ± 1.4	1201 ± 1.9	1197 ± 0.1	-
Active S IV	1120 ± 11.9	1224 ± 1.5	1223 ± 1.4	1217 ± 1.1	-
Active S V	1146 ± 10.3	1217 ± 1.1	1221 ± 1.4	1212 ± 0.1	-
Active S VI	1139 ± 9.1	1219 ± 0.4	1230 ± 1.5	1212 ± 0.1	-
Active S VII	1135 ± 7	1221 ± 0.4	1234 ± 1.4	1215 ± 0.1	-
Active S VIII	1163 ± 12.6	1217 ± 4.5	1232 ± 1.1	1200 ± 1.4	-
Active D I	1179 ± 6.8	1146 ± 0.6	1180 ± 5.2	1137 ± 0.3	-
Passive S I	1146 ± 39	1253 ± 12	1198 ± 2.5	1184 ± 1.7	1302 ± 65
Passive S II	1154 ± 47.7	1242 ± 11.1	1206 ± 2.3	1186 ± 1.6	1251 ± 29
Passive S III	1209 ± 4.2	1216 ± 3.9	1219 ± 0.9	1213 ± 1.6	-
Passive S IV	1051 ± 24.4	1221 ± 27.3	1090 ± 32.5	1075 ± 36.3	1024 ± 1046
Passive D I	1229 ± 193	1181 ± 11	1258 ± 442	1158 ± 2.4	1166 ± 2

Table 2.5: Velocity results for the different experiments. Values are in meters per second. More details about the results can be found in the Discussion section.

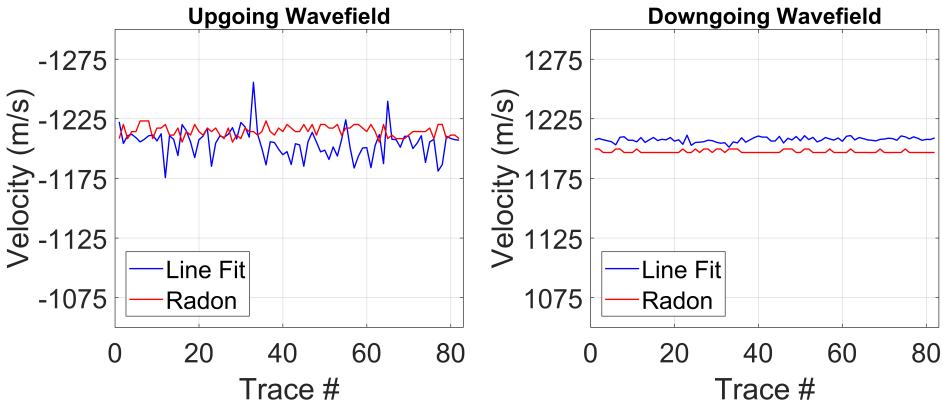

Figure 2.19: Velocity calculation for upgoing (**Left**) and downgoing (**Right**) events in experiment **Active S I**. Blue line is the result obtained with least-square line fit, and red line is the result obtained with Radon transform. A summary of average and standard deviation of velocities can be seen in Table 2.5.

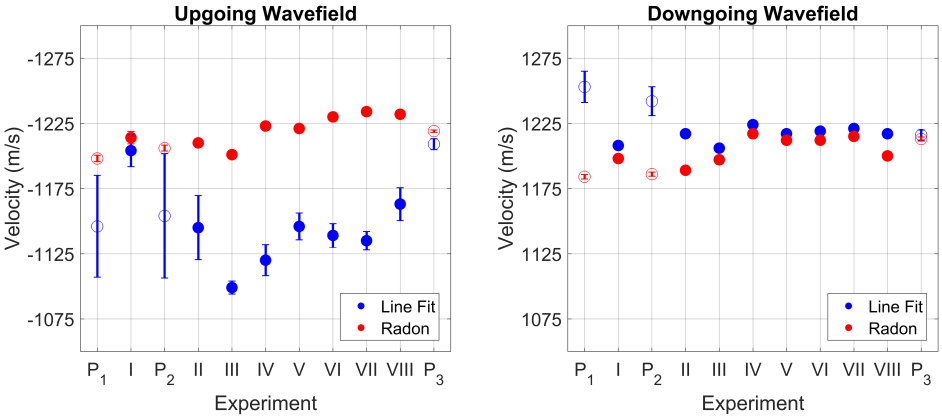

Figure 2.20: Velocity calculation for upgoing (**Left**) and downgoing (**Right**) modes for all experiments in the shallow well. Blue circles are results obtained with least-square line fit, and red circles are results obtained with Radon transform. Full circles represent active experiments, and open circles are passive recordings. Error bar is one standard deviation. Data is plotted in chronological order of acquisition.

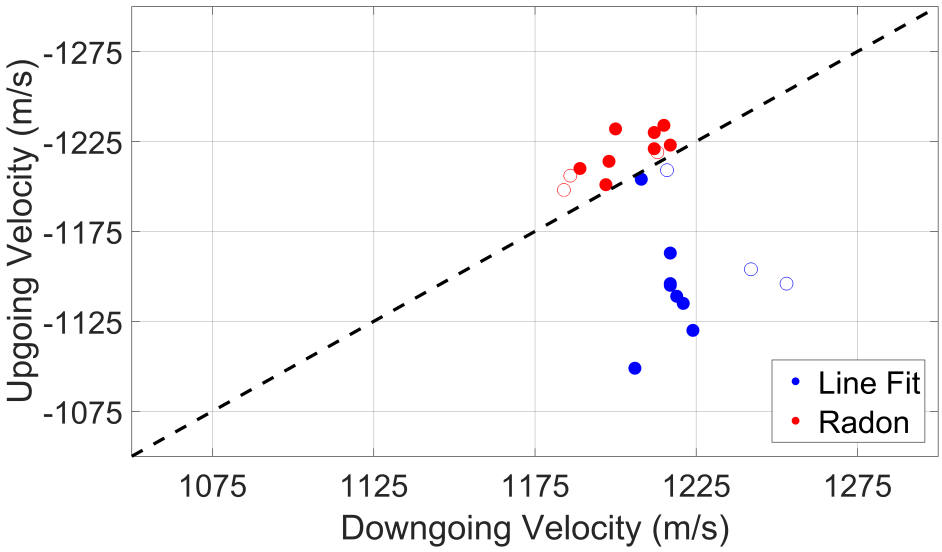

Figure 2.21: Crossplot of velocity calculation for all experiments in the shallow well. Blue circles are results obtained with least-square line fit, and red circles are results obtained with Radon transform. Full circles represent active experiments, and open circles are passive recordings. Black dotted line bisects the plot ($V_{\text{Up}} = V_{\text{Down}}$).

Cepstrum

The results for velocity estimation using the cepstrum method in the shallow well were very poor, with high standard deviations. On the other hand, the results for the deep well were quite stable, and have a remarkable precision. Simple statistical filtering, removing the points there are more than 3 standard deviations away from the average (about 2% of samples), yields a very consistent result (Figure 2.22)

Figure 2.23 shows the results for the deep well, comparing the cepstrum method with the downgoing Line Fit velocities. Both methods yield similar results, which reinforces the belief that the same event is being measured. The higher variability of line fit velocities is caused by its continuous variation, as it is the least-square fit of hundreds of points; the cepstrum velocities, coming from picking a maximum in a discrete grid, have a more "blocked" pattern.

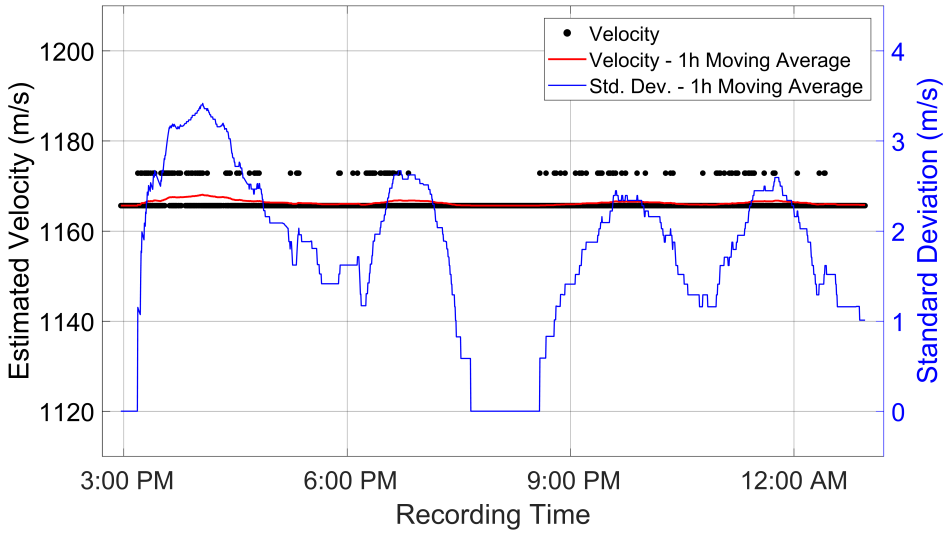

Figure 2.22: Velocity calculation using cepstrum method for experiment **Passive D I**, after removing outliers. Black dots are calculated velocity, red line is the one-hour moving average, and blue line is the one-hour moving standard deviation (right vertical axis).

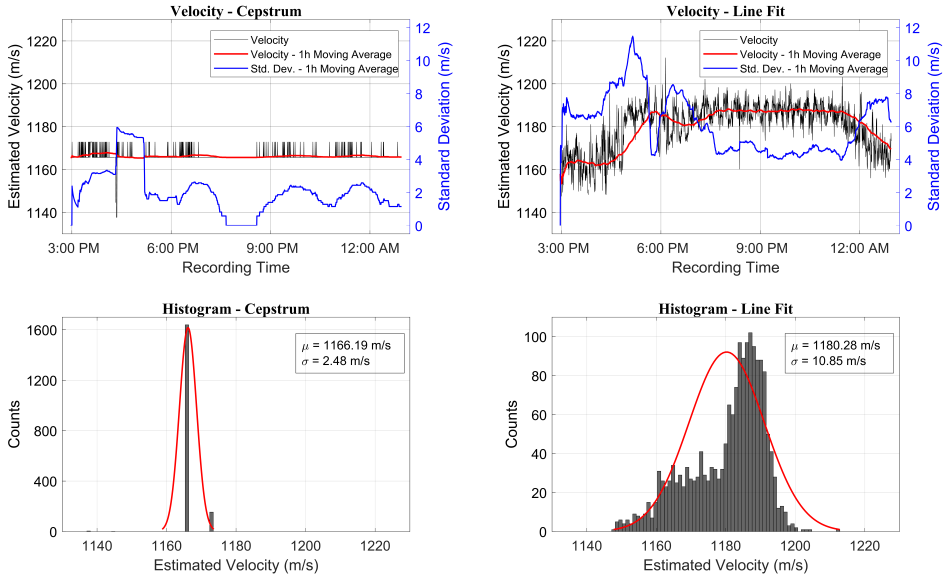

Figure 2.23: Velocity calculation for experiment **Passive D I** using cepstrum (**Left**) and downgoing Line Fit (**Right**). Top plots are velocity as function of time (black), with a one-hour moving average (red) and standard deviation (blue). Bottom plots are histograms of results, with a superimposed best-fit normal distribution.

Feasibility for Velocity Monitoring

The consistency of the tube-wave velocity estimation suggests that the formation shear modulus and S-wave velocity could be estimated within a reasonable range. Although the absolute characterization of the shear modulus in the formation from the measured tube wave is hardly possible, we can check whether consistent results can be achieved from the measurements in both wells. The relation given in equation 2.2 is used to estimate the shear modulus and S-wave velocity within the formation, using measurements from the active experiments in both wells. For this purpose, we use the results from the line-fit method. Because the coupling parameter is difficult to measure, we assume $\zeta = 0.5$, in between a perfectly coupled and an uncoupled well from the formation. For the velocity estimation, we assume a density value of $\rho_s = 2000$ kg/m^3. These results can be seen in Figure 2.24.

2.4.2 Attenuation Estimation

Figure 2.25 shows the estimated Q for the tube wave in the shallow well and deep wells. The solid lines are the median values of 80 experiments, excluding spurious values (negative Q). Error bars are plus or minus one standard deviation. The black lines show the results assuming the shallowest receiver (z = 2.6 m) as a reference, while the blue lines are the results using the second shallowest receiver (z = 3.6 m) as a reference. The values are plotted in the depth of the receiver where they were calculated.

The results for Q were estimated from two different reference points to verify the robustness of the method: it can be seen in Figure 2.18a that the power spectra of the receivers have notches at different frequencies. Therefore, to verify that the data registered is consistent, different receivers were also used as references for the calculation of absorption (blue lines in Figure 2.25), yielding results very close to the computations with the shallow reference hydrophone.

Figure 2.26 shows the estimated shear quality factors of the tool and formation, in the three hypotheses mentioned previously. As we can see, only hypothesis 3, where both quality factors are constant in the analyzed depth range, result in positive Q values for the whole depth range.

Sensitivity of Q to Different Parameters

The estimation of the formation shear absorption depends on several parameters. Also, the partition coefficients (equation 2.8) are a function of geometric and mechanical aspects, which needs to be incorporated into the estimations when boreholes of different geometries/materials are studied. Here we present some sensitivity plots to investigate how these parameter sin different conditions.

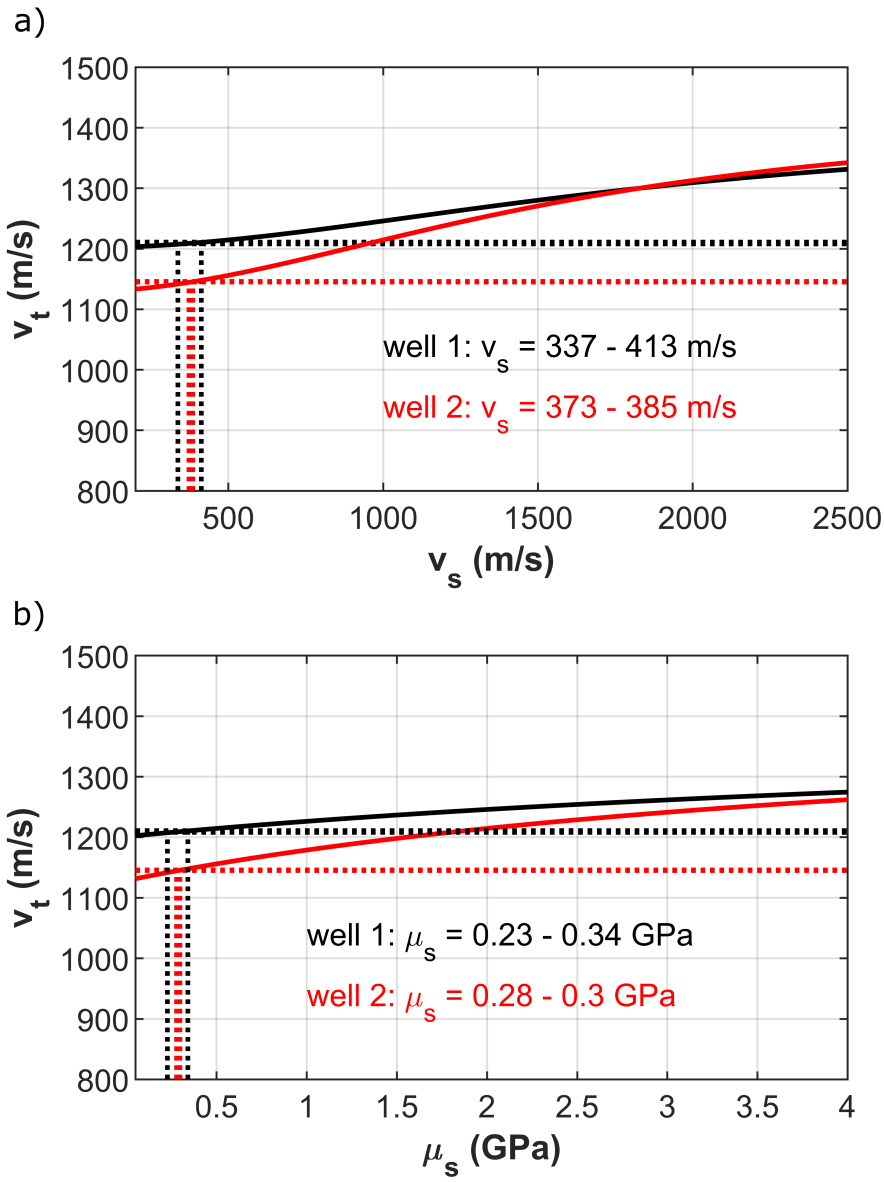

Figure 2.24: Relation between the tube wave v_t and (a) S-wave velocity v_s and (b) shear modulus μ_s for well 1 (black) and well 2 (red). The horizontal dotted lines indicate the range of the measured tube wave accounting for the measured precision. The vertical dotted lines are the resultant v_s and μ_s range (Wehner et al., 2021).

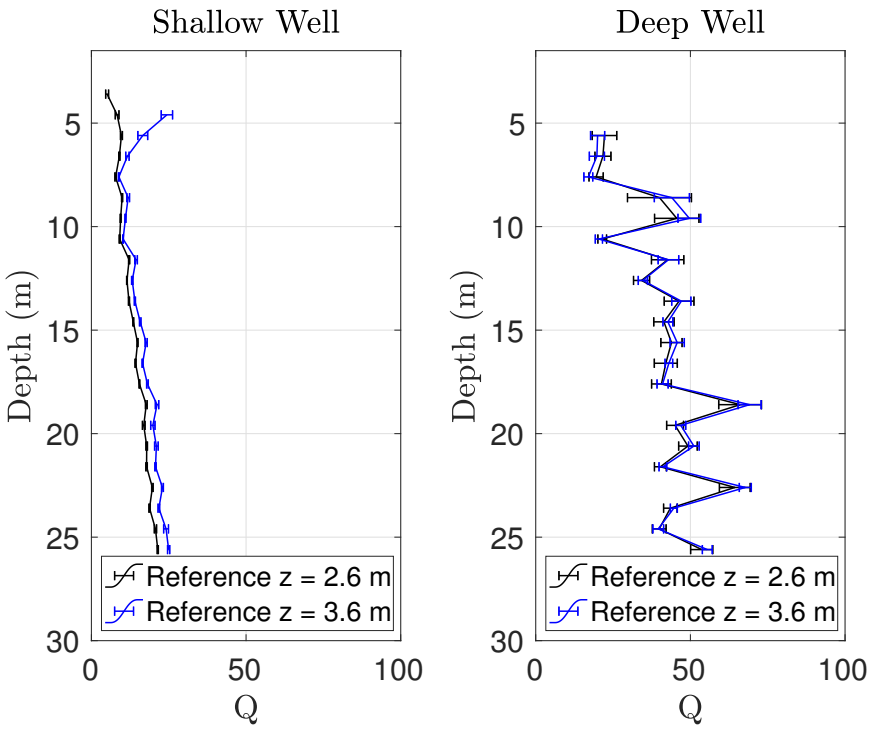

(a) Shallow well **(b)** Deep well

Figure 2.25: Estimated tube wave absorption Q in the shallow well **(a)** and deep well **(b)**. Each line is the median of 80 experiments. Black lines use the shallowest receiver (z = 2.6 m) as a reference for the spectral ratio method, and blue lines assume the second shallowest receiver (z = 3.6 m). Error bars represent plus or minus one standard deviation.

Figure 2.27 shows how the estimated formation shear absorption would change according to the different shear absorption values of the tool, considering different measurements of tube wave absorption Q in the deep well (well 2). In the experimental configuration used in this work, values of Q_{β_t} higher than 4 would have little impact on the estimation of Q_β.

In practice, when $\frac{\beta_t}{c}\frac{\partial c}{\partial \beta_t}\frac{1}{Q_{\beta_t}} \ll \frac{1}{Q}$, equation 2.15 can be approximated as

$$Q_\beta = \frac{\beta}{c}\frac{\partial c}{\partial \beta}\frac{Q}{1-\frac{\beta_t}{c}\frac{\partial c}{\partial \beta_t}\frac{Q}{Q_{\beta_t}}} \approx \frac{\beta}{c}\frac{\partial c}{\partial \beta}Q \tag{2.20}$$

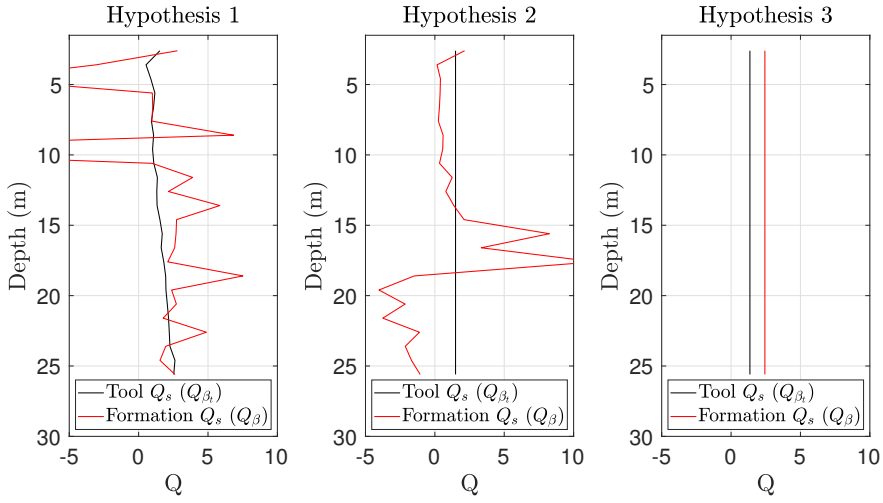

(a) Hypothesis 1 **(b)** Hypothesis 2 **(c)** Hypothesis 3

Figure 2.26: Estimated shear quality factors of the hydrophone tool (Q_{β_t}, in black) and formation (Q_β, in red), for the 3 hypothesis considered.

Figure 2.28 shows the sensitivity of the partition coefficients (equation 2.8) to the different geometry and mechanical parameters, when all other parameters are held constant (according to the values shown in Table 2.1). The interpretation of these plots, which for simplicity are obtained only for the deep well geometry, is discussed in the next section.

Feasibility for Q Monitoring

As observed in Figure 2.26, the estimated quality factor for formation shear absorption is quite low (about 2.5). A change of 60% in its value due to partial saturation changes, as discussed previously, might seem small (an increase from $Q_\beta = 2.5$ to $Q_\beta = 4$, for example). However, because the partition coefficient of the formation shear absorption is also small, the effect in the tube wave attenuation would be significant, as can be seen in Figure 2.29. The error bars represent a standard deviation of 7.9% of the absolute tube wave Q for the deep well and 1.4% for the shallow well, based on the results shown in Figure 2.25. The modeled results indicate that even minor changes in formation shear absorption could be detected with a relatively simple experimental setup, particularly if a measurement tool with higher shear quality factor can be used.

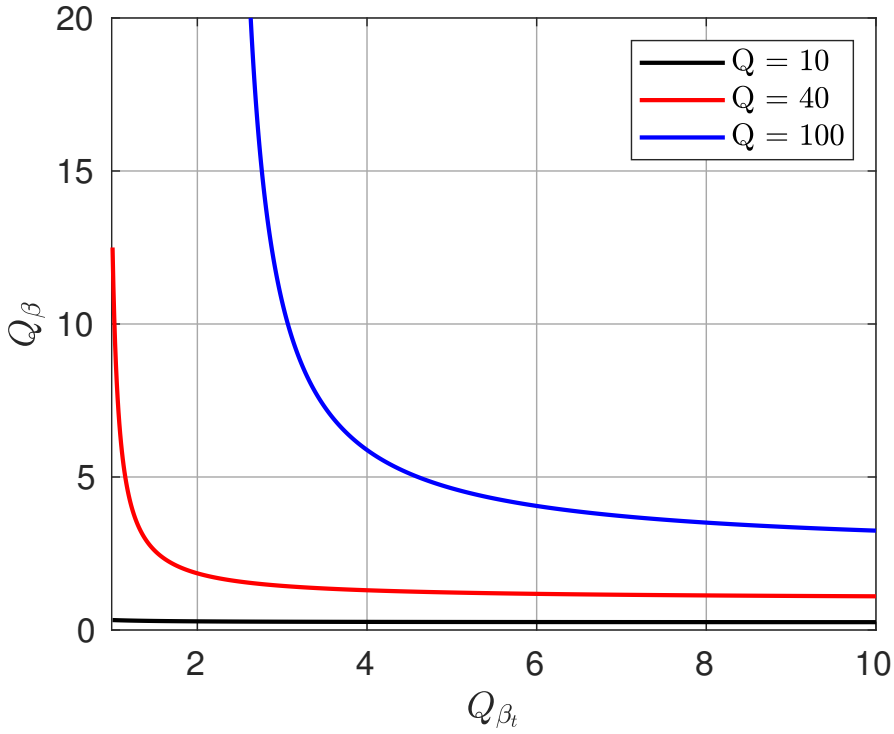

Figure 2.27: Sensitivity of Q_β estimation to the tool shear absorption Q_{β_t}, for scenarios of different measurements of tube wave absorption Q.

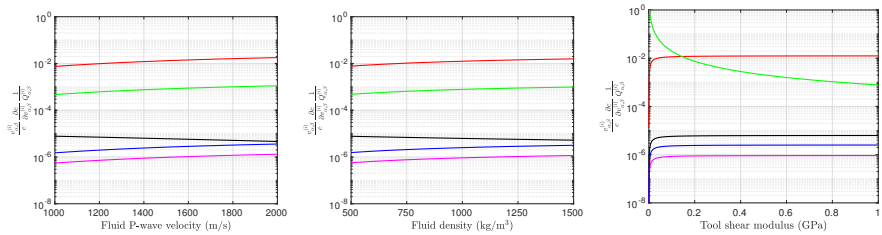

(a) Fluid P-wave velocity (α_f). **(b)** Fluid density (ρ_f). **(c)** Tool shear modulus (μ_t).

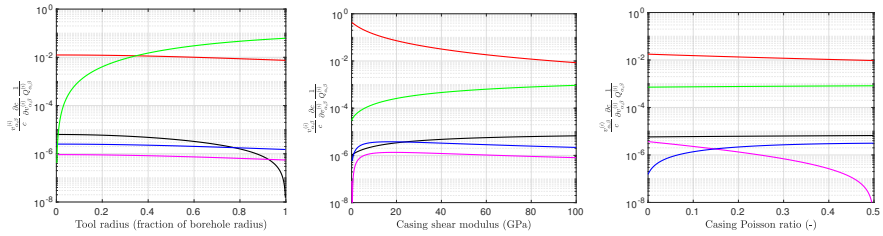

(d) Tool radius ($r_{\min}$). **(e)** Casing shear modulus (μ_c). **(f)** Casing Poisson ratio (ν_c).

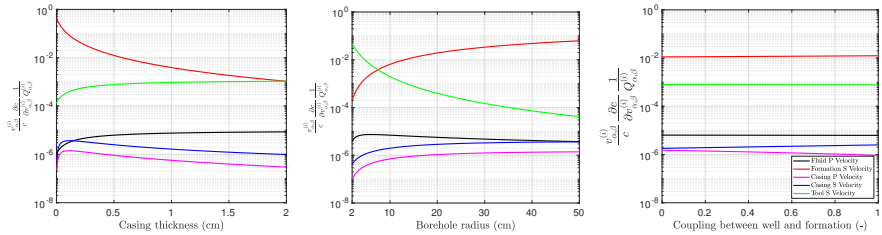

(g) Casing thickness (d_c) **(h)** Borehole radius (R) **(i)** Well coupling (ζ)

Figure 2.28: Sensitivity of partition coefficients to geometry, fluid, and mechanical parameters. Black lines represent the borehole fluid compressional velocity, red lines are formation shear velocity, magenta and blue are compressional and shear velocity of the casing material, and green lines are the hydrophone tool shear velocity.

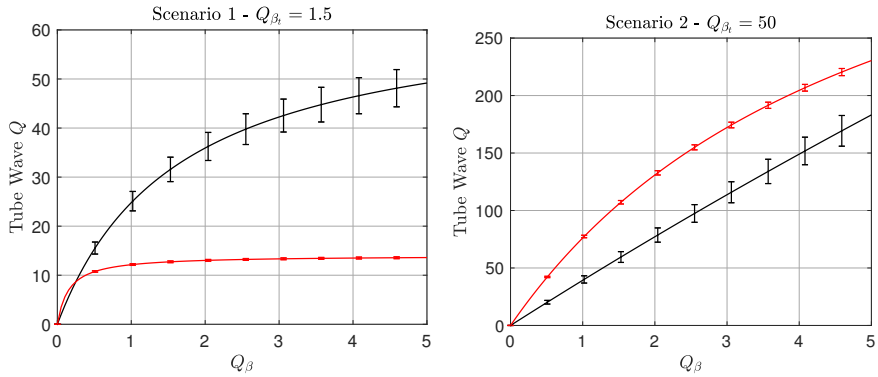

(a) Scenario 1 - $Q_\beta = 1.5$ **(b)** Scenario 2 - $Q_\beta = 50$

Figure 2.29: Tube wave quality factor Q as a function of different formation shear absorption Q_β, using equation 2.15. Two scenarios of tool shear quality factor Q_{β_t} are presented. Black lines show the result for the deep well, and red lines, for the shallow well, with error bars representing an estimated standard deviation of 7.9% and 1.4%, respectively.

2.5 Discussion

2.5.1 Velocity Estimation

Line Fit and Radon

As mentioned before, the results of the velocity estimations with these methods seem to present some bias. To better understand the causes of this behavior, we will investigate how both methods fare with modeled data. Figure 2.30 shows synthetic seismograms representing a series of up-and down-going tube waves in the shallow well, with a velocity of 1225 m/s. Data was generated using a convolutional model (left panel), and then white Gaussian noise was added to the result (right panel). A hundred experiments were generated, each with different random noise.

A possible explanation for the lower standard deviation of Radon velocities can be found by analysis of 2D Fourier plots of modeled data. In Figure 2.31 (right plot), the presence of the upgoing wave (reflections at the top and bottom of the well) creates a modulation in the wavefield, strengthening the amplitude at some frequencies and notching it at others. The modulation causes the least-square fit to be affected by noise in these notched frequencies and hence increases the variability of the velocity calculated with the line fit. Notice that by removing the upgoing wave, as in the left panel of Figure 2.31, the search for maxima - white lines - is much smoother, and the result for velocity calculation improves, as can be checked in Figure 2.32 (blue lines).

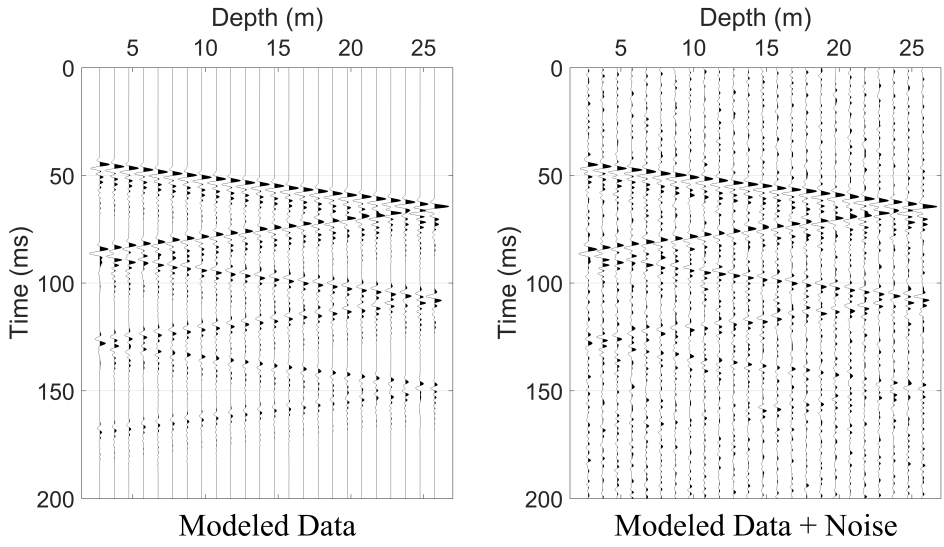

Figure 2.30: Synthetic seismograms modelling a tube wave with velocity of 1225 m/s. Data on the left is noise-free, and data on the right has random noise added to it.

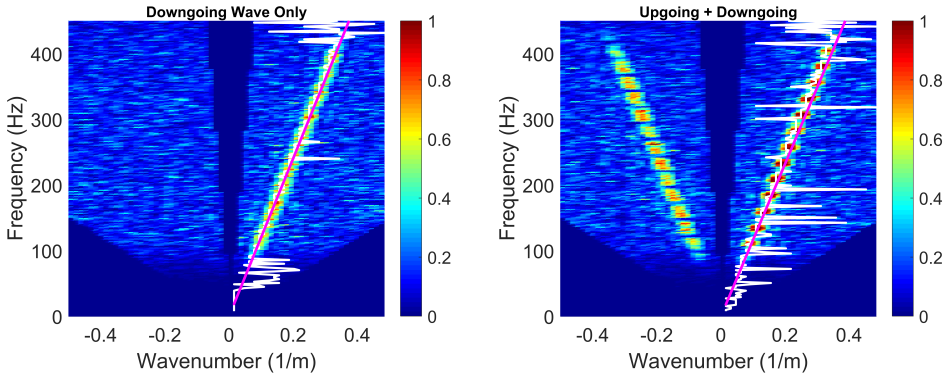

Figure 2.31: Left 2D Fourier transform of modeled downgoing wavefield. **Right** 2D Fourier transform of modeled up- and downgoing wavefields. White lines are maxima in frequency-wavenumber domain, and magenta line is the fit of downgoing event. Color scale is arbitrary intensity.

The Radon transform, on the other side, does not suffer so much from the lack of amplitudes at the notched frequencies, as the line integral still yields its maximum at the same angular coefficient. This can be noticed as a very consistent result in the Radon velocities for the modeled data (Figure 2.32, red lines), and it is believed to be the chief motive behind more steady Radon velocities.

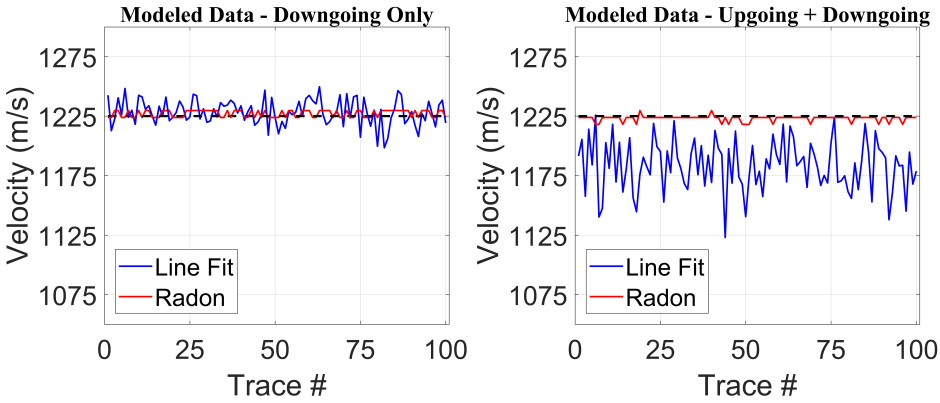

Figure 2.32: Velocity calculation for downgoing wave in modeled data, when we consider only downgoing wavefield (**Left**) and when upgoing wavefield is also modeled (**Right**). Blue line is the result obtained with least-square line fit, and red line is the result obtained with Radon transform. Black dotted line is the modeled velocity (1225 m/s).

Another thing that draws our attention is the fact that line-fit results from modeled data are consistently lower than the Radon ones. This can also be noticed in the right plot of Figure 2.31, with the white line - amplitude maxima - showing more spurious values to the right of the main downgoing event (or to the left of the main upgoing event), pushing the line fit towards lower velocities. This was an unexpected behavior: the noise added to this synthetic data is random, so it shouldn't have any sort of bias for higher or lower velocities.

The explanation for that lies in the size of the area to the left and right of the "correct" linear event. In the frequency-wavenumber plots presented so far, the area to the right of the modeled downgoing event is larger than the area to the left (Figure 2.33, left): the red region has events with an angular coefficient lower than the main event (thick black line), whereas the blue region contains faster events. As the noise is random, there is a higher probability that values in the area in red are picked as maxima, simply because there are more samples on this side. This creates a bias toward lower velocities for our modeled data, and also for the field data, a behavior that is confirmed by the measurements of the upgoing wavefield, but not for downgoing events (Figure 2.20).

Results for calculation of velocity from modeled data with fan filter in the range 900 m/s - 1800 m/s are shown in Figure 2.34. The bias for lower velocities in the line fit method disappeared, and the variability in the estimated velocity is reduced.

Figure 2.35 shows an updated version of Figure 2.20, using the tighter fan filter.

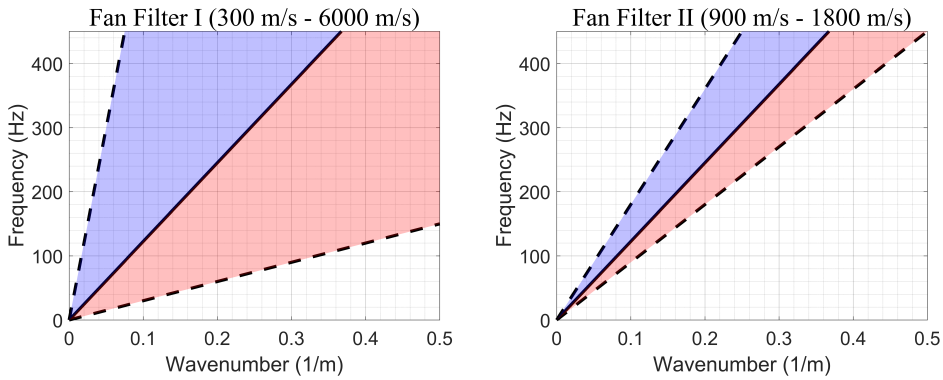

Figure 2.33: Left: Sketch of 2D Fourier plot, showing the areas where velocity is lower (red) or higher (blue) than the main modeled event (thick black line). Dotted lines are the limits of the fan filter (300 m/s - 6000 m/s). **Right** Same plot, but with fan filter range of 900 m/s - 1800 m/s.

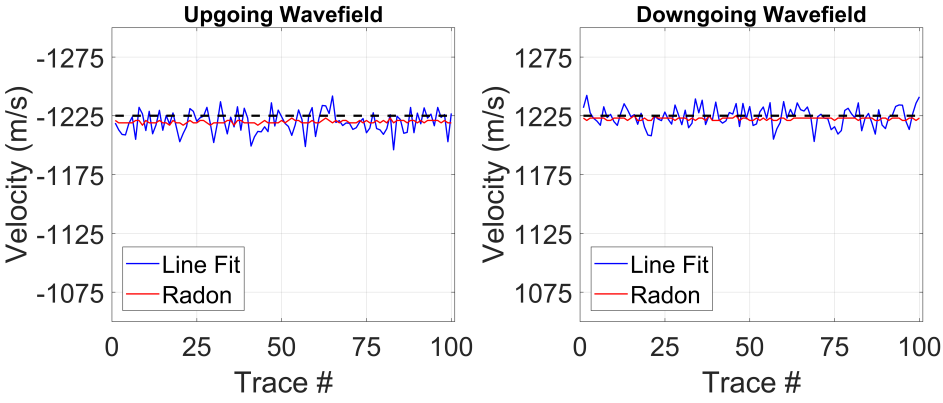

Figure 2.34: Velocity calculation for upgoing (**Left**) and downgoing (**Right**) events with noisy modeled data, with tighter fan filter (900 m/ - 1800 m/). Blue line is the result obtained with least-square line fit, and red line is the result obtained with Radon transform. Black dotted line is the modeled velocity (1225 m/s).

We can notice that the gap between line fit and Radon velocities was narrowed for the upgoing events (left panel), but did not cease to exist. For the downgoing events (right panel), little has changed: the line fit velocities are still higher. Radon velocities barely change due to the different fan filter.

To investigate the faster downgoing line fit velocities, we go back to Figure 2.9. Despite being arguably the signal with higher amplitude, tube waves are not the only coherent events in the data. There are several other modes propagating in the

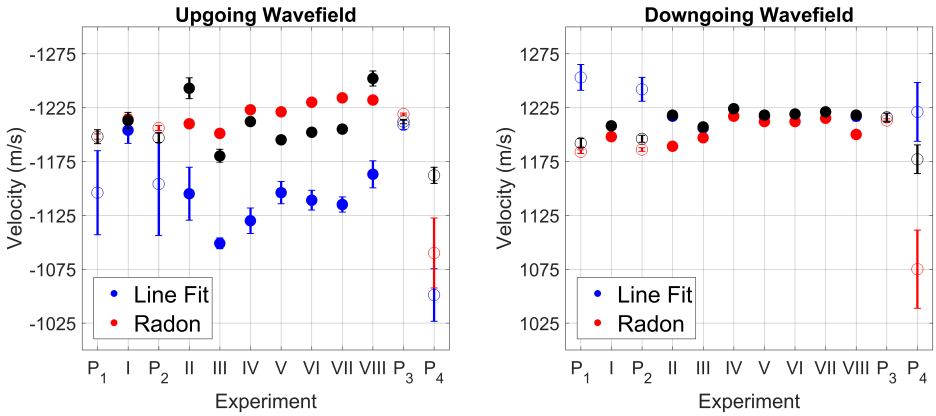

Figure 2.35: Velocity calculation for upgoing (**Left**) and downgoing (**Right**) modes for all experiments in the shallow well, with tighter fan filter. Blue circles are results obtained with least-square line fit and fan filter of 300 m/s - 6000 m/s, black circles are results obtained with least-square line fit and fan filter of 900 m/s - 1800 m/s, and red circles are results obtained with Radon transform. Full circles represent active experiments, and open circles are passive recordings. Error bar is one standard deviation. Data is plotted in chronological order of acquisition.

medium, and we highlight here two of them: the P-wave in the water inside the well (with a velocity of roughly 1500 m/s) and the compressional mode in the steel casing (about 5000 m/s).

These two events are significantly weaker than the tube waves but, because of the notches in the frequency, they could affect the calculation of velocity with the line fit method. The steel casing event - pointed by an arrow in the center panel of Figure 2.9 - is filtered out by the fan filter, but the P-wave in the water remains. Its effect can be noticed on the right panel of Figure 2.36, where it has the effect of deflecting the fitted line towards higher angular coefficients when compared with the panel that only includes tube waves (left).

Figure 2.37 shows the results of velocity calculation in noisy modeled data when we include downgoing waves with water velocity. Notice that the behavior shown in Figure 2.35 is now better represented.

We now move to discuss the results of the experiments in the deep well. This well was equipped with production liners and other tools shortly after we started performing experiments with it, and so there are much less data available. Regardless of the propagation mode or method applied, results for the deep well experiment show slower velocities when compared to the shallow well. This can be promptly checked in equation 2.2 or, more clearly, in Figure 13a of Wehner et al. (2021):

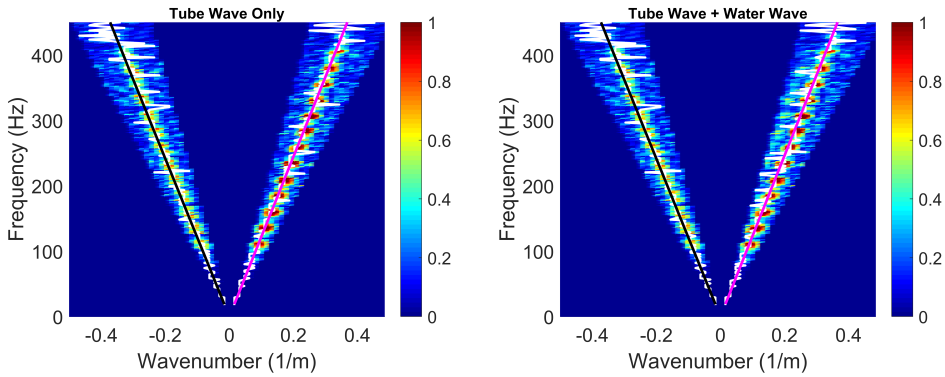

Figure 2.36: Left 2D Fourier transform of modeled data with tube waves only. **Right** 2D Fourier transform of modeled data with tube waves and water P-wave. White lines are maxima in the frequency-wavenumber domain, the Black line is the least-square fit of an upgoing event, and the magenta line is the fit of a downgoing event. The color scale is arbitrary intensity.

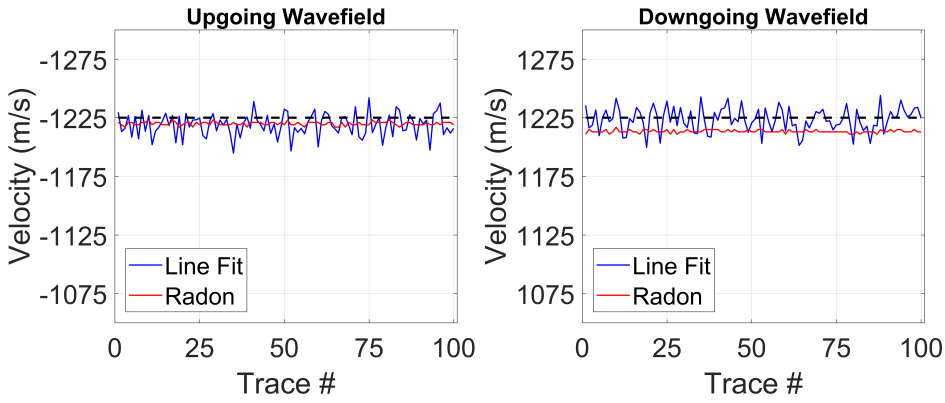

Figure 2.37: Velocity calculation for upgoing (**Left**) and downgoing (**Right**) events with noisy modeled data, including P-wave in water. Blue line is the result obtained with least-square line fit, and red line is the result obtained with Radon transform. Black dotted line is the modeled tube wave velocity (1225 m/s).

when all parameters are kept the same, a larger borehole diameter results in a slower tube wave velocity, and the deeper well has twice the diameter of the shallow one (Table 2.1).

This becomes more interesting when we also analyze the result of the experiment **Passive S III**, where data was recorded in the shallow well while a drill string was active in the deep one. This is the only experiment in which the upgoing

velocity has a smaller standard deviation than the downgoing velocity, which can be interpreted as a strong upgoing energy source since the wells are close (less than 5 m apart).

As presented in Figure 2.5, the fast tube wave propagating in the deep well will create Mach waves, which will reach the bottom of the shallow well and show up in the data as a linear event of velocity equal to the deep well's tube wave velocity. To account for the effect of this upgoing Mach wave, we model an upgoing event of velocity 1100 m/s - the chosen velocity was smaller than the measured in the deep well to account for the impact of water P-wave velocity, which probably also increases the velocity in the deep well. By including a downgoing water wave and an upgoing Mach wave, the modeled data reproduces the behavior that was observed in the experiments (Figure 2.38).

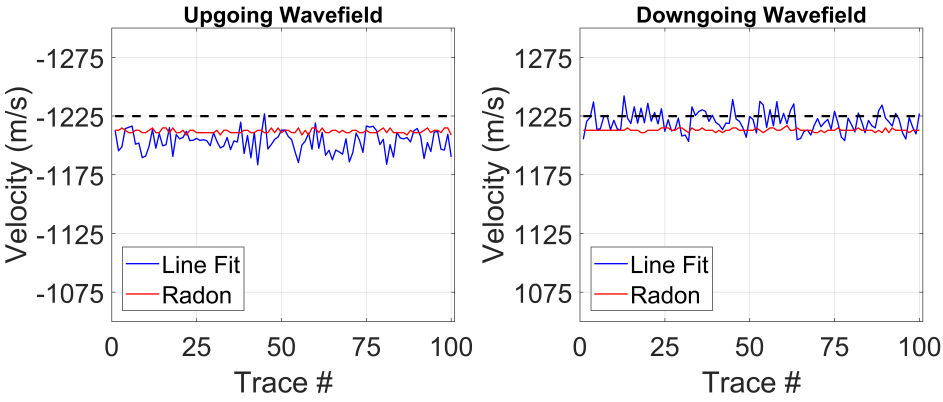

Figure 2.38: Velocity calculation for upgoing (**Left**) and downgoing (**Right**) events with noisy modeled data, including P-wave in water and upgoing Mach wave. Blue line is the result obtained with least-square line fit, and red line is the result obtained with Radon transform. Black dotted line is the modeled tube wave velocity (1225 m/s).

The combination of casing waves, water waves, reflections at the well bottom, and Mach waves seem to account for biases that we observed in our data. The representation of these events would be more accurate if a more robust modeling method, like finite differences, were used to model the wave propagation. Because of the broad frequency range and the presence of very thin layers, the adequate grid for such modeling is quite fine, making it challenging in terms of memory and computational time. Some approaches to this issue are still being considered.

Cepstrum

The disappointing results for the cepstrum method in the shallow well, when compared to the nice results in the deep well, prompted us to further study the behavior

of the harmonics. Two additional tests were performed, where we varied the depth of the water table in the well. For these tests, the receivers were deployed in the shallow well (the deep well was not accessible), following the same configuration shown in Figure 2.1, and a signaling gun was used as source. This gun creates a very loud noise when fired, and the reverberations echo in the whole working hall. Figure 2.39 shows data of one shot for each experiment, with water table depths of 280 cm (left) and 45cm (right). Data from both experiments show a ringing pattern, with different periods for the different water table depths. This is highlighted in the power spectrum (Figure 2.40) and in the frequency-wavenumber domain (Figure 2.41).

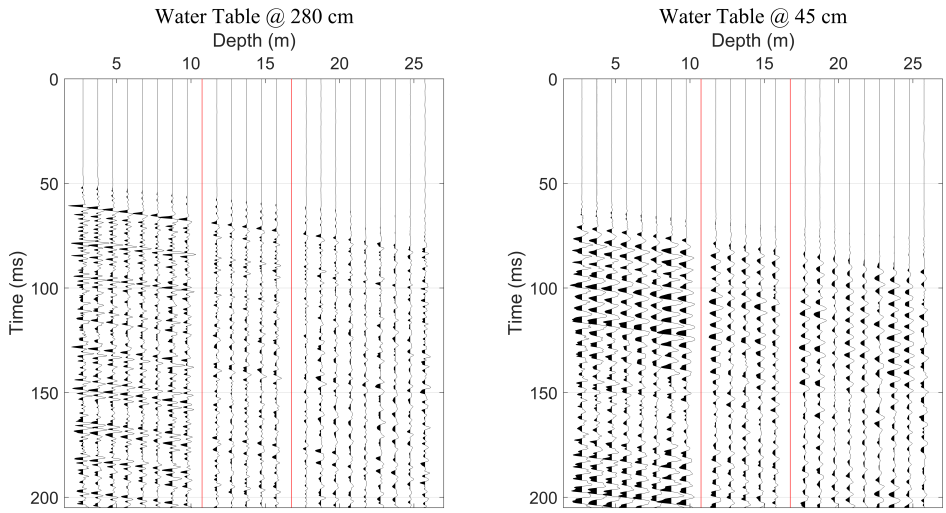

Figure 2.39: Example of seismic recordings for signalling gun source, with different water table depths: 280 cm (**Left**) and 45 cm (**Right**). Channels 10 and 16, plotted in red, are muted due to malfunctioning. Data has been high-pass filtered.

A clear periodicity in the frequency domain can be noticed - a behavior similar to that observed for the spectrogram of data from experiment **Passive D I** (Figure 2.14). The spacing in the frequency peaks is 60 Hz for a water table depth of 280 cm and 360 Hz for a depth of 45 cm. These frequency peaks, combined with the depths of the water table, yield a velocity in the range of 330-240 m/s, meaning that the reverberation was caused by trapped modes in the air between the water surface and the open end of the well - that is, it is possible to identify normal modes in the well.

Given the results of these last two experiments, which allowed us to clear identify the normal modes, it was not clear why calculations of velocity from cepstrum

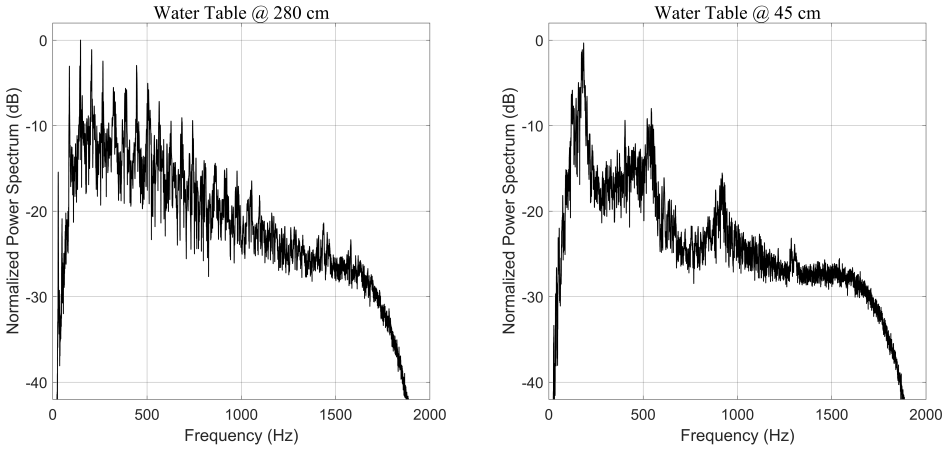

Figure 2.40: Power spectrum of data shown in Figure 2.39.

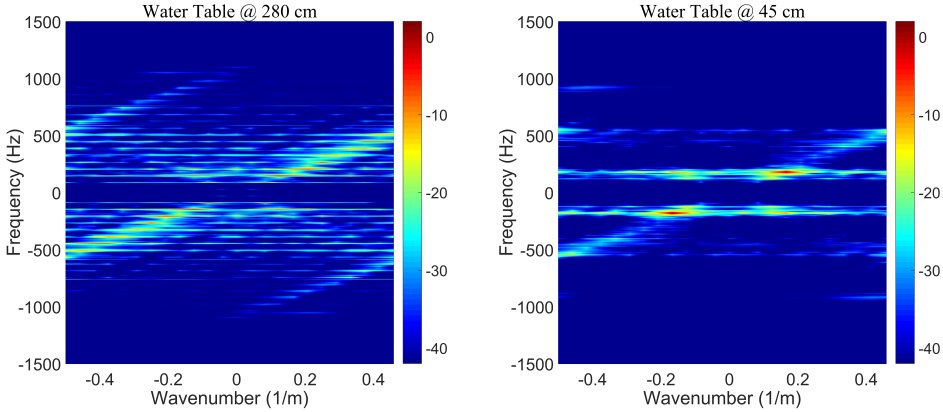

Figure 2.41: 2D Fourier plot of data shown in Figure 2.39. Data has been normalized, and color scale is in decibels. Notice that data is aliased above 500 Hz.

fared so poorly for the shallow well. A hypothesis is that the proximity between the deepest hydrophone and the bottom of the well could affect the signal in the deeper sensors. We attempted to calculate the velocity from the cepstrogram of the data recorded by the shallower hydrophones, but the results were equally poor. Ultimately, this effect was not clearly understood.

Feasibility for Velocity Monitoring

The results in Figure 2.24 show that the range of the estimated shear modulus μ_s and S-wave velocity v_s from both wells overlap - which is a good sign since the wells are close to each other. The range of the computed v_s in the deep well is

smaller due to the lower standard deviation of the measured tube-wave velocity and differing well geometry. From those results, we could estimate a shear modulus of about 0.29 GPa and an S-wave velocity of about 379 m/s for the formation between 3 m and 26 m depth, where the hydrophone array is deployed.

We do not have additional measurements of the S-wave velocity at the location of the wells, but several measurements have been conducted in the area around our location (Long and Donohue, 2007; L'Heureux et al., 2013; L'Heureux and Long, 2016). In particular, the Eberg test site (Long and Donohue, 2007), located within a distance of 500 m to 1000 m to the location of the wells, has an estimated S-wave velocity between 120 m/s and 300 m/s for depths down to 12 m. This might indicate that our results are in a reasonable range, as we are in a similar geological setting. If the movement of the casing is restricted ($\zeta = 0$), the estimated S-wave velocity for our experiments is about 280 m/s. The absolute estimation of the formation shear modulus from the measured tube-wave velocity is very difficult to achieve, and these results mainly support the measurement consistency between both wells.

For the modeled monitoring scenario, the tube wave velocity would vary within a range of 32 m/s, with a drop of 14 m/s at time t_1. These changes could be identified with precise tube wave velocity measurements, like the ones presented in this chapter. Still, the variations of the tube wave are small - tests at larger field sites would be beneficial to verify the method.

Looking back at Figure 2.4, we can verify how the tube wave velocity becomes less dependent on shear modulus changes when the initial modulus is too high. For our example with an initial shear modulus of 8 GPa, the sensitivity of the tube wave on the formation properties is not exactly high. Assuming the same geometry and an initial shear modulus μ_s of 5 GPa instead of 8 GPa, the tube wave velocity would vary within a range of 51 m/s, which would facilitate the detection.

2.5.2 Attenuation Estimation

The measurement of the tube wave absorption is the crucial step to be performed to estimate the shear absorption of the formation. The partition coefficient of the formation shear velocity is quite low ($\approx 1/90$ for the shallow well, and $\approx 1/40$ for the deep one), and the other terms in equation 2.8, with the exception of the shear tool absorption, contribute little to the total absorption. Consequently, the quality factor for the tube wave should be about 1 to 2 orders of magnitude higher than that of the formation. This alone implies that we should expect a much weaker absorption of the tube wave. On top of that, the hydrophone array available for this experiment was quite short (23 meters long), which limited our ability to measure

the absorption for several wavelengths at lower frequencies.

The results in Figure 2.25 show relatively strong absorption of the tube wave, which allowed us to detect the decay of this mode within the limitations of our experimental setup. This seems to be caused by a very low formation Q_β, in the range 1-3, combined with a strong shear absorption of the measuring tool (Figure 2.26). We emphasize that the "seismic source" was a manually operated hammer hitting the floor (Figure 2.1), with a very variable signature between events. Still, the results presented (which are the median of 80 measurements) have a small error bar, indicating that the obtained values are consistent. The more realistic result is that shown in Figure 2.26c, with estimated $Q_{\beta_t} = 1.35$ and $Q_\beta = 2.44$.

The values shown in Figure 2.25 represent an average Q between the measured point and the reference sensor. There seems to be a trend of decrease of absorption with depth (increase in Q), which breaks one of the basic assumptions in the spectral ratio method - that of a constant Q (White, 1992). Some attempts were made to estimate the absorption in shorter intervals for deeper receivers, and the observed trend was quite similar. Still, the Q increase with depth is relatively slow (nearly constant within a wavelength).

The power spectrum of the receivers is strongly modulated by a notch filter (from the ghost). Some deghosting methods were tried, but ultimately this effect could not be corrected in our data. Despite that, if a different receiver is used as a reference, the absorption values estimated are quite similar to the ones obtained from the shallowest hydrophone, suggesting that the data is not compromised.

The obtained values of formation shear absorption are fairly low, especially when compared with absorption estimated in deep sedimentary rocks (Stainsby and Worthington, 1985; Raji and Rietbrock, 2013; Carter et al., 2020). The values are however in the range of those observed in measurements for soils (Ketcham et al., 2001; Campbell, 2009; Pilz and Parolai, 2017). It was not possible to retrieve any information on absorption measurements on nearby sites so that these values could be compared.

Among the several experimental parameters necessary for the estimation of the formation shear absorption, the largest uncertainty in our configuration lies in the shear absorption of the hydrophone array. The sensitivity of the formation absorption to this parameter was presented in Figure 2.27. It can be noted that with exception of the scenario where the tool absorption is very strong ($Q_{\beta_t} < 2$), the effect of this parameter on the estimation of Q_β would be close to irrelevant. The effect of tool absorption becomes more significant when the estimated absorption is lower, as can be seen in the red and blue curves in the plot.

Sensitivity Analysis of Q measurements

The sensitivity analysis shown in Figure 2.28 indicates how the parameters affect the non-zero partition coefficients, using as an example the geometry of the deep well (well 2). The fluid P-wave velocity and density (Figures 2.28a and 2.28b) seem to show a "trade-off" between the contribution of fluid and casing absorption to the total Q, with little effect in the other coefficients.

The tool shear modulus (Figure 2.28c) shows a strong effect on all partition coefficients for low values but quickly stabilizes, except for the tool partition coefficient itself, which has an asymptotic nature. The tool radius (Figure 2.28d) has an intuitive behavior in the "limit" cases: when $r_{\text{min}} \rightarrow 0$, the partition coefficient of the tool vanishes; when $r_{\text{min}} \rightarrow R$ (the well radius), the partition coefficient of the fluid vanishes, since the well is completely taken by the tool. We can observe that in the shallow well: because its radius is smaller, the tool takes a larger fraction of the borehole volume, and its contribution to the total attenuation increases. This is represented in the higher partition coefficient of the tool shear modulus in the shallow well, as shown in Tables 2.3 and 2.4. The other coefficients show little sensitivity to this parameter.

The casing parameters play different roles. The shear modulus plot (Figure 2.28e) indicate that, for low values, the partition coefficient of the formation increases: the tube wave absorption becomes more sensitive to the formation's, and less to that of fluid and casing. Because the casing in our experiment is made of steel, with a high shear modulus (78 GPa), we find ourselves closer to the right end of this plot, where the formation contribution is lower, and the fluid and casing's, higher. As for the sensitivity of the partition coefficients to the Poisson ratio (Figure 2.28f), the major effect seems to be a trade-off between the casing's compressional and shear absorption, as we move between low and high values of ν_c. For the casing thickness (Figure 2.28g), a similar analysis of limit values can be done: when $d_c \rightarrow 0$, we fall into the scenario of an open hole with a tool, which is shown in Figure 2.6b; when d_c grows, the formation contributes less and less to the total absorption.

The two last parameters investigated are the borehole radius (Figure 2.28h) and the coupling between well and formation (Figure 2.28i). A small well radius increases the contribution of the tool: the tool's radius was kept constant and, as R gets smaller, the tool occupies a larger fraction of the well (as in Figure 2.28d). As the well radius increases, the formation contributes more to the absorption - as do the casing properties. The coupling between well and formation has little influence on the tool, formation, or fluid coefficients, only mildly affecting the casing parameters.

The interpretation of Figure 2.28 can shed some light on what kind of configuration will be more favorable to the estimation of the formation absorption in a slow formation, behind the casing: a well with a thin casing, a material with low shear modulus, and with a large borehole radius. The thinner the tool deployed to measure to tube wave, the smaller its contribution to the total absorption. Because the only data needed are the pressure measurements, this method can be implemented with 1C sensors - perhaps permanently installed in wells, as a monitoring device. This could be advantageous for measurements with fiber optics (Tertyshnikov and Pevzner, 2020; Kiyashchenko et al., 2020a).

Feasibility for Q Monitoring

The results presented in Figures 2.26 and 2.29 suggest the potential of monitoring the formation shear wave absorption through measurements of tube wave attenuation. Changes in Q_β are magnified by the small partition coefficient of this term in equation 2.8. Ironically, what makes our experimental setup have a low sensitivity to the formation shear absorption also makes it quite sensitive to changes in this parameter. The measurements could be used to detect, for example, an eventual increase in gas saturation in shallow soils or rock formations, in the context of surveillance wells.

The increase in shear absorption for partial saturation, when compared with fully saturated rocks, has also been observed in tight sandstones, where the effect is almost linear with fluid saturation (Murphy III, 1984). Temperature and pressure variations are also a potential source of changes in the formation shear absorption. Because pressure and temperature gauges are already common instruments in observing wells, we believe that adding the possibility of monitoring small changes in fluid saturation, as presented here, could be advantageous for long-term well surveillance.

2.6 Conclusions

We recorded data with hydrophones in two water-filled shallow wells. In those experiments, a coherent, non-dispersive event, identified as the Stoneley mode between the well casing and the formation, was studied. This event was detected in data acquired with an active source and also in ambient noise recordings.

The velocity of the event was computed with three methods: line fit in the frequency-wavenumber domain, Radon transform, and cepstrum. The first two methods resulted in consistent velocities for both wells, while the last one only yielded good results for the deeper well. Seismic modeling shows that the minor differences in the velocities obtained from the up-and-downgoing modes in the shallow well are likely caused by other wave modes - like the P-wave velocity in the water and the

Mach wave from the deeper well.

The accurate measurement of tube wave velocities is crucial to employing the method as a monitoring tool, as the dependence between velocity and shear modulus of the formation is not very strong. The accuracy of the methods presented here seem to be enough to detect variations of the shear modulus caused by pore pressure changes, as was investigated by modeling. Tube wave velocities do not depend on the formation's density, and hence can be a powerful tool, when combined with other measurements, to separate between pressure and fluid effects.

Field tests are required to verify if the method is applicable in operational sites. Formations with low shear modulus / S-wave velocities are more sensitive to the tube wave and are hence potential candidates. Larger borehole diameter and thinner casings are beneficial for this method.

In addition to velocity measurements, the tube wave absorption was also studied. The absorption measurements can be used to estimate the shear wave absorption of a slow formation behind a cased well. The sensitivity of the method also depends on the well geometry and materials used for the casing and measuring tool. Despite limitations with low repeatability in source signature and a short array of geophysical sensors, we were able to estimate consistent values of shear absorption in a series of measurements. The results suggest the feasibility of measuring and monitoring formation shear Q behind cased wells, with the use of simple sources and geophysical sensors.

In general, the tube wave velocity and attenuation are a function of many different parameters, which makes the absolute estimation of the shear properties in the formation very challenging. However, monitoring changes in the formation from tube wave measurements should be feasible - especially in engineering applications and shallow reservoirs, where the initial shear modulus is low. For monitoring purposes, it is also important to measure the temperature of the borehole fluid and to correct the estimated formation parameter accordingly. Here, it is assumed that no changes in the casing parameters occurred.

For the acquisition setup, it is recommended to have the source close to the well, to create tube waves with high energy. New advances in the use of fiber optic cables for seismic purposes could improve the method, as longer arrays and smaller receiver spacing would be possible. The estimation of the tube wave velocity worked better in the frequency-wavenumber domain. The implementation of fan filters and regularization algorithms in the f-k domain increase the accuracy of the measured tube wave velocity. In general, the tube wave monitoring technique could be used as a detection method, that pinpoints depths where changes happened. In a second

step, more precise measurements could be performed to investigate the detected variations in detail.

Ambient noise recordings also represent a possibility for monitoring. The results are encouraging, and perhaps could be improved by longer recordings and the use of interferometry, which was not possible due to operational restrictions. Still, non-continuous recordings of 16 seconds resulted in remarkably good precision, particularly for the Radon method.

Continuous recording can lead to vast amounts of data: A well with a 100-sensors array would generate roughly 1 TB of raw seismic data per month of continuous monitoring for a sampling frequency of 1000 Hz. We emphasize that the methodology presented here can be easily automated, without the need for large data storage: once the data is recorded, filtered, and transformed to frequency-wavenumber, Radon, or cepstrum domain, the velocity can be promptly calculated, and the seismic data is no longer necessary.

Chapter 3

Time-lapse Seismic and Geomechanics

In this chapter, we discuss some geomechanical effects of oil production and water injection, and how these effects can be monitored with time-lapse geophysical measurements. The findings and results presented here were summarized and published in a journal paper:

Borges, F., M. Landrø, and K. Duffaut, 2020, Time-lapse seismic analysis of overburden water injection at the ekofisk field, southern north sea: Geophysics, **85**, B9–B21

The main goal of the work in this chapter was to analyze some available time-lapse data in the area of the Ekofisk field: 4D seismic, time-lapse bathymetry, and GPS positions of the surface installations. In the interval between the acquisition of these data, a seismic event of moderate magnitude happened inside field boundaries. The integrated analysis of the data could clarify the causes behind the seismic event, and that was the main scientific question to be addressed.

In addition to the content presented in the published paper, this chapter exhibits a more detailed explanation of the uncertainty analysis using different estimations of elastic moduli for the overburden, as well as a longer discussion on the changes in the stress regime induced by reservoir compaction and inflation.

I take to opportunity to thank ConocoPhillips Skandinavia AS and the PL018 license partners (Total E&P Norge, Vår Energi, Equinor ASA, and Petoro AS) for making the data available for this study, as well as for the permission to publish the results.

3.1 Introduction and Background

Extraction of hydrocarbons from porous rocks changes not only their elastic properties but also the stress pattern of the subsurface, since the fluid in the pore space supports part of the load of the overburden. Stress changes can lead to fault reactivation, depending on the local tectonic setting and the strength of the rocks in the formation (Grasso, 1992; Healy et al., 1968). For similar reasons, fluid injection also impacts both reservoir and surrounding rocks.

The most "visual" geomechanical effect caused by hydrocarbon production is arguably reservoir compaction, which can lead to significant surface subsidence, as has been documented in the literature on different occasions (Nagel, 2001; Pattillo et al., 1998; Schoonbeek et al., 1976). Other consequences for field operations are damages to well casing (Bruno et al., 1992) and difficulties to drill new wells, due to restriction of mud weight window (Van Oort et al., 2003). Geomechanical simulation is then a crucial part of field development, as it can help anticipate future problems and provide extra time to plan solutions (Costa et al., 2011; Settari et al., 1998).

The work presented in this chapter was developed with field data from the Ekofisk field, operated by ConocoPhillips Norway. Ekofisk, located in the southern part of the Norwegian continental shelf, is the largest chalk oil field in the north sea. Production started in 1971, shortly after its discovery in 1969 by Phillips Petroleum Company. At the date of publication of this work (December/2021), Ekofisk has produced over 4 billion BOE and, with a current production above 120.000 bpd, still stands as one of the major oil fields in Norway.

In addition to the impressive volume of hydrocarbons produced, Ekofisk is also known for the significant reservoir compaction caused by oil production, which led to subsidence of several meters of the seafloor (Sylte et al., 1999). Acute compaction can function as a powerful production drive (Sulak et al., 1991), but also impacts well stability: several wells in the field show buckling and/or shear failure (Vudovich et al., 1988).

Ekofisk's expressive compaction can be accredited to a number of reasons. The main reservoir zones - Ekofisk and Tor formations - are high-porosity chalks with thicknesses ranging from 100 m to 300 m, which favors an intense compaction. Moreover, a soft, uncompacted overburden transfers the effect of compaction to the seafloor. To counterbalance compaction and improve oil recovery, an extensive water injection program was implemented (Hermansen et al., 2000). Despite its extent, Ekofisk compaction has been considered mostly aseismic. On May 7th, 2001, however, a seismic event of estimated magnitude $M_W = 4.1 - 4.4$ was

felt on platforms in the field (Ottemöller et al., 2005). Detailed studies placed the epicenter of the event inside field boundaries, which led to a deeper investigation of its possible causes.

A bathymetry survey was acquired two months after the event. Compared with a previous survey acquired in 1999, it identified the expected subsidence in the central bowl (Baade et al., 1988; Rentsch et al., 1988), and also a noticeable uplift in the northeastern part of the field. The area was later found to be subjected to unintentional water injection in the overburden. This injection is thought to have begun in 1999, after a collapse in well 2/4-K-22, which had been injecting water in the reservoir since 1989. The depth of the zone of unintentional injection (ZUI) suggests that it might be related to the seismic event. Besides, overburden injection could also be the cause of the seafloor uplift.

Surface seismic data was acquired in the area in 1999, before the event happened - it is not clear if that was before the unintentional water injection started. A new survey was performed in 2003. In this chapter we compare those two datasets, and study the differences between them. The results are interpreted to understand the reason behind the seismic event, and its possible connection to the unintentional water injection.

Available Data

The seismic volumes used in this study are marine surface seismic acquired in 1999 and 2003. Both datasets have been through the same processing flow (only stacked data were available), but sailing obstructions were different in each acquisition, which manifests in the data as uneven imaging in the central part of the field. A map of difference bathymetry and GPS measurements on the platforms, both published by Ottemöller et al. (2005), were also used for visual validation of results: baseline bathymetry was acquired in 1999, and monitor was acquired in 2001, shortly after the May 7th event.

We draw attention to the timeline of the events discussed in this work: the intervals between water injection, seismic event, and field measurements (bathymetry and surface seismic) will play a role when interpreting the results. Figure 3.1 presents this timeline: overburden water injection probably commenced in 1999. This same year, a seismic survey and a bathymetry survey were acquired. The seismic event took place in 2001. Shortly after, a new bathymetry survey was acquired. The injection well was shut down in 2002. Another seismic survey was shot in 2003. Hence, time-lapse bathymetry reveals changes between 1999 and 2001, while 4D seismic shows the contrast between 1999 and 2003.

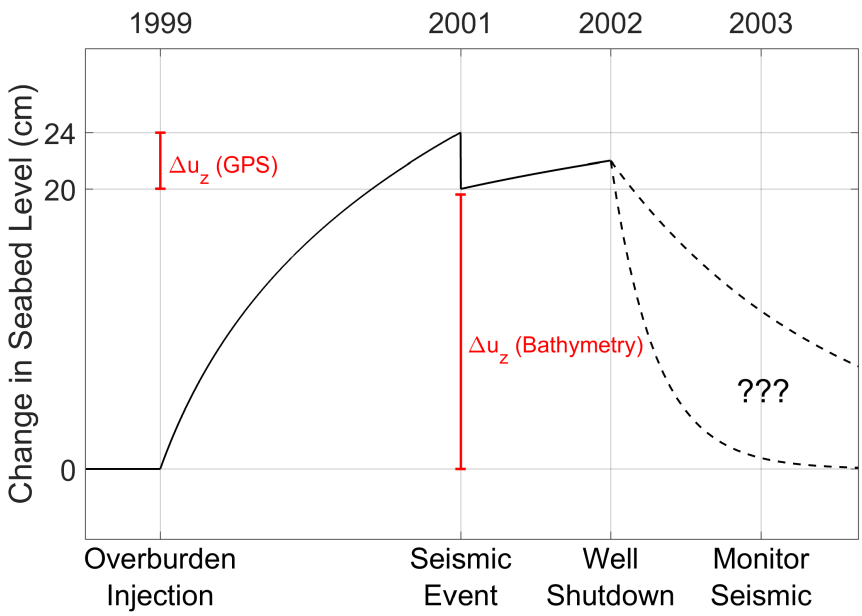

Figure 3.1: Timeline of events and data acquisition. Behavior of the seabed after well 2/4-K-22 was shut down is not clear. Values for seabed uplift are estimated from bathymetry surveys and platform GPS measurements, published by Ottemöller et al. (2005).

3.2 Method

The most common methods for time-lapse seismic interpretation are amplitude analysis and time-shift analysis, having the latter a key role in geomechanical studies (Johnston, 2013). In addition to those, geomechanical modeling and fault displacement modeling were also performed. We proceed to detail the methodology employed in each of those steps.

3.2.1 4D Time-Shift

In a time-lapse experiment, the shift in time Δt of a certain event can be caused by two chief reasons: different wave velocity V in the medium, or change in the depth z of the event. Frequently, a measured time-shift is a combination of both effects. A good approximation of the relative 4D time-shift (Landrø and Stammeijer, 2004) is

$$\frac{\Delta t}{t} = \frac{\Delta z}{z} - \frac{\Delta V}{V}, \tag{3.1}$$

where $\Delta z/z$ represents the vertical strain ϵ_{zz}. This approximation - valid for vertical propagation in a single horizontal layer, when relative changes are small ($\Delta V/V$, $\epsilon_{zz} << 1$) - can be used in regions of smooth variations of velocity and

gentle dips. From equation 3.1, a negative time-shift is caused by the uplift of the target horizon ($\Delta z < 0$ - positive axis points downwards) and/or by an increase in velocity along the travel path (*hardening* - $\Delta V > 0$). Positive time-shifts can be interpreted in the opposite way: sinking of event of interest ($\Delta z > 0$) and/or slower overburden velocities (*softening* - $\Delta V < 0$). The color convention used in this paper follows the standards proposed by Stammeijer and Hatchell (2014).

It may prove difficult to ascertain the contribution of each term in equation 3.1 to the total time-shift, especially in stacked data. Hatchell and Bourne (2005) and Røste et al. (2005) independently suggested that a linear relation between $\Delta V/V$ and $\Delta z/z$ can be assumed, so that $\Delta V/V = -R\epsilon_{zz}$. R is often referred to as the *dilation factor*, and equation 3.1 then becomes

$$\frac{\Delta t}{t} = (1 + R)\epsilon_{zz}. \tag{3.2}$$

Equation 3.2, though approximate, has the advantage of connecting time-shift (a seismic measurement) to vertical strain, a common output of geomechanical models.

For this study, time-shift was computed by finding the maximum correlation between the 2003 and 1999 seismic volumes, on a trace-by-trace basis ($\Delta t_{4D} = t_{2003} - t_{1999}$). The correlation was computed in a 256 ms moving window, with steps of one sample (4 ms). The vertical axis is taken as positive in the downward direction, so a positive (negative) time-shift means that 2003 seismic is displaced towards later (earlier) times, when compared to data from 1999.

3.2.2 4D Amplitude Change

Time-lapse amplitude differences are the typical measurement for production surveillance of reservoirs, when significant changes in elastic attributes are expected (Landrø et al., 1999). They are a measurement of local changes between two layers, at a scale of one wavelength. Interpretation of 4D amplitude data is quantitatively linked to reservoir properties via rock physics models, such as the poroelasticity model (Biot, 1941). To compare amplitude values, it is necessary to first match them in time. This is done by applying the calculated time-variant time-shifts to the 2003 data, and then subtracting the 1999 data from it, so that the 4D amplitude difference is given by $\Delta A_{4D} = A_{2003} - A_{1999}$.

3.2.3 Seismic Interpretation

Several seismic horizons were mapped along a broad depth range. These horizons allow us to study the effect of time-shifts and amplitude changes through the overburden and reservoir zones. Six marker horizons were selected for a more

thorough evaluation (Figure 3.2).

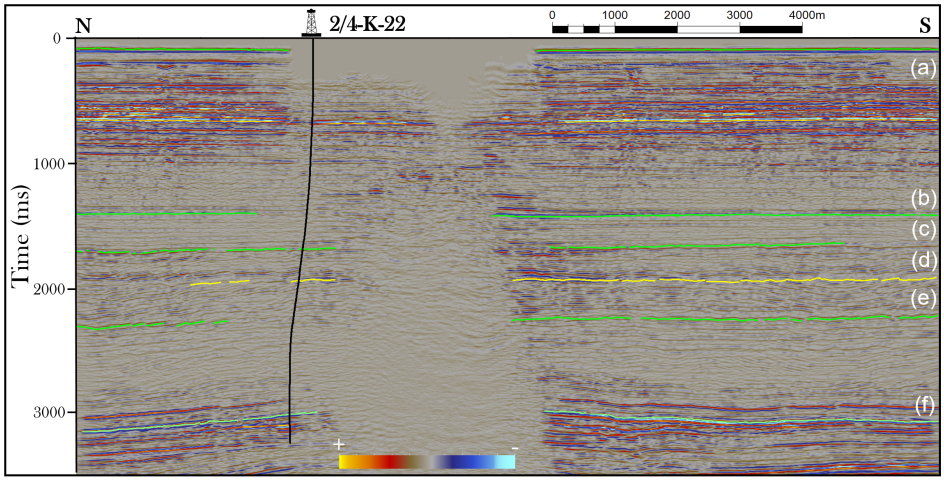

Figure 3.2: Time section with mapped horizons: (a) Sea bottom, (b) shallow horizon 1, (c) shallow horizon 2, (d) horizon in the injection zone (in yellow), (e) intermediate horizon, and (f) top Ekofisk formation. Seismic data from 1999.

We highlight two interesting features in Figure 3.2. The first is the lack of data in the central part of the shallow section, caused by the presence of surface installations that obstruct the path of the seismic vessel. The second feature, also in the central area, is the characteristic seismic obscured area (SOA) of Ekofisk, where the presence of gas degrades the image and causes push-down of deeper seismic events (Van Den Bark and Thomas, 1981). The mapped horizons are used to create maps that tell us how the time-shift changes with depth. Figure 3.3 shows the cumulative time-shift in horizon slices, for the horizons displayed in Figure 3.2.

The sea bottom has a distinct acquisition footprint, which extends for the first few hundred milliseconds, and shows a central area compromised by poor repeatability. The effect of lack of coverage is different in each acquisition, and affects interpretation even for deeper horizons. There is a clear trend of negative time-shifts northeast of the wellhead, reaching its maximum at a depth of around 1900 - 2000 m, in the horizon labeled as **(d)**. Injector well 2/4-K-22 is deviated to the northeast, and the negative time-shift matches the position where it crosses this horizon. The central part of the field shows increasing positive time-shifts, and the deeper horizons show the effect of the SOA (black ellipse in the last images), which degrades the seismic data quality.

The time-shift effect can be better visualized in the cross-section shown in Figure 3.4. Northeast of the well (rightmost traces), seismic data from 2003 show an

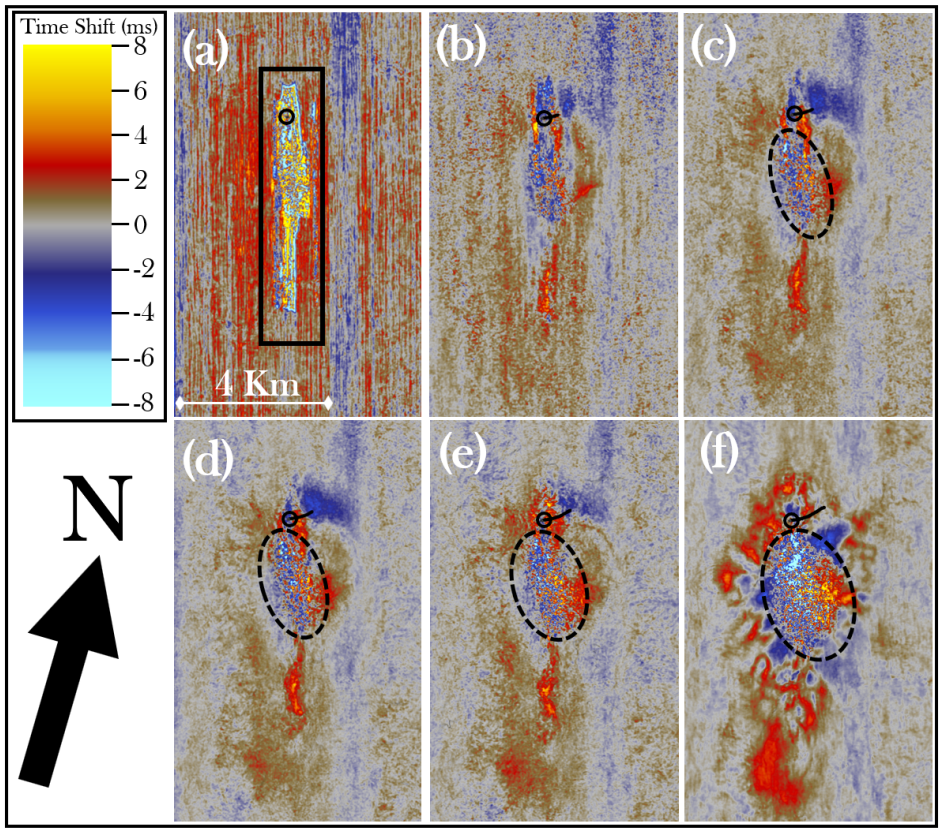

Figure 3.3: Calculated time-shifts at marker horizons: (a) Sea bottom, (b) shallow horizon 1, (c) shallow horizon 2, (d) horizon in the injection zone, (e) intermediate horizon, and (f) top Ekofisk formation. The black rectangle in (a) is the low-coverage area due to surface obstructions; the black ellipse in (c)-(f) is the SOA. Positive values of time-shift mean downward shift, and the black arrow points to the geographical north. The black circle is the wellhead of well 2/4-K-22, whose path is shown as a thick black line.

upward shift, with $\Delta t < 0$. In other areas (leftmost traces), the effect of reservoir compaction dominates, and 2003 seismic data are displaced downwards relative to the 1999 data ($\Delta t > 0$).

The time-shift measurements are in agreement with the expected behavior of injection-caused inflation. The excess pore pressure in the ZUI decreases the effective stress and causes the rock to expand: the top of the layer becomes shallower ($\epsilon_{zz} < 0$). This expansion is partly accommodated by the overburden - in the form of compaction - and partially transferred to the seabed, where it can be observed as uplift. The overburden compaction causes an increase in P-wave velocity ($\Delta V > 0$).

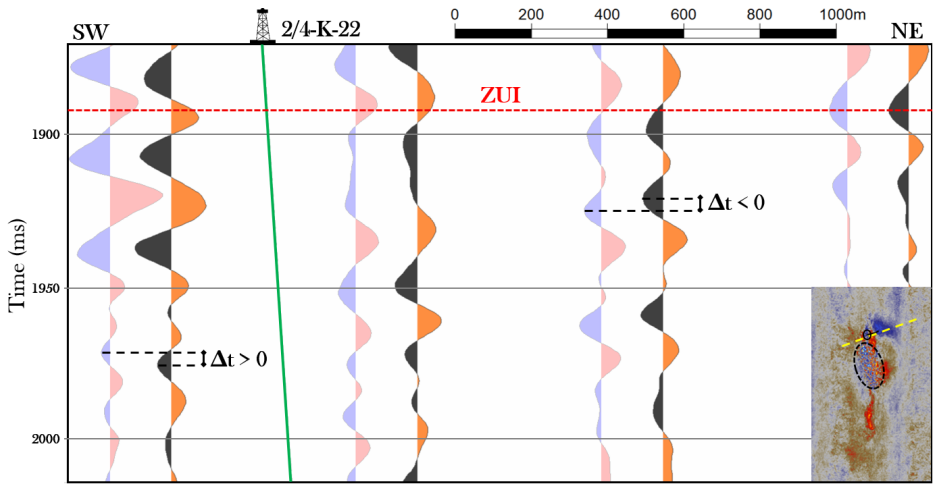

Figure 3.4: Section through well 2/4-K-22 and center of negative time-shift anomaly, with traces from both seismic surveys. The position of section is shown as a yellow traced line at the bottom right corner (same as Figure 3.3d). Orange and black wiggles show 2003 data, while red and blue represent 1999 data. The thick red line marks the top of ZUI, and the green line is the path of well 2/4-K-22. Notice the time shift of 2003 data. To ease visualization, only one trace in 50 (625 m) is plotted.

A closer examination of the time-shift map reveals more details: Figure 3.5 shows a zoom-in Figure 3.3d, and also displays the RMS of the 4D amplitude difference in the same horizon. There is a sharp change from negative to positive time-shifts close to the injector well. Some faults mapped in the area (vertically projected as white lines) seem to adequately delineate this change, indicating that perhaps they act as barriers to fluid flow. Figure 3.6 shows two sections close to the injection area. The mapped faults seem to separate the two regions, reinforcing this interpretation. The amplitude changes, in this case, could be an effect of the reservoir subsidence on the overburden, since the actual area of injection shows only moderate 4D amplitude variations. Another possibility is that this is the border effect of the inflation (in that case, the opposite of the arching effect), causing the signal around the ZUI to have an opposite signal (Røste et al., 2015). We also cannot disregard the effect of poor seismic acquisition repeatability in this area: as the obstructions change between acquisitions, the low-repeatability region is larger than the usual cone-shaped shadow observed in streamer data. Low coverage cannot be discarded as a reason for the strong amplitudes and time-shift signal change.

The overburden sediments above the Ekofisk reservoirs show little differentiation, being mostly composed of low-permeability claystones and shales, with some intercalated limestones (Ofstad, 1980). Amplitude maps calculated from 3D seismic

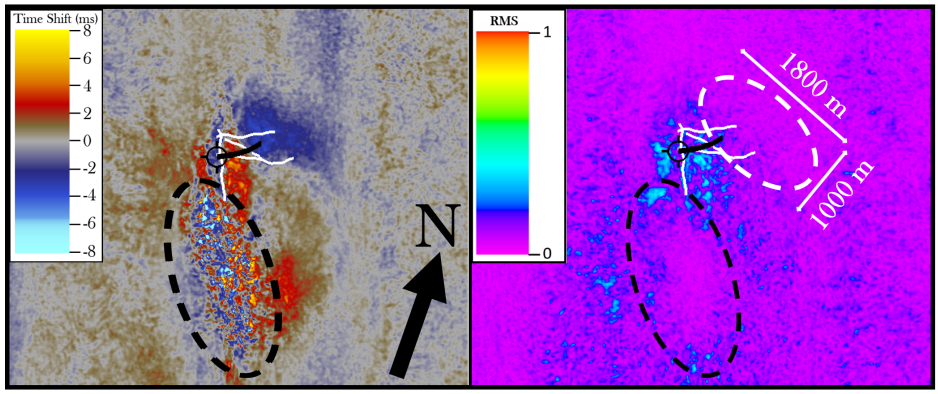

Figure 3.5: Left Zoom of time-shift map in an horizon inside the ZUI (Figure 3.3d). **Right** RMS of amplitude difference ($A_{2003} - A_{1999}$) calculated in 20 ms window around the same horizon. Black ellipse is the SOA. White lines are vertical projection of mapped faults. White ellipse highlights the dimension of the negative time-shift anomaly, and wellpath of 2/4-K-22 is represented in black.

data around the injection time-shift anomaly do not suggest any significant high-permeability zone, hinting that the water injection in the overburden layers could have happened via hydraulic fracturing. Teufel and Farrell (1990) built a stress map from samples collected in Ekofisk, and showed that the maximum horizontal stress (σ_H) in the reservoir is usually radial to the main structure. The fault pattern in the overburden close to the injection zone points in a similar direction for σ_H. Fractures would then be expected to grow in a vertical plane, perpendicular to the minimum horizontal stress (σ_h).

This is not the case: the detected anomaly in Figure 3.3d is elongated in an intermediate direction. There is no indication that vertical fractures were created - the fractures seem to have propagated in a horizontal plane, which is the pattern observed in a stress regime of reverse faulting ($\sigma_3 = \sigma_V$). The homogeneity of the overburden, with no obvious stress contrasts that could impede vertical fracture growth, makes these observations even more curious - an outcome also discussed by Ottemöller et al. (2005). The possibility of horizontal fractures will be considered both for amplitude and for geomechanical modeling.

3.2.4 Amplitude Modeling

Qualitatively, the measured 4D time-shift to the northeast of well 2/4-K-22 can be interpreted as caused by water injection in the overburden. As for the amplitude anomalies, the expected effect of the injection is *softening* of the formation, caused by an increase in pore pressure and consequent reduction of effective stress. Smal-

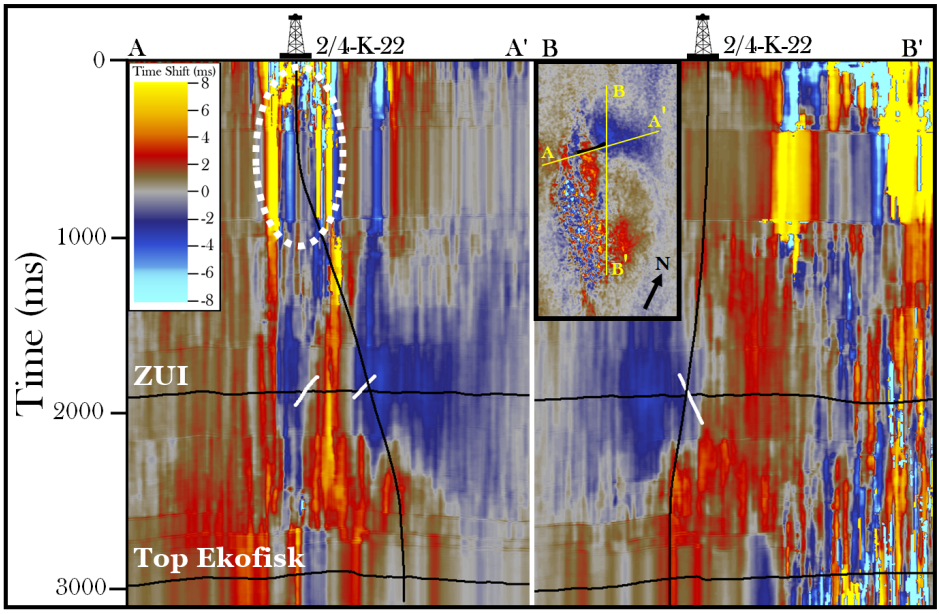

Figure 3.6: Time-shift sections through the injection zone. Horizons in black are the injection zone (upper) and top Ekofisk (lower). White thick lines are mapped faults, and white dotted ellipse delineates zone of poor signal quality, caused by uneven surface coverage. The map on the corner of the rightmost figure shows the position of lines. The strong negative time-shift anomaly, centered at the horizon in the ZUI, is "isolated" by the fault.

ler effective stress usually leads to smaller elastic moduli and velocities (Mindlin, 1949), so we should expect the acoustic impedance to decrease in the injection zone. Figure 3.7 shows two seismic traces, from 1999 and 2003 data (in black and red, respectively). Traces are extracted along the path of well 2/4-K-22, and the 2003 data are corrected for the observed time-shifts. We note some minor differences in amplitudes starting around 1.9 s, which continue up to 2.2 s. In an event around 2.1 s, there is a stronger increase in amplitude.

Using traces in the center of the time-shift anomaly, we calculated a mean time-shift curve between the two data sets (Figure 3.8). The maximum time-shift occurs at approximately the same time as the shallow amplitude increase. This is also the region with the lowest standard deviation between the traces, showing a consistent areal effect. The expected injection zone is between 1800 m and 2100 m, or between 1.9 s and 2.2 s. This is the zone we will model.

To perform elastic seismic modeling, we need density and P- and S-wave velocit-

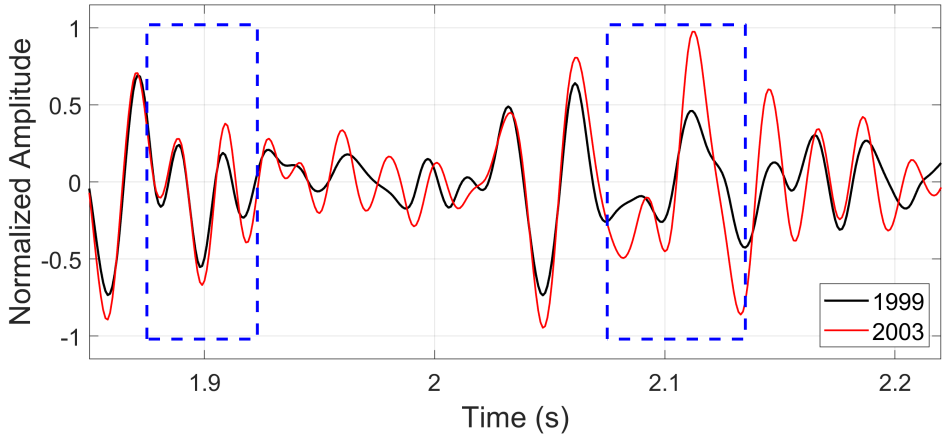

Figure 3.7: Seismic traces along the path of well 2/4-K-22, using data from 1999 (in black) and 2003 (in red). Notice the increase in reflection amplitude starting around 1.9 s and 2.1 s (highlighted with blue rectangles).

ies, usually obtained from logs. Well 2/4-K-22 is significantly deviated in the ZUI (27°), which affects log quality. No S-wave log data are available - shear sonic data from a nearby well were used instead. A decrease in velocities (softening) was modeled taking low GR values as criteria, as these could indicate zones/streaks with lower V_{sh} and larger permeability. This has been done before by Landrø et al. (2001) to account simultaneously for amplitude changes and low time-shifts inside the zone of interest - a configuration akin to the one we have here. The logs prior to and after modeling can be seen in Figure 3.9. From them, reflectivity was calculated, converted to time, and convolved with a Ricker of 35 Hz - this frequency was chosen based on Fourier analysis of the data in this interval (Figure 3.10)

To account for a scenario of water injection through fracturing, amplitude changes based on a fracture model were also estimated. There are no direct measurements to support fracture characterization, so we will resort to analytic methods for this. If we interpret the fractures as infinitely thin, water-filled cracks embedded in an isotropic background medium, models as proposed by Hudson (1980) and Schoenberg and Douma (1988) give a similar outcome: the fracture does not add any normal compliance to the effective medium (there is no discontinuity in the normal displacement), so the compressional modulus does not change - there is only an increase in the compliance parallel to the fracture plane. For horizontal fractures, the equivalent effective modulus c_{44}^{eff} of the fractured medium is given by

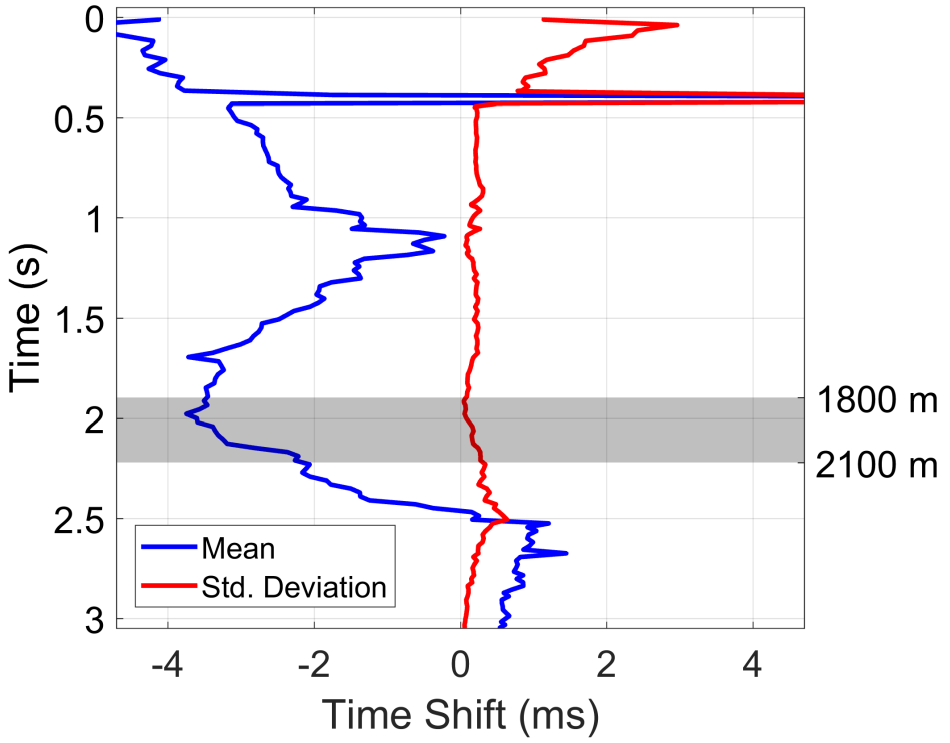

Figure 3.8: Mean and standard deviation of time-shift, calculated from traces falling within a 10m radius around the center of the anomaly. Shaded gray area represents the ZUI.

$$c_{44}^{\text{eff}} = \mu_b \left(1 - \frac{16}{3(3-2\eta_b)}\varepsilon\right), \tag{3.3}$$

where μ_b is the shear modulus of the unfractured, isotropic background medium, η_b is the square of the V_s/V_p ratio, and ε is the crack density. This effective medium approximation is valid for crack densities up to 0.05 (Thomsen, 1987). Combining equation 3.3 with equations for anisotropic reflectivity (Graebner, 1992a), the amplitude response for different fracture densities was modeled.

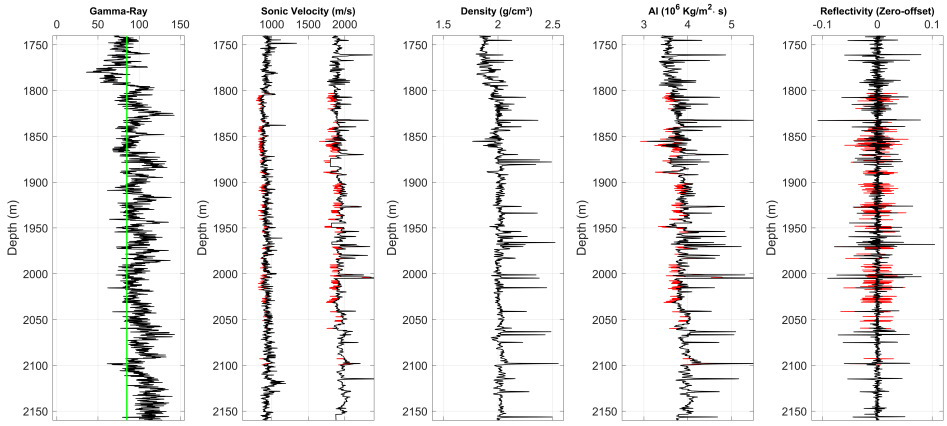

Figure 3.9: From left to right: Gamma ray, sonic velocities, density (RHOB), acoustic impedance (AI), and zero-offset reflectivity. Black lines are original data, and red lines are modeled changes caused by injection. Green line on gamma ray log shows cutoff used to define changes in P- and S-wave velocities, between 1800 m and 2100 m.

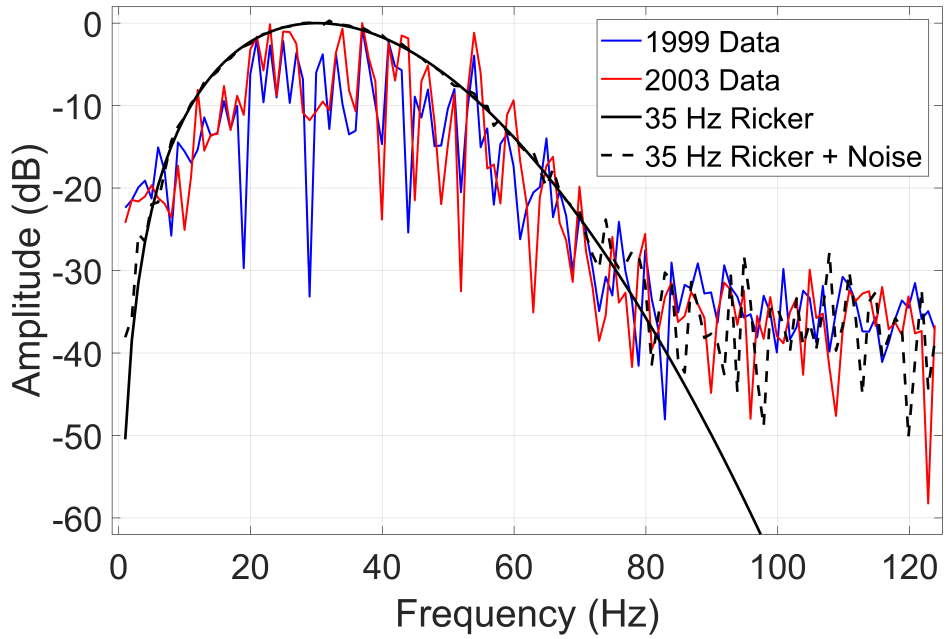

Figure 3.10: Power spectrum of seismic data from 1999 (blue) and 2003 (red), calculated between 1500 ms and 2500 ms. Black thick line is spectrum of a 35 Hz Ricker wavelet, and dotted line is the Ricker spectrum plus additive white Gaussian noise.

3.2.5 Quantitative Estimation of Pressure Change

Quantifying changes in dynamic properties directly from seismic data is a challenging task. Since we are modeling the impact of the injection as a decrease in seismic velocity (Figure 3.9), we will try to extract the pore pressure changes by establishing a relation between pressure and velocity, and then finding the velocity changes that better fit the observed data. To do so, we crossploted P-wave sonic velocity and net stress for some wells in the field (Figure 3.11a). Net stress σ_{Net} is the difference between lithologic stress and hydrostatic pressure, or the equivalent of effective stress $\sigma_{\text{eff}} = S - \alpha P_{\text{P}}$ when the Biot coefficient α is 1. Pore pressure was calculated using gradients published by Nagel et al. (1998), and only points in the Hordaland group (the same as the ZUI) were used. A possible regression line is also displayed - the end-member for zero net stress is the lower Hashkin-Shtrikman bound of a brine-shale mixture (Hashin and Shtrikman, 1963; Mondol et al., 2008), which would be the extreme case for injection, when the rock becomes fluid-supported, in a process of liquefaction. By inverting the regression function, we can extract the pressure increase necessary to cause the modeled velocity changes (Figure 3.11b). Notice that, since the curve $V_p(\sigma_{\text{Net}})$ is convex, the inverse function is concave, and small changes in V_p - particularly close to the Reuss limit - imply in a big change in σ_{Net}.

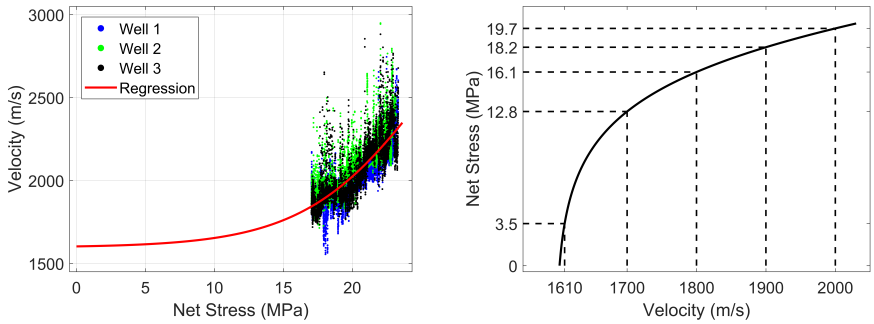

Figure 3.11: **(a)** Crossplot between P-wave sonic velocity and net stress. Thick red line is a regression with end-member calculated as the lower Hashkin-Shtrikman bound of a brine-shale mixture. **(b)** Regression curve between P-wave velocity and net stress. Small velocity changes close to the Reuss limit are associated with big changes in σ_{Net}.

3.2.6 Geomechanical Modeling

An effective approach for assessing whether the overburden water injection is connected to the seabed uplift is geomechanical modeling. We will use a solution

presented by Geertsma (1973) to estimate the impact of the pore pressure change on the overburden. Geertsma's nucleus of strain model expresses the effect of the strain in a limited volume dV on its surroundings. This effect is linear in the pore pressure change, and can be interpreted as a Green's function for the strain. The total effect of any distribution of pore pressure changes can be integrated by using the nucleus of strain function as a weighting factor. Numerical methods can be used to calculate the effect of an arbitrarily shaped pore pressure change in a heterogeneous medium. An analytic solution is available for a disk-shaped reservoir, embedded in a homogeneous medium. The vertical displacement u_z in a line above the disk center is (Fjær et al., 2008):

$$u_z = -\frac{1}{2} C_m h \alpha \Delta P_P \left(\frac{2r^2 z}{(r^2 + (D+z)^2)^{3/2}} + \frac{D-z}{|D-z|} - \frac{D-z}{\sqrt{r^2 + (D-z)^2}} - \frac{(D+z)(3-4\nu)}{\sqrt{r^2 + (D+z)^2}} - 4\nu + 3 \right) \tag{3.4}$$

In equation 3.4, displacement is caused by a pore pressure change ΔP_P in a reservoir of radius r and thickness h. C_m, α and ν represent, respectively, the uniaxial compressibility, Biot coefficient and Poisson's ratio of both reservoir and surrounding medium - which are assumed to be equal, homogeneous, isotropic and linear. D is reservoir depth and z is the depth where displacement is calculated. The geometry of the compaction zone (radius, thickness and depth) can be estimated from time-lapse seismic data (Figure 3.5). The shape of the anomaly is elliptical, and for the Geertsma model we replaced it with a circle of equivalent area ($r = 670$ m). For amplitude modeling, we chose depths from 1800 m to 2100 m, so the ZUI is modeled as a cylinder of thickness $h = 300$ m and $D = 1950$ m.

For the elastic properties, we have an ensemble of values published by Nagel (1998). The closest available values that match our needs are those measured for depths between 4000 ft and 9000 ft (1220 m to 2745 m). According to the author, the data was obtained from three different sets of measurements: core, dipole sonic, and VSP. No details were provided about a number of samples for each type of measurement, but we believe it is safe to assume that the number of dipole sonic and VSP measurements far outnumber that of core samples. For that reason, we are less confident about the elastic moduli derived from core measurements: there is an actual chance that no sample comes from the ZUI, or that this zone is undersampled compared to other parts of the overburden. On top of that, the experimental setup for the core measurements was also not stated. We assumed that the calculated elastic moduli represent the *static* moduli of the overburden, and

that the experiment was performed in undrained conditions, as this is a common setup for rock mechanics experiments in shales (Fjær et al., 2008).

Dipole sonic measurements better describe the *dynamic* moduli, and likely also represent an experiment in undrained conditions. The moduli obtained from the sonic are significantly higher, which is a usual outcome: most experiments yield dynamic moduli higher than the static ones (Ide, 1936; King, 1983). VSP values are in an intermediate range, closer to the sonic's. The low frequencies of seismic waves make it so that seismic-derived moduli usually are closer to the static measurements. As for being the drained or undrained moduli, that depends on the capacity of pore fluid to equalize in a time frame similar to that of the wave frequency.

Core measurements are arguably the obvious candidates for being used in equation 3.4, since a static measurement is more representative of the actual loading conditions. Remains to be verified if the pore fluid can move and equalize the pressure in the time scale of the events (1-2 years), for this tells us which measurement - drained or undrained - is more suitable for our model.

As previously mentioned, the overburden in the Ekofisk area is mostly composed of low-permeability claystones and shales, with some intercalated limestones (see Figure 3.12). This low permeability can lead to overpressure, when the rate of pore pressure increase during sedimentation is higher than the rate of pore pressure equalization (Osborne and Swarbrick, 1997). This is believed to be the case of overpressure in Ekofisk (Sulak et al., 1988), and it is a cue that we should use the undrained moduli in the Geertsma model.

Under these conditions, the dynamic moduli (sonic) and the low-frequency VSP moduli can be considered undrained. Following our assumption on the experimental setup for core measurements, these were also performed in undrained conditions. Given the degree of uncertainty in our hypothesis, we chose to perform the modeling with the three datasets independently and compare the results. To account for the uncertainty in the elastic moduli, we assumed that the actual values follow a normal distribution, and that the mean of this distribution is captured by the values published by Nagel (1998). The final numbers used as input for modeling are shown in Table 3.1.

Uncertainty analysis due to the range of elastic moduli is performed with an approach similar to that presented in section 1.2.1 (Equation 1.34). For this case, the function f is the the vertical displacement u_z calculated with equation 3.4, and the variables x_i are Young's modulus E and Poisson's ratio ν.

For matrix Σ^x, the variances σ_i^2 and covariances $\sigma_{ij} = \text{cov}(x_i, x_j)$ can be obtained

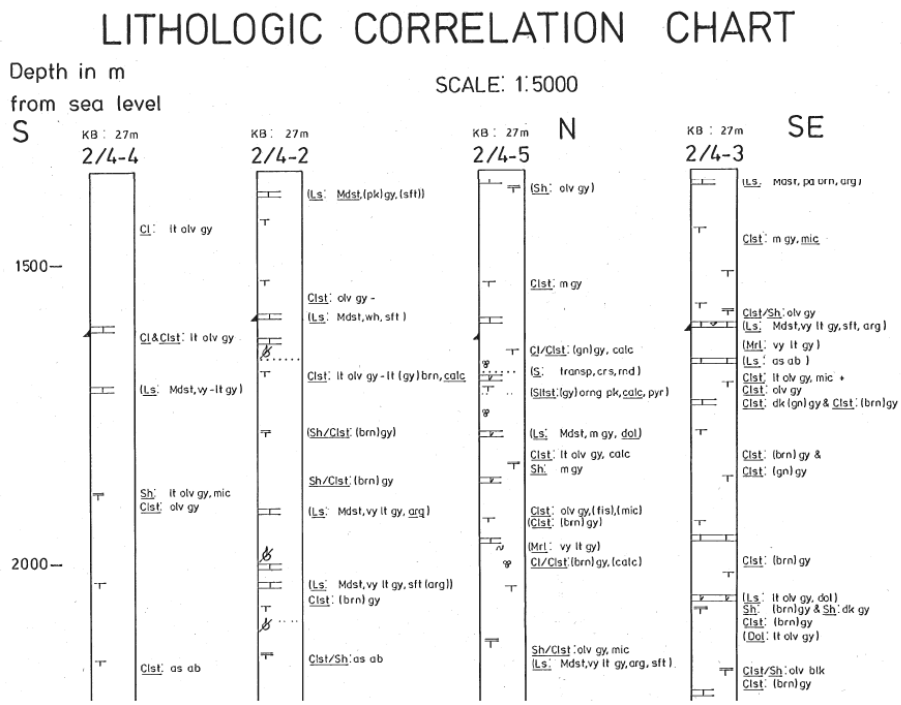

Figure 3.12: Lithology columns of some exploratory wells in the Ekofisk field. Even though none of these wells is particularly close to well 2/4-K-22, similar depths in the whole field show a lack of permeable zones. Modified from Ofstad (1980).

from the measured data. In principle, one expects no correlation in the errors between two elastic moduli in a homogeneous medium. We assume no covariance between the measurements, and all off-diagonal terms in the variance-covariance matrix are zero. The standard deviation σ_u of the modeling result is given by

$$\sigma_u = \sqrt{\left|\frac{\partial u_z}{\partial E}\right|^2 \sigma_E^2 + \left|\frac{\partial u_z}{\partial \nu}\right|^2 \sigma_\nu^2} \tag{3.5}$$

To estimate the pore pressure change, we used information on pressure gradients (Ottemöller et al., 2005, Figure 11). Taking as depth of injection an SSTVD of 1950 m, leak-off test data indicate a minimum horizontal stress of 34 MPa - consistent with other published information about the σ_h gradient in the field (Nagel et al., 1998). For this depth, the lithostatic stress is close to 40 MPa (considering overpressure and undercompaction), hydrostatic pressure measured from gradient is 20 MPa, and injection pressure is 47 MPa.

	E (GPa)	μ^* (GPa)	ν
Core	$\mathbf{1.67 \pm 0.48}$	$\mathbf{0.63 \pm 0.17}$	$\mathbf{0.32 \pm 0.02}$
Dipole Sonic	$\mathbf{3.10 \pm 0.52}$	$\mathbf{1.08 \pm 0.18}$	$\mathbf{0.44 \pm 0.01}$
VSP	$\mathbf{2.76 \pm 0.35}$	$\mathbf{0.96 \pm 0.12}$	$\mathbf{0.43 \pm 0.01}$

Table 3.1: Elastic moduli used for Geertsma's model - Young's modulus (E), shear modulus (μ) and Poisson's ratio (ν). Labels on the left are the source of the data: core measurements, sonic logging, and vertical seismic profiling. Shear modulus was obtained using $\nu = E/2G - 1$.

The increase in pore pressure was strong enough to lift the entire overburden weight, and the horizontal growth of fractures suggests an injection pressure superior to the vertical stress. We could expect the pore pressure increase to be between 20 MPa and 27 MPa. The first value is more likely, as the pressure for fracture propagation is usually closer to the stress perpendicular to the plane of propagation (Gaarenstroom et al., 1993; Zoback, 2010).

Another factor to be taken into account is Ekofisk's production history: the field has been producing for over 40 years, with total seabed subsidence superior to 8 m in 2001 (Doornhof et al., 2006). Reservoir compaction also changes the stress field in the overburden, and can even induce changes in anisotropy (Probert et al., 2004). To quantify the stress changes caused by reservoir compaction, we run Geertsma's modeling also for the reservoir, using an approximate geometry (depth of 3000 m, thickness of 300 m, radius of 3500 m). As we do not know the total pore pressure change, we will employ a simplified version of equation 3.4, presented by Landrø et al. (2019), which uses a single parameter H_0 accounting for rock properties and pore pressure change. H_0 was calculated to fit a subsidence of 8 m.

The effect of water temperature has not been considered to any extent. The injected water is colder than the formation, and the thermal strain caused by cooling will also play a role in the mechanical behavior of the rocks. The total amount of water injected in the overburden could have reached $2 \times 10^6 \mathrm{m}^3$, or a bit less than 0.5 % of the total volume of the modeled injection zone. Fakcharoenphol et al. (2013) showed that the effect of cooling is very significant at the vicinity of the

injector well, but quickly fades away after a few hundred feet, where the pressure-caused strain dominates. As the injection happened in the shallow overburden, it is plausible to expect no temperature differences higher than 45-50°C between the formation and the injected water, so we expect temperature to have a small influence here.

Once all inputs are defined, stress changes and displacements are calculated (Fjær et al., 2008, Appendix D.5). Implementation of Geerstma's equations was made with MATLAB, and is available for download and use under BSD license (Borges, 2018).

3.2.7 Fault Displacement Modeling

The May 7th event caused permanent displacement of some surface facilities in Ekofisk, and this displacement was captured by GPS measurements. To incorporate this data in our analysis, we modeled the effect of a fault displacement in the ZUI. Modeling was performed using the results originally presented by Okada (1985), which were implemented and made available by Beauducel (2010). Okada's equations allow for the calculation of vertical and horizontal displacements, tilts and strains caused by a shear or tensile fault. The medium is assumed to be an infinite half-space, and fault shape is rectangular. Input parameters for modeling are fault geometry (depth, length, width, dip, strike, rake), intensity of movement (slip for shear faults, open/closure for tensile faults) and the medium's Poisson ratio ν.

Ottemöller et al. (2005) modeled the far-field seismic waveform as being caused by a pure shear event, with nodal planes being a near-vertical dip-slip and near-horizontal oblique-normal slip. Unfortunately, as the authors themselves state, it is difficult to explain the GPS measurements using these nodal plane movements alone. Since there is significant uncertainty in both the geometry of the nodal plane and its location, we performed a search for different combinations of epicenters, depths, sizes and movement directions. For every set of inputs, surface displacements were calculated. These displacements were compared with GPS measurements on 3 platforms, and an error function was calculated. The best solutions were ranked in decreasing order of squared error. The effect of tilt on the GPS antennas, which are approximately 300 m above the seafloor, was also accounted for, despite its contribution to total displacement being at least one order of magnitude smaller than the pure horizontal and vertical movements.

3.3 Results

Modeled seismic traces are compared with field data in Figure 3.13. With the modeled changes in velocity, we were able to reproduce qualitatively the amplitude

differences. The most significant discrepancy between synthetic and field data is at the event just after 2.1 s (rightmost blue rectangle), where there is a significant increase in amplitude. Apart from that, the modeled decrease in velocities seems to reproduce well the mild differences between base and monitor. Both field and synthetic data have been corrected for the observed time-shifts.

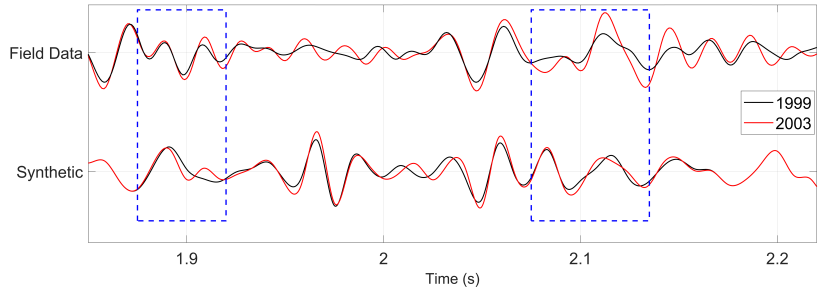

Figure 3.13: Comparison between field data (top) and synthetic results (bottom). The black and red lines show the 1999 and 2003 data, respectively. Data are corrected for time-shift. Blue boxes mark approximate top and bottom of injection zone.

To match the observed 4D amplitude around 2.1 s, we would need an extra decrease of 10% in impedance, which means either a decrease in density or a further decrease in velocity (or a combination of both). A substantial decrease in density is hard to explain from injection only: inflation of the modeled zone would need to be much stronger than the one we got from Geertsma's equations. As for a velocity decrease, the modeled values already create a significant time-shift inside the injection zone, and any further decrease in velocity would not fit the observed data. There is also another limitation on how much the velocity can drop, which is the lower velocity limit for this rock. Figure 3.14 shows the upper and lower Hashkin-Shtrikman bounds of P-wave velocity for a brine-shale mixture. Both the original logs (in black) and the logs we modeled in Figure 3.9 (in red) fall within the bounds, while the velocity necessary to fit the amplitude data (green dots) falls below the lower bound.

The fracture model has similar results for the modeled amplitudes. The extreme value of fracture density ($\varepsilon = 0.05$) creates a 2% reduction in P-wave velocity and a 5% reduction in shear-wave velocity, still not enough to match the observed amplitude changes. We believe this is nevertheless worth investigating: the presence of crack/fractures can have a large effect on shear strength and anisotropy, without significant impact on P-wave velocity (Schoenberg and Sayers, 1995). These changes alter the AVO behavior of the reflection, which is of particular interest here: the obstructions on surface interfere with the acquisition of near off-

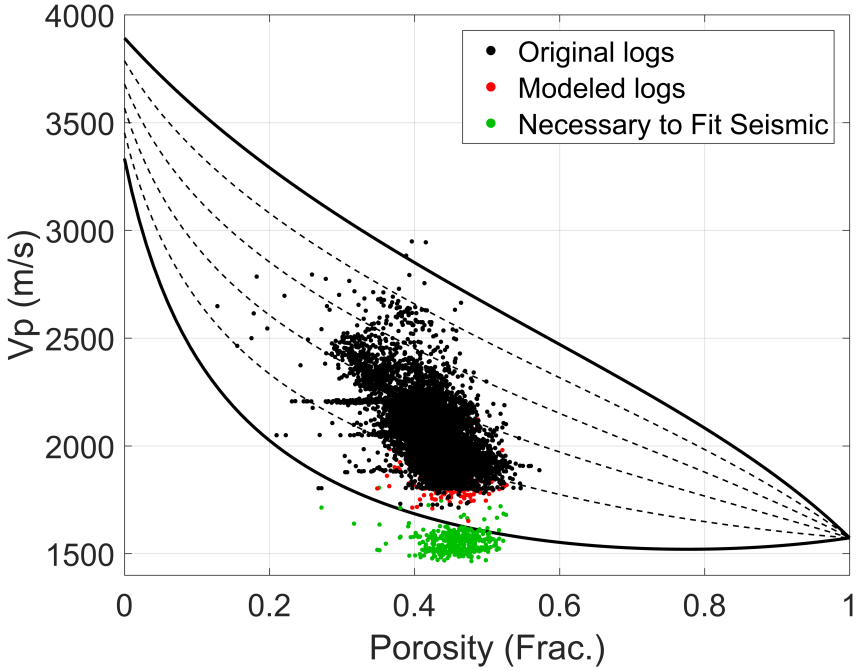

Figure 3.14: Hashkin-Shtrikman upper and lower bounds (thick black lines) for a brine-shale mixture. Traced lines are intermediary stages between lower and upper bounds. Black dots are original log data, red dots are modeled velocity decrease (Figure 3.9), and green dots are the values that would match the amplitude difference shown in the rightmost rectangle in Figure 3.13.

sets, and the stacked data has more contribution of far offsets, where anisotropy and shear velocity contrasts play a more significant role (Graebner, 1992a). For our estimation of fracture density, however, we would have Thomsen's $\gamma = 0.06$, which still does not account for the differences in amplitude.

From the estimated velocity changes (Figure 3.9) and the pressure-velocity regression line (Figure 3.11a), a profile of pore pressure change can be estimated. The result is shown in Figure 3.15.

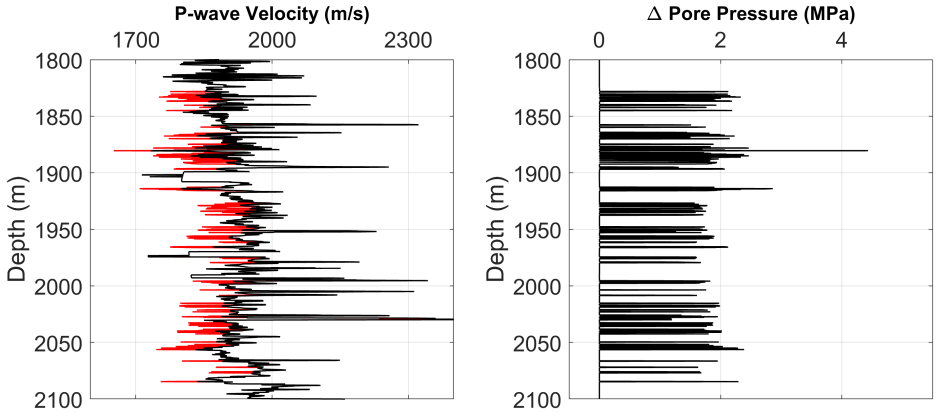

Figure 3.15: Left P-wave velocity log (black) and modeled P-wave velocity after injection (red). **Right** Estimated increase in pore pressure P_P, using the regression line shown in Figure 3.11a.

The vertical displacement profile for the uplift modeling with the core data elastic moduli (the one which showed best fit to the data) is shown in Figure 3.16. The profile was calculated using equation 3.4, assuming a change in pore pressure ΔP_P of 20 MPa, and with the average elastic moduli presented in Table 3.1. Uncertainty analysis for the different sets of elastic moduli can be seen in Figure 3.17.

The estimated uplift at the seafloor is 18 cm for the modeling with core measurements and circa 4 cm for dipole sonic and VSP. Measurements with bathymetry (Ottemöller et al., 2005) indicate 20-25 cm uplift. At the top of the injection zone, the modeled uplift values are respectively 101, 21 and 26 cm - equivalent to 0.5 milistrain for the model with core measurements, and 0.1 for the other two. An attempt to use empirical relations to derive static moduli from the dynamic measurements (Eissa and Kazi, 1988) was not fruitful - the resulting modeled uplifts were still quite far from the measured time-lapse bathymetry. Despite the large variability in the results, both Sonic and VSP moduli still yield a sea bottom uplift smaller than the bathymetry results. The range of values is equivalent to one standard deviation in the elastic moduli (Table 3.1).

As we have a time-shift curve (from the seismic data) and a modeled strain (from Geertsma), we can calculate the dilation factor R. Results are summarized in Table 3.2.

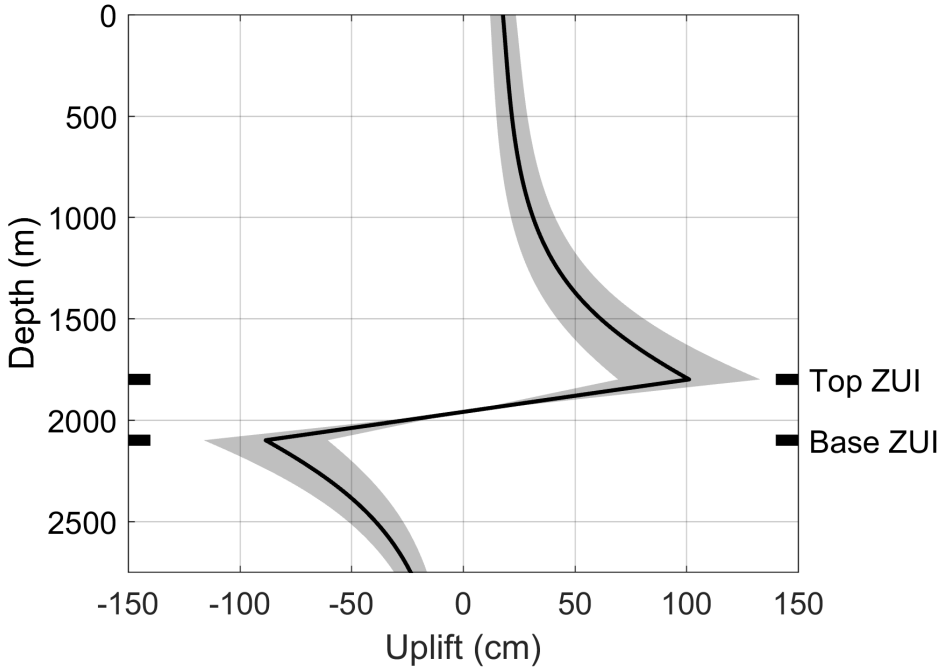

Figure 3.16: Vertical displacement profile in the line going through the center of a disk-shaped injection zone, according to Geertsma's model. Full black line represents the result of modeling with the average value of the elastic moduli, and shaded zone represents one standard deviation. Thick black boxes on the sides mark the modeled top (1800 m) and base (2100 m) of the ZUI.

R values obtained for core-derived moduli are in agreement with Hatchell and Bourne (2005), who modeled values in the range 1-3 for rocks undergoing compaction. As the core elastic moduli provided results closer to the measured data, we will perform the rest of the analysis taking them as the base scenario. Assuming $R = 3$, we can also model the time-shift caused by the injection. This result is shown in Figure 3.18.

Injection-induced displacements and stress changes are displayed as depth sections in Figure 3.19. The injection increases the vertical stress above the ZUI (positive $\Delta\sigma$ means compression) and decreases the horizontal stress. Total stress change and total displacement can be seen in Figure 3.20: the displacement section shows the inflation of the injection zone, while total stress change shows the opposite of the arching effect: inflation of the injection zone compacts the overburden - increasing the vertical stress - and causes a relief in the horizontal direction.

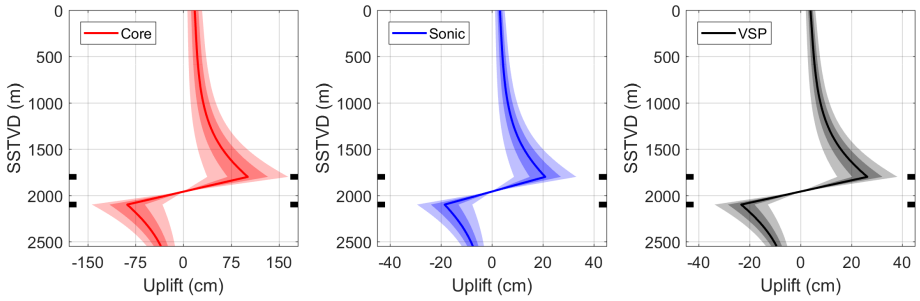

Figure 3.17: Uncertainty in modeled uplift for different sets of elastic moduli: core measurements (**left**, in red), dipole sonic (**center**, in blue) and VSP (**right**, in black). Thick line is the average modeled value, dark shaded zone represents one standard deviation, and light shaded zone represents two standard deviations. Black bars on the side of the plots mark top and bottom of ZUI. The plots have different scales for the horizontal axis.

	Core	Sonic	VSP
u_z (Seabottom)	12 - 27	2 - 4	3 - 5
u_z (Top of ZUI)	72 - 152	15 - 29	19 - 35
R (Overburden)	1.5 - 4.2	11 - 24	10 - 18

Table 3.2: Modeled injection-caused displacement (in cm) at seabottom and top of ZUI, and dilation factor R on the overburden, above the ZUI, for the different sets of elastic moduli presented in Table 3.1.

The effect of reservoir compaction during the life of the field can be seen in Figure 3.21. Reservoir compaction leads to decrease in the vertical stress above the reservoir disk, and an increase in horizontal stress in the same area (left panel). The magnitude of these changes becomes clear when we compare them with the initial stress state of the field: Nagel (1998) published values for gradients of vertical stress and minimum horizontal stress for Ekofisk - those values are 20.36 kPa/m (0.9 psi/ft) and 19.23 kPa/m (0.85 psi/ft), respectively. Thus, in general, the field

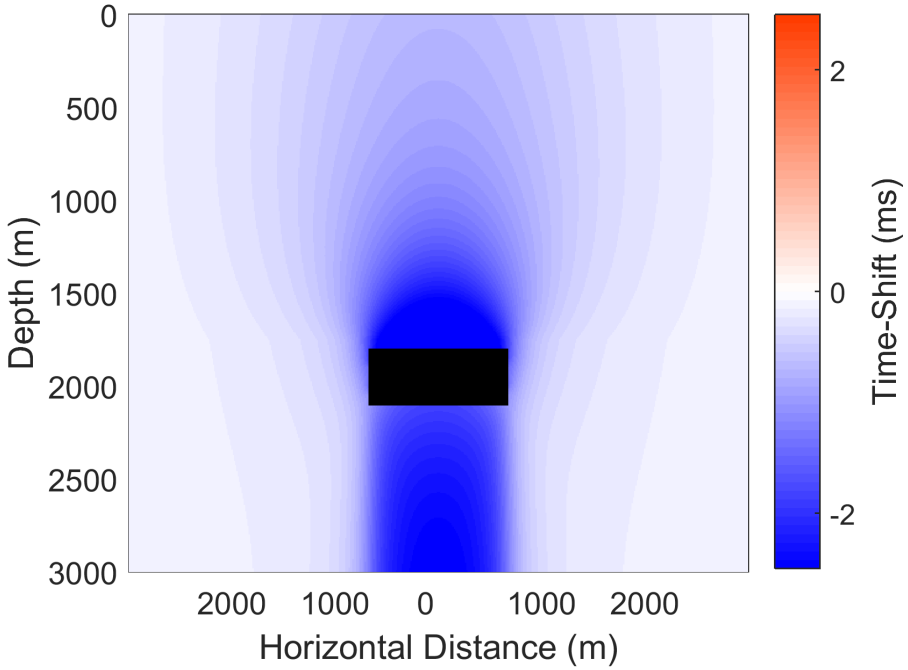

Figure 3.18: Depth section of modeled time-shifts for ZUI, assuming $R = 3$. Color scale is in milliseconds.

is in a regime of normal faulting ($\sigma_V > \sigma_H > \sigma_h$). The modeled stress changes, when combined with the initial stress gradients in the field, suggest a zone above the reservoir where the minimum horizontal stress becomes larger than the vertical stress (region in light red shade in the rightmost panel). It is interesting to see that the ZUI is inside this region.

The results of the fault displacement modeling are shown in Figures 3.22 and 3.23. The configuration that showed the best fit with the observed GPS data was a nearly horizontal, oblique-normal movement, with a length 6500 m and a width 3000 m. Strike, dip and rake were, respectively, $335°$ (clockwise from north), $3°$ and $-70°$. Slip was 20 cm, and tensile component (closure) was 10 cm. The tensile component was essential to fit the subsidence measured by GPS (Figure 3.23, top plot). Opening/closure of faults are identified as isotropic components in the moment tensor (Zheng et al., 1995).

There is a significant difference between the size of the detected time-shift anomaly (ellipse of 1800m x 1000m) and the modeled fault movement. A possible

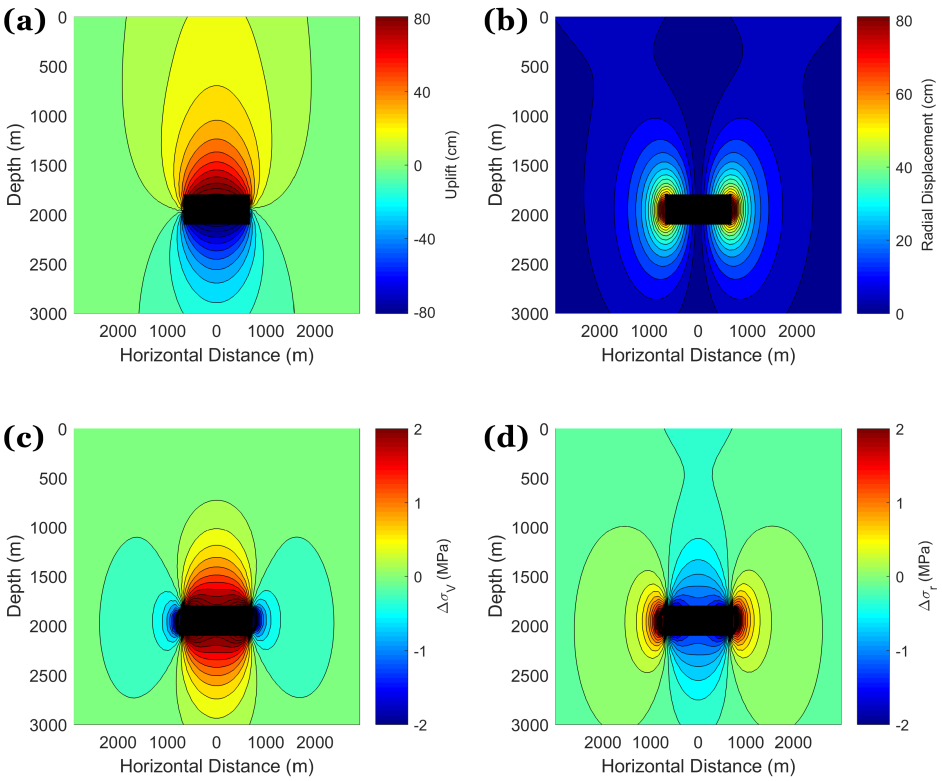

Figure 3.19: Depth sections of modeled displacements and stress changes: vertical displacement (a), radial displacement (b), vertical stress change (c) and radial stress change (d). Black rectangle represents cross-section of injection zone.

reason for that is the pressure release after the seismic event, which would make the seismic measurement (acquired more than two years after the event) detect a smaller time-shift anomaly. Another possibility, that we deem more likely, is that the injection time-shift anomaly is indeed larger, but its effect is masked by the overall trend of reservoir compaction. If we take a rate of subsidence of 10 cm/year for the seabed at the central bowl of the Ekofisk field after 1999 (Doornhof et al., 2006), the zone of injection must be significantly larger to create the same 20-25 cm uplift: the radius would have to be around 1500m, as can be verified in Figure 3.24. Time-shifts modeled using this configuration (assuming $R = 3$ for overburden compaction and $R = 4$ for expansion) are in good agreement with the observed time-shifts (Figures 3.25 and 3.26), suggesting that this model is more representative. The main discrepancies are the noise levels and the more elongated, elliptical shape of the field data.

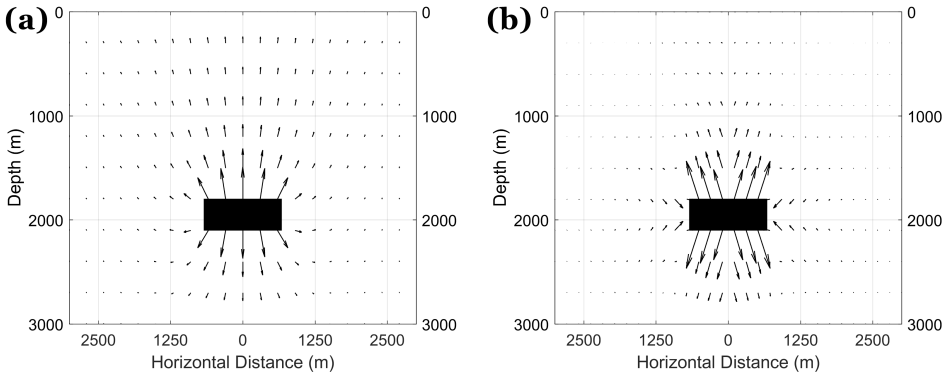

Figure 3.20: Left Depth section of modeled displacement. Arrows represent the direction of displacement, with size proportional to magnitude of displacement (not in the same scale of the horizontal and vertical axis). **Right** Depth section of modeled stress changes. Arrows represent the direction of total stress change, with size proportional to magnitude of change.

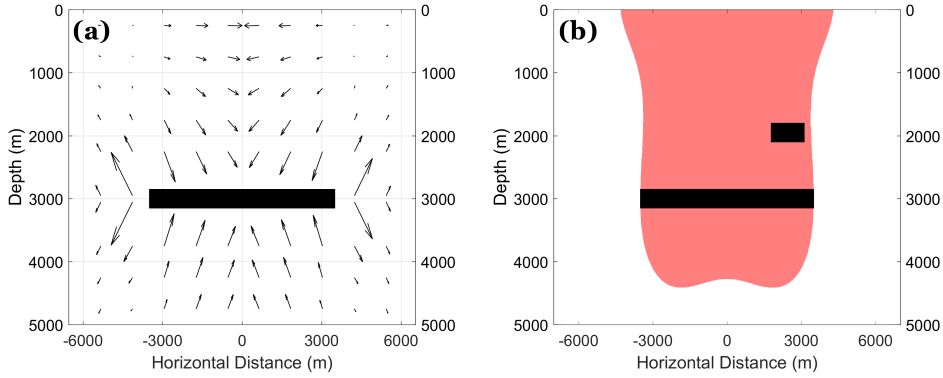

Figure 3.21: Left Depth section of the geomechanical model, showing the stress changes caused by the reservoir compaction. Arrows represent the direction of total stress change, with size proportional to the magnitude of change. **Right** Same depth section, showing in light red the regions where the minimum horizontal stress would become higher than the vertical stress. The lower black box represents the reservoir, and the smaller box to the right represents the ZUI.

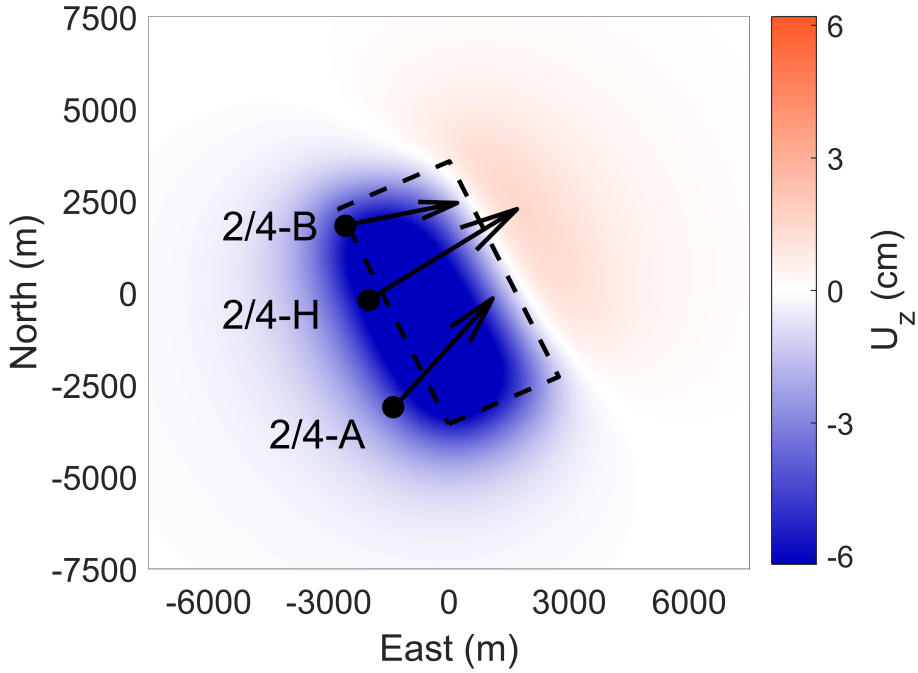

Figure 3.22: Map view of modeled displacement of platforms - arrows for horizontal components, color scale for vertical. Size of arrows represent intensity of movement. Rectangle in traced lines delineates the surface projection of the fault, which dips to the NE quadrant.

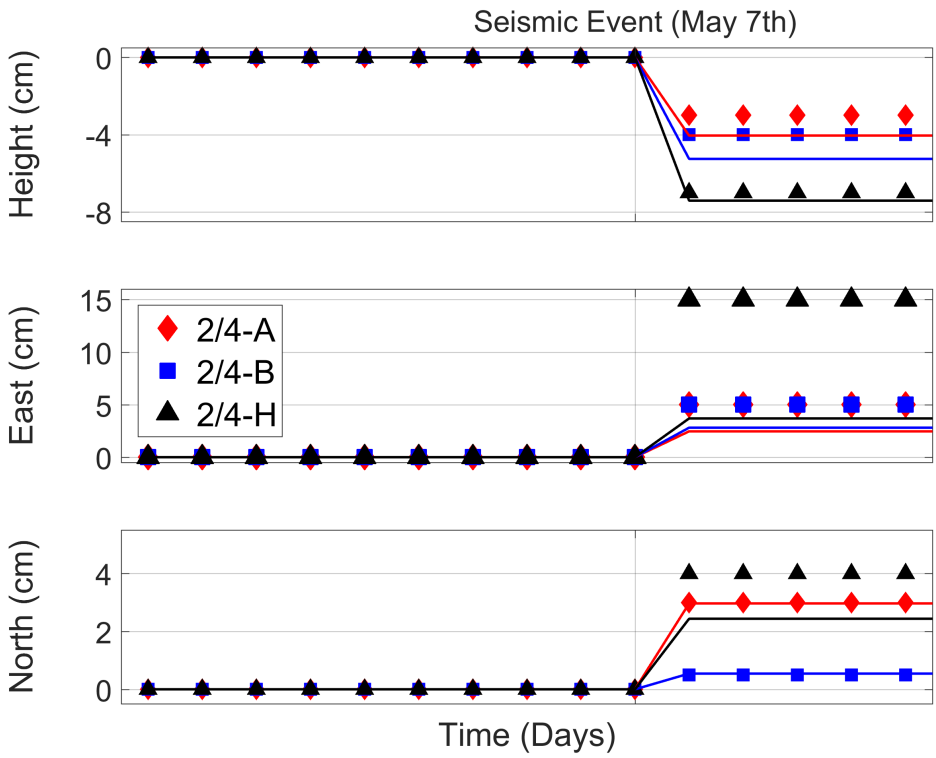

Figure 3.23: Comparison of modeled surface displacement (full lines) with GPS measurements at three platforms.

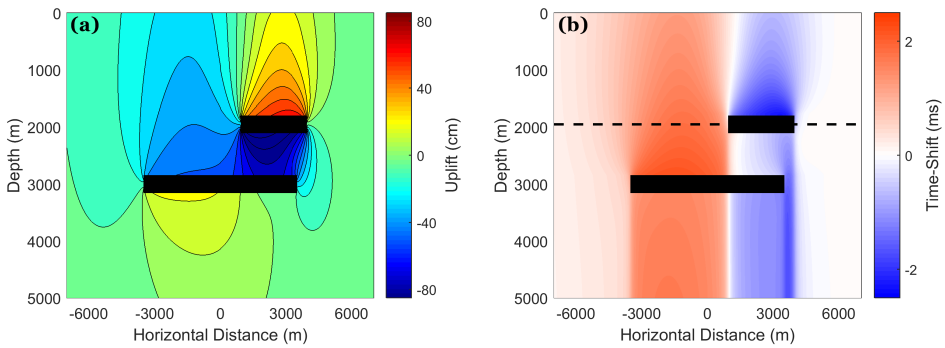

Figure 3.24: Left Depth section of modeled displacements between 1999 and 2001, considering both the reservoir effect and a larger ZUI, of radius 1500m. **Right** Modeled time-shift section for this same configuration. Black dotted line shows the depth where the time-shift map in Figure 3.26 was extracted.

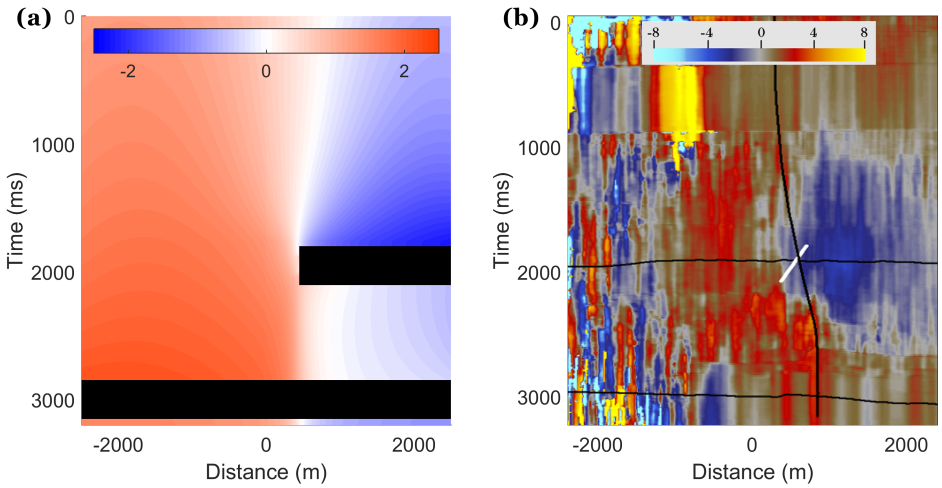

Figure 3.25: Left Modeled time-shift section shown in Figure 3.24b, converted to time, zoomed in and slightly shifted to the left to ease comparison. **Right** Panel in Figure 3.6b. Color scales are in milliseconds.

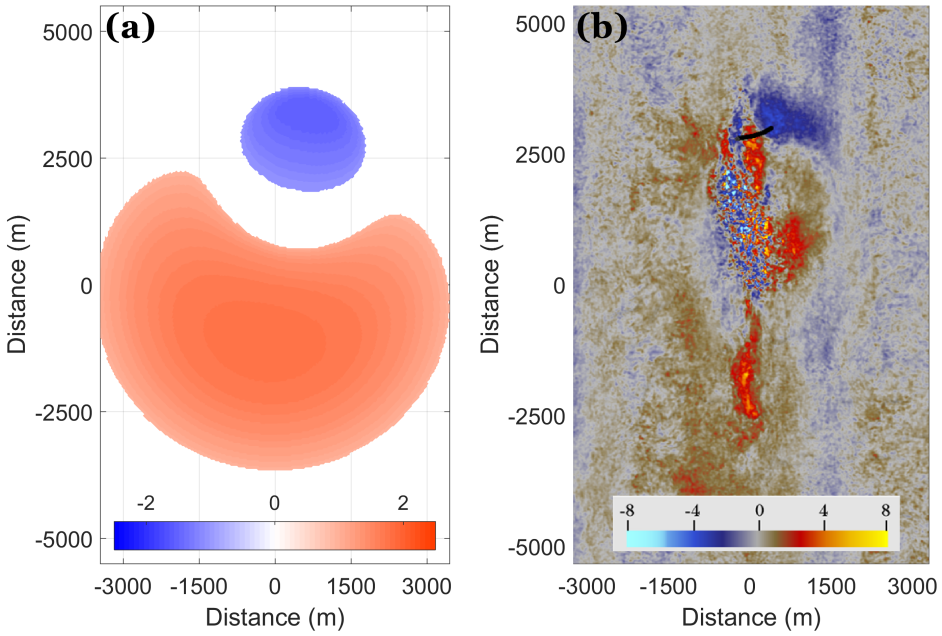

Figure 3.26: Left Modeled time-shifts extracted at a depth of 1950 m, for configuration shown in Figure 3.24. To ease visualization, values between -1 ms and 1 ms were removed from the plot. **Right** Horizon slice from Figure 3.3d, showing the time-shifts in the injection zone. Color scales are in milliseconds.

3.4 Discussion

Before starting to discuss the results, we draw attention again to the fact that bathymetry differences are between 1999 and 2001 (with ongoing injection), while seismic differences are between 1999 and 2003 - one year after well 2/4-K-22 was shut down (Figure 3.1). Time-lapse seismic should then measure the effect of one extra year of injection, when compared to bathymetry. The mechanism of relaxation/pore pressure equalization is nevertheless difficult to assess, and may interfere with quantitative estimations of the volume of injected water from seismic data. Still, the qualitative effect of overburden compaction, leading to velocity increase and negative time-shifts, is remarkably clear in the seismic data (Figure 3.3).

3.4.1 Amplitude Modeling

The lack of significant amplitude changes in the ZUI (Figure 3.5) is most likely due to the injection/inflation being slow, and over a fairly thick interval: as these changes occur over three hundred meters, there is hardly any change in reflectivity, except for a stronger event around 2.1 s (Figure 3.13). These amplitudes changes were modeled as a depth-variant decrease in compressional velocity. The pressure changes obtained from them (Figure 3.15) are lower than the constant 20 MPa used in Geertsma's model: such increase in P_P would take net stress close to zero, and the resulting velocity wouldn't match the low observed time-shifts inside the ZUI. One could argue that, between 2002 and 2003 (after injection was shut down), pore pressure slowly equalized, and the pressure increase measured in seismic was milder. Due to the low permeability in the area, however, this is not expected to happen in such a short period.

The amplitudes modeled under the fracture assumption are similar, and also do not match the strong reflectivity change at 2.1 s. Better characterization of the fracture system (via image logs, core samples, shear-wave splitting, etc.) could greatly improve the understanding of our dataset, since crack models usually demand several parameters for characterization, most of which were unavailable to us at the moment of this study. With more knowledge about crack geometry, crack density and crack compliance, other models, like those of Eshelby (1957) or Thomsen (1995), could - and should - be investigated.

3.4.2 Geomechanical and Fault Displacement Modeling

An analytical, simplified model such as Geertsma's is not the optimal way to describe the complex 3D geomechanical behavior of an oil field under production, but can be used for a low-cost, prompt assessment of the problem. Figures 3.16, 3.19a and 3.24 show that the modeled surface displacement is in reasonable agreement with the measured uplift. The calculated values for the dilation factor R

are small when compared to measurements of overburden extension. *R* values are indeed expected to be lower for compaction: MacBeth et al. (2019) published a comprehensible review of time-shifts in 4D seismic, and the R values and relative time-shifts presented by them are in the range of the values obtained in this study.

The size of the fault obtained from modeling with Okada's equations (6500m x 3000m) is considerable, but is compatible with the necessary movement to generate the measured event magnitude, given the low strength of the overburden rocks (Ottemöller et al., 2005). Such significant movement is needed to match the observed GPS displacement in the platforms. We should have in mind that the GPS measurements may be the combination of several fault movements: normal faults could have been triggered by a big, horizontal displacement, and then reactivated aseismically. This would also explain the subsidence in the platforms, which is hard to justify with the nodal planes inverted from the seismologic recordings. Finally, the tilting of the GPS antennas may differ from the modeled values, especially if non-elastic deformation of the seabed is present. That would compromise our ability to use such measurements as control points for modeling.

No direct signal of the triggered event was identified in the seismic data. According to the analysis of seismologic recordings (Ottemöller et al., 2005), the source could be either a near-vertical or a near-horizontal slippage. Since no damage was caused to nearby wells, the displacement is likely to be inferior to a few centimeters. That would demand an area of slippage of radius larger than 3 km to explain the magnitude of the seismic event. This basically rules out the possibility of a single near-vertical fault reactivation, even though modeled stress changes caused by injection can lead to normal faulting, due to the increase in σ_V and decrease in σ_h (Figure 3.19). In addition, results of fault displacement modeling (Figures 3.22 and 3.23) show that the best fit of the GPS data is obtained by assuming a near-horizontal, oblique-normal movement. The tensile term of the model, corresponding to a collapse of 10 cm in the fault, could be caused by sudden escape of the trapped, pressurized fluid. We present here a possible explanation for a near-horizontal fault movement.

3.4.3 The Stress Regime in Ekofisk

As previously mentioned, the general trend in the Ekofisk area is that of normal stress regime. When the effect of decades of reservoir compaction is considered, however, this regime can change: the modeling result presented in Figure 3.21 shows how relaxation of the overburden, combined with arching effect, can create a zone above the reservoir where $\sigma_h > \sigma_V$. In this zone, the stress regime would become reverse (explaining why the fractures propagated horizontally), and eventual reactivation of faults would have to follow this new configuration. As the

majority of visible faults in the area are normal, the reactivation in a reverse regime is unlikely. Sibson (1985) shows in a very didactic way that, above a certain critical angle, the reactivation is not possible. Considering average values for fault dip and friction coefficient, reactivation of a preexisting normal fault as a reverse one would only occur in the case of a tensile stress, which does not seem to be the case here.

The ZUI is then in a very particular state: it is an overpressured layer in a regime of reverse stress. Hubbert and Rubey (1960) show that the excess of pore pressure can reduce the necessary stress to move a block, to the point that when the pore pressure is equal or superior to the vertical stress, a block can slide with little or no resistance - a situation analogous to the phenomenon of hydrostatic lubrication, employed in several mechanical devices (Bassani and Piccigallo, 1992; Karelitz, 1938). This is of special attention because the observed pattern in the horizontal displacement of the surface installations (Ottemöller et al., 2005, Figure 9) shows a very strong horizontal movement, an indication that the overburden may have moved horizontally - perhaps under the influence of gravity (gravitational sliding), as the increase in pore pressure dramatically reduced the effective vertical stress and, therefore, the friction. This is also compatible with the GPS measurements and the focal mechanism of the event, and we suggest that it was the source of the seismic event.

To look for lateral displacements between the datasets, we used one of the most common metrics in time-lapse seismic analysis: *Normalized Root Mean Square*, or NRMS (Kragh and Christie, 2002; Landrø, 1999). Low NRMS values mean small changes between two surveys. NRMS is usually calculated in regions where little to no seismic change is expected, e.g. in the overburden (when there are no expected geomechanical effects), or far away from production zones. In the case of lateral displacement between surveys, the proper comparison of traces for time-lapse studies may be compromised: a certain geological feature that was in a position $\mathbf{r}$ during survey 1 may have moved to a position $\mathbf{r} + \Delta\mathbf{r}$ in survey 2. Not accounting for this effect would lead to erroneous computation of 4D attributes, since seismic traces from different locations would be compared.

The expected displacement is $|\Delta\mathbf{r}| \approx 10$ cm, much smaller than the inline and crossline spacing of the seismic surveys (12.5 m). It may seem counter-intuitive that such small changes are even object of consideration, given the acquisition grid. Nevertheless, according to the sampling theorem (Shannon, 1948a), proper sampling of the wavefield allows for its full reconstruction, once appropriate care to avoid spatial and temporal aliasing has been taken (Rosa, 2018; Bracewell, 1986; Petersen and Middleton, 1962). This is the same principle used when time-shifts smaller than the sampling frequency are calculated in time-shift analysis

(Buizard et al., 2013). To search for lateral displacements between 1999 and 2003, we interpolated the original datasets to a regular grid of 5 cm spacing. In this refined grid, NRMS maps were calculated in 300 ms windows centered in three horizons: shallow horizon 2, injection horizon, and intermediate horizon (Figures 3.2c, 3.2d and 3.2e, respectively). The results with this method did not show any lateral variations - the NRMS of the survey is above 25%, which probably masks any small changes that might arise from lateral variations in the dataset. The explicit detection of the horizontal movement in the seismic data remains a future task in this work.

3.5 Conclusions

A seismic event of moderate magnitude was observed at the Ekofisk field on May 7th, 2001. The probable cause of the event was unintentional water injection in the overburden. An increase in pore pressure around the injection well shows up both as time-shift and small amplitude changes in the 4D seismic data. The expected pressure increase is sufficient to lift the overburden, and geomechanical modeling indicates that it is compatible with the seabed uplift measured by time-lapse bathymetry.

The increase in pore pressure, combined with the subsurface stress changes caused by decades of production and reservoir compaction, creates a situation of hydrostatic lubrication, which can lead to block sliding/low-dip slippage in the overburden. Horizontal slippage is the most probable source mechanism of the overburden movement, and we suggest that this is the potential source of the 2001 event.

This dataset presents a very rare opportunity to evaluate dilation factors and time-shifts in an environment of overburden compaction, as opposed to the majority of case studies for time-lapse seismic, which deal with overburden relaxation caused by depletion of a deeper reservoir. The R values obtained are in the range $1 - 4$, compatible with predictions from literature. We believe that further work, using pre-stack data and numerical modeling, could help increase our understanding of injection-induced overburden compaction.

Chapter 4

Normal Modes, Diving Waves and Shallow Monitoring

In this chapter, we analyze data recorded by the Valhall Life of Field Seismic (LoFS) system in 2014, during an ongoing acquisition in a nearby field (Ekofisk). The recorded data shows a clear arrival of at least four propagating normal modes (harmonics), despite the distance of over 30 km between source and receivers. These harmonics can be used to monitor the shallow sediment layer, based on an analytical model. Low-frequency diving waves were also identified. Finite differences modeling was used to reproduce the complex wave patterns detected in the data. Besides, a method to estimate the seafloor P-wave velocity based on passive measurements is suggested. A summary of the analysis performed here was published in the following journal paper:

Borges, F. and M. Landrø, 2021, Far-offset detection of normal modes and diving waves: a case study in valhall, southern north sea: Geophysics, **87**, 1-50 (doi: 10.1190/geo2021-0267.1)

In addition to the published content, this chapter contains supplementary information and plots about the passive velocity estimation for the shallow section.

I take to opportunity to thank the Valhall Joint Venture companies, Aker BP ASA (operator) and Pandion Energy AS (partner), for making the data available for this study, as well as for the permission to publish the results.

4.1 Introduction and Background

Seismic data is a fundamental input for hydrocarbon reservoir exploration and characterization, being commonly the only available data with continuous coverage over the area of interest. In addition to that, it has become usual to employ repeated seismic surveys for reservoir monitoring (Landrø et al., 1999; Mitchell et al., 2009). The business value of time-lapse seismic has been recognized to the point of justifying the installation of permanent offshore arrays with this sole purpose, including some in complex, deepwater environments (Thedy et al., 2013; Ebaid et al., 2017). Among the several projects operating today in the world, the most prolific are undoubtedly the ones installed in Valhall (Van Gestel et al., 2008) and Ekofisk (Bertrand et al., 2014). Both systems are located on the Norwegian continental shelf, circa 30 km distant from each other.

Apart from the recording of high-repeatability active source seismic data, a permanent array of receivers opens the possibility of continuous recording, enabling novel monitoring techniques that were not possible with standard deploy-and-retrieve systems. Among these new opportunities we can cite the use of interferometry (De Ridder et al., 2014; de Ridder and Biondi, 2015) and microseismicity (Chambers et al., 2010; Oye et al., 2014). Other than recording of passive data ("noise"), another possibility is to use energy from nearby surveys to register events typical from large offsets - namely, normal modes and diving waves.

A comprehensive study of normal modes in seismic data was presented by Landrø and Hatchell (2012), and an in-depth explanation of the phenomenon can be found in Ewing et al. (1957). For the particular case of offshore seismic, the normal modes arise as a combination of reflections and refractions of the trapped energy between the free surface and the seafloor, and have a distinct behavior of decaying with the inverse of the square root of distance ($r^{-1/2}$). When compared to usual 3D body waves, which have their amplitude decaying with r^{-1}, the normal modes will become comparably stronger for far offsets, which makes them relatively easy to detect and isolate in the field data. Besides, they carry information about the interface between water and sediment, presenting us with the possibility of shallow characterization and monitoring.

In this chapter, we present the analysis of field data recorded in the Valhall Life of Field Seismic (LoFS) system, which was active while a seismic survey was ongoing in the Ekofisk area, in April 2014. We show that the normal modes are remarkably clear in the data, and we also identify low-frequency diving waves. The normal modes are in good agreement with a two-layer model of the water/seafloor interface, and the diving waves can be reproduced with a regional velocity model of the southern North Sea area. We also propose a method to passively monitor the

velocity of the shallow sediment between the receivers and noise sources nearby. The results are in good agreement with other estimations in the literature, and raise the possibility of using ultra-far offset data for monitoring the shallow layers.

4.2 Theory and Method

In this section we present the available data for this work, and introduce some theoretical concepts that are important for understanding the study.

4.2.1 Normal Modes

As mentioned in the Introduction, a deep and comprehensive description of harmonics in layered media can be found in Ewing et al. (1957), and more recently in Landrø and Hatchell (2012). Of particular interest in this study is the period equation, which can be solved for the phase velocities of the harmonics. In an acoustic two-layers model of water depth H, with p-wave velocities and densities of the water and seabed being respectively (α_1, ρ_1) and (α_2, ρ_2), the phase velocity c can be obtained by solving

$$\tan Hk\kappa_1 = -\frac{\rho_2 \kappa_1}{\rho_1 \kappa_2}, \tag{4.1}$$

where $\kappa_1 = \sqrt{(c/\alpha_1)^2 - 1}$, $\kappa_2 = \sqrt{1 - (c/\alpha_2)^2}$, and $k = 2\pi f/c$ is the wavenumber, and f is the frequency. Figure 4.1 shows the plots of the left and right sides of Equation 4.1 for parameters similar to those found in Valhall, and a frequency $f = 55$ Hz. The periodic behavior of the tangent term on the left side of the equation leads to multiple solutions, which are the normal modes - 3 solutions for this example, with phase velocities of 1503 m/s, 1563 m/s and 1683 m/s. From Equation 4.1, the group velocities can be explicitly obtained (Landrø and Hatchell, 2012). Figure 4.2 shows phase and group velocities for the first four modes, for the same set of parameters used in Figure 4.1.

As can be seen in Figure 4.2, each mode has a cutoff frequency f_{cut}, below which the mode does not exist. At the cutoff frequency, both phase and group velocities are equal to the bottom layer velocity α_2. This information will be important to interpret the results presented later in this work.

4.2.2 Available Data

The data available for this study were recorded by the Valhall LoFS during April, 2014. The data are sampled at a frequency of 250 Hz, and the recording is continuous, since there is no active survey ongoing in Valhall. The receiver array is composed of over 2300 multicomponent stations, trenched in the seafloor. Each receiver station comprises three orthogonal geophones and one hydrophone. The

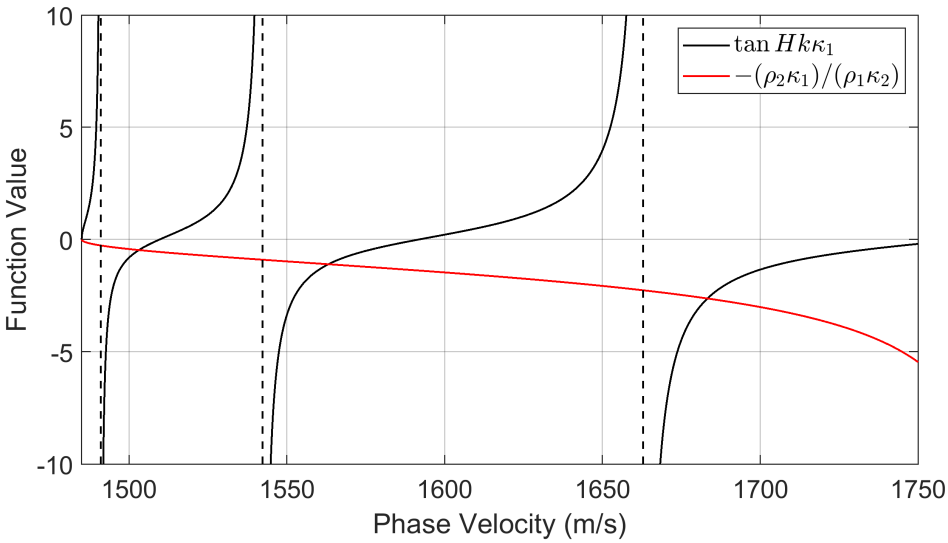

Figure 4.1: Comparison of left and right sides of Equation 4.1 for $\alpha_1 = 1485$ m/s, $\alpha_2 = 1780$ m/s, $H = 75$ m, $\rho_2/\rho_1 = 1.6$ and $f = 55$ Hz. Dotted lines mark the discontinuity in the tangent function. Three solutions are possible for these parameters.

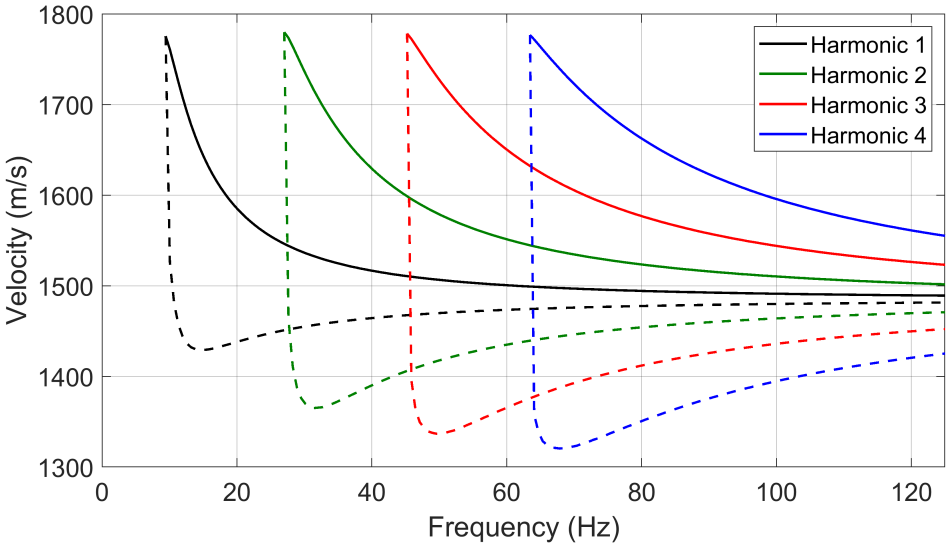

Figure 4.2: Phase (full lines) and group (dashed lines) velocities for the first four normal modes, using $\alpha_1 = 1485$ m/s, $\alpha_2 = 1780$ m/s, $H = 75$ m and $\rho_2/\rho_1 = 1.6$.

stations are separated by a 50 m interval along the cable (Kommedal et al., 2004). Figure 4.3 shows the system configuration, together with the bathymetry in the

area and the outline of some other fields. To make the results more compact, one line of receivers was selected, and the results presented from now on refer to data from this array (see red arrow in the rightmost panel).

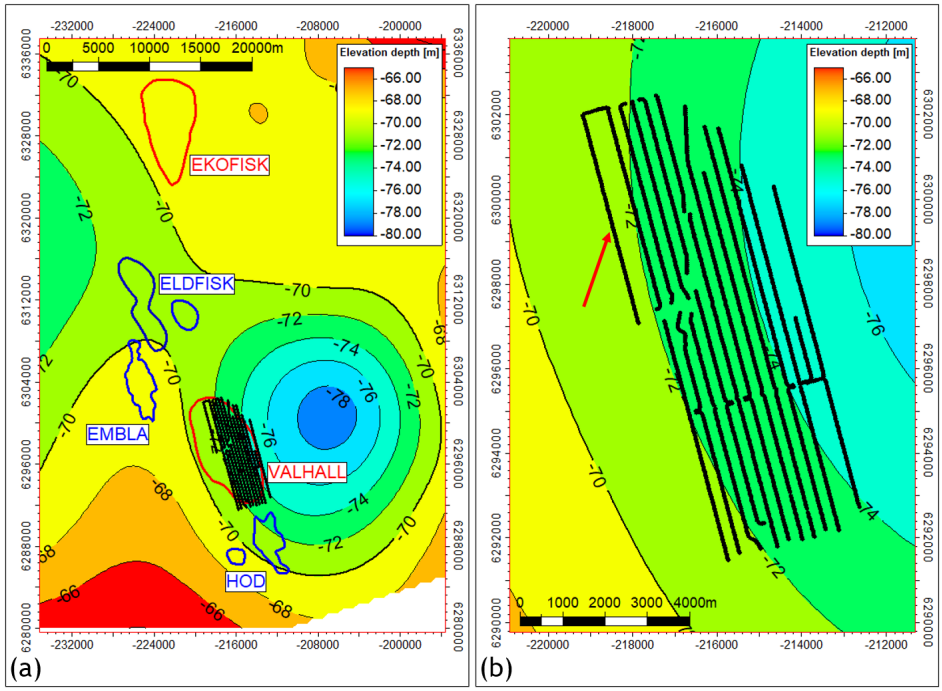

Figure 4.3: (a) Seafloor bathymetry on southern North Sea area. Ekofisk and Valhall field outlines are highlighted in red, and some other field outlines are highlighted in blue. LoFS receivers are marked as black dots. **(b)** Zoom in around LoFS receivers. Red arrow points to the array that was used in this study. The data in this map come from several sources, and there might be inaccuracies due to geodesic datum conversion.

The first step in the analysis is to identify when the Ekofisk survey started, so the data can be studied with and without the seismic energy from an active source. Although no specific source position and firing time were available, a daily report from Ekofisk stated that the shooting started on Sunday 6th, at about 19:17, and that the shotpoint interval is 25m. Valhall data show coherent signals arriving a few minutes before, at about 19:11, probably indicating gun testing prior to production. Figure 4.4 shows 100 seconds of hydrophone recordings in the selected array, depicting the arrival of the first events, as well as its periodicity. Auto-correlation of the data shows peaks roughly every 12 seconds, compatible with what can be seen by visual inspection of the seismogram.

Figure 4.5 shows a zoom in the arrival of the first shot (from 37 s to 44 s in Figure

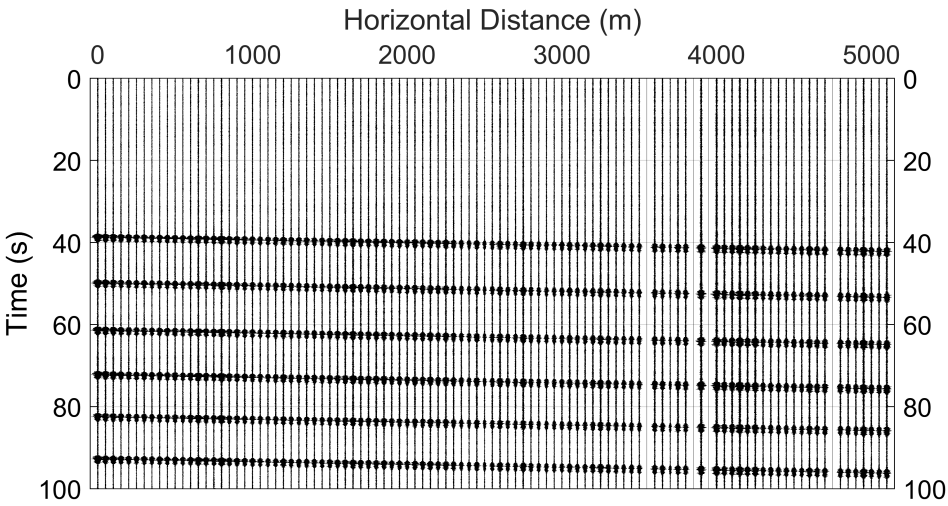

Figure 4.4: Hydrophone recording of the selected receiver line. Horizontal distance starts from zero in the northwesternmost receiver, and increases by 50 m up to 5100 m at receiver 103. Time axis is arbitrary and is not synchronized with the Ekofisk survey.

4.4). The signal consists of an extensive wave-train (about 2 seconds long), which seems to be a composition of several different types of waves.

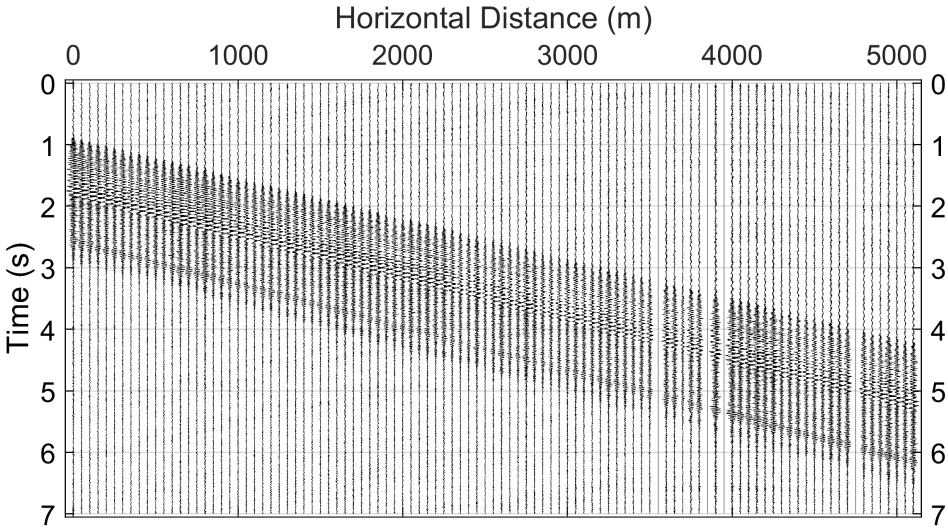

Figure 4.5: Hydrophone recording of the selected receiver line, showing the first arrival. Time axis is arbitrary.

4.2.3 Group Velocities

To better analyze the nature of the events, we select trace number 50, in the middle of the array, and calculate its spectrogram. The results are displayed in Figure 4.6. The clusters in the power spectrum plot have a very distinct pattern, similar to the ones seen for the group velocity in Figure 4.2. The similarity between the plots happens because the phase velocity is a function of frequency: the lower frequencies (above the cut-off frequency) are the slowest in each harmonic, and therefore show a later arrival in the time-frequency plot.

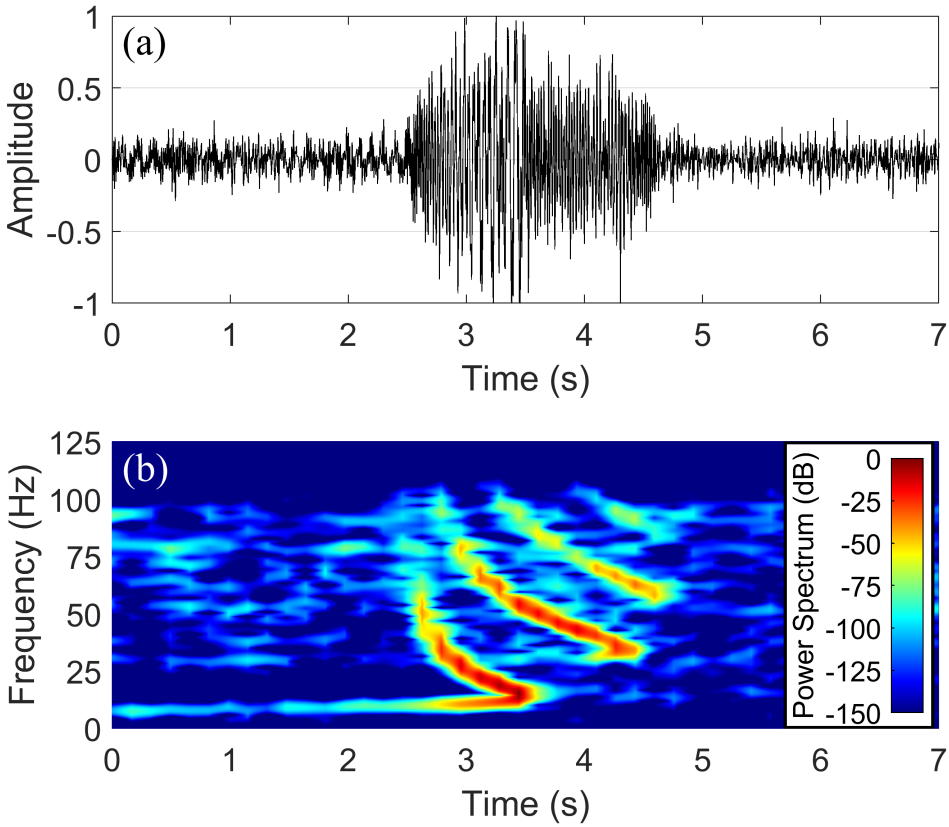

Figure 4.6: **(a)** Trace #50 in Figure 4.5. **(b)** Normalized spectrogram of trace in panel **(a)**.

By applying a set of narrow band-pass filters to the trace in Figure 4.6, we can obtain a better representation of how each frequency of the wave-train propagates. A 2.5 Hz-wide Butterworth filter was used, starting with center at 1.25 Hz and moving in steps of 2.5 Hz. The analysis of the band-passed data is made using the Hilbert phase-quadrature envelope of the signal. Figure 4.7 shows envelope of the filtered trace, for the different frequency filters. Red curves superimposed on the

plot are the group velocities from Figure 4.2, which show good agreement with the data.

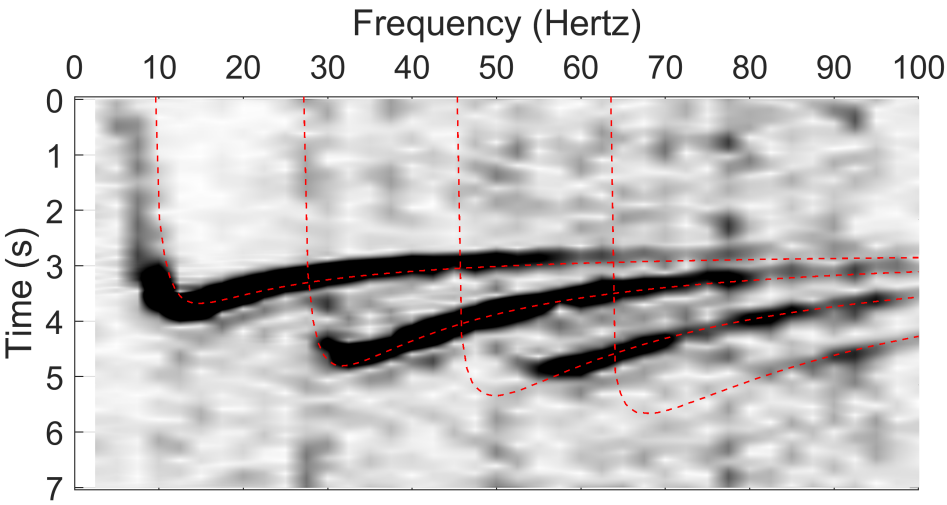

Figure 4.7: Envelope of analytic signal of trace in Figure 4.6, after application of several narrow band-pass filters. Time axis is the same of Figure 4.6, and horizontal axis is the central frequency of the applied bandpass filter. Darker color means higher envelope amplitude. Red lines are group velocities for the normal modes shown in Figure 4.2.

From the Hilbert transform, the instantaneous frequency can be calculated. However, the quantitative interpretation of the instantaneous frequency is not accurate for signals composed of a superposition of several wave-trains. To have a quantitative estimation of this frequency, we use the results shown in Figure 4.7 to obtain the frequency of the maximum envelope for each receiver, at each time sample. The result is plotted in Figure 4.8.

The plot in Figure 4.8 shows that the arrival of the wave-train is marked by a peak in high frequencies, which slowly moves towards lower frequencies. This suddenly changes to a new peak in higher frequencies, that again decays towards lower frequencies (but still higher than the previous low). This behavior can be understood by analysis of Figures 4.6 and 4.2: The high-frequency group velocity of the normal modes is higher than the low-frequency one, so they arrive first - the delay is made clearer in this data set due to the significant offset between source and receivers. For an offset r, the travel time difference $\Delta t_n(f_1, f_2)$ between two frequencies f_1 and f_2 for a mode n with group velocity $U_n(f)$ is

$$\Delta t_n(f_1, f_2) = r\left(\frac{1}{U_n(f_2)} - \frac{1}{U_n(f_1)}\right) \tag{4.2}$$

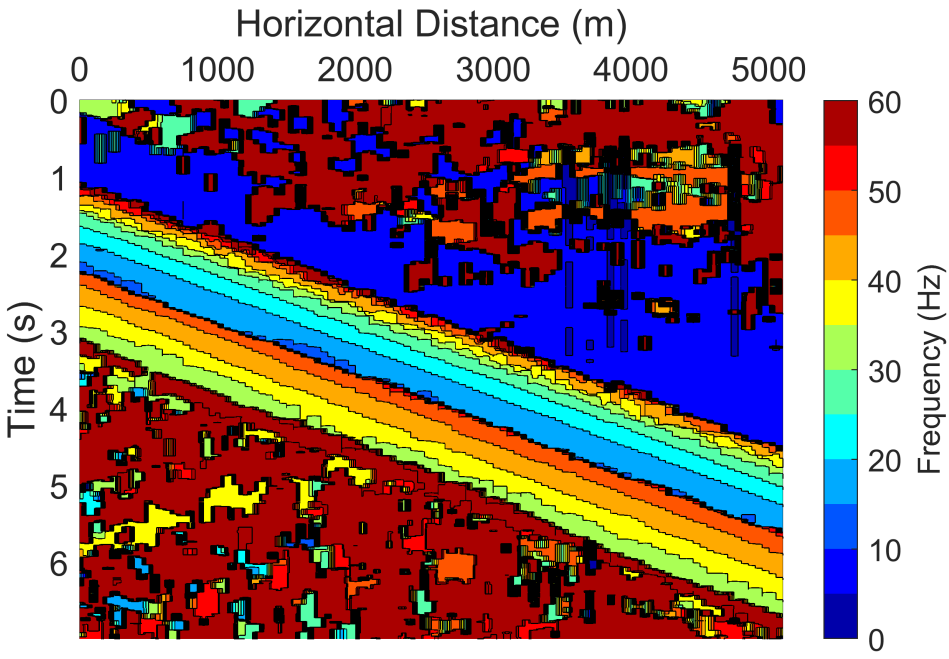

Figure 4.8: Frequency of maximum Hilbert envelope for every trace in Figure 4.5.

Although we do not have proper control of the shot position in this experiment, the distance between Ekofisk and the middle of the receiver array can be estimated as 35 Km. Using this offset, and noting that $U_1(50\text{Hz}) = 1472$ m/s and $U_1(15\text{Hz}) = 1429$ m/s, the expected time difference between them is 0.72 seconds, which coincides with the values seen in the plots. A similar exercise can be done by checking the time difference between the lower frequencies for each mode - mode 1 versus mode 2, for example. By doing so, the travel time difference $\Delta t_{n_1,n_2}(f_{low})$ would be

$$\Delta t_{n_1,n_2}(f_{low}) = r\left(\frac{1}{U_{n_1}(f_{low})} - \frac{1}{U_{n_2}(f_{low})}\right) \tag{4.3}$$

Equation 4.3, when applied to the first and second modes shown in Figure 4.2, yields a difference of 1.15 seconds, also compatible with the results seen in Figure 4.8.

One last point to highlight in Figure 4.8 is the sudden decrease in dominant frequency prior to the arrival of the normal modes - this can be observed also in the spectrogram of Figure 4.6, where a low-frequency "stripe" appears several seconds prior to the normal modes. This pattern is consistent throughout all the data set, and

we associate it with the arrival of diving waves and head waves. These waves, having traveled through fast sediment layers, arrive before the harmonics, but show a lower frequency content and amplitude due to absorption and geometrical spreading. Diving waves and head waves will be discussed later in this work.

4.2.4 Phase Velocities

The phase velocities can be investigated with the method proposed by Park et al. (1998). Following their derivation, if we have a seismic recording $s(x,t)$, its time-domain Fourier transform $S(x,\omega)$ can be expressed as the multiplication of a power spectrum $A(x,\omega)$ and a phase spectrum $P(x,\omega) = e^{-i\Phi x}$, with $\Phi = \omega/c_w$, where c_w is the phase velocity and $\omega = 2\pi f$ is the angular frequency. A phase velocity-frequency map $D(\omega,c)$ can be obtained by the following integral transform:

$$D(\omega,c) = \int \frac{A(x,\omega)}{|A(x,\omega)|} e^{-i(\Phi-\omega/c)x} dx. \tag{4.4}$$

Because the exponential term in the integration oscillates rapidly, the integral will result in a small number, except for values of c close to the phase velocity c_w, when $\omega/c \approx \Phi$. The peaks in the map $D(\omega,c)$ can then be used to find the phase velocities of the signal $s(x,t)$.

Figure 4.9 shows the map $D(\omega,c)$ for the data in Figure 4.5. The black lines show the theoretical phase velocities for the first 4 normal modes, as displayed in Figure 4.2. These velocities are corrected for the azimuthal angle of arrival of the wave (horizontal angle - 15°), since the line of receivers is slanted when compared to the estimated direction of the incoming energy. As in Figure 4.7, the fit between modeled and measured values is very good, indicating that the two-layer model with the selected parameters is reasonable enough to describe the main events as normal modes.

4.2.5 Low Frequency Events

Figures 4.6 and 4.8 show that, a few seconds prior to the arrival of the normal modes, there is an increase in the energy of low-frequency waves. This phenomenon is consistent during the active survey in Ekofisk, and indicates that the normal modes are preceded by a faster, low-frequency signal. Figure 4.10 shows a map view of the envelope and frequencies of maximum envelope (same methodology as in Figure 4.8) for all active receivers during the survey - this “snapshot" is calculated at t = 45 seconds in Figure 4.4. The strong amplitudes in the upper panel mark the arrival of the water wave. As in Figure 4.8, we can observe a slow decrease in frequency after the arrival of a mode, followed by a sudden increase when the subsequent harmonic appears (pointed by red arrow). However, despite

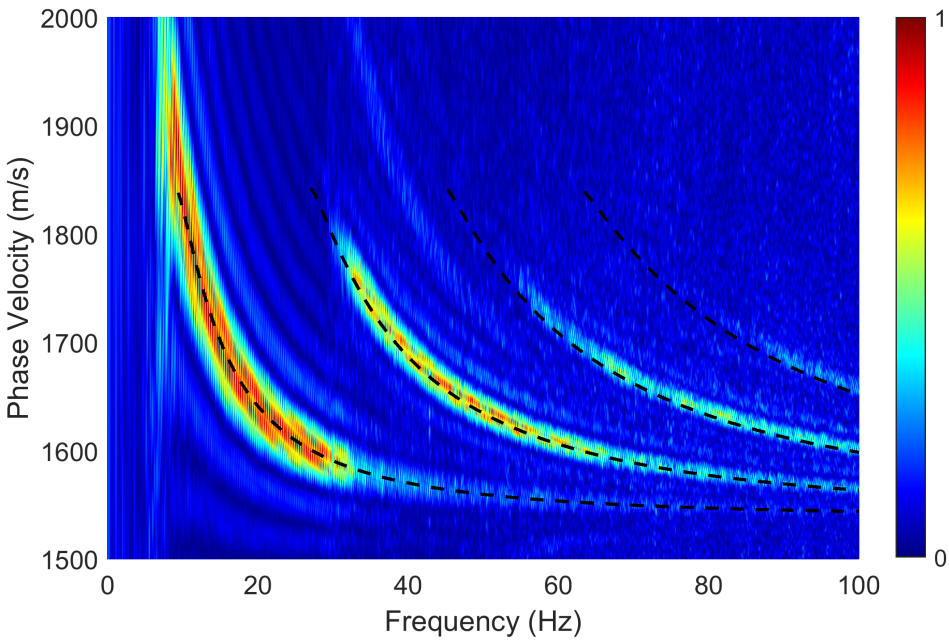

Figure 4.9: Normalized dispersion panel of data in Figure 4.5, for energy arriving from the NW direction. Black lines are the solutions for phase velocities shown in Figure 4.2, adjusting for an azimuthal angle of arrival of 15°.

not showing up in the envelope map, there is a substantial decrease in the frequency of maximum envelope ahead of the normal modes arrival - this is more evident in the two receiver lines on the upper left corner, and prompts a further inspection of this pattern.

In the water layer, the fastest event expected is the head wave at the seafloor, which should have a linear moveout with the same velocity of this layer. Besides, as discussed by Landrø and Hatchell (2012), the arrival of the refracted wave should happen close to specific frequencies f_n, given by

$$f_n \approx \frac{(2n-1)\alpha_1\alpha_2}{4H\sqrt{\alpha_2^2 - \alpha_1^2}}. \tag{4.5}$$

Figure 4.11 shows a comparison of the power spectrum in 3-seconds windows for the trace shown in Figure 4.6, in 3 different moments, which we labeled *noise recording* (1 minute prior to arrival of Ekofisk energy), *pre-recording* (the two first seconds of the data shown in Figure 4.6, plus one second before that) and *recording*, which is from 2 to 5 seconds in Figure 4.6. It can be seen that the peak in energy of the early arrival happens at about 7.9 Hz. Using equation 4.5, that

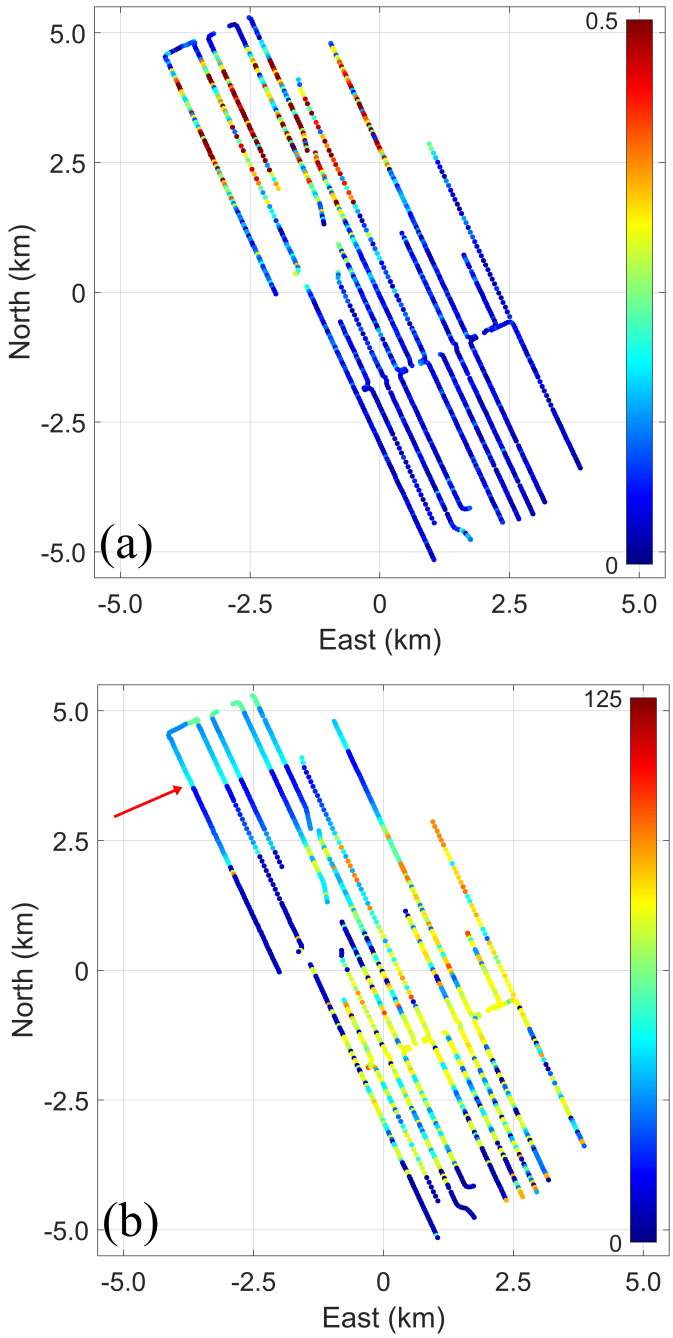

Figure 4.10: Values of envelope **(a)** and frequency of maximum envelope **(b)** of all active hydrophone receivers, calculated at t = 45 seconds, according to the time axis of Figure 4.4. Red arrow points to peak in frequency of maximum envelope, marking the arrival of an harmonic of superior order.

would imply a velocity at the seafloor of about 1905 m/s - significantly higher than the values used to model the good-fitting dispersion curves shown in Figures 4.7 and 4.9.

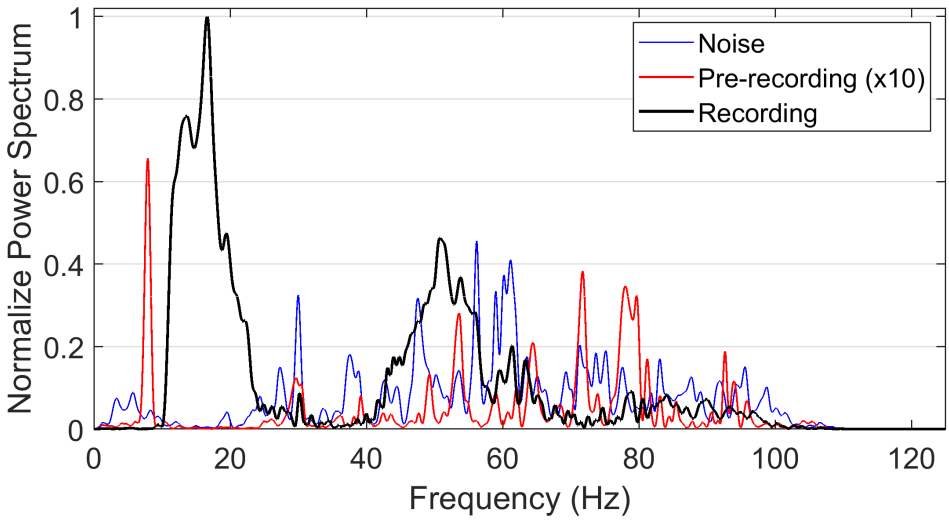

Figure 4.11: Normalized power spectrum of trace shown in Figure 4.6, for different time windows: one minute before energy from Ekofisk arrives (blue), 3 seconds prior to energy arrival (red), and from 2 to 5 seconds in Figure 4.6 (black). All curves are normalized by the maximum power amplitude of the normal modes arrival (black curve), and pre-recording spectrum (red curve) is multiplied by 10 to ease visualization.

To remove the strong normal modes and isolate the low-frequency signals, different bandpass filters were applied to the data. The results can be seen in Figures 4.12, 4.13, 4.14 and 4.15.

The use of the 10 Hz lowpass filter in Figure 4.13 removes the bulk of the normal modes - which, as seen in Figure 4.1, have a cut-off frequency of about 10 Hz. Despite some energy still being visible at the same arrival time of the propagating normal modes, some earlier events are highlighted, at about 75 seconds. The slope of these events in the *x*-*t* suggest that they are faster.

The use of a more restrictive filter, with cutting frequency of 8 Hz (Figure 4.14), completely removes the events arriving simultaneously with the normal modes, and further eases the visualization of the events at about 75 seconds. Besides, some other events also appear, indicated by red arrows in Figure 4.14. These events precede the normal modes by 6 to seven seconds, a sign that they traveled with significantly higher velocities. Besides, a similar event can be seen at about 82 seconds (blue arrow), preceded by several seconds of the normal modes of the

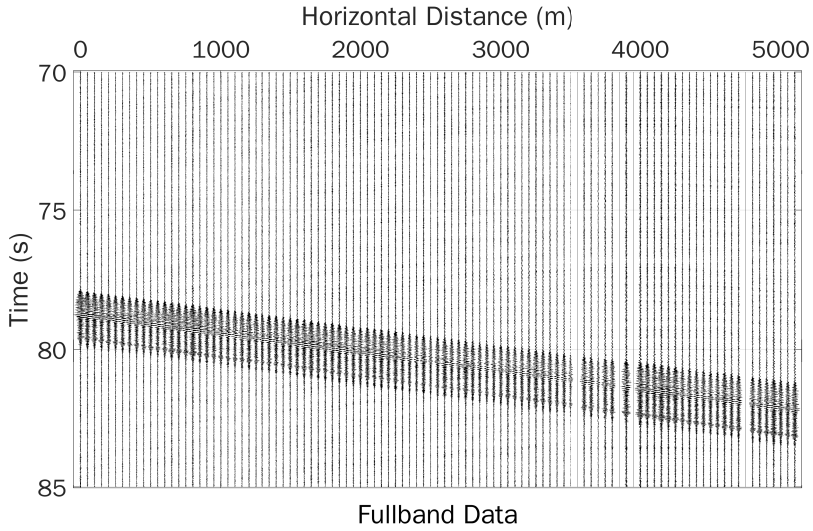

Figure 4.12: Zoom of data in Figure 4.4 (same time axis), showing arrival of the first modes.

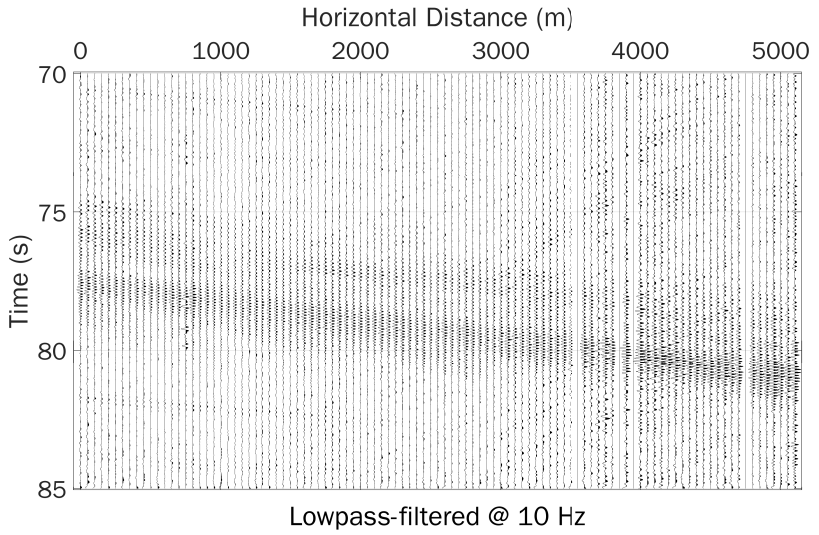

Figure 4.13: Same data of Figure 4.12, after a lowpass filter of 10 Hz.

subsequent shot. These events seem therefore to be connected with the firing of the seismic source in Ekofisk.

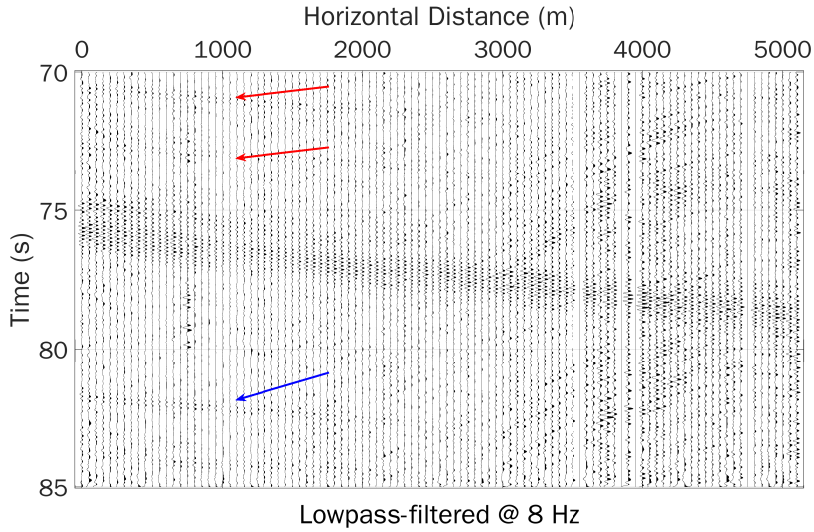

Figure 4.14: Same data of Figure 4.12, after a lowpass filter of 8 Hz.

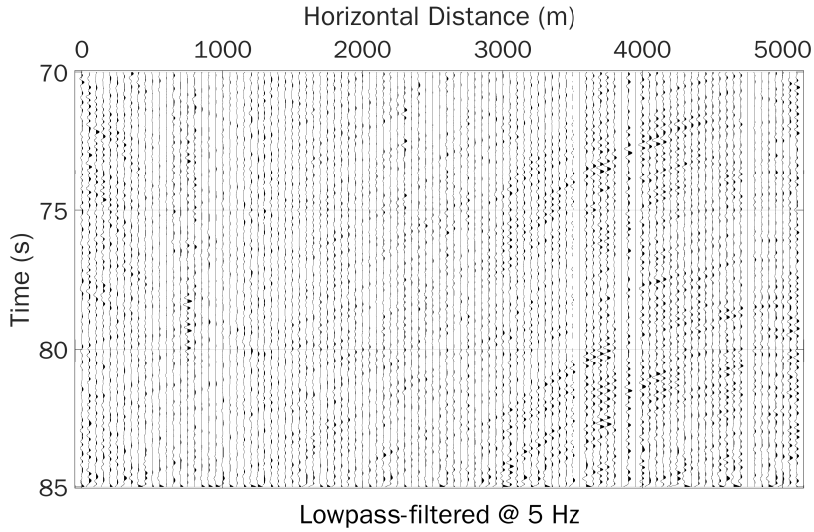

Figure 4.15: Same data of Figure 4.12, after a lowpass filter of 5 Hz.

The use of a lowpass filter with cut-off at 5 Hz (Figure 4.15) seems to remove most signs of coherent energy, except for some low-velocity diffraction hyperbolas on the rightmost (southeastern) end of the receiver array. Looking back at Figure 4.3, some void spaces can be seen in the LoFS layout - these are the places where the

surface facilities are attached to the seafloor. Analysis of low-frequency data in other arrays show that the center of the field acts as the "source" of these hyperbolas. The moveout of these events show good fit with a modeled source at the sea bottom, with wave velocities in the range 230-280 m/s These values are compatible both with shear wave velocity at the shallow layer (Mordret et al., 2014) and with Scholte wave velocities estimated at the area (De Ridder et al., 2014). Due to the high amplitude of the events, and also because they highlight only in the lower frequencies, we believe Scholte waves, generated at the places where the surface facilities are attached to the loo, are the most probable nature of these events.

To study the moveout of the low-frequency events, the linear moveout (LMO) semblance of the data was calculated. Figure 4.16 shows semblance plots for the data in Figures 4.12-4.15.

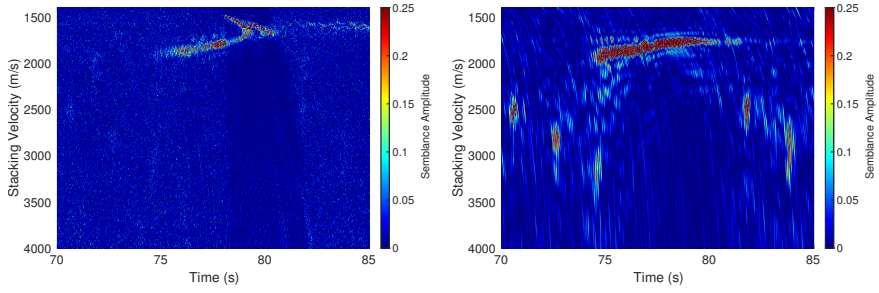

(a) Full bandwidth data

(b) Lowpass-filtered data (10 Hz)

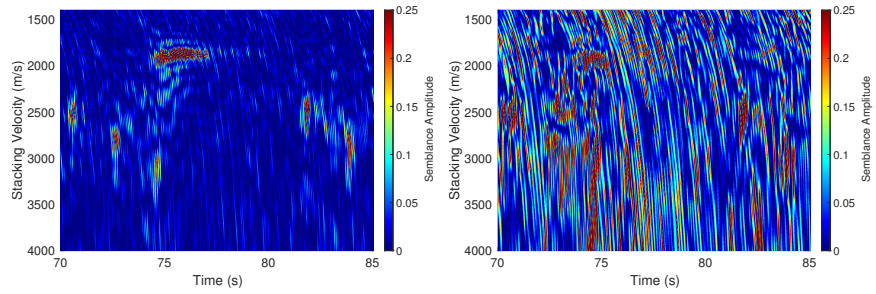

(c) Lowpass-filtered data (8 Hz)

(d) Lowpass-filtered data (5 Hz)

Figure 4.16: Linear moveout semblance of data in Figure 4.12, for different lowpass filters. Every panel is normalized individually.

The strong amplitudes between 1485 m/s and 1780 m/s in Figure 4.16a represent the arrivals of normal modes, which are present in all frequencies above the cutoff of the fundamental mode. The three higher-velocity, low-frequency events in Figures 4.16b and 4.16c (between 70 and 75 seconds) arrive before the normal

modes' energy, hinting that they might have traveled deep inside the sediment, through faster layers with strong attenuation. Two similar events can be identified arriving after the normal modes, preceding the next shot. If the window of analysis is widened, the periodicity of these events can be observed: Figure 4.17 shows the LMO semblance of the 100 seconds of data shown in Figure 4.4. The low-frequency events (f < 10 Hz) in Figure 4.17b have a clear periodicity, suggesting their connection with the active survey.

Because the moveout of the low-frequency events is not strictly linear, there is a strong indication that these are deep diving waves. This possibility will be discussed further in the next sections. Besides, as anticipated by the lack of coherent events in the *x-t* plot, Figure 4.16d does not indicate strong coherence for the frequencies below 5 Hz.

4.2.6 Ray-Tracing and FD Modeling

Because several wave phenomena seem to be present in the data set, the analytic solution for the two-layers velocity model is not enough to explain all events - diving waves, for example, would not exist in that case. To understand our data better, two velocity scenarios were built for modeling: a two-layers scenario, and one with a depth-dependent velocity.

The two-layers model is the same one used for generating the plot in Figure 4.2: a water layer with sound velocity $\alpha_1 = 1485$ m/s and density $\rho_1 = 1.0$ g/cm^3, interfacing with a sediment layer at depth $H = 75$ m, P-wave velocity $\alpha_2 = 1780$ m/s and density $\rho_2 = 1.6$ g/cm^3.

For the depth-dependent velocity model, the water layer properties and depth are the same as described above, but the sediment layer is no longer constant. The southern North Sea exhibits a velocity inversion trend in some areas (e.g. Hordaland formation), due to overpressure caused by fast compaction of low-permeability shales (Aven, 2017; Storvoll et al., 2005). We used data from one well log in Ekofisk, as well as regional velocity models in the area (Jerkins et al., 2020), to create a 1D velocity model. Figure 4.18 shows the depth-dependent velocity, as well as the modeled positions of source and receivers. The velocity models were used for two 2D modeling studies: ray-tracing (RT) and finite differences (FD).

The goal of the ray-tracing study (Hovem, 2012) is to verify the arrival times of diving waves for the configuration we observe in the field. The FD modeling, on the other hand, might help us interpret the events observed in the data. FD modeling was performed using a viscoacoustic wave equation implementation (Carcione, 2007; Schuster, 2017). Due to limitations in grid size and computation time, the

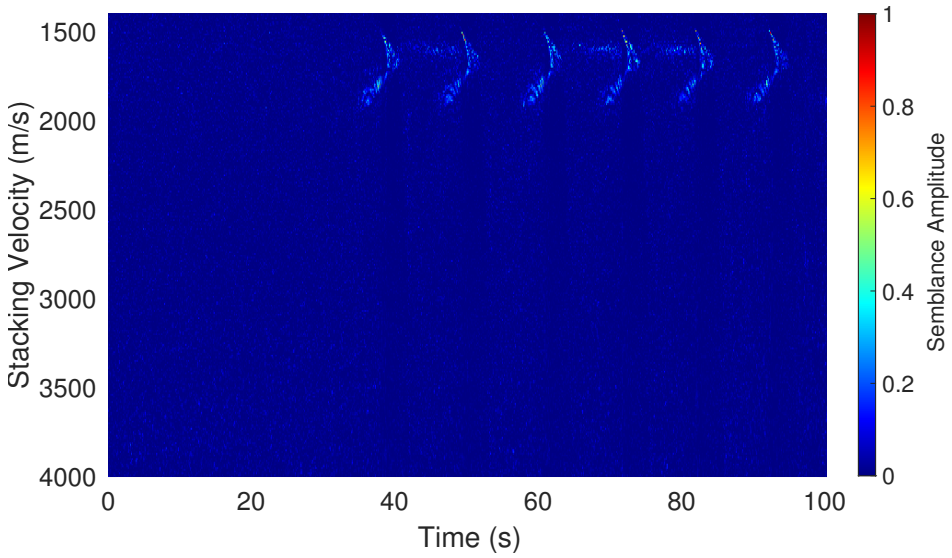

(a) Full bandwidth data

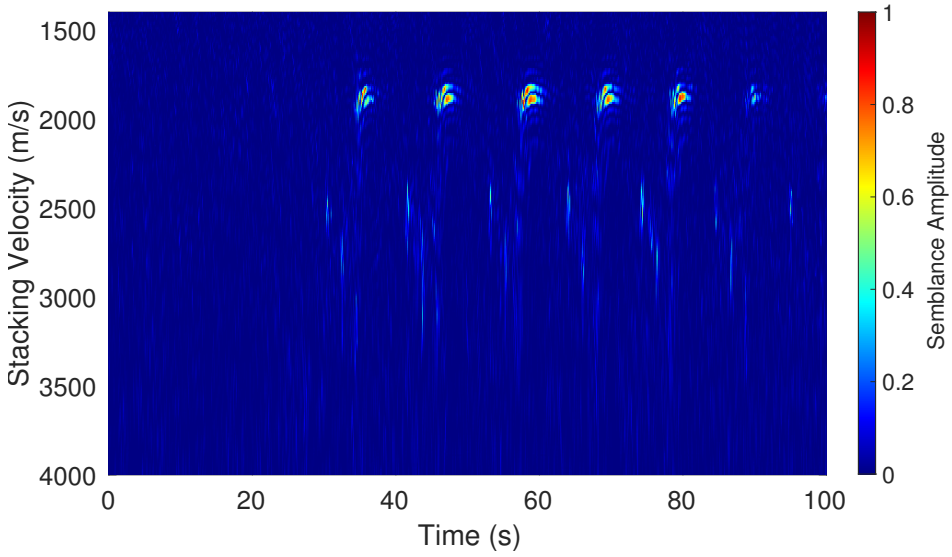

(b) Lowpass-filtered data (8 Hz)

Figure 4.17: Linear moveout semblance of data in Figure 4.4, for full bandwidth data **(a)** and after a lowpass filter at 8 Hz **(b)**. The fast events (LMO velocities between 2500 m/s and 3500 m/s) seen in Figure 4.16c can be identified in panel **(b)**. Every panel is normalized individually.

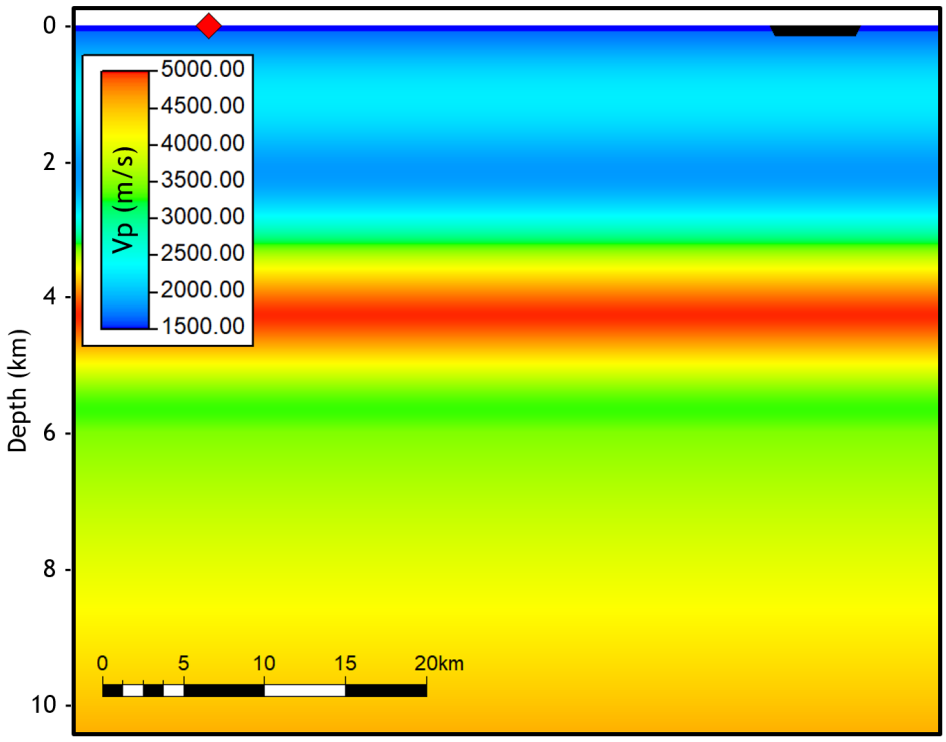

Figure 4.18: Depth-dependent velocity model for ray-tracing and finite differences modeling. Red rhombus is the position of a source at 5 m depth, and black triangles are a line of 100 receivers, separated by 50 m distance, at a depth of 75 m. The model extends down to 20 km depth, but only the first 10 km are shown here. After 6 km depth, the velocity increases with a constant gradient of 0.25 s^{-1}.

wavelet selected for modeling was a Butterworth with a maximum frequency of 100 Hz. The modeled wavefield is registered with a sampling of 4 milliseconds, and the grid size is 5 meters. Density in the sediment layer was obtained from the P-wave velocity, using an empirical equation similar to the one proposed by Gardner et al. (1974), but with different coefficients. For the absorption coefficient, a depth-dependent quality factor Q was used, based on values found in the literature (Carter et al., 2020). The results of both modeling methods will be presented in the Results section.

4.2.7 2D Fourier Transform and Seafloor Velocity Estimation

One last piece of information can be obtained from the analysis of data in the frequency domain. Figure 4.19 shows the 2D Fourier transform, or *f-k* plot, of the data in Figure 4.5. There is a clear set of strong events, which we associate with the

arrival of the energy from Ekofisk. Some of these events only exist after a certain cutoff frequency, as seen in the results of the period equation. For comparison, we plot side by side the *f-k* plot of 7 seconds of recording of “passive" data for the same receivers, acquired 1 week before the survey started in Ekofisk.

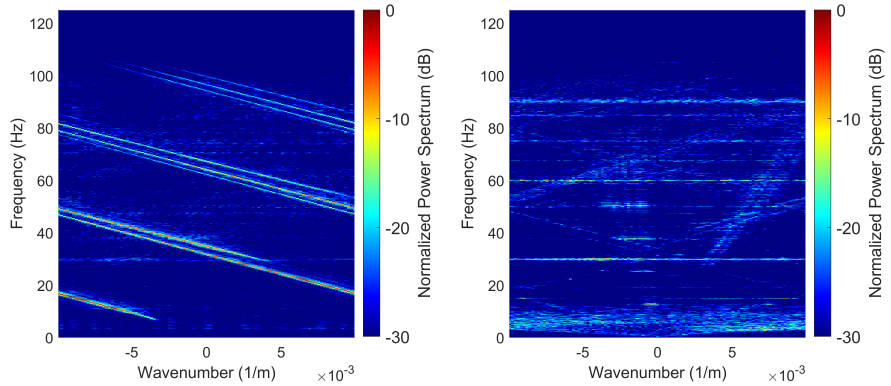

(a) Normalized *f-k* plot of data in Figure 4.5.

(b) Normalized *f-k* plot for data recorded 1 week before the Ekofisk survey started.

Figure 4.19: Normalized *f-k* plots for data recorded in different moments. Plots are normalized independently, with power spectrum on plot **(a)** being about 10 times stronger than the noise recordings on plot **(b)**.

The *f-k* plot of the passive recordings is mostly dominated by low-frequency noise. Still, it is possible to identify what seems to be linear events both for positive and negative wavenumbers, some of which become aliased at about 16 Hz. These events are also candidates to being normal modes propagating in the ocean, as they arrive from both directions in the array: northwest (Ekofisk direction) and southeast (possibly Hod - see Figure 4.3).

Despite showing a nonlinear behavior in phase velocity, the normal modes plot almost as a straight line in the *f-k* domain. Assuming an acoustic two-layer model, we can use the modeled velocities and the *f-k* plots to estimate the velocity α_2 of the second layer, if the other parameters are kept fixed. Figure 4.20 shows an example, with a magnification of Figure 4.19b. The white dots are the points of maximum *f-k* amplitude - one point for each frequency, in the frequencies below 16.5 Hz (to avoid alias), and within a velocity range of 1600 m/ and 2000 m/s, to avoid amplitude of faster and slower events. Once these points are selected, the solutions of Equation 4.1 for several α_2 velocities are tested, and the absolute error between the selected points and the theoretical curve is calculated. The velocity which yields the smaller error is considered the estimation for α_2.

The red line in Figure 4.20 shows this line for a velocity of 1920 m/s, and the magenta line is the phase velocity for our two-layer model, with sediment velocity $\alpha_2 = 1780$ m/s. The procedure described above was applied to longer data recordings, both in passive and active data, and the results will be shown in the next section.

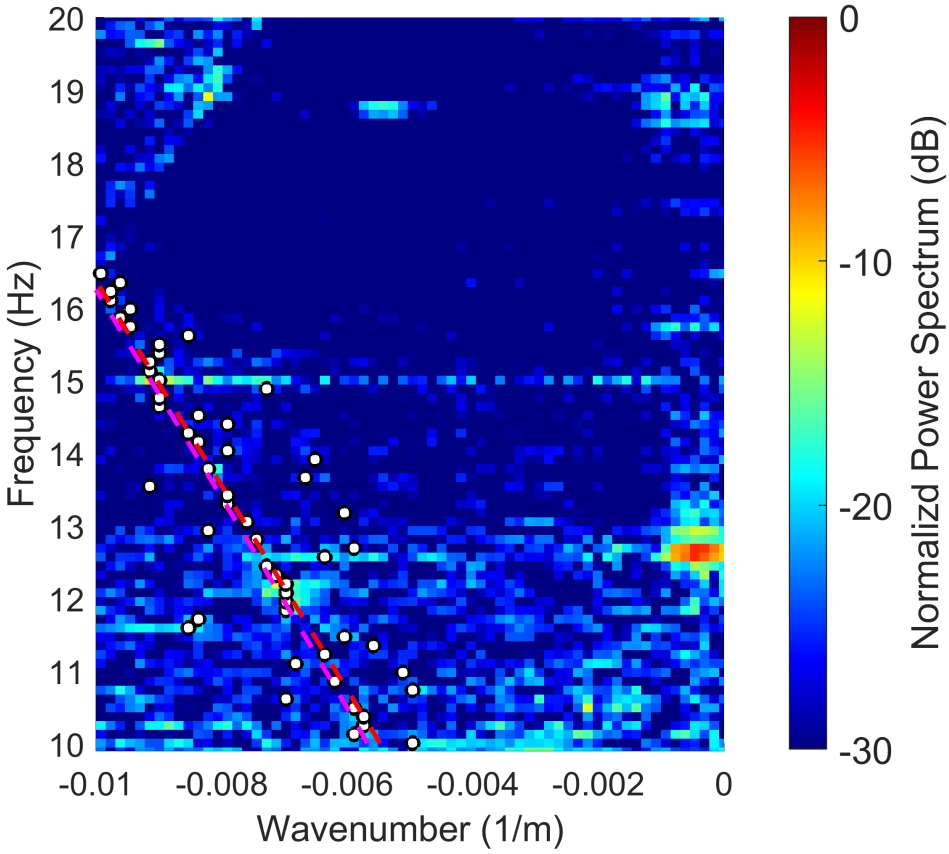

Figure 4.20: *f-k* transform for passive recording. White dots are maxima in amplitude, red dotted line is the modeled phase velocity with best fit, and magenta line is phase velocity for $\alpha_2 = 1780$ m/s.

4.3 Results

We proceed now to discuss the results of the methods mentioned in the previous section. Figure 4.21 shows the results of ray-tracing for the configuration (velocity and geometry) in Figure 4.18, assuming different grazing angles at the source. The several reflections shown in the top panel are the reflections on the seafloor (the free surface was not considered in this plot). There is a hidden zone caused by

velocity inversion, where barely any diving wave penetrates - except the one with a very steep incidence angle, which only returns to the surface at large distances (receivers are positioned in offsets between 35 and 40 km).

The bottom panel of Figure 4.21 shows the travel times for several of those diving waves - each color represents a grazing angle at the source. The modeled events arrive at the first receivers with travel times between 20 and 23 seconds. Compared to about 25 seconds of travel time for the water wave, this indicates that we should expect the diving waves to start appearing in the field data about 3-5 seconds before the water wave. Unfortunately, this is roughly the expected arrival time for the head wave at the seafloor, making it difficult to separate the events on a travel time basis alone.

The time series and spectrograms for trace #50 in the modeled finite differences scenarios are shown in Figure 4.22, where they are compared with the same trace from field data. The y-axis of the time series is the same for both modeled scenarios, and the spectrograms are normalized individually. The blue line in Figures 4.22b and 4.22c marks the exact arrival time of the head wave, and the red lines in Figure 4.22c are the ray-traced times of diving waves from Figure 4.21. The low-frequency event in the two-layers model does not match the head wave time, but the ones in the depth-gradient model are in good match with the diving waves.

Figures 4.23 show the LMO semblances for the modeled scenarios. To facilitate the comparison, the semblance for the first shot of the field data was also plotted in Figure 4.23. The strong semblance of the high-velocity events before two seconds in Figure 4.23c are caused by the very low amplitude of the pre-stacking events, which makes the denominator of the semblance calculation close to zero. All three plots were calculated using full bandwidth data.

Figure 4.24 shows a comparison of the theoretical results for the phase velocities (Figure 4.2) and the *f-k* plots of the field data. Black lines are corrected from an azimuthal arrival angle of 15°. There seems to be an excellent match between modeled velocities and field data.

Figure 4.25 shows the results of the estimation of the seafloor velocity α_2 from 1h of recording - one velocity value is calculated for every 60 seconds of data. Azimuthal arrival angles are 10° for noise coming from NW (black) and 25° for SE (red). The values for the arrival angles were the ones that provided the results with smaller variation - this will be discussed in the next section. The velocity values estimated from the recording of the active survey in Ekofisk were also plotted - these are corrected by an arrival angle of 15°.

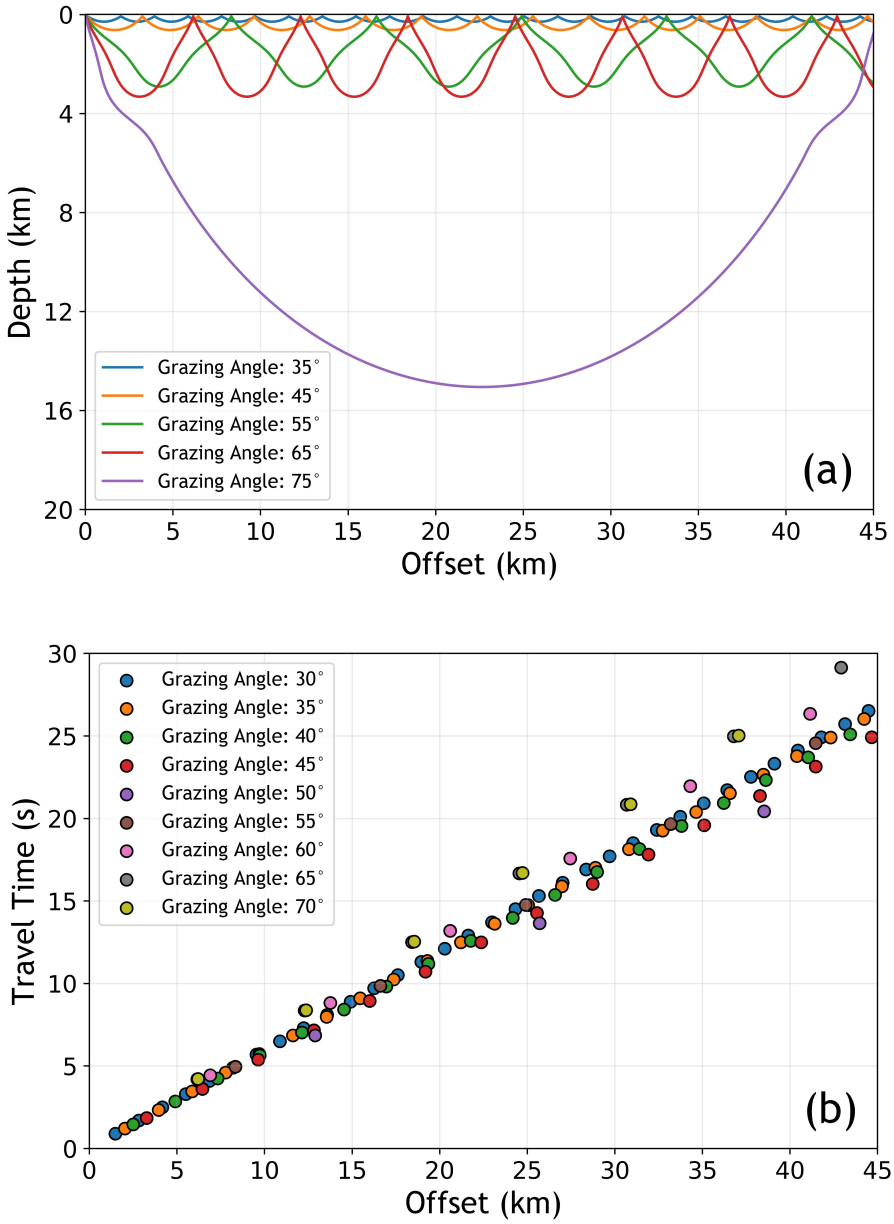

Figure 4.21: **(a)** Raypaths modeled using the velocity model and geometry from Figure 4.18, for several departure angles from the source. **(b)** Travel times estimated from ray-tracing for several angles.

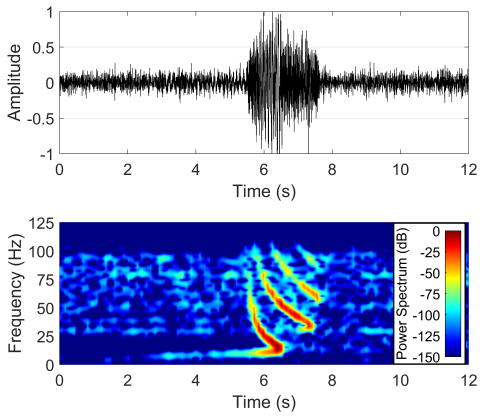

(a) Field Data (same as Figure 4.6)

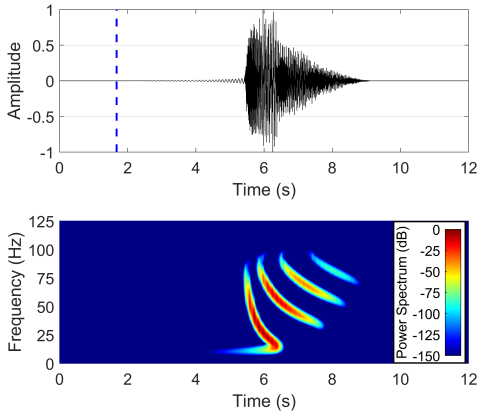

(b) Two-layers velocity model

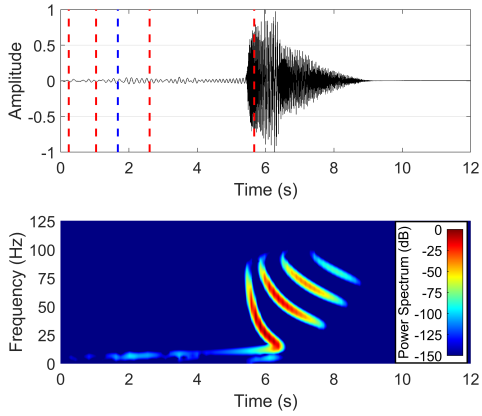

(c) Velocity with depth gradient

Figure 4.22: Time series (top) and spectrograms (bottom) of field data and traces modeled with viscoacoustic finite difference method. Time scale is arbitrary for field data, and was adjusted to ease comparison with modeled traces (for those, source was fired at about t = -19 s). Blue lines are exact head wave arrival, and red lines are diving wave times from Figure 4.21. Plots are normalized individually.

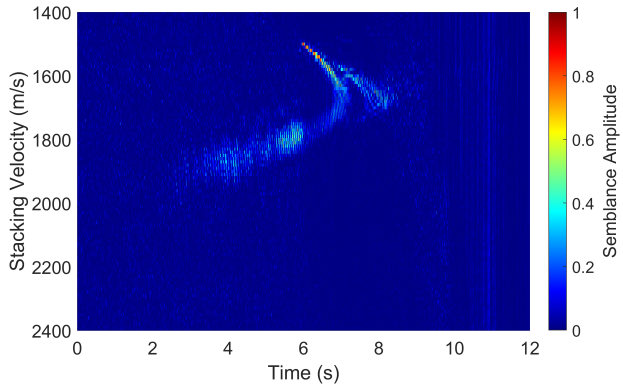

(a) Field data

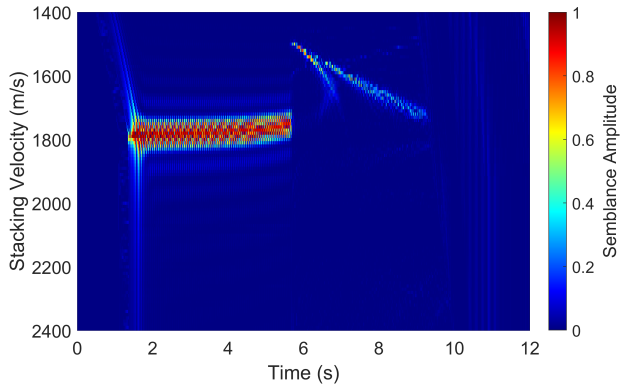

(b) Two-layer velocity model

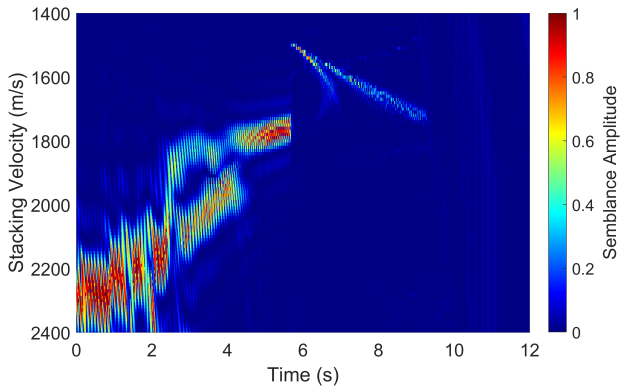

(c) Velocity with depth gradient

Figure 4.23: Linear moveout semblance of field data and modeled scenarios. Time axis on modeled data was adjusted to ease comparisson - source was fired at t = -15 s. Plots are normalized independently.

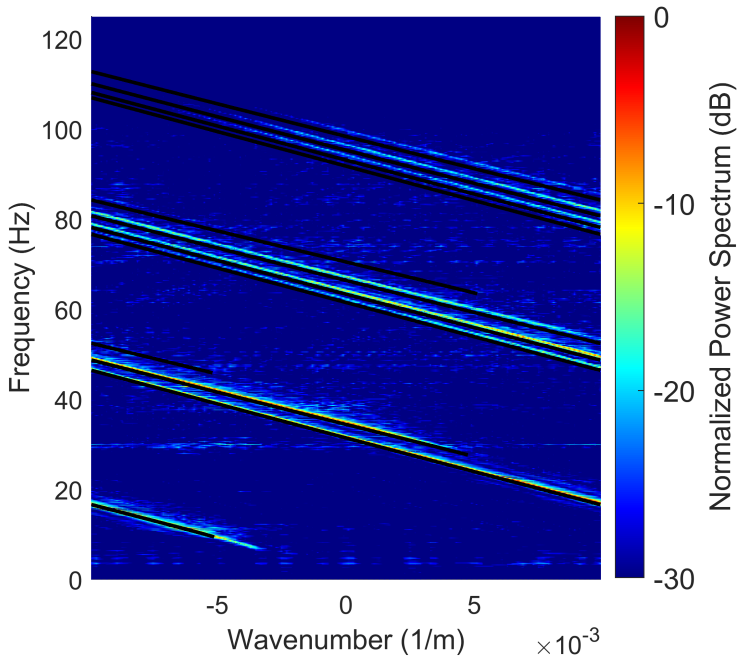

Figure 4.24: Normalized *f-k* plot shown in Figure 4.19a. Thick black lines are phase velocities from Figure 4.2, corrected for azimuthal arrival angle of 15°.

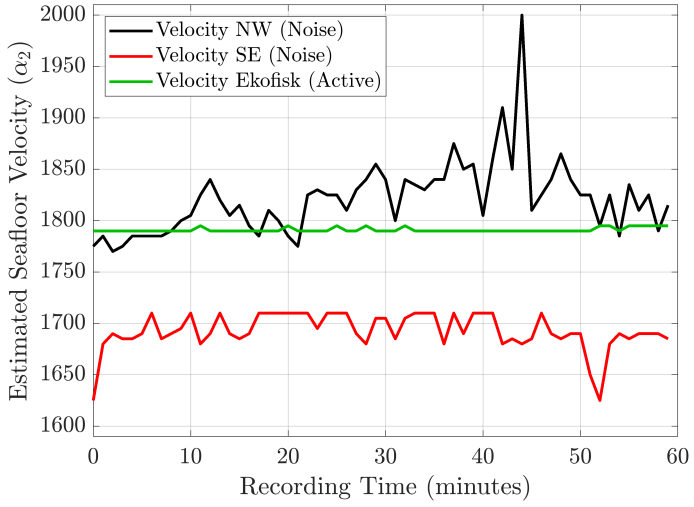

Figure 4.25: Estimated seafloor velocities for 1h of noise recording, for normal modes arriving from NW (black line - assumes azimuthal arrival angle of 10°) and SE (red lines - assumes azimuthal arrival angle of 25°). Green line represents velocities estimated from Ekofisk for the active survey.

4.4 Discussion

4.4.1 Ray Tracing and FD modeling

The modeled travel times and raypaths using a depth-dependent velocity model (Figure 4.21) indicate that, because of the reversion in velocity-depth trend, most of the diving waves are trapped in the shallower 5 km. A part of these waves should arrive at the receiver array a few seconds prior to the normal modes, which is verified in the spectrograms (4.22c) and in the linear moveout semblance (Figure 4.23c) of the data modeled using finite differences. The moveout analysis of the field data also reveals events with faster apparent velocities, which arrive before the normal modes and are consistent during the Ekofisk survey.

The results displayed in Figure 4.22 show that, in the two-layers velocity scenario, the arrival of low-frequency events happens about two seconds before the strong normal modes, while in the field data there are almost 5 seconds of low-frequency events arriving prior to the harmonics. If the depth gradient model is considered, a series of early, low-frequency events appear. When compared to the modeled ray-tracing times, it seems clear to us that these events are originally caused by diving waves, which might also be converted to normal modes and head waves when they reach the water-sediment interface.

To further investigate this hypothesis, we can use the FD modeling to "isolate" the diving waves. This was done by repeating the modeling in the same conditions, but replacing the reflections at the free surface with an absorbing boundary conditions. This way, no trapped mode will exist in the water layer, and the only energy arriving should come from diving waves, the direct water wave, and head waves. Figure 4.26 compares modeled data with and without the free surface reflections. To reinforce the low-frequency events, a lowpass filter at 8 Hz is applied to both seismograms. We can see, in Figure 4.26b, the arrival of earlier, faster events, similar to what is seen in Figures 4.13 and 4.14.

The modeled events shown in Figure 4.21 alternate between reflections at the seafloor (where part of the energy is transmitted to the water, generating more normal modes) and continuous turns after increasing their propagation angles. The reflection coefficient for normal incidence at the seafloor is about 0.3, so after several reflections the amplitude of the wave is severely diminished. That, combined with geometric spreading and strong absorption in the shallow layers, are the probable reasons why these events are quite feeble (although still detectable) both in field and in modeled data.

Despite only showing here the results for the modeled hydrophone seismogram, the particle velocities were also evaluated and compared to the field data. The

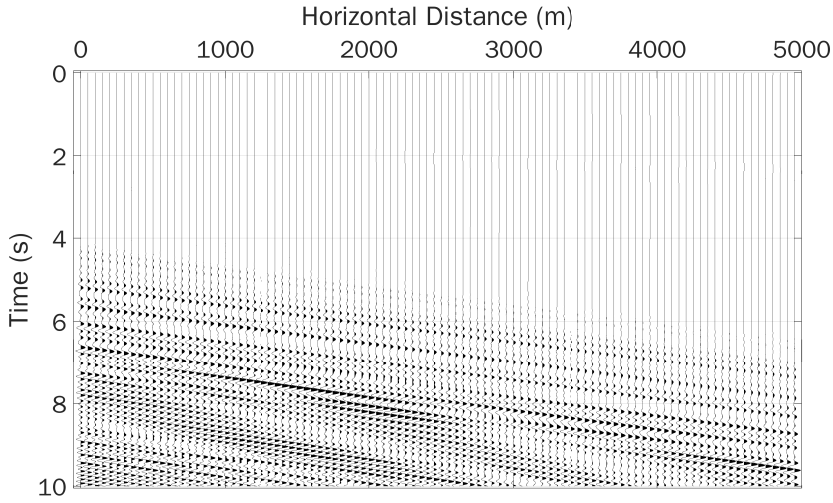

(a) Modeled data, with free surface multiples.

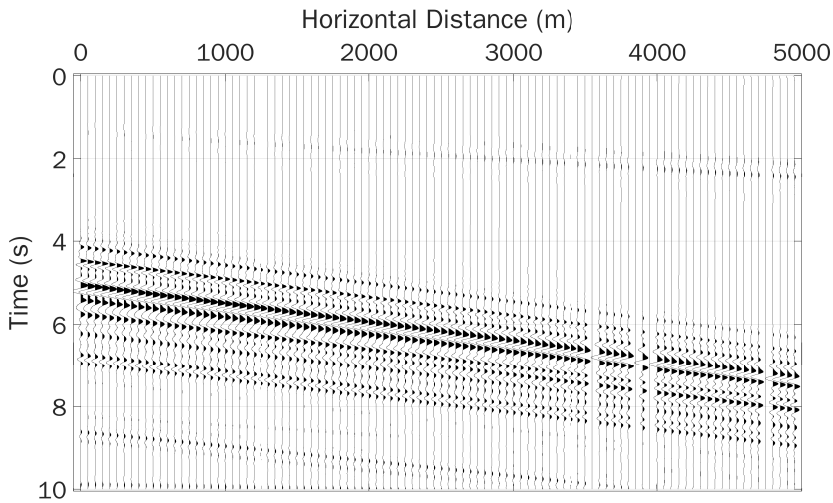

(b) Modeled data, without free surface multiples.

Figure 4.26: Modeled seismograms (scenario with velocity gradient), after application of a 8 Hz lowpass filter. Panel **(a)** includes surface multiples, whereas panel (b) does not.

normal modes have a strong horizontal wavenumber component, and it seemed natural to use the horizontal geophone measurement in the analysis. However, this

component proved to be quite noisy (perhaps due to some cable movement, or some environmental noise caused by the production facilities). All four components of the field data show clearly the arrival of normal modes, but the hydrophone component has the best signal-to-noise ratio in the evaluated data. The vertical and longitudinal geophone components also have a quite good SNR, while the transverse component is significantly poorer (for the normal modes analysis presented here).

Apart from the Ekofisk well log data and the regional velocity model employed, we couldn't verify how is the velocity behavior between Ekofisk and Valhall. The fact that fast events do not appear in the LMO stack of the FD modeling with a two-layers velocity, but appear in the depth-dependent one, reinforces the interpretation that diving waves are the probable nature of these events. Deep reflections are also a candidate for these fast events, since the offset between source and receiver would make the moveout seem linear. Some FD modeling scenarios with a deep reflector were studied, but none of them improved the similarity with the events observed in the field data. The availability of more detailed velocity models would be highly beneficial to the interpretation of these events.

4.4.2 Velocity Estimation in the *f-k* Domain

Figure 4.24 shows the comparison between the events in the *f-k* plots and the modeled phase velocities for the normal modes. The matching between the analytic and field values is significant. As the *f-k* transform reveals the apparent phase velocity, it is necessary to correct for the angle of arrival of the energy, relative to the array orientation.

Figure 4.25 presents the results of velocity estimation using the normal modes in the *f-k* domain, both for the active shooting (green line) and passive recordings (black and red lines). The results obtained with the active survey are quite uniform, because of the higher signal-to-noise ratio of the coherent signal. One advantage of this method is that, for being performed in the *f-k* domain, it does not require precise knowledge of the source position and firing time. However, it is necessary to know the azimuthal arrival angle θ of the wave in relation to the receiver array, as the velocity needs to be corrected by a factor of $\cos\theta$. Since most permanent reservoir monitoring systems have 4C sensors and commonly have arrays in perpendicular directions, this task can easily be automated.

The interpretation of the passive data is more intricate. Despite showing a stable result for the velocity estimation of the active data, 15° was a bad choice for fitting noise coming from the NW direction - 10° provided better results (black line), disputing our interpretation of this being the azimuthal arrival angle of the noise

from Ekofisk. Looking back at Figure 4.3, a smaller arrival angle for the NW energy might indicate that the noise is not coming from Ekofisk, but actually from Eldfisk - or, very likely, a combination of both. Ekofisk might be a busier field, but Eldfisk is significantly closer, which implies higher noise levels.

The azimuth that yields the best velocity estimate from normal modes from SE is 25°. The initial assumption was that the noise came from the Hod field, but an attempt on estimating the seafloor velocity based on the *f-k* plots suggested that the angle providing the smaller variance in velocity was not compatible with that hypothesis. Checking Figure 4.3, 25° is the angle between the selected receiver line and the "void" in the middle of the array, which is the location of most of Valhall's surface facilities. As these are much closer than the Hod field, we believe the facilities' noise dominates the recordings, and the velocity estimation is compromised.

To verify this hypothesis, another receiver line was selected, with a different azimuthal arrival angle from the possible facility noise. The selected line is the third line parallel to the initial one, also in the northern part of the array (Figure 4.3). From the map, we estimate the angle of arrival of the noise from SE as being 6°. This angle might vary along the line, as the approximation of a plane wavefront is likely not valid due to the short distance between source and receivers. Still, the estimated velocity is significantly improved when assuming this premise. Figure 4.27 shows the result of velocity estimation in this line, assuming an arrival angle of 10° for NW and 6° for SE. The SE velocities are now much more stable, and closer to the values estimated from active data (which assume an angle of 12° for this receiver line). This result supports the interpretation that the dominant passive normal modes detected from SE in this line originate in the surface facilities in Valhall, and that they can be used for shallow velocity monitoring. The arrivals from NW show less stable values for the velocity, presumably due to the longer distance from the noise source.

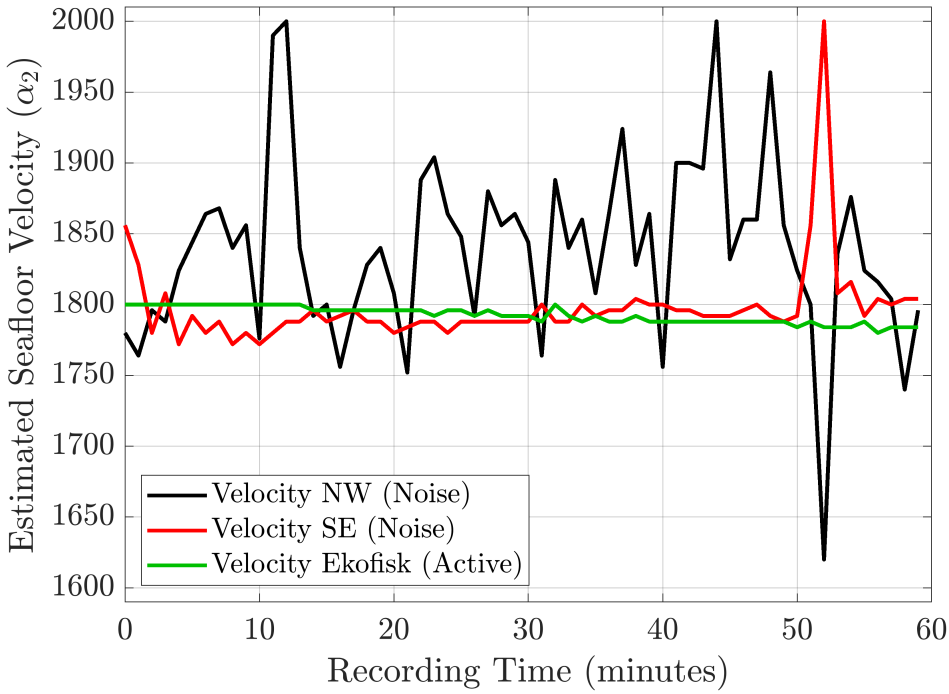

Figure 4.27: Estimated seafloor velocities for 1h of noise recording in an alternative receiver line, for normal modes arriving from NW (black line - assumes azimuthal arrival angle of 10°) and SE (red lines - assumes azimuthal arrival angle of 6°). Green line represents velocities estimated from Ekofisk for the active survey, at an azimuthal arrival angle of 12° for this plot.

4.5 Conclusions

The use of permanent arrays for reservoir monitoring allows for continuous recording in several oil fields. When an active survey is happening nearby, these arrays can be used to estimate the properties of the shallow layers, through the recording of normal modes. We presented a case study in which data is recorded in the LoFS system in Valhall, during an active seismic survey in Ekofisk, more than 30 km away. The data show a clear arrival of at least four normal modes. The analytic solutions of the period equation in a two-layers acoustic model show good agreement with the field data, and were used to estimate the shallow sediment velocities, without the necessity of source position or firing time. The estimation was also performed with noise recordings, yielding similar (albeit less precise) results, and could potentially be used as an alternative method for passive shallow monitoring. Some faster, low-frequency events present in the data are interpreted as a combination of head waves and diving waves. These are well reproduced

with a depth-dependent velocity model using raytracing and viscoacoustic finite-difference modeling, indicating that deep diving waves can be detected at remarkably large distances from their source.

Chapter 5

Water Layer Velocity and Survey Geometry

In this fifth and last chapter, we present the modeling and analysis of synthetic time-lapse data, using parameters similar to those of a Brazilian Pre-salt field. The goal was to investigate how seasonal changes in the sound speed of the water layer affects the quality of offshore time-lapse data. For this, a scenario of ocean bottom nodes (OBN) survey was considered. The uncertainties in source and receiver positioning were also accounted for. The synthetic data were compared in terms of 4D attributes. We believe the results are a first step towards a more robust methodology for time-lapse feasibility studies, which incorporates imaging uncertainties and allows us to understand the contribution of each element that could affect the 4D seismic image quality.

A journal paper about the work presented in this chapter, with the title "**Analysis of water velocity changes in time-lapse ocean bottom acquisitions - a synthetic 2D study in Santos Basin, offshore Brazil**", was published in the Journal of Applied Geophysics.

5.1 Introduction

A time-lapse seismic project aims at reproducing, as closely as possible, all the parameters of baseline and monitor surveys, including the source-receiver raypath. In offshore surveys, a part of the seismic wave travelpath happens inside the water layer. This layer is subject to seasonal velocity variations (Simao, 2009) which, despite low in absolute value, have some impact on the imagining process (Han et al., 2012). This effect is magnified in areas of deep water, where the water

column can extend beyond 2 km deep. In such environments, the ability to reproduce, or correct for, different velocities in the water layer becomes essential to achieve better repeatability. Such corrections are crucial for reservoirs with faint 4D signals, like the Pre-salt reservoirs in Santos Basin, in Brazilian deep waters (Cypriano et al., 2019; Kiyashchenko et al., 2020b).

The purpose of the work presented here is to quantify the subtle effects of water velocity changes in time-lapse seismic imaging. To achieve this goal with a methodology that can be reproduced in other fields, synthetic seismic data were modeled with a 2D finite differences (FD) algorithm. High-resolution elastic property models were created for the baseline and monitor calendar times, and several combinations of water layer velocities and geometry uncertainties were investigated. The time-lapse effect was analyzed using 4D amplitude sections. Finally, the normalized root mean square attribute (NRMS) was calculated, and the results were compared to quantify which parameters are more relevant in disturbing the interpretation of the time-lapse data.

5.2 Theory and Method

In this section, we discuss our assumptions in terms of model building, modeling algorithm, and uncertainty in survey geometry. We also present some background on the area of study.

5.2.1 Background and Available Data

The area selected for this study is located in the Santos basin, a Brazilian offshore rift basin formed during the south Atlantic opening. It is an oil field with carbonate reservoirs of Aptian age, deposited under a thick salt layer, which acts as a seal (Carminatti et al., 2008). The water depth in the area of study ranges from 1800 m to 2200 m. Due to confidentiality constraints, the data presented in this work were stripped of their names and geographical locations.

Figure 5.1 shows a depth section extracted from the 3D seismic in the area of study. The horizons mapped in green are the top and base of the salt layer. The salt thickness varies expressively in the area, and is not homogeneous, as can be seen by the internal reflections - this heterogeneity makes model building and imaging in the area quite challenging (Maul et al., 2019a).

The available seismic data in the area were reverse time migrated, and the velocity model was also made available for this study, together with the elastic log suite of some wells, and a 3D reservoir model with both static (effective porosity, electrofacies, mineralogy) and dynamic (fluid saturation, pore pressure) properties. Figure 5.2 shows both the migration velocity and the porosity model in the same

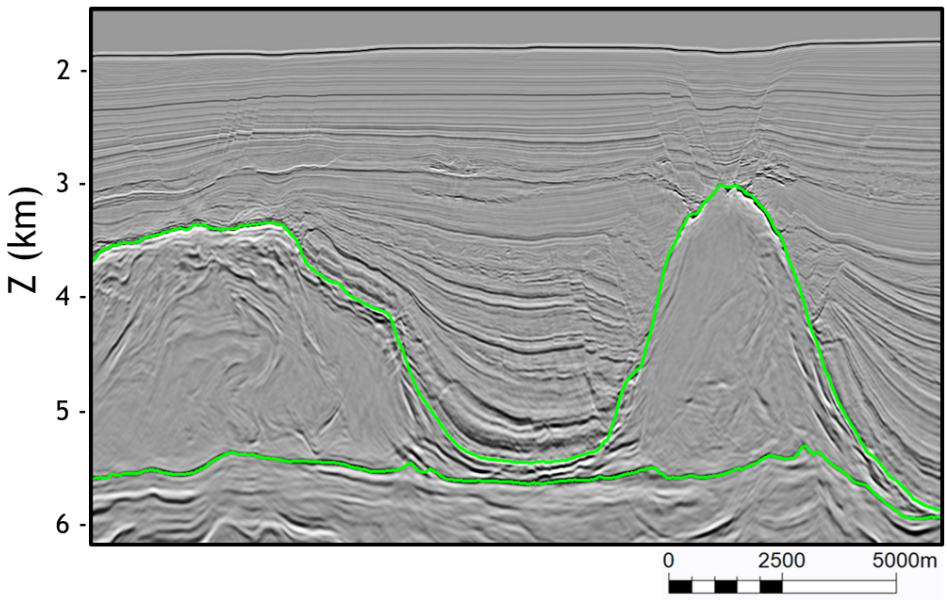

Figure 5.1: Seismic section in the study area. Green lines represent the top of salt (ToS) and base of salt (BoS) horizons.

section of Figure 5.1.

The velocity model shown in Figure 5.2a is quite smooth both above and below the salt layer, and therefore not adequate for finite-difference modeling - because of the low-velocity contrast between layers, it will not generate the reflections observed in the seismic section. The adequate solution consists of a combination of sophisticated wave equation modeling (Schuster, 2017) and elastic property models that show some contrast. Using the available data and our conceptual knowledge of the area of study, high-resolution models of compressional and shear velocity, as well as density, were built. The next two sections describe this step.

5.2.2 Water Layer Velocity

The physics of sound propagation in water is a rich field of research (Hovem, 2012). The speed of sound in seawater is a complex function of different parameters like water temperature, salinity, and pressure (Batzle and Wang, 1992). As these variables commonly show a complex, time-varying distribution over large areas, the proper structure of the water velocity is difficult to incorporate into a seismic processing workflow - historically, it has been common practice to use a constant velocity in the water layer for offshore seismic imaging. This practice has evolved into steps such as water statics correction and depth-dependent water

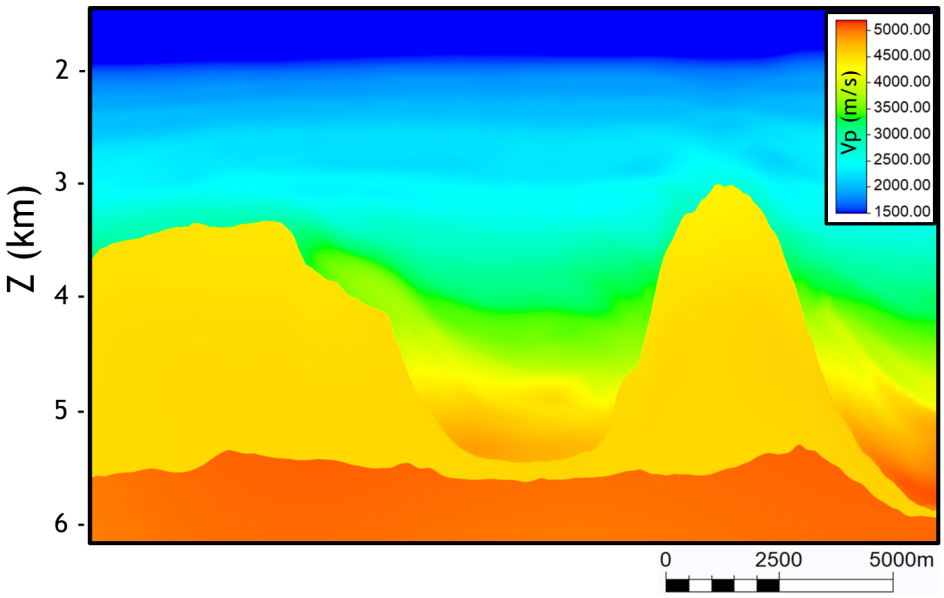

(a) Migration velocity

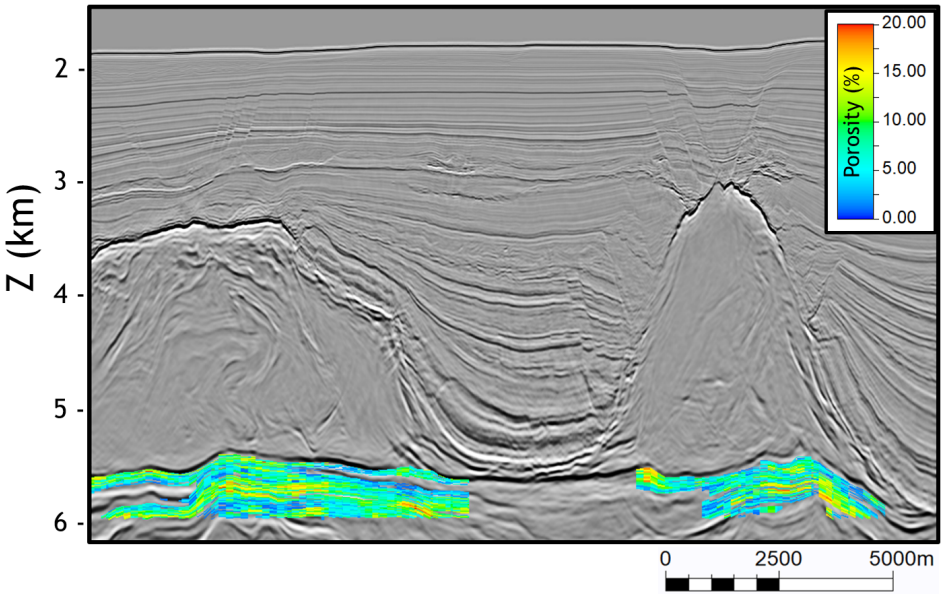

(b) Effective porosity model

Figure 5.2: Some available data in the area of study: migration velocity **(a)** and effective porosity, from a 3D geological model **(b)**.

layer velocity (MacKay et al., 2003; Wang et al., 2012), especially in deepwater environments.

The effects of not taking into account the correct water velocity are magnified in deep offshore surveys, where the cumulative effect over longer paths in the water leads to significant inaccuracies between the modeled and "real" behavior of the seismic wavefield (Han et al., 2012). In the case of time-lapse seismic surveys, seasonal variations in the water layer can have a significant impact on the water velocity (Vesnaver et al., 2003). Despite the many available solutions for correcting the time-shift caused by velocities varying from baseline to monitor surveys, the different raypaths in each vintage decrease the repeatability, and interfere with our ability to isolate the 4D effect in the reservoir.

In the latest seismic acquisition in our area of study, daily measurements of water velocity, water salinity and water temperature were taken in uniformly distributed sampling points of the area. As the survey took about one year to complete, 12 months of the velocity profiles can be created. Figure 5.3a shows the median water velocity profiles for each month. To model a seasonal variation in this profile, two months were selected for representing the water velocity scenarios in our time-lapse modeled acquisitions: April (baseline) and October (monitor). These two profiles are highlighted in Figure 5.3b.

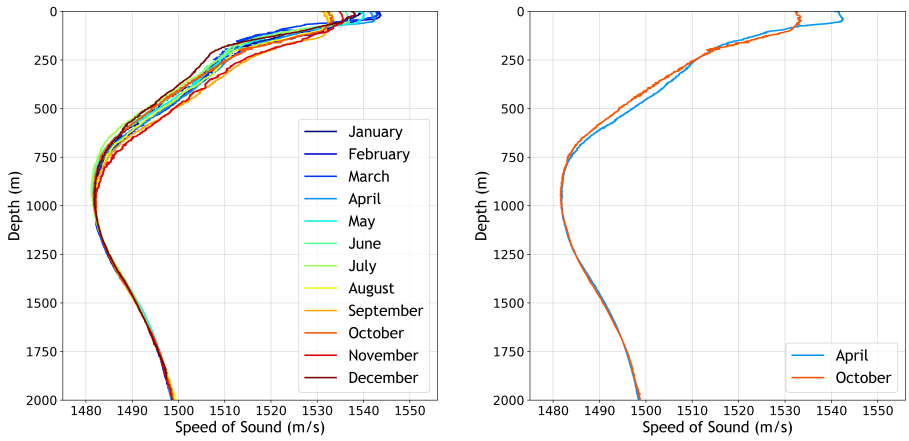

(a) Median speed of sound - all months

(b) Speed of sound used in this study

Figure 5.3: Measurements of the speed of sound profiles in the area of study. Values presented are a median for each month, with one measurement per day. Panel **(a)** shows the measurements for the whole year, and panel **(b)** highlights the profiles selected for modeling the baseline (April) and monitor (October) scenarios.

Despite the variations in temperature and salinity, the water layer density will be kept constant in both vintages, at a value of 1.00 g/cm^3. We now proceed to detail the methodology to construct the elastic property models in the sediments.

5.2.3 Property Model Building for Sediments

The building of the high-resolution property models in the sediments can be separated into three regions: post-salt overburden, salt layer, and reservoir.

For the post-salt sediments, an internal Petrobras workflow was used. The workflow starts with an AVO inversion using the Fatti approximation to obtain P- and S-wave reflectivities (Fatti et al., 1994a). The resulting reflectivities are integrated into pseudo-impedance volumes, containing the middle and high ends of the frequency spectrum. Using an empirical equation for the density-velocity dependence, volumes of pseudo-Vp, Vs and density are obtained. To account for the low frequencies, the P-wave migration velocity can be used. For that, it is also necessary to use empirical equations to derive low-frequency density and S-wave velocity. These empirical equations were obtained from the well logs in the area, and they are similar to the broadly used results published by Gardner et al. (1974) and Greenberg and Castagna (1992), but adjusted with different coefficients. Once the low-frequency property models are obtained, they are combined with the results of the AVO inversion to obtain full-band property cubes, which are adequate to be used in FD modeling.

In the salt layer, a slightly different approach was employed, based on the use of seismic inversion for salt characterization (Teixeira and Lupinacci, 2019). A model-based acoustic inversion, which assimilates information from both seismic and well logs, provided a volume of acoustic impedance (I_p) for the salt, which already contains the low-frequency information. Equally to what was done for the post-salt, well log-derived empirical relations were applied to this acoustic impedance volume, and volumes of velocities and density were obtained. Although similar to the workflow employed in the post-salt section, the use of acoustic impedance instead of velocity for salt characterization has over time delivered more consistent results for this area (Maul et al., 2019b), and hence this approach was selected.

The construction of the property model in the reservoir layers is more intricate. Because this is the layer that will undergo the pressure- and fluid-induced changes between baseline and monitor vintages, not only the elastic properties need to be established, but also how they change under the different reservoir conditions - namely, different fluid saturations and pore pressures. The connection between pore pressure/fluid saturation and elastic properties is obtained through rock phys-

ics, and hence a petroelastic model (PEM) was built.

The most common model for understanding the behavior of fluid-filled rocks under different stresses is Biot's poroelastic model (Biot, 1941). Briefly, Biot's assumptions are that rocks are porous and permeable (allowing for fluid movement and pressure equalization), linearly elastic, homogeneous, and isotropic - the model was later extended to handle anisotropy as well (Biot and Willis, 1957). Biot's results can be used to calculate the compressibility of rock under different fluid contents. This result, known as the Biot-Gassmann equation (Gassmann, 1951), is expressed in Equation 5.1. Through it, one can obtain the P-wave velocity V_p of a rock for different pore fluid properties. To do so, it is necessary to know the density (ρ) of the rock matrix and fluids, the rock porosity (φ), the bulk modulus of the rock matrix (K_{ma}), the bulk modulus of the dry rock frame (K_{dry}), the bulk modulus of the fluid in the pore space (K_{fl}), and the shear modulus of the rock frame (μ) - see Section 1.1.1.

$$\rho V_p^2 = K_{\text{dry}} + \frac{4}{3}\mu + \frac{\left(K_{\text{ma}} - K_{\text{dry}}\right)^2}{K_{\text{ma}}\left(1 - \varphi + \varphi\frac{K_{\text{ma}}}{K_{\text{fl}}} - \frac{K_{\text{dry}}}{K_{\text{ma}}}\right)} \tag{5.1}$$

The rock properties used in Equation 5.1 were obtained from well logs, calibrated by laboratory ultrasonic tests and analysis of rock mineralogy. The density was obtained by averaging the density of the rock matrix (ρ_{ma}) and fluid density, weighted by the porosity.

There are in principle three fluids in the pore space: brine, oil and gas. The hydrocarbon properties were obtained via Pressure-Volume-Temperature (PVT) analysis of sampled reservoir fluid, while the brine properties were calculated using the results published by Batzle and Wang (1992).

In this study, no effect of the pore fluid on the dry rock properties (K_{dry}, μ and φ) was considered. That means that we disregard, for example, chemical interactions between rock and fluid that could weaken the rock frame. It is also assumed that porosity is constant - this hypothesis is supported by geomechanical modeling for the time frames selected for the study. For the dry rock properties, the results of laboratory tests on core samples were used to determine the relation between K_{dry} and μ and the effective pressure.

Following the steps described above, the information in the reservoir model was used to generate a 3D grid with values of P- and S-wave velocities and density for all the calendar times for which fluid saturation and pore pressure are available. This information is limited to the reservoir layers, and needs to be combined with

the previous results of post-salt and salt models in order to obtain a full property model of the area of study.

Table 5.1 compiles the sources of information used in each part of the model, and Figure 5.4 shows the final models used for forward seismic modeling in this study, for the baseline scenario. The monitor models are identical to the baseline in the post-salt sediments and salt layer, but not in the reservoir, where the properties change due to production, nor in the water layer. Figure 5.5 shows changes in reservoir pore pressure and fluid saturation, as well as relative P- and S-wave velocities and density between the monitor and baseline surveys.

Table 5.1: Summary of rules used to build the elastic properties models for FD seismic modeling.

Layer	P-wave Velocity (V_p)	S-wave Velocity (V_s)	Density (ρ)
01 - Water	Variable (Figure 5.3)	0	1.00 g/cm^3
02 - Post-salt sediments	Velocity + AVO	Empirical relation $V_s(V_p)$	Empirical relation $\rho(V_p)$
03 - Salt	Empirical relation $V_p(I_p)$	Empirical relation $V_s(I_p)$	Empirical relation $\rho(I_p)$
04 - Reservoir	Petroelastic model	Petroelastic model	Petroelastic model

5.2.4 Acquisition Geometry

Besides environmental conditions and water columns velocity changes, the quality of time-lapse projects is highly affected by the repeatability of seismic measurements. Because nodes need to be deployed and retrieved for every acquisition program, the receivers' positions are not entirely repeatable - there is some deviation between the position of the nodes in the baseline and monitor vintages. The same is valid for the sources' positions, since the most common offshore seismic sources (airguns) are towed behind a boat, and hence prone to difficulties in repeating the shot position of a legacy survey. Because of that, different positioning of sources and receivers was also considered in our analysis. Starting from a parametrization of 50 m source spacing and 500 m receiver spacing (the standard parameters for Brazilian Pre-salt prospects), the non-repeatability in these variables is modeled according to the hypothesis below:

Uncertainty in source position Assuming that the source depth is maintained fairly constant during the survey, the deviations from the planned shot positions are inherently 2D, as they are usually dominated by local currents slanted with respect to the navigation direction. In this study, due to 2D approxima-

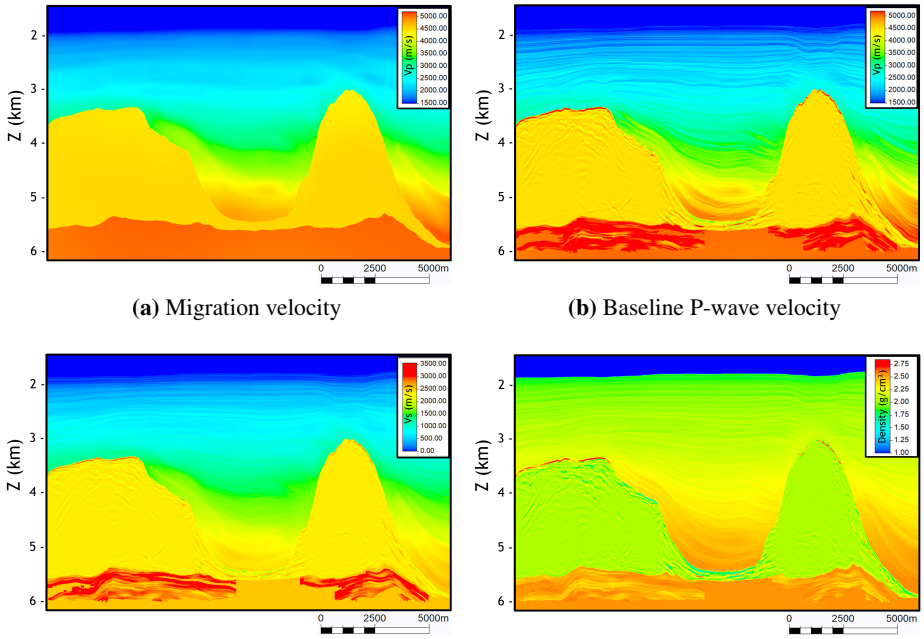

(a) Migration velocity

(b) Baseline P-wave velocity

(c) Baseline S-wave velocity

(d) Baseline density

Figure 5.4: Property models used for migration (all vintages) and forward FD modeling (baseline vintage).

tion, source position deviation from a regular grid was modeled as a random variable following a normal distribution of zero mean, and two scenarios for standard deviation: 0 (perfect repeatability) or 5 m. That means that we start with a regular shooting grid of 50 m spacing, and every shot position is "perturbed" according to the selected standard deviation. These assumptions are the result of the statistical analysis of previous OBN acquisitions in the area of interest.

Uncertainty in receiver position The most common geophysical sensor for ocean bottom surveys are Nodes, typically comprising 3 orthogonal geophones (or accelerometers) and one hydrophone. In this study, the non-repeatability effect considered on the receiver side is mispositioning between baseline and receiver surveys. Like in the source position, the non-repeatability for the receiver is modeled as a random variable with normal distribution of zero mean and standard deviations of 0 (perfect repeatability) or 5 m. These numbers are also based on an analysis of previous nodes surveys in the study area.

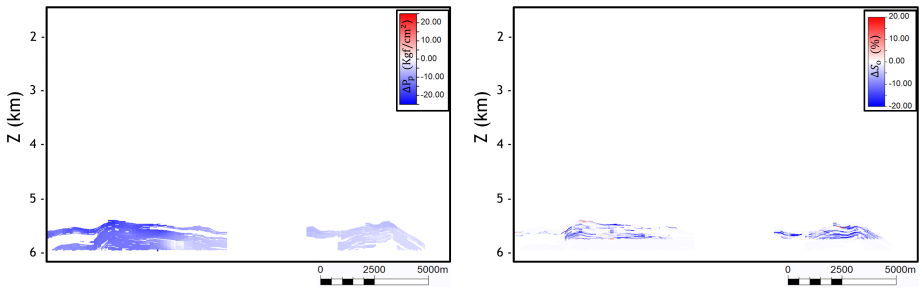

(a) Change in pore pressure

(b) Change in oil saturation

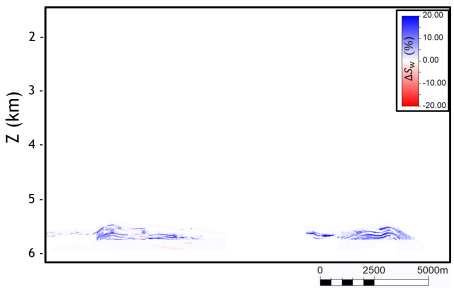

(c) Change in water saturation

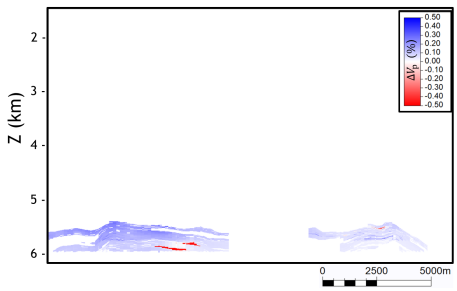

(d) Relative change in V_p

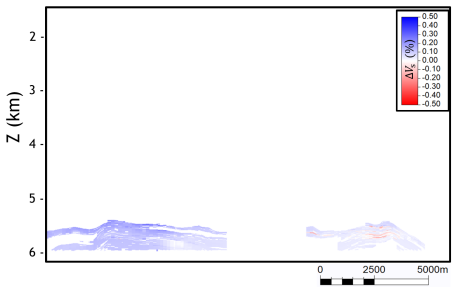

(e) Relative change in V_s

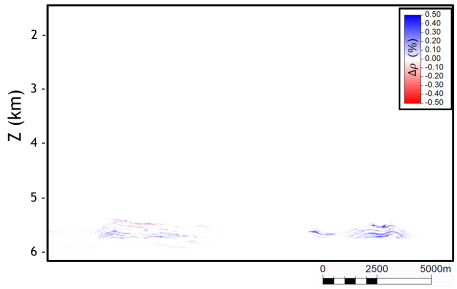

(f) Relative change in ρ

Figure 5.5: Modeled changes between baseline and monitor vintages. Changes are calculated using monitor minus baseline.

Figure 5.6 illustrates the implementation of source and position deviations, with 5 m uncertainty in both source and receiver positions - notice how neither spacing remains regular. The lack of regularity itself is not a problem for 4D repeatability, but the inability to reproduce the same geometry is. Hence, the geometry scenarios are created by starting with a regular grid and disturbing it using a random deviation, both for source and receivers. This process is performed both for baseline and monitor surveys. Since the position changes in sources (dS) and re-

ceivers (dR) from baseline to monitor are the difference between two zero-mean, normally-distributed random variables, they also follow a normal distribution with zero mean, but a standard deviation increased by a factor of $\sqrt{2}$ (Figure 5.6c).

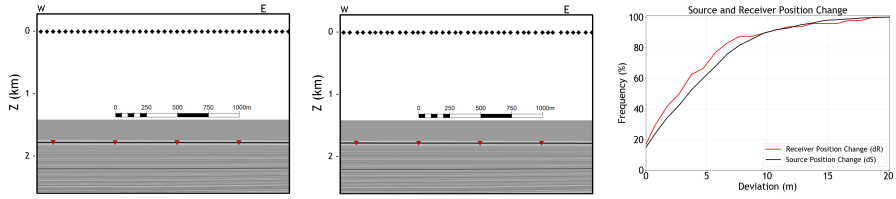

(a) Regular grid **(b)** Perturbed grid **(c)** Cumulative distribution of misfit

Figure 5.6: Comparison of regular (**a**) and perturbed (**b**) grids, applying a normally-distributed perturbation to both sources and receivers. Black diamonds represent the sources (at 8 m depth), and red triangles are the receivers (at the sea bottom). Panel (**c**) shows the cumulative distribution of the misfit for receivers (dR - red) and sources (dS - black) between baseline and monitor.

Following those assumptions, two realizations were independently generated for sources and receivers. We will use the mnemonics S1 and R1 for the positions of sources and receivers in realization 1, and S2 and R2 for realization 2. The baseline vintage is always modeled with the geometry S1R1, and the geometry of the monitor vintage can vary. There are four possible geometry combinations, described below:

Perfect Repeatability (S1R1-S1R1) Both sources and receivers positions are kept the same for baseline and monitor surveys, i.e., the perturbed (non-regular) geometry of the baseline survey is repeated for the monitor. This scenario is used as a benchmark.

Non-repeatable Receiver (S1R1-S1R2) Sources are kept in the same positions in baseline and monitor surveys (same realization - S1), but the receiver positions change (R1 on baseline and R2 on monitor). The aim of this scenario is to isolate the effect of receiver non-repeatability. It can also be interpreted as an OBN field experiment in which, despite the uncertainty in receiver positioning, the dense shooting grid allows for reconstruction of a regular source grid, leading to perfect repeatability on the source position between baseline and monitor vintages.

Non-repeatable Source (S1R1-S2R1) Sources are in different positions in baseline and monitor surveys (different realizations - S1 for baseline, S2 for monitor), but the receivers are repeated (same realization - R1). The purpose of

this scenario is to isolate the effect of source non-repeatability. It can also be thought of as a permanent reservoir monitoring (PRM) geometry, where the receivers are perfectly repeated in the baseline and monitor surveys, but there is some uncertainty in source position.

Non-repeatable Geometry (S1R1-S2R2) The whole geometry is different between acquisitions (different realizations for sources and receivers positions - S1R1 and S2R2). It is the situation that is closest to an ocean bottom nodes (OBN) field experiment, if no improvement can be achieved in the source regularization during processing.

The four geometries described above, together with the property models, are the inputs for the FD seismic modeling and migration steps, which we will detail in the next section.

5.2.5 Finite Difference Seismic Modelling and Imaging

Forward modeling was performed using an implementation of the elastic wave equation (Carcione, 2007; Schuster, 2017). The wavelet selected for modeling was a Butterworth type ("spike") with a maximum frequency of 50 Hz. The modeled wavefield was registered with a 4 milliseconds sampling, and the grid size was 5 m, both in the inline direction and in-depth (for the 2D modeling) - the grid size is not an impediment to having source and receiver uncertainties smaller than 5 m (Hicks, 2002). Since the number of receivers is one order of magnitude lower than that of sources, reciprocity was used, and the receiver positions were treated as sources during the seismic modeling and migration process. This was done purely for practical reasons and in the text we refer to sources and receivers without the reciprocity principle for the hydrophone measurements.

Baseline forward modeling was performed using the properties models which include water velocity from April (Figure 5.3b), reservoir properties from the baseline date, and only for the geometry S1R1.

Monitor forward modeling was performed using the properties models which include water velocity from October (Figure 5.3b) and reservoir properties from the monitor date. It was performed four times, for the geometries S1R1, S1R2, S2R1, S2R2.

The synthetic seismograms were directly used as input for a reverse time migration (RTM), performed with the same migration velocity used in the field data (Figure 5.2a), except for the water layer velocity - for this layer, two scenarios were considered:

I. **Fixed water velocity** In this hypothesis, both the baseline and monitor vintages were reverse-time migrated with the smoothed velocity model shown in Figure 5.2a, and the same water velocity used in the baseline vintage was kept for the monitor. This is the "worst-case scenario" for the water layer migration velocity, where no correction is applied prior to migration - only a post-stack time-shift correction, based on cross-correlation, was applied (see next section). This can be interpreted as a lower bound on repeatability.

II. **Variable water velocity** In this hypothesis, each vintage was migrated with a velocity that includes the same water velocity used for the respective forward modeling. This is the "best-case scenario" for the water layer migration velocity, where we are able to incorporate the velocity changes in the migration velocity itself, and could be interpreted as an upper limit on repeatability for scenarios with 4D water velocity changes.

With exception of the water layer, the same migration velocity was used for both vintages. Prior to migration, a mute on the direct wave was applied - other than that, no other pre-stack processing routine, like 4D binning or cross-equalization, was applied. The data were modeled without source or receiver ghosts, and only the downgoing wavefield was migrated for the analysis presented in this work.

When we consider the different geometry and water velocity scenarios, only one single scenario was modeled and imaged for the baseline vintage, whereas 8 monitor scenarios were considered. These combinations are summarized in table 5.2. Modeling and imaging so many scenarios were possible only because of the implementation of the FD routines on graphic cards (GPUs). With this resource available, the full cycle (modeling and imaging) takes only a few minutes for 2D sections, unlocking our ability to simulate a broad set of scenarios.

5.2.6 Time-lapse Amplitude, Time-Shifts and NRMS

The quantitative metric selected in this study to evaluate the quality of the time-lapse data was the normalized root mean square (NRMS), whose formula is shown below:

$$\text{NRMS} = 200 \times \frac{\text{RMS}_{\text{Monitor - Baseline}}}{\text{RMS}_{\text{Baseline}} + \text{RMS}_{\text{Monitor}}} \tag{5.2}$$

There is some discussion in the literature about the use of NRMS as a repeatability metric, particularly concerning data of different frequency content (Lecerf et al., 2015) or in the occurrence of time-shifts (Cantillo, 2012). To circumvent those discussions, we chose to model all scenarios with the same frequency content, and to calculate NRMS only after the time-shift correction was applied. The

Table 5.2: Summary of possible combinations of reservoir properties, water layer velocities and imaging velocities. Highlights in blue represent the cases that were modeled and imaged.

Vintage	Water Layer Velocity		Geometries			
	Modeling	Migration				
Baseline	April	April	S1R1			
Monitor	October	April	S1R1	S1R2	S2R1	S2R2
Monitor	October	October	S1R1	S1R2	S2R1	S2R2

NRMS was calculated around the top of salt (ToS) and 100 m below the base of salt (BoS), using a window of 40 meters (9 samples). To avoid degradation of the NRMS calculation with the actual 4D signal (which was modeled as happening below the base of salt), we independently modeled a set of "monitor" vintages in which the property models are the same as the baseline vintage - only the geometry and the water layer velocity changes between the surveys. We believe that the NRMS calculated with this hypothesis should be the fairest one to compare the different scenarios, since it measures only the non-repeatability effects. For the 4D amplitude plots shown in the Results section (Figure 5.9), the property models of the monitor vintage were used, so the calculated attributes are compatible with the expected result from a field experiment.

For time-shift computation, the migrated depth images were converted to time using the same velocity model adopted in the RTM. Then, time-shifts were computed by finding the lag associated with the maximum cross-correlation value between monitor and baseline data, on a trace-by-trace basis ($\Delta t_{4D} = t_{\text{Monitor}} - t_{\text{Baseline}}$). The cross-correlation was computed in a 128 ms moving window, with steps of one sample (4 ms). To obtain the 4D amplitude, it is necessary to first match the different vintages in time. This was done by applying the calculated time-shifts to the monitor data, and then subtracting the baseline data from it. The 4D amplitudes ΔA_{4D} are given by $\Delta A_{4D} = A_{\text{Monitor}} - A_{\text{Baseline}}$.

The color convention used for time-lapse amplitudes in this study follows the standards proposed by Stammeijer and Hatchell (2014), with warm colors rep-

resenting *softening* and cold colors representing *hardening*.

5.3 Results

Figure 5.7 shows a comparison of some modeled seismograms (receiver gathers) of the hydrophone component (pressure). All plots were generated for the same receiver, but for different configurations. Figure 5.7a is from the baseline scenario. Figure 5.7b is the time-lapse seismogram in the scenario of perfect geometry repeatability (S1R1-S1R1) and if there were no water velocity changes. Figure 5.7c is the time-lapse with perfect geometry repeatability (S1R1-S1R1), but with water velocity changes, and Figure 5.7d considers both water velocity changes and different positions for sources and receivers (S1R1-S2R2). No random noise was added to those seismograms, and no time-shift was applied prior to subtraction to obtain the 4D seismograms. To ease visualization, the 4D seismograms have tighter color scales.

Figure 5.8 compare a migrated depth section for the 3D field data (same as in Figure 5.1) and for the 2D migrated synthetic data in the baseline scenario. The similarity is striking.

Figure 5.9 shows 4D amplitude data (time-shifted monitor minus baseline) for the modeled scenarios. In the plots, “incorrect water velocity” indicates that the monitor vintage was migrated with the water velocity of the baseline vintage, and “correct velocity” means that the same water velocity of forward modeling was used to image the monitor vintage. In all plots, post-stack time-shift was calculated and applied to the monitor data, prior to subtraction to calculate the 4D amplitude. The color scale is 20 times tighter than that of Figure 5.8b. Figure 5.10 shows the same Figures, but with a zoom in the reservoir level. Table 5.3 compiles the values of NRMS calculated for all the modeled scenarios.

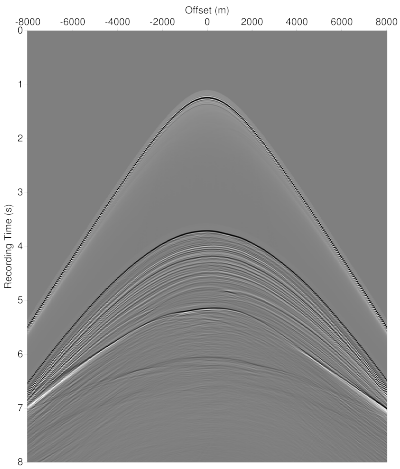

(a) Baseline receiver gather

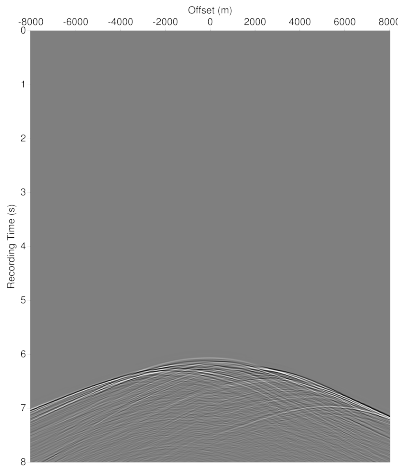

(b) 4D receiver gather - perfect geometry and same water velocity (200x scale)

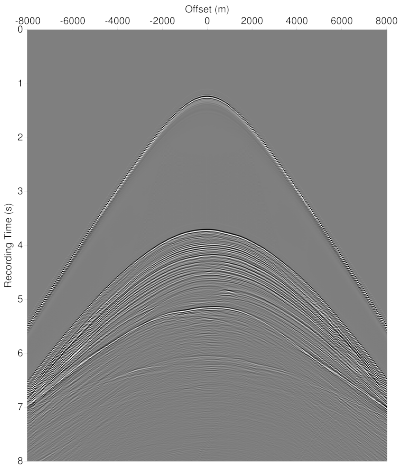

(c) 4D receiver gather - perfect geometry, different water velocity (10x scale)

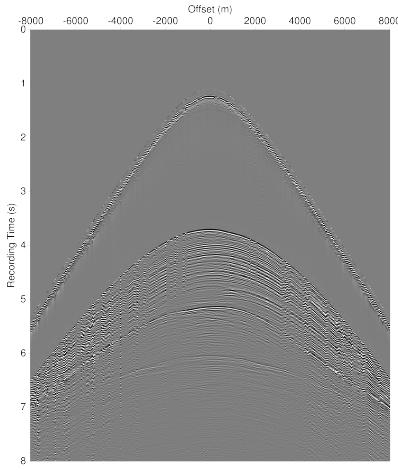

(d) 4D receiver gather - imperfect geometry, different water velocity (10x scale)

Figure 5.7: Receiver gather of baseline scenario (**a**) and 4D difference of seismograms with repeatable geometry (S1R1-S1R1) for same water velocity (**b**) and different water velocity (**c**). Figure 5.7d shows the the 4D seismogram with different water velocities and non-repeatable geometry (S1R1-S2R2). The color scales of the 4D seismogram were tightened to ease visualization.

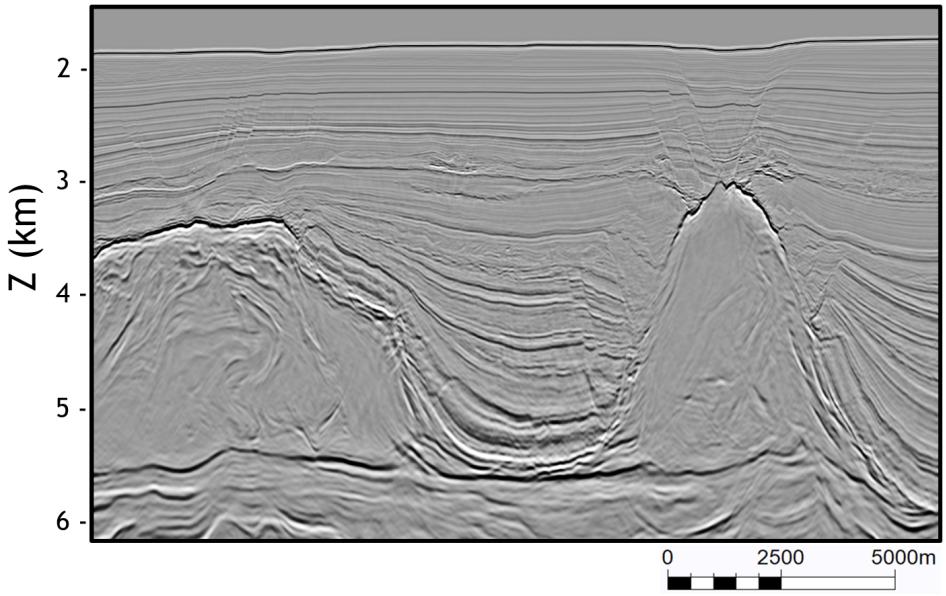

(a) Field Data

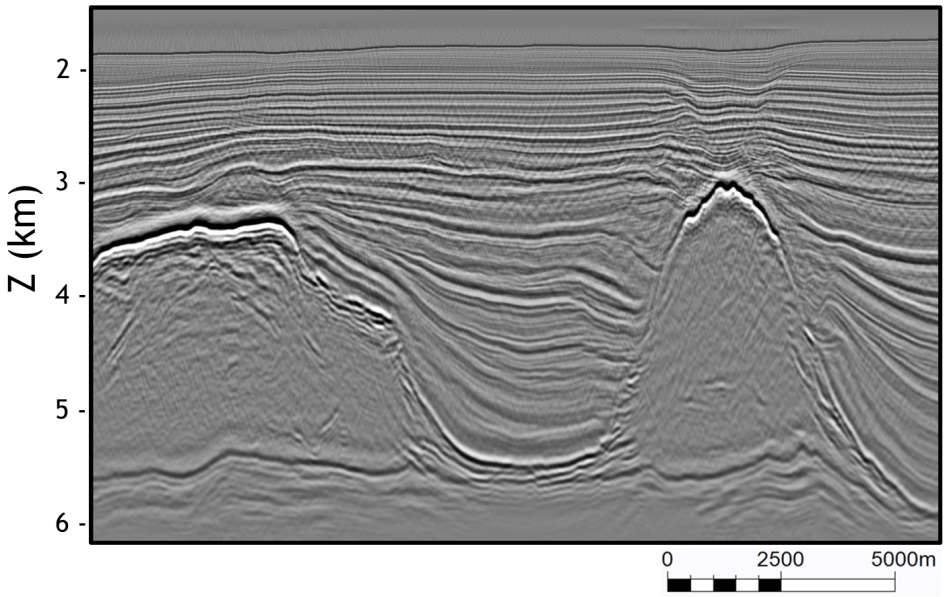

(b) Modeled Data

Figure 5.8: Comparison between the field (**a**) and synthetic (**b**) migrated sections in the study area. Modeled data is from the baseline scenario.

Table 5.3: Resulting NRMS for the selected scenarios (see table 5.2), calculated at top of salt (blue rows) and in the reservoir zone (100 meters below the base of salt - red rows).

Water Layer Velocity		**Monitor Vintage Geometry**			
Modeling	**Migration**	S1R1	S1R2	S2R1	S2R2
October	April	1.41	2.15	1.70	2.19
October	October	0.71	1.63	1.12	1.74
October	April	2.62	4.60	3.44	5.09
October	October	2.02	4.51	3.22	3.99

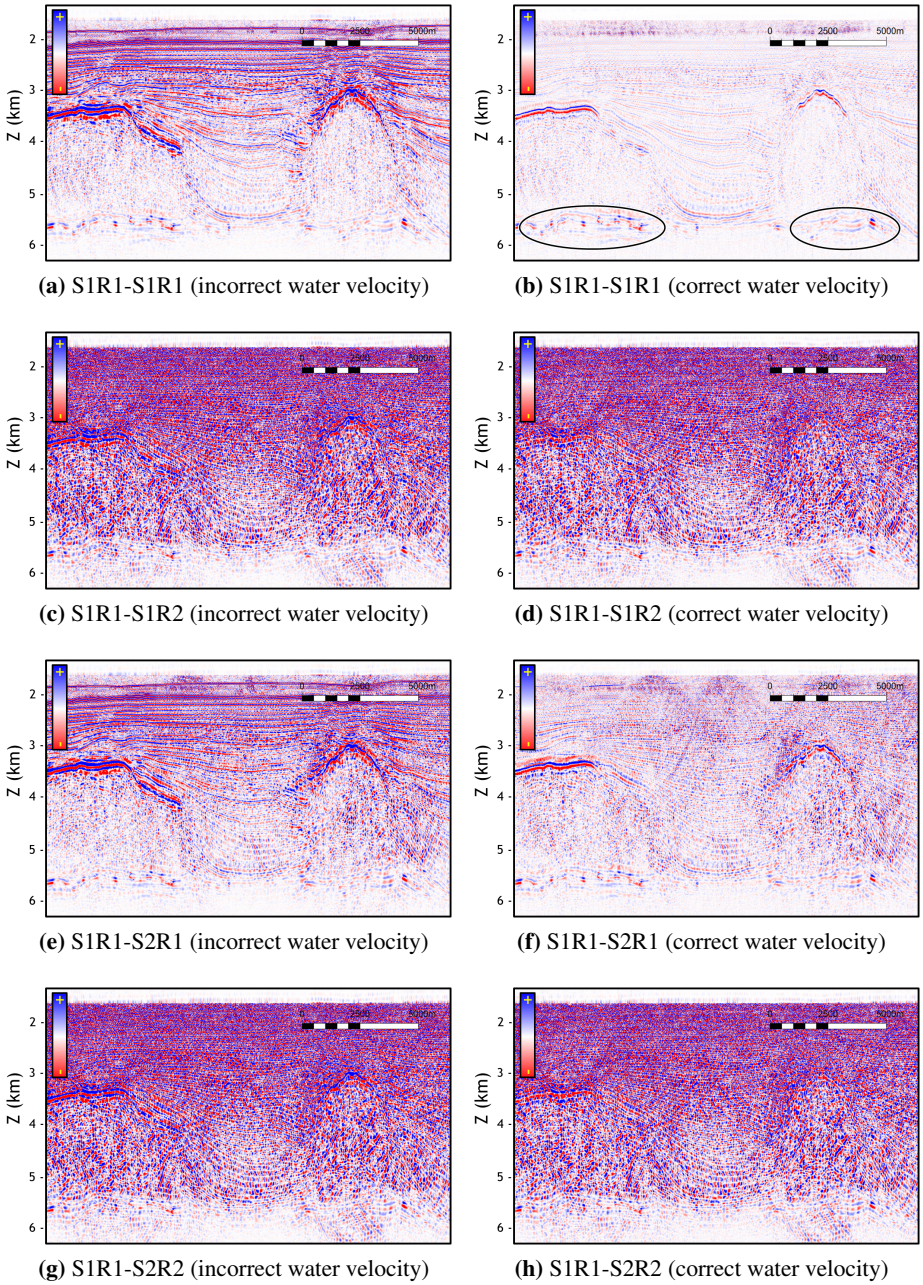

(a) S1R1-S1R1 (incorrect water velocity)

(b) S1R1-S1R1 (correct water velocity)

(c) S1R1-S1R2 (incorrect water velocity)

(d) S1R1-S1R2 (correct water velocity)

(e) S1R1-S2R1 (incorrect water velocity)

(f) S1R1-S2R1 (correct water velocity)

(g) S1R1-S2R2 (incorrect water velocity)

(h) S1R1-S2R2 (correct water velocity)

Figure 5.9: Comparison of time-lapse amplitudes for the modeled scenarios. Black ellipses in panel **(b)** indicate the 4D signal. Color scales are the same in all plots, and are 20x tighter than that of Figure 5.8b.

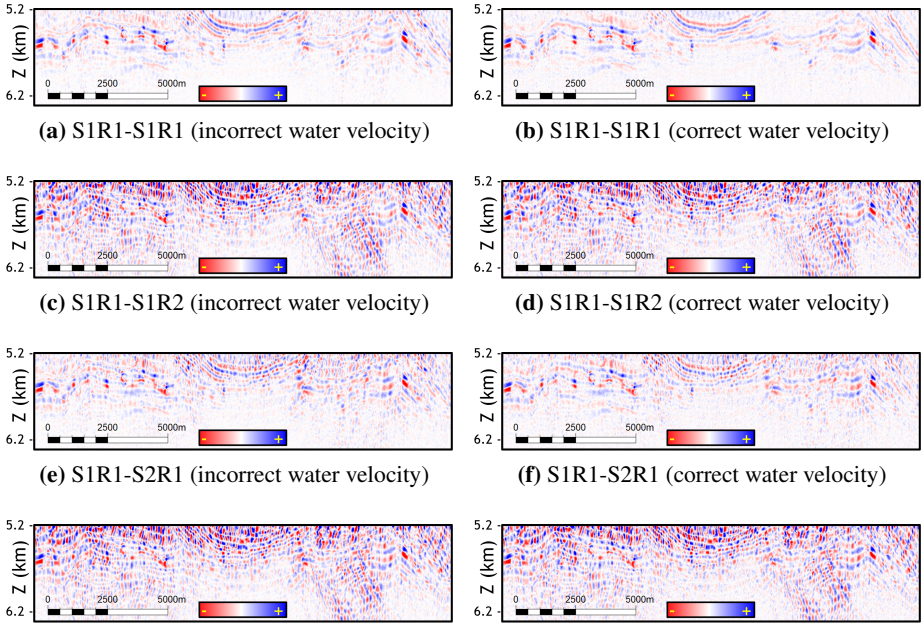

(a) S1R1-S1R1 (incorrect water velocity)

(b) S1R1-S1R1 (correct water velocity)

(c) S1R1-S1R2 (incorrect water velocity)

(d) S1R1-S1R2 (correct water velocity)

(e) S1R1-S2R1 (incorrect water velocity)

(f) S1R1-S2R1 (correct water velocity)

(g) S1R1-S2R2 (incorrect water velocity)

(h) S1R1-S2R2 (correct water velocity)

Figure 5.10: Magnification of plots in Figure 5.9. Color scales are the same in all plots, and are 20x tighter than that of Figure 5.8b.

5.4 Discussions

We start by discussing the remarkable similarity between 3D field and 2D synthetic data (Figure 5.8). The full-wave elastic modeling, combined with high-resolution property models, was able to deliver a 2D migrated depth image comparable to the 3D real data. This is a qualitative sign of the robustness of the model building methodology, as well as of the FD modeling and migration algorithms.

The time-lapse seismograms shown in Figure 5.7 are a visual representation of coherent noise caused by non-repeatability: geometry mispositioning and/or different water velocity between baseline and monitor surveys leads to the appearance of "noise", but - in synthetic cases - only where there is data on either vintage. This type of noise, usually proportional to the amplitude of the 3D reflections, might be challenging to mitigate during 4D pre-processing. The actual 4D signal is visible only when both the geometry and the water velocity are repeated (Figure 5.7b). It is also important to take into account that the amplitudes scales on those pictures are different: 200x tighter for the Figure 5.7b and 10x tighter for Figures 5.7c and 5.7d.

Figures 5.9 and 5.10 visually summarizes this study. The time-lapse amplitudes can be seen for all scenarios. As in Figure 5.7, the change in the water velocity causes coherent 4D noise, which can be seen in Figure 5.9a as a noise that almost tracks the strong reflectors, like the top of the salt. This effect becomes less pronounced for deeper parts of the data, and is strongly reduced when the correct velocity model is used for imaging (Figures 5.9b and 5.10b).

In general, it seems that the variations in water velocity have a stronger effect on the shallow part of the data (above 3km – 4km). The shallow section is normally illuminated by reflections at larger angles, with raypaths that deviate more between baseline and monitor vintages, when the water velocity changes. This effect has been modeled by Han et al. (2012) - see Table 1 and Figures 8 and 9 in their paper. Bertrand and MacBeth (2003), in a time-lapse analysis of water velocity variations in the Gulf of Mexico, also identified a similar effect. The stronger deterioration of repeatability is quantified in Table 5.3: NRMS values at top of salt (blue rows) get quite worse when the wrong velocity is used in migration. Despite the same effect being present in the deep section (red rows), its intensity is fairly lower. This is also noticeable by comparing the left and right columns of Figure 5.10.

The non-repeatability of sources and receivers also undermines our ability to identify and isolate the 4D signal. The effect of non-repeatable receivers is significantly stronger than that of non-repeatable sources (Figure 5.10c and 5.10d *vs* 5.10e and 5.10f). This effect is partially reduced in the shallow section by using the cor-

rect imaging velocity, and can lead to a fairly decent time-lapse reservoir data for the source non-repeatability, but not for the imperfect receiver geometry (S1R1-S1R2). The combination of both geometry uncertainties leads to the worse result (Figures 5.10g and 5.10h).

It is interesting to notice that, in the scenario of non-repeatable sources (S1R1-S2R1 - Figures 5.9e and 5.9f), there is a cone-shaped 4D noise in the shallow part of the section - a noise that does not disappear when the correct imaging velocity is used. This pattern is not observed in the scenario with imperfect receiver (S1R1-S1R2), or more likely is hidden below the intense noise. Because the variation in acquisition geometry is random, sometimes this change in position from baseline to monitor can be quite significant (Figure 5.6c). This pattern is caused by the typical cone-shaped image obtained in the migration of OBN in the receiver domain - once these cones are "shifted" by the geometry randomness, they do not cancel out in the 4D image.

The NRMS values shown in Table 5.3 indicate that, for the parameters used in this study, non-repeatability of receiver positions played a stronger role in degrading the 4D signal. The effect is strong regardless of the velocity model selected for imaging. The higher NRMS values in the reservoir zone are also caused by the lack of strong reflections in this area - NRMS is a relative measure, and lack of energy in the baseline and monitor data lead to the high numbers seen in the bottom rows of Table 5.3.

Because the source grid is 10 times denser than the receiver grid, one might wonder if the interpretation of the numbers observed in Table 5.3 would be the same for an equal density of shots and receivers. To investigate this point, we reproduced the study with a source spacing of 500 m - the same as the receiver. All other parameters were kept the same. The results of this analysis can be seen in Table 5.4. Despite the higher NRMS values (due to the reduced number of sources), the interpretation remains: the non-repeatability of the receivers seems to play the main role in degrading the 4D signal.

No dedicated 4D processing has been applied to the data prior to the computation of the time-lapse attributes. Although source mispositioning also had a strong effect on NRMS for our study, our experience with processing field data in the receiver domain shows that a dense shooting grid allows for a good wavefield reconstruction in a regular grid, which could severely reduce this non-repeatability impact. Since in practice the sources can be better handled during processing (and also because currently there are no feasible acquisition solutions for achieving actual perfect repeatability on the source side), the efforts to reduce the NRMS should be focused on improving receiver repeatability, measuring (and using) the

Table 5.4: Resulting NRMS for the selected scenarios (see table 5.2), assuming a 500 m spacing for both sources and receivers. NRMS was calculated at top of salt (blue rows) and in the reservoir zone (100 meters below the base of salt - red rows).

Water Layer Velocity		**Monitor Vintage Geometry**			
Modeling	**Migration**	S1R1	S1R2	S2R1	S2R2
October	April	3.72	6.77	6.16	7.44
October	October	1.46	5.40	4.59	6.67
October	April	3.02	5.94	5.57	7.51
October	October	2.09	5.50	5.07	7.42

water velocity as accurately as possible, and development of pre-processing methodologies to improve the dataset.

Narrowing our discussion to scenarios S1R1-S1R1 and S1R1-S1R2, the use of the correct velocity model diminishes the NRMS in the case of perfect geometry repeatability, but the improvement is not so significant when there is mispositioning of the receivers. Better receiver repeatability can be achieved via reduction of OBN positioning uncertainty (Hatchell et al., 2019) or with the use of PRM systems, for example (Thedy et al., 2013; Ebaid et al., 2017). While the differences in the values in Tables 5.3 and 5.4 seem small, even a minor NRMS improvement can significantly expand our ability to detect the time-lapse signal in the area (Mello et al., 2019). This is reinforced by the results presented in Figure 5.10, where it can be difficult to distinguish 4D signal and noise even in the "benchmark" scenario (Figure 5.10b).

The parameters selected in this work (water velocity variations, geometry uncertainty, source and receiver grids) aimed at reproducing field data acquired in the area of study, therefore leading us to conclude that they are adequate for quantify-

ing the contribution of each factor to the total NRMS. An analysis performed with different parameters might of course lead to a different conclusion, which does not invalidate the results and the methodology presented here.

5.5 Conclusions

We analyzed the non-repeatability of synthetic ocean bottom seismic data, considering the contribution of seasonal water velocity changes and geometry uncertainty. Seismic images for baseline and monitor vintages were generated using 2D high-resolution property models from a pre-salt field in Santos Basin, full-wave elastic modeling, and revere-time migration. The synthetic data were compared in terms of time-lapse amplitude, and the NRMS of the difference sections were calculated. The results indicate that, in the lack of dedicated 4D processing, NRMS was dominated by non-repeatability of the receivers, with source mispositioning playing a secondary role. The effect of water velocity variations appeared more significant for the shallow section. For the deeper sections, this effect seemed to be fairly well accounted for with a post-stack correction - particularly in the case of poor receiver repeatability, where the geometry uncertainty dominated the NRMS. This means that early-out processing products, which usually rely on post-stack methods to deliver fast results, can achieve good correction of the water velocity variation, therefore enhancing the appeal of these solutions.

Conclusions

In this thesis, some cases of quantitative seismic monitoring were presented. These examples ranged from the use of synthetic data to study different fluid effects and acquisition geometry in reservoir monitoring (**Chapter 1** and **Chapter 5**) to the use of field data to study unintentional water injection and its geomechanical consequences (**Chapter 3**). The examples and case studies presented show how quantitative reservoir monitoring can be challenging, particularly in the presence of limited information and/or noisy data.

In addition to oil field surveillance, studies of shallow geophysical monitoring were also presented. These examples illustrated the use of well data (**Chapter 2**) and long-offset seismic (**Chapter 4**) to monitor the surrounds of wells and the shallow sediment layers of the ocean, respectively. In both chapters, case studies of active and passive monitoring were analyzed, with discussions of different methodologies and their limitations.

With increasing field instrumentation, more and more data is acquired worldwide, and new methods of monitoring are made possible. Besides, data-driven methods become more powerful and robust when large data sets are available. A clear trend in geosciences is the use of machine learning methods for classification and regression, as well as AI (eg. neural networks) for reservoir characterizations and monitoring. A significant share of current research in geophysics is based on those methods, and I believe this share will increase during the next years, as more and more data (and processing capacity) is made available to researchers.

Appendix A

Rock Physics and Fluid Parameters for Modelling

A.1 Brine and Temperature Modelling - Section 1.2.1

The parameters used to build the rock framework were

- $\rho_{matrix} = 2.65$ g/cm^3
- $\varphi = 0.2$ (20%)
- $K_{matrix} = 37$ GPa
- $K_{dry}(\sigma_{eff}) = 10\Big[0.2864\ln(\sigma_{eff}) - 0.165\Big]$ GPa
- $\mu(\sigma_{eff}) = 6.25\Big[0.2535\ln(\sigma_{eff}) - 0.034\Big]$ GPa

The effective stress σ_{eff} is in megapascal (MPa).

Oil acoustic parameters were calculated with Batzle & Wang's empirical relations for an oil of 20° API and GOR of 75 (m^3/m^3).

- $\rho_{oil} = 0.82$ g/cm^3
- $K_{oil} = 1.12$ GPa

A.2 CO_2 and Fluid Mixing Modelling - Section 1.3

The parameters used to build the rock framework were

- $\rho_{matrix} = 2.648$ g/cm^3
- $\varphi = 0.2$ (20%)
- $K_{matrix} = 37.8$ GPa

$$C^0_{dry} = \begin{bmatrix} 14.3204 & 4.7876 & 4.7876 & 0 & 0 & 0 \\ 4.7876 & 14.3204 & 4.7876 & 0 & 0 & 0 \\ 4.7876 & 4.7876 & 14.3204 & 0 & 0 & 0 \\ 0 & 0 & 0 & 4.7876 & 0 & 0 \\ 0 & 0 & 0 & 0 & 4.7876 & 0 \\ 0 & 0 & 0 & 0 & 0 & 4.7876 \end{bmatrix} \text{ GPa}$$

The TOE coefficientes (Equation 1.10) are $A_{111} = -7400$ GPa, $A_{112} = -1400$ GPa, and $A_{123} = 600$ GPa.

Brine acoustic parameters were calculated with Batzle & Wang's empirical relations for a temperature of 80°C, a salinity of 120,000 ppm, and a pore pressure of 30 MPa. The values are

- $\rho_{Brine} = 1.0694$ g/cm^3
- $K_{Brine} = 3.1010$ GPa

For CO_2 properties, the script provided by Mavko et al. (2009b) was used. Using the same pressure and temperature as in the brine modeling, we get

- $\rho_{CO_2} = 0.7548$ g/cm^3
- $K_{CO_2} = 0.1791$ GPa

A.3 Anisotropic Modelling - Section 1.4

The parameters used to build the rock framework were

- $\rho_{matrix} = 2.648$ g/cm^3
- $\varphi = 0.2$ (20%)
- $K_{matrix} = 37.8$ GPa

$$C^0_{dry} = \begin{bmatrix} 17.1845 & 6.6984 & 5.4786 & 0 & 0 & 0 \\ 6.6984 & 17.1845 & 5.4786 & 0 & 0 & 0 \\ 5.4786 & 5.4786 & 14.3204 & 0 & 0 & 0 \\ 0 & 0 & 0 & 4.7664 & 0 & 0 \\ 0 & 0 & 0 & 0 & 4.7664 & 0 \\ 0 & 0 & 0 & 0 & 0 & 5.2430 \end{bmatrix} \text{ GPa}$$

The TOE coefficientes (see Equation 1.10) are $A_{111} = -7400$ GPa, $A_{112} = -1400$ GPa, and $A_{123} = 600$ GPa.

Brine acoustic parameters were calculated with Batzle & Wang's empirical relations, according to the different temperatures, salinities, and pore pressures. For scenario **2B**, a 20% saturation of irreducible water was assumed.

The stiffness matrix for the overburden is

$$C_{Overburden} = \begin{bmatrix} 27.1002 & 15.4677 & 13.1030 & 0 & 0 & 0 \\ 15.4677 & 27.1002 & 13.1030 & 0 & 0 & 0 \\ 13.1030 & 13.1030 & 22.5835 & 0 & 0 & 0 \\ 0 & 0 & 0 & 5.2875 & 0 & 0 \\ 0 & 0 & 0 & 0 & 5.2875 & 0 \\ 0 & 0 & 0 & 0 & 0 & 5.8163 \end{bmatrix} \text{GPa}$$

Appendix B

Jacobian Matrix for Uncertainty

This appendix shows the derivatives necessary to calculate the uncertainty, as described in section 1.2.1.

B.1 Constant Salinity and Temperature

If we assume that all time-lapse change is caused by the pressure effect, the most convenient and reliable measurement to obtain the pore pressure change is the zero-offset reflectivity, or intercept (Equation 1.18). Using also Equation 1.13 and the assumption that pressure-caused density changes are negligible, we have

$$\Delta R(0) = \frac{1}{2}\left(\frac{\Delta\rho^{(4D)}}{\rho}^{\nearrow 0} + \frac{\Delta V_p^{(4D)}}{V_p}\right) = \frac{1}{2}\left[l_\alpha \Delta P_P + m_\alpha (\Delta P_P)^2\right]$$

Rearranging,

$$(\Delta P_P)^2 + b_1 \Delta P_P + c_1 = 0, \tag{B.1}$$

with

$$b_1 = \frac{l_\alpha}{m_\alpha} \qquad \text{and} \qquad c_1 = -2\frac{\Delta R(0)}{m_\alpha}.$$

The derivatives necessary to calculate the Jacobian can be computed in the following form:

$$\frac{\partial(\Delta P_P)}{\partial x_i} = \frac{\partial(\Delta P_P)}{\partial b_1}\frac{\partial b_1}{\partial x_i} + \frac{\partial(\Delta P_P)}{\partial c_1}\frac{\partial c_1}{\partial x_i}. \tag{B.2}$$

Putting B.1 in Bhaskara form,

$$\Delta P_P = \frac{-b_1 + \mathrm{sgn}(b_1)\sqrt{b_1^2 - 4c_1}}{2}.$$

The partial derivatives with relation to b_1 and c_1 are then

$$\frac{\partial(\Delta P_P)}{\partial b_1} = \left[-\frac{1}{2} + \frac{|b_1|}{2\sqrt{b_1^2 - 4c_1}}\right] \quad \text{and} \quad \frac{\partial(\Delta P_P)}{\partial c_1} = -\frac{\mathrm{sgn}(b_1)}{\sqrt{b_1^2 - 4c_1}}$$

B.1.1 Pressure

Apart from the seismic-dependent derivatives, shown here just out of completeness, the terms with zero derivative will be omitted. The non-zero components are then

$$\begin{aligned}\frac{\partial(\Delta P_P)}{\partial(\Delta R(0))} &= \frac{\partial(\Delta P_P)}{\partial b_1}\cancelto{0}{\frac{\partial b_1}{\partial(\Delta R(0))}} + \frac{\partial(\Delta P_P)}{\partial c_1}\frac{\partial c_1}{\partial(\Delta R(0))} \\ &= -\frac{2}{m_\alpha}\frac{\partial(\Delta P_P)}{\partial c_1},\end{aligned}$$

$$\begin{aligned}\frac{\partial(\Delta P_P)}{\partial(\Delta G)} &= \frac{\partial(\Delta P_P)}{\partial b_1}\cancelto{0}{\frac{\partial b_1}{\partial(\Delta G)}} + \frac{\partial(\Delta P_P)}{\partial c_1}\cancelto{0}{\frac{\partial c_1}{\partial(\Delta G)}} \\ &= 0,\end{aligned}$$

$$\begin{aligned}\frac{\partial(\Delta P_P)}{\partial(\Delta\tau/\tau)} &= \frac{\partial(\Delta P_P)}{\partial b_1}\cancelto{0}{\frac{\partial b_1}{\partial(\Delta\tau/\tau)}} + \frac{\partial(\Delta P_P)}{\partial c_1}\cancelto{0}{\frac{\partial c_1}{\partial(\Delta\tau/\tau)}} \\ &= 0,\end{aligned}$$

$$\frac{\partial(\Delta P_P)}{\partial l_\alpha} = \frac{\partial(\Delta P_P)}{\partial b_1}\frac{\partial b_1}{\partial l_\alpha} + \frac{\partial(\Delta P_P)}{\partial c_1}\cancelto{0}{\frac{\partial c_1}{\partial l_\alpha}}$$
$$= \frac{1}{m_\alpha}\frac{\partial(\Delta P_P)}{\partial b_1}, \qquad \text{and}$$

$$\frac{\partial(\Delta P_P)}{\partial m_\alpha} = \frac{\partial(\Delta P_P)}{\partial b_1}\frac{\partial b_1}{\partial m_\alpha} + \frac{\partial(\Delta P_P)}{\partial c_1}\frac{\partial c_1}{\partial m_\alpha}$$
$$= -\frac{1}{m_\alpha}\left[b_1\frac{\partial(\Delta P_P)}{\partial b_1} + c_1\frac{\partial(\Delta P_P)}{\partial c_1}\right].$$

B.2 Constant Temperature

When a variable brine salinity is considered, we can no longer rely only on the zero-offset reflectivity to obtain the reservoir changes, since our system now has two unknowns to be solved for. We will choose as an extra source of information the time-travel changes, in the form of Equation 1.22.

If a constant fluid temperature is assumed, only salinity can cause density changes. From 1.18,

$$\Delta R(0) = \frac{1}{2}\left(\frac{\Delta\rho^{(4D)}}{\rho} + \frac{\Delta V_p^{(4D)}}{V_p}\right) \Longrightarrow \frac{\Delta\rho^{(4D)}}{\rho} = 2\Delta R(0) - \frac{\Delta V_p^{(4D)}}{V_p}.$$

Combining the result above with 1.11 and 1.22, we get

$$\Delta\eta = \frac{1}{f_\rho}\left(2\Delta R(0) - \frac{1-\sqrt{1+4\dfrac{\Delta\tau}{\tau}}}{2}\right) \tag{B.3}$$

For the pressure, we can put together 1.11 and 1.13 to get

$$\frac{\Delta V_p^{(4D)}}{V_p} = f_\alpha\Delta\eta + l_\alpha\Delta P_P + m_\alpha(\Delta P_P)^2,$$

which, combined with B.3, yields,

$$(\Delta P_P)^2 + b_2 \Delta P_P + c_2 = 0, \tag{B.4}$$

with

$$b_2 = \frac{l_\alpha}{m_\alpha} \qquad \text{and} \qquad c_2 = \left[\left(f_\alpha + f_\rho \right) \Delta\eta - 2\Delta R(0) \right] / m_\alpha.$$

B.2.1 Salinity

The non-zero salinity derivatives are

$$\frac{\partial(\Delta\eta)}{\partial(\Delta R(0))} = \frac{2}{f_\rho}, \qquad \frac{\partial(\Delta\eta)}{\partial(\Delta G)} = 0, \qquad \frac{\partial(\Delta\eta)}{\partial f_\rho} = -\frac{1}{f_\rho}\Delta\eta \qquad \text{and}$$

$$\frac{\partial(\Delta\eta)}{\partial(\Delta\tau/\tau)} = \frac{1}{f_\rho \sqrt{1 + 4\dfrac{\Delta\tau}{\tau}}}.$$

B.2.2 Pressure

The derivatives for pressure are carried out in the same fashion showed in B.2, only replacing b_1 and c_1 by b_2 and c_2, respectively. We then have

$$\begin{aligned} \frac{\partial(\Delta P_P)}{\partial(\Delta R(0))} &= \frac{\partial(\Delta P_P)}{\partial b_2} \cancelto{0}{\frac{\partial b_2}{\partial(\Delta R(0))}} + \frac{\partial(\Delta P_P)}{\partial c_2} \frac{\partial c_2}{\partial(\Delta R(0))} \\ &= \frac{1}{m_\alpha} \frac{\partial(\Delta P_P)}{\partial c_2} \left[\left(f_\alpha + f_\rho \right) \frac{\partial(\Delta\eta)}{\partial(\Delta R(0))} - 2 \right], \end{aligned}$$

$$\frac{\partial(\Delta P_P)}{\partial(\Delta G)} = \frac{\partial(\Delta P_P)}{\partial b_2}\cancelto{0}{\frac{\partial b_2}{\partial(\Delta G)}} + \frac{\partial(\Delta P_P)}{\partial c_2}\cancelto{0}{\frac{\partial c_2}{\partial(\Delta G)}}$$
$$= 0,$$

$$\frac{\partial(\Delta P_P)}{\partial(\Delta\tau/\tau)} = \frac{\partial(\Delta P_P)}{\partial b_2}\cancelto{0}{\frac{\partial b_2}{\partial(\Delta\tau/\tau)}} + \frac{\partial(\Delta P_P)}{\partial c_2}\frac{\partial c_2}{\partial(\Delta\tau/\tau)}$$
$$= \frac{\partial(\Delta P_P)}{\partial c_2}\frac{f_\alpha + f_\rho}{m_\alpha}\frac{\partial(\Delta\eta)}{\partial(\Delta\tau/\tau)},$$

$$\frac{\partial(\Delta P_P)}{\partial l_\alpha} = \frac{\partial(\Delta P_P)}{\partial b_2}\frac{\partial b_2}{\partial l_\alpha} + \frac{\partial(\Delta P_P)}{\partial c_2}\cancelto{0}{\frac{\partial c_2}{\partial l_\alpha}}$$
$$= \frac{1}{m_\alpha}\frac{\partial(\Delta P_P)}{\partial b_2},$$

$$\frac{\partial(\Delta P_P)}{\partial m_\alpha} = \frac{\partial(\Delta P_P)}{\partial b_2}\frac{\partial b_2}{\partial m_\alpha} + \frac{\partial(\Delta P_P)}{\partial c_2}\frac{\partial c_2}{\partial m_\alpha}$$
$$= -\frac{1}{m_\alpha}\left[b_2\frac{\partial(\Delta P_P)}{\partial b_2} + c_2\frac{\partial(\Delta P_P)}{\partial c_2}\right],$$

$$\frac{\partial(\Delta P_P)}{\partial f_\rho} = \frac{\partial(\Delta P_P)}{\partial b_2}\cancelto{0}{\frac{\partial b_2}{\partial f_\rho}} + \frac{\partial(\Delta P_P)}{\partial c_2}\frac{\partial c_2}{\partial f_\rho}$$
$$= \frac{1}{m_\alpha}\frac{\partial(\Delta P_P)}{\partial c_2}\left[(f_\alpha + f_\rho)\frac{\partial(\Delta\eta)}{\partial f_\rho} + \Delta\eta\right], \qquad \text{and}$$

$$\frac{\partial(\Delta P_P)}{\partial f_\alpha} = \frac{\partial(\Delta P_P)}{\partial b_2}\cancelto{0}{\frac{\partial b_2}{\partial f_\alpha}} + \frac{\partial(\Delta P_P)}{\partial c_2}\frac{\partial c_2}{\partial f_\alpha}$$
$$= \frac{1}{m_\alpha}\frac{\partial(\Delta P_P)}{\partial c_2}\Delta\eta.$$

B.3 All Variables

If we consider pressure, temperature and salinity changing simultaneously, the solutions are the ones presented in equations 1.31, 1.31 and 1.33. Again, we dis-

play only the seismic-related derivatives and the non-zero derivatives with respect to the rock physics constants.

B.3.1 Pressure

The derivatives for pressure are carried out in the same fashion showed in equation B.2, only replacing b_1 and c_1 by b_P and c_P, respectively. We have

$$\begin{aligned}\frac{\partial(\Delta P_P)}{\partial(\Delta R(0))} &= \frac{\partial(\Delta P_P)}{\partial b_P}\cancelto{0}{\frac{\partial b_P}{\partial(\Delta R(0))}} + \frac{\partial(\Delta P_P)}{\partial c_P}\frac{\partial c_P}{\partial(\Delta R(0))} \\ &= 0,\end{aligned}$$

$$\begin{aligned}\frac{\partial(\Delta P_P)}{\partial(\Delta G)} &= \frac{\partial(\Delta P_P)}{\partial b_P}\cancelto{0}{\frac{\partial b_P}{\partial(\Delta G)}} + \frac{\partial(\Delta P_P)}{\partial c_P}\frac{\partial c_P}{\partial(\Delta G)} \\ &= \frac{\partial(\Delta P_P)}{\partial c_P}\frac{V_p^2}{4m_\beta V_s^2},\end{aligned}$$

$$\begin{aligned}\frac{\partial(\Delta P_P)}{\partial(\Delta\tau/\tau)} &= \frac{\partial(\Delta P_P)}{\partial b_P}\cancelto{0}{\frac{\partial b_P}{\partial(\Delta\tau/\tau)}} + \frac{\partial(\Delta P_P)}{\partial c_P}\frac{\partial c_P}{\partial(\Delta\tau/\tau)} \\ &= \frac{\partial(\Delta P_P)}{\partial c_P}\frac{V_p^2}{8m_\beta V_s^2}\frac{1}{\sqrt{1+4\dfrac{\Delta\tau}{\tau}}},\end{aligned}$$

$$\begin{aligned}\frac{\partial(\Delta P_P)}{\partial l_\beta} &= \frac{\partial(\Delta P_P)}{\partial b_P}\frac{\partial b_P}{\partial l_\beta} + \frac{\partial(\Delta P_P)}{\partial c_P}\cancelto{0}{\frac{\partial c_P}{\partial l_\beta}} \\ &= \frac{1}{m_\beta}\frac{\partial(\Delta P_P)}{\partial b_P}, \qquad \text{and}\end{aligned}$$

$$\begin{aligned}\frac{\partial(\Delta P_P)}{\partial m_\beta} &= \frac{\partial(\Delta P_P)}{\partial b_P}\frac{\partial b_P}{\partial m_\beta} + \frac{\partial(\Delta P_P)}{\partial c_P}\frac{\partial c_P}{\partial m_\beta} \\ &= -\frac{1}{m_\beta}\left[b_P\frac{\partial(\Delta P_P)}{\partial b_P} + c_P\frac{\partial(\Delta P_P)}{\partial c_P}\right].\end{aligned}$$

B.3.2 Temperature

The derivatives for temperature can also be carried out in the same fashion showed in B.2, only replacing b_1 and c_1 by b_T and c_T, respectively. We then have

$$\begin{aligned}\frac{\partial(\Delta T)}{\partial(\Delta R(0))} &= \frac{\partial(\Delta T)}{\partial b_T}\cancelto{0}{\frac{\partial b_T}{\partial(\Delta R(0))}} + \frac{\partial(\Delta T)}{\partial c_T}\frac{\partial c_T}{\partial(\Delta R(0))} \\ &= \frac{2f_\alpha}{r_\alpha f_\rho}\frac{\partial(\Delta T)}{\partial c_T},\end{aligned}$$

$$\begin{aligned}\frac{\partial(\Delta T)}{\partial(\Delta G)} &= \frac{\partial(\Delta T)}{\partial b_T}\cancelto{0}{\frac{\partial b_T}{\partial(\Delta G)}} + \frac{\partial(\Delta T)}{\partial c_T}\frac{\partial c_T}{\partial(\Delta G)} \\ &= \frac{1}{r_\alpha}\frac{\partial(\Delta T)}{\partial c_T}\left[l_\alpha\frac{\partial(\Delta P_P)}{\partial(\Delta G)} + 2m_\alpha\Delta P_P\frac{\partial(\Delta P_P)}{\partial(\Delta G)}\right],\end{aligned}$$

$$\begin{aligned}\frac{\partial(\Delta T)}{\partial(\Delta\tau/\tau)} &= \frac{\partial(\Delta T)}{\partial b_T}\cancelto{0}{\frac{\partial b_T}{\partial(\Delta\tau/\tau)}} + \frac{\partial(\Delta T)}{\partial c_T}\frac{\partial c_T}{\partial(\Delta\tau/\tau)} \\ &= \frac{1}{r_\alpha}\frac{\partial(\Delta T)}{\partial c_T}\left[l_\alpha\frac{\partial(\Delta P_P)}{\partial(\Delta\tau/\tau)} + 2m_\alpha\Delta P_P\frac{\partial(\Delta P_P)}{\partial(\Delta\tau/\tau)} + \right. \\ &\quad \left.\frac{1}{\sqrt{1+4\dfrac{\Delta\tau}{\tau}}}\left(1+\frac{f_\alpha}{f_\rho}\right)\right],\end{aligned}$$

$$\begin{aligned}\frac{\partial(\Delta T)}{\partial l_\alpha} &= \frac{\partial(\Delta T)}{\partial b_T}\cancelto{0}{\frac{\partial b_T}{\partial l_\alpha}} + \frac{\partial(\Delta T)}{\partial c_T}\frac{\partial c_T}{\partial l_\alpha} \\ &= \frac{1}{r_\alpha}\frac{\partial(\Delta T)}{\partial c_T}\Delta P_P,\end{aligned}$$

$$\frac{\partial(\Delta T)}{\partial m_\alpha} = \frac{\partial(\Delta T)}{\partial b_T}\cancelto{0}{\frac{\partial b_T}{\partial m_\alpha}} + \frac{\partial(\Delta T)}{\partial c_T}\frac{\partial c_T}{\partial m_\alpha}$$
$$= \frac{1}{r_\alpha}\frac{\partial(\Delta T)}{\partial c_T}\left(\Delta P_P\right)^2,$$

$$\frac{\partial(\Delta T)}{\partial l_\beta} = \frac{\partial(\Delta T)}{\partial b_T}\cancelto{0}{\frac{\partial b_T}{\partial l_\beta}} + \frac{\partial(\Delta T)}{\partial c_T}\frac{\partial c_T}{\partial l_\beta}$$
$$= \frac{1}{r_\alpha}\frac{\partial(\Delta T)}{\partial c_T}\left[l_\alpha\frac{\partial(\Delta P_P)}{\partial l_\beta} + 2m_\alpha\Delta P_P\frac{\partial(\Delta P_P)}{\partial l_\beta}\right],$$

$$\frac{\partial(\Delta T)}{\partial m_\beta} = \frac{\partial(\Delta T)}{\partial b_T}\cancelto{0}{\frac{\partial b_T}{\partial m_\beta}} + \frac{\partial(\Delta T)}{\partial c_T}\frac{\partial c_T}{\partial m_\beta}$$
$$= \frac{1}{r_\alpha}\frac{\partial(\Delta T)}{\partial c_T}\left[l_\alpha\frac{\partial(\Delta P_P)}{\partial m_\beta} + 2m_\alpha\Delta P_P\frac{\partial(\Delta P_P)}{\partial m_\beta}\right],$$

$$\frac{\partial(\Delta T)}{\partial f_\alpha} = \frac{\partial(\Delta T)}{\partial b_T}\frac{\partial b_T}{\partial f_\alpha} + \frac{\partial(\Delta T)}{\partial c_T}\frac{\partial c_T}{\partial f_\alpha}$$
$$= -\frac{q_\rho}{r_\alpha f_\rho}\frac{\partial(\Delta T)}{\partial b_T} + \frac{1}{r_\alpha f_\rho}\frac{\partial(\Delta T)}{\partial c_T}\left[2\Delta R(0) - \frac{1-\sqrt{1+4\dfrac{\Delta\tau}{\tau}}}{2}\right],$$

$$\frac{\partial(\Delta T)}{\partial f_\rho} = \frac{\partial(\Delta T)}{\partial b_T}\frac{\partial b_T}{\partial f_\rho} + \frac{\partial(\Delta T)}{\partial c_T}\frac{\partial c_T}{\partial f_\rho}$$
$$= -\frac{f_\alpha q_\rho}{r_\alpha f_\rho^2}\frac{\partial(\Delta T)}{\partial b_T} + \frac{1}{r_\alpha}\frac{\partial(\Delta T)}{\partial c_T}\left[\frac{2\Delta R(0) f_\alpha}{f_\rho^2} + \frac{f_\alpha}{f_\rho}\frac{1-\sqrt{1+4\dfrac{\Delta\tau}{\tau}}}{2}\right],$$

$$\frac{\partial(\Delta T)}{\partial q_\alpha} = \frac{\partial(\Delta T)}{\partial b_T}\frac{\partial b_T}{\partial q_\alpha} + \frac{\partial(\Delta T)}{\partial c_T}\cancelto{0}{\frac{\partial c_T}{\partial q_\alpha}}$$
$$= \frac{1}{r_\alpha}\frac{\partial(\Delta T)}{\partial b_T},$$

$$\frac{\partial(\Delta T)}{\partial q_\rho} = \frac{\partial(\Delta T)}{\partial b_T}\frac{\partial b_T}{\partial q_\rho} + \frac{\partial(\Delta T)}{\partial c_T}\cancelto{0}{\frac{\partial c_T}{\partial q_\rho}}$$
$$= -\frac{f_\alpha}{r_\alpha f_\rho}\frac{\partial(\Delta T)}{\partial b_T}, \qquad \text{and}$$

$$\frac{\partial(\Delta T)}{\partial r_\alpha} = \frac{\partial(\Delta T)}{\partial b_T}\frac{\partial b_T}{\partial r_\alpha} + \frac{\partial(\Delta T)}{\partial c_T}\frac{\partial c_T}{\partial r_\alpha}$$
$$= -\frac{1}{r_\alpha}\left[b_T\frac{\partial(\Delta T)}{\partial b_T} + c_T\frac{\partial(\Delta T)}{\partial c_T}\right].$$

B.3.3 Salinity

For salinity, the derivatives are

$$\frac{\partial(\Delta\eta)}{\partial(\Delta R(0))} = \frac{2}{f_\rho} - \frac{q_\rho}{f_\rho}\frac{\partial(\Delta T)}{\partial(\Delta R(0))},$$

$$\frac{\partial(\Delta\eta)}{\partial(\Delta G)} = -\frac{q_\rho}{f_\rho}\frac{\partial(\Delta T)}{\partial(\Delta G)}$$

$$\frac{\partial(\Delta\eta)}{\partial(\Delta\tau/\tau)} = \frac{1}{f_\rho}\left[\sqrt{1+4\frac{\Delta\tau}{\tau}} - q_\rho\frac{\partial(\Delta T)}{\partial(\Delta\tau/\tau)}\right]$$

$$\frac{\partial(\Delta\eta)}{\partial l_\alpha} = -\frac{q_\rho}{f_\rho}\frac{\partial(\Delta T)}{\partial l_\alpha},$$

$$\frac{\partial(\Delta\eta)}{\partial l_\beta} = -\frac{q_\rho}{f_\rho}\frac{\partial(\Delta T)}{\partial l_\beta},$$

$$\frac{\partial(\Delta\eta)}{\partial m_\alpha} = -\frac{q_\rho}{f_\rho}\frac{\partial(\Delta T)}{\partial m_\alpha},$$

$$\frac{\partial(\Delta\eta)}{\partial m_\beta} = -\frac{q_\rho}{f_\rho}\frac{\partial(\Delta T)}{\partial m_\beta},$$

$$\frac{\partial(\Delta\eta)}{\partial f_\alpha} = -\frac{q_\rho}{f_\rho}\frac{\partial(\Delta T)}{\partial f_\alpha},$$

$$\frac{\partial(\Delta\eta)}{\partial q_\alpha} = -\frac{q_\rho}{f_\rho}\frac{\partial(\Delta T)}{\partial q_\alpha},$$

$$\frac{\partial(\Delta\eta)}{\partial r_\alpha} = -\frac{q_\rho}{f_\rho}\frac{\partial(\Delta T)}{\partial r_\alpha},$$

$$\frac{\partial(\Delta\eta)}{\partial f_\rho} = -\frac{1}{f_\rho}\Delta\eta - \frac{q_\rho}{f_\rho}\frac{\partial(\Delta T)}{\partial f_\rho}, \qquad \text{and}$$

$$\frac{\partial(\Delta\eta)}{\partial q_\rho} = -\frac{1}{f_\rho}\left[\Delta T + q_\rho\frac{\partial(\Delta T)}{\partial q_\rho}\right].$$

Appendix C

Decision Trees and Random Forest

C.1 Introduction

A *decision tree* can be thought of as a methodology to classify data, following a previously established metric. As an example, imagine that we have a dataset of samples that are separated into two different classes, **A** and **B**, and that there are two independent variables (also called *features*) that can be used to classify these samples: X_1 and X_2 (we will keep this example restricted to two variables and two classes, to ease visualization). A collection of 500 points is plotted in Figure C.1.

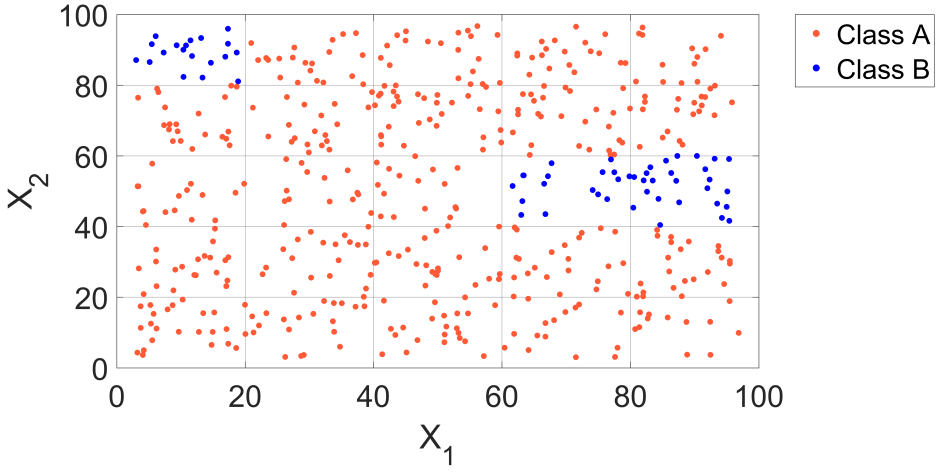

Figure C.1: Collection of samples of classes **A** and **B**.

The classes could mean two different fluids in a formation, and the variables X_i, different log measurements - density and neutron porosity to separate gas- and water-bearing sands, for example. In Figure C.1, we assume that these measurements have been verified somehow (e.g. fluid sampling), and that we trust this result. How can the calibrated dataset in C.1 help classify new data?

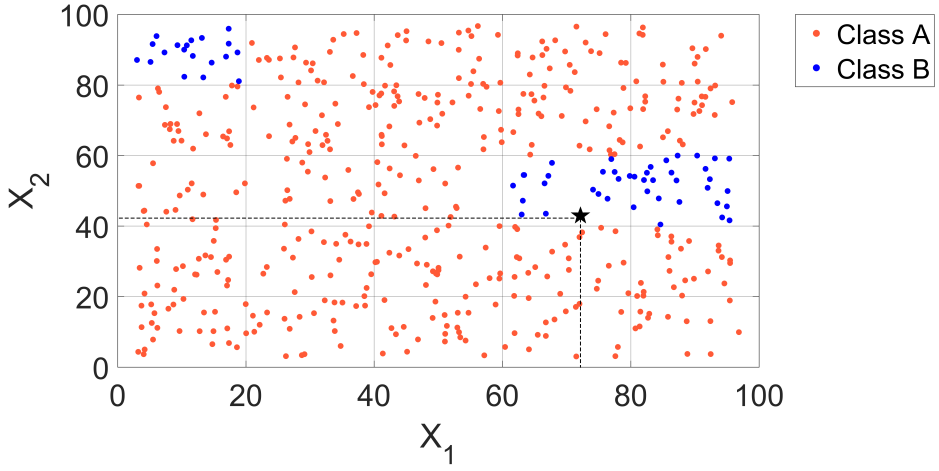

Figure C.2: A new point is registered (black star).

We start by looking for some criteria to divide the samples into groups, trying to reach groups which contain only samples of a single class, and using as few divisions as possible. An easy first step would be to divide the plot between points where $X_2 < 40$ and $X_2 > 40$ (Figure C.3). This division has the advantage of already creating a whole group where all samples belong to the same class - in this case, class **A**, for points with $X_2 < 40$. This can be visualized in terms of a *decision tree* (Figure C.4).

After the first split, or *branch*, we have now one final set of points that fit into the same class. We call these end groups a *leaf*. For the group on the right, called generically a *node*, the split process continues. One possible next split is for $X_1 = 60$ (Figure C.5). This second split, however, still cannot isolate the cloud of Class B-points, but a further split at $X_2 = 60$ (Figure C.6) does the job. In terms of a decision tree, these last two splits can be seen in Figure C.7.

If we keep applying the same logic, we get a final configuration as in Figure C.8, represented by the decision tree in Figure C.9. Now, if we want to find to which class our new data point belongs, all we have to do is to follow the decision tree. If the point has coordinates $(X_1, X_2) = (73, 42)$, it will be labeled as **B**, nesting in the left deeper leaf in Figure C.9.

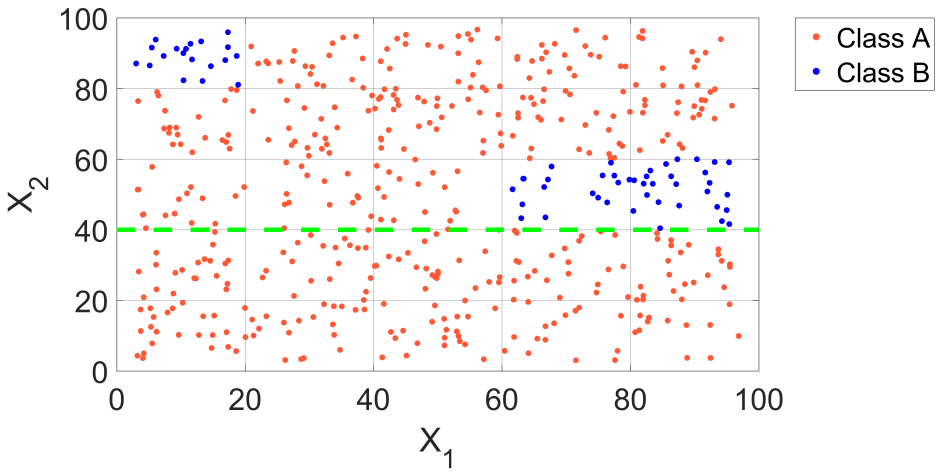

Figure C.3: First split, separating points where $X_2 < 40$ and $X_2 > 40$.

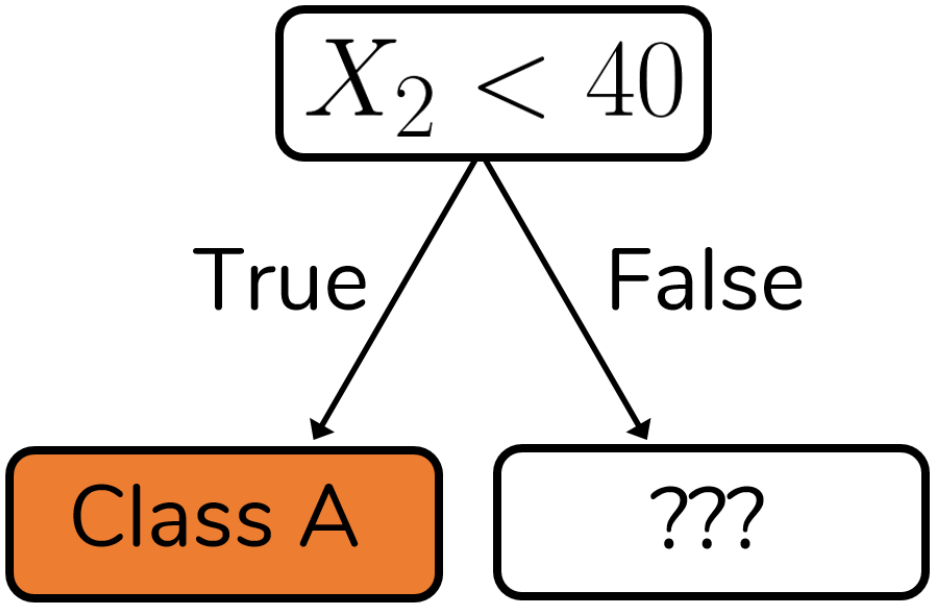

Figure C.4: Sketch of first split, separating points where $X_2 < 40$ and $X_2 > 40$.

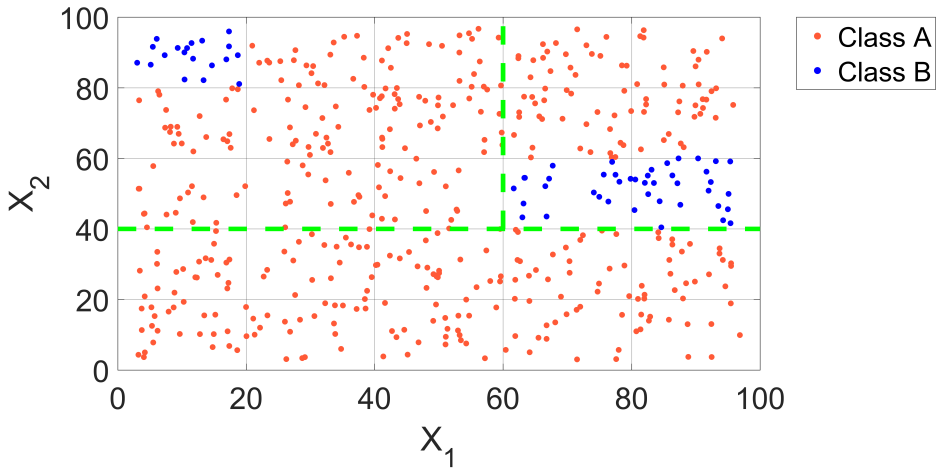

Figure C.5: Second split, separating points where $X_1 < 60$ and $X_1 > 60$.

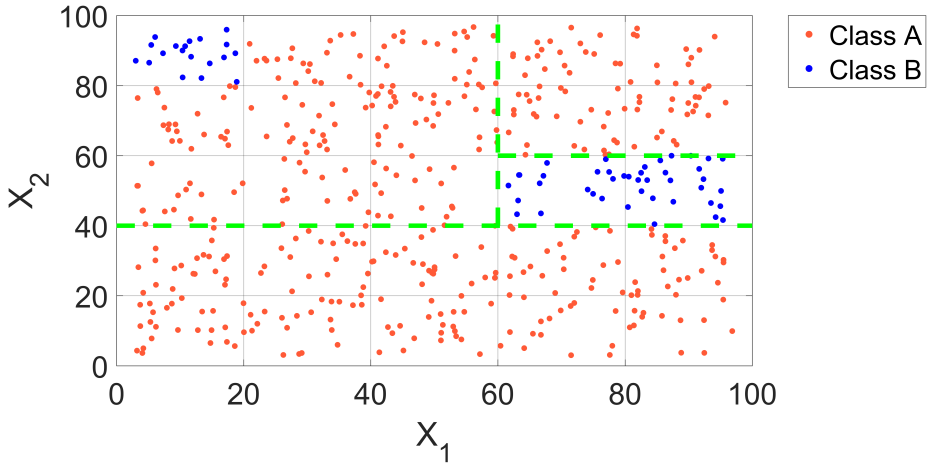

Figure C.6: Third split, separating points where $X_2 < 60$ and $X_2 > 60$.

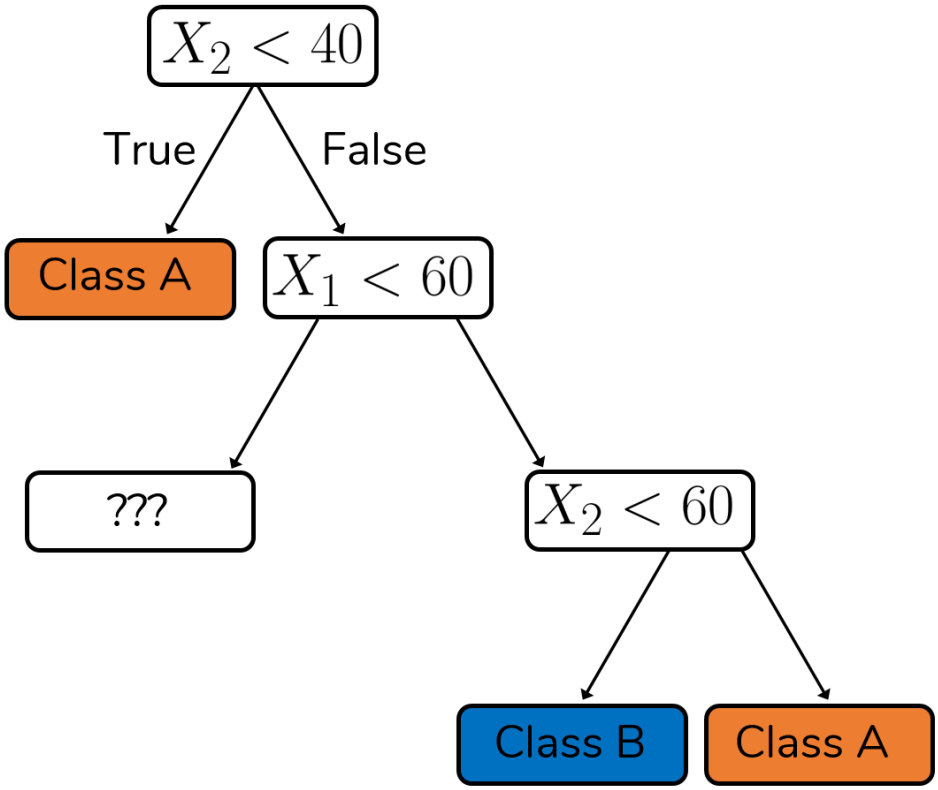

Figure C.7: Second and third splits, creating two new leaves.

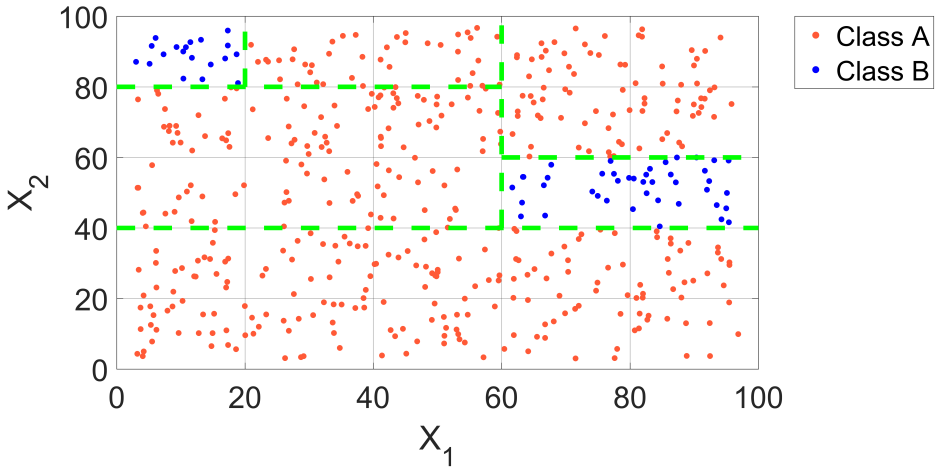

Figure C.8: 2D plot of final classification.

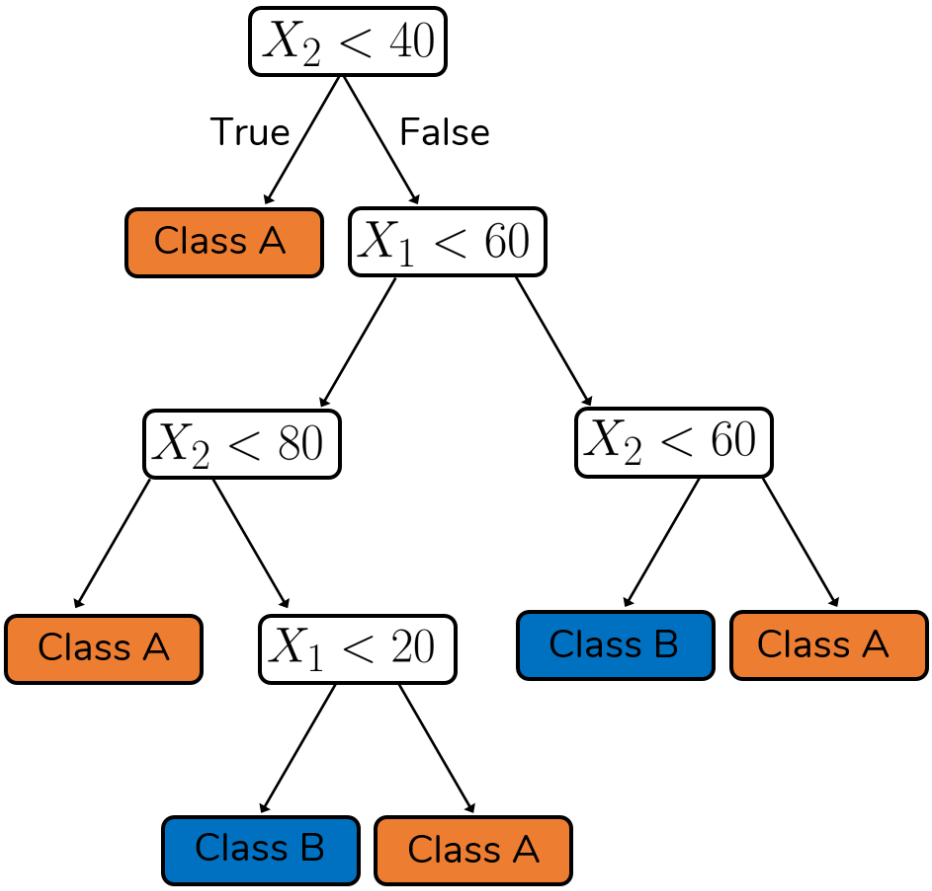

Figure C.9: Decision tree of final classification.

Criteria for splitting

In the example just presented, splitting of the dataset was performed on a visual evaluation basis. This is of course not possible for high dimensionality data. Besides, it is necessary to create a metric to decide when and where the split should be performed. Several methods are available for making this decision (also called *recursive binary splitting*), and we discuss here the two most common metrics for classification: *Gini Impurity* and *Entropy*.

Gini Impurity The gini impurity I_G is defined as the sum, over all classes n, of the product between of probability p_n of a random item being classified in its correct category, and the probability of it being wrongly classified. For a set of N classes,

$$I_G = \sum_{n=1}^{N} p_n(1 - p_n). \tag{C.1}$$

Entropy The definition of entropy used here is the one employed in information theory, also known as Shannon entropy (Shannon, 1948b). In terms of bits of information, the entropy I_H is given by

$$I_H = -\sum_{n=1}^{N} p_n \log_2 p_n. \tag{C.2}$$

The lower bound for both metrics is zero, representing a node in which all the samples belong to the same category. Figure C.10 shows a comparison of the metrics for different values of probability p_i. The "classification error" metric plotted is equal to $1 - \max(p_i, 1 - p_i)$.

To make the concept of those metrics clearer, let us take the dataset shown in Figure C.1 as a numerical example. We have initially 12% of the points belonging to class **B**, and 88% belonging to class **A**. The Gini impurity of the dataset is

$$I_G^{\text{Initial}} = \sum_{n=1}^{N} p_n(1 - p_n) = 0.12 \times 0.88 + 0.88 \times 0.12 = 0.2112$$

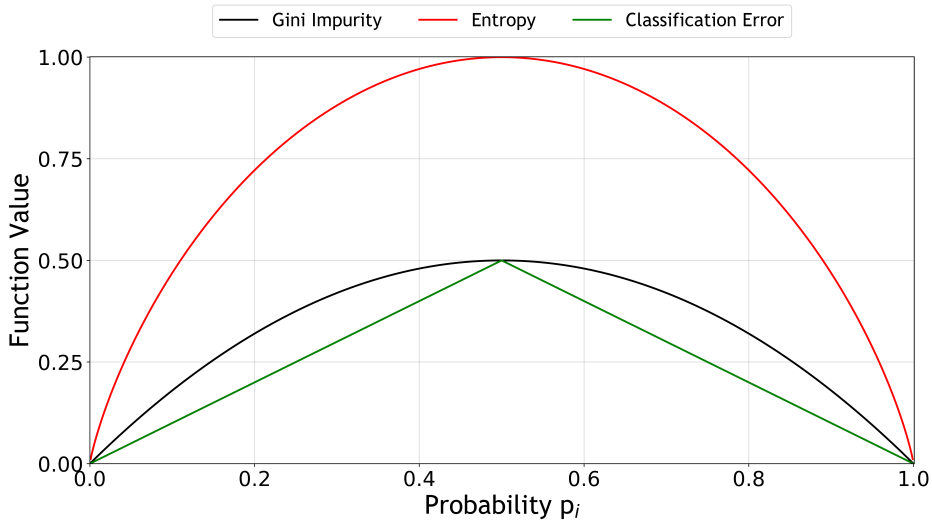

Figure C.10: Comparison of Gini Impurity (black) and Entropy (red) metrics for different probabilities p_i.

We proceed now to repeat this calculation for the dataset after the first split (Figures C.3 and C.4). On the left node, where all points belong to class **B**, the Gini impurity is zero. For the right node, we have

$$I_G^{\text{Right}} = \sum_{n=1}^{N} p_n(1-p_n) = 0.2 \times 0.8 + 0.8 \times 0.2 = 0.32.$$

When the gini impurity is used as criteria, the goal of the split is to maximize the reduction in impurity. The final impurity I_G^{Final} is given by the average of the impurities in each node, weighted by the relative number of samples in each of them. For the first split,

$$\begin{aligned}\Delta I &= I_G^{\text{Final}} - I_G^{\text{Initial}} \\ &= (0.4 \times 0 + 0.6 \times 0.32) - 0.2112 = -0.0192\end{aligned}$$

This criterion is followed repeatedly, until we reach the final tree - in our case, with Gini impurity equal to 0.

Let us now repeat the same exercise, but for entropy. Using again the dataset in Figure C.1, we have

$$I_H = -\sum_{n=1}^{N} p_n \log_2 p_n = -(0.12 \times \log_2 0.12 + 0.88 \times \log_2 0.88)$$
$$= 0.5294$$

After the first split, the left node has entropy 0 (since $\log_2 1 = 0$) and the entropy of the right node in Figure C.4 is

$$I_H^{\text{Right}} = -\sum_{n=1}^{N} p_n \log_2 p_n$$
$$= -(0.2 \times \log_2 0.2 + 0.8 \times \log_2 0.8) = 0.7219$$

The *Information Gain* ΔI_H of the split is given by the difference between the initial entropy and the weighted average entropy of the children nodes:

$$\Delta I_H = I_H^{\text{Initial}} - I_H^{\text{Final}}$$
$$= 0.5294 - (0.4 \times 0 + 0.6 \times 0.7219) = 0.09626$$

Under this metric, the splits should maximize the information gain, and the process is repeated until all nodes are leaves.

Although there are some minor differences involving the performance between the two metrics (Raileanu and Stoffel, 2004), in general the results are very similar, with Gini being sometimes preferred because of faster computation times (no need to compute a logarithm function).

C.2 A Practical Example

Several datasets are available for the practice of pattern recognition and regression algorithms (Dheeru and Karra Taniskidou, 2017). For this example, the dataset employed will be the *Iris* dataset (Duda and Hart, 1973), consisting of 150 flower samples. For each sample, 4 features were measured: length of sepals, width of

sepals, length of petals, and width of petals, all in centimeters. These features are used to classify the flowers into one of three categories: *Iris setosa*, *Iris virginica*, or *Iris versicolor*. In the Iris dataset, there are 50 samples in each category.

Figure C.11 shows the Iris dataset in two plots - one for each pair of measurements. We can see that it is no longer obvious which splits should be performed to classify the dataset, except perhaps for the Iris setosa, which clusters away from the other two classes. This can be promptly checked in Figure C.12, showing the decision tree for the first split (criteria is Gini impurity).

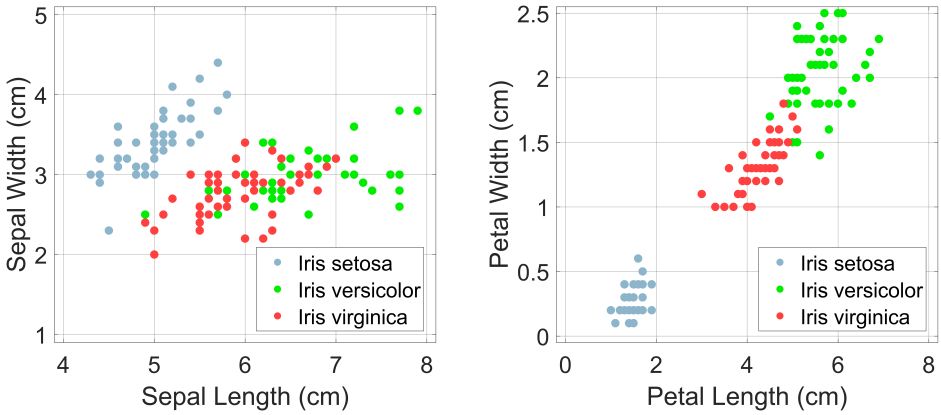

Figure C.11: Plots of Iris dataset. **Left** Classification (as color) in the Sepal width - Sepal length space. **Right** Classification (as color) in the Petal width - Petal length space.

Figure C.13 shows the full decision tree for this problem. It is significantly longer and more complex than the one presented in Figure C.9, due to the extra number of features (4) and categories (3). This tree would be the one used to classify any new samples whose petal and sepal widths and lengths had been measured.

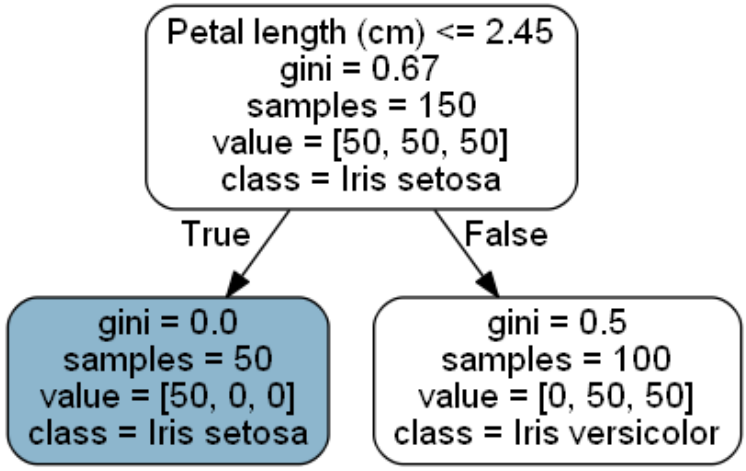

Figure C.12: First split of decision tree. Numbers inside the "value" array represent number of samples in each class: [setosa, versicolor, virginica].

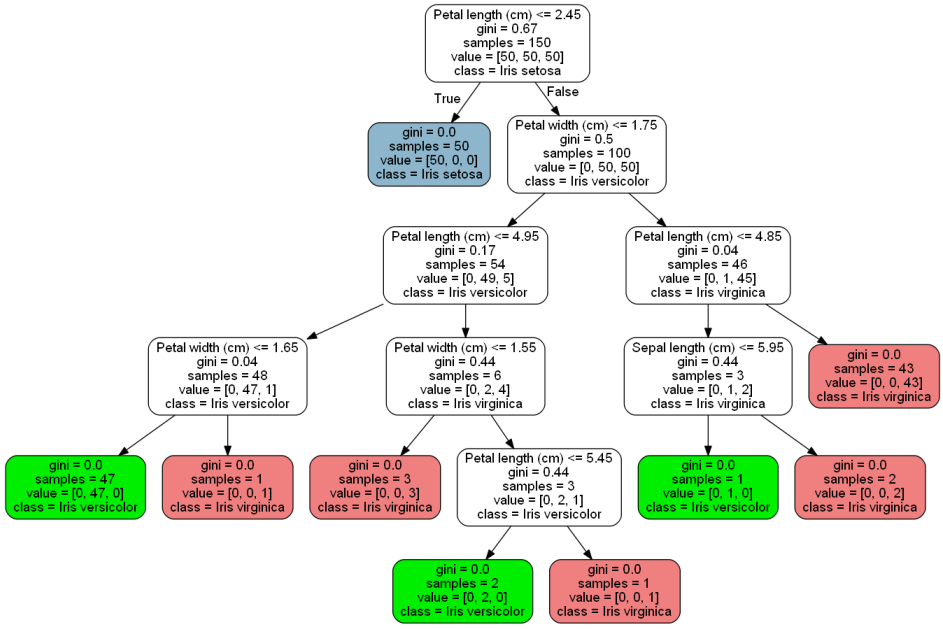

Figure C.13: Full decision tree for Iris dataset. Numbers inside the "value" array represent number of samples in each class: [setosa, versicolor, virginica]. Figure in full resolution is available here.

C.3 Regression Trees

The last two sessions presented a brief introduction to *classification* trees, which are useful when the output variable is a class or category. They are also more intuitive to understand, and that's why they were used as examples. When we aim at a numerical output, however, the method we need to use is called *regression tree*.

A regression tree follows the same logic as a decision tree, with the main difference being the metric used to define the best split. As the variable we are searching for is now continuous, the Gini and entropy criteria are no longer ideal. The most common metric is the *mean square error* (MSE).

Let us take a dataset of N samples, each with M inputs and one response. That means we have $(X_i, y_i) = (x_{1i}, x_{2i}, ..., x_{Mi}, y_i)$ for $i = 1, 2, ..., N$. It is common to model the response within a node S as the average $\bar{y}$ of all the points in that node, so that $\bar{y}_S = \text{mean}(y_i | x_i \in S)$.

The splitting process is performed by picking one feature x_j and creating two new nodes S_1 and S_2, which will contain values above or below a certain threshold s:

$$S_1(j, s) = \{X \mid x_j < s\} \qquad \text{and} \qquad S_2(j, s) = \{X \mid x_j > s\}.$$

The spliting criteria will be to minimize the square error between the average of the values y_i inside that node and their mean value:

$$\min_{j,s} \left[\sum_{X \in S_1(j,s)} \left(y_i - \bar{y}_{S_1} \right)^2 + \sum_{X \in S_2(j,s)} \left(y_i - \bar{y}_{S_2} \right)^2 \right] \tag{C.3}$$

C.4 Bagging and Random Forest

Decision and regression trees are relatively simple and intuitive to understand, and have been used for quite some time. One of the main issues with tree-based methods is *overfitting*. This happens when the tree grows too much in complexity, and hence loses its ability to properly classify new data. There are some proposed ways to deal with that, like limiting the maximum depth of the tree (number of splits far from the root node) or "pruning" some leaf nodes, on a bottom-up analysis.

A different approach is the use of *ensemble methods*, which employ several decision trees, instead of a single one (Strobl et al., 2009). A common way of doing that is via *bagging*, when the initial set of samples used to build the tree is selected as a subset of the complete training set. If the sampling is performed with reposition, the procedure is called *bootstrap sampling*. Several trees are built from those sampled sets and, as the decision tree is an unbiased estimator (Bühlmann et al., 2002), the final results show less variance than the results obtained using a single tree.

Another popular ensemble method is *random forest*. In the random forest algorithm, not only the initial dataset is subjected to bootstrap sampling, but also the samples used in every node to decide the splitting. Hence, when trying to optimize equation C.3, only a random selection of points in the node will be used. This has also been showed to improve the result of the method (Lin and Jeon, 2006; Biau et al., 2008).

In this thesis, the random forest algorithm was used in sections 1.3.2 and 1.4. It consisted of 1000 trees, using the mean square error criteria, and performing the bootstrap sampling.

Bibliography

Aadnøy, B. S., 2010, Modern well design: CRC Press.

Ainslie, M. A., and J. G. McColm, 1998, A simplified formula for viscous and chemical absorption in sea water: The Journal of the Acoustical Society of America, **103**, 1671–1672.

Aki, K., and P. G. Richards, 2002, Quantitative seismology.

Anderson, D. L., and C. Archambeau, 1964, The anelasticity of the earth: Journal of Geophysical Research, **69**, 2071–2084.

Anderson, E. M., 1951, The dynamics of faulting and dyke formation with applications to britain: Hafner Pub. Co.

Anderson Jr, J. D., 2010, Fundamentals of aerodynamics: Tata McGraw-Hill Education.

Aven, E., 2017, Is it possible to estimate the magnitude of uplift and erosion by the use of check-shot data and average velocity?: Master's thesis, NTNU.

Baade, R., L. Chin, W. Siemers, et al., 1988, Forecasting of ekofisk reservoir compaction and subsidence by numerical simulation: Presented at the Offshore Technology Conference, Offshore Technology Conference.

Backus, G. E., 1962, Long-wave elastic anisotropy produced by horizontal layering: Journal of Geophysical Research, **67**, 4427–4440.

Bakulin, A., and V. Grechka, 2003, Effective anisotropy of layered media: Geophysics, **68**, 1817–1821.

Bassani, R., and B. Piccigallo, 1992, Hydrostatic lubrication: Elsevier, **22**.

Batzle, M., R. Hofmann, M. Prasad, G. Kumar, L. Duranti, and D.-h. Han, 2005, Seismic attenuation: Observations and mechanisms, *in* SEG Technical Program Expanded Abstracts 2005: Society of Exploration Geophysicists, 1565–1568.

Batzle, M., and Z. Wang, 1992, Seismic properties of pore fluids: Geophysics, **57**, 1396–1408.

Beauducel, F., 2010, Deformation analytical models,

https://github.com/ipgp/deformations-matlab/, last accessed 16 october 2018.

Bergslid, T. S., E. B. Raknes, and B. Arntsen, 2015, The influence of anisotropy on elastic full-waveform inversion, *in* SEG Technical Program Expanded Abstracts 2015: Society of Exploration Geophysicists, 1425–1429.

Berry, R. B., T. F. Chan, J. Demmel, J. M. Donato, J. Dongarra, V. Eijkhout, R. Pozo, C. Romine, and H. Van der Vorst10, 1994, Templates for the solution of linear systems: Building blocks for iterative methods1: Society for Industrial and Applied Mathematics, Philadelphia, USA, 64–68.

Bertero, M., and P. Boccacci, 1998, Introduction to inverse problems in imaging: CRC press.

Bertrand, A., P. Folstad, B. Lyngnes, S. Buizard, H. Hoeber, N. Pham, S. De Pierrepont, J. Schultzen, and A. Grandi, 2014, Ekofisk life-of-field seismic: Operations and 4d processing: The Leading Edge, **33**, 142–148.

Bertrand, A., and C. MacBeth, 2003, Seawater velocity variations and real-time reservoir monitoring: The Leading Edge, **22**, 351–355.

Biau, G., L. Devroye, and G. Lugosi, 2008, Consistency of random forests and other averaging classifiers: Journal of Machine Learning Research, **9**, 2015–2033.

Biot, M., and D. Willis, 1957, The elastic coefficients of the theory of consolidation: J. appl. Mech, **15**, 594–601.

Biot, M. A., 1941, General theory of three-dimensional consolidation: Journal of applied physics, **12**, 155–164.

Bjorlykke, K., 2010, Petroleum geoscience: Springer Berlin Heidelberg.

Bjørlykke, K., and K. Gran, 1994, Salinity variations in north sea formation waters: implications for large-scale fluid movements: Marine and Petroleum Geology, **11**, 5–9.

Bogert, B. P., 1963, The quefrency analysis of time series for echoes: cepstrum, pseudo-autocovariance, cross-cepstrum and saphe cracking: Presented at the Proc. Symposium on Time Series Analysis, 1963, John Wiley & Sons.

Borges, F., 2018, Matlab implementation of Geertsma's equations, https://github.com/borgesf/geertsma, last update 30 october 2018.

Borges, F., and M. Landrø, 2017, Analysis of the influence of water salinity on time-lapse seismic response: Presented at the 79th EAGE Conference and Exhibition 2017.

Borges, F., M. Landrø, and K. Duffaut, 2020, Time-lapse seismic analysis of overburden water injection at the ekofisk field, southern north sea: Geophysics, **85**, B9–B21.

Borges, F., M. Muzzette, L. E. Queiroz, B. Pereira-Dias, R. Dias, and A. Bulcão, 2022, Analysis of water velocity changes in time-lapse ocean bottom

acquisitions-a synthetic 2d study in santos basin, offshore brazil: Journal of Applied Geophysics, **197**, 104521.

Borges, F., D. Wehner, and M. Landrø, 2018, Calculation of tube wave velocity in a shallow borehole using passive seismic recordings: Presented at the 80th EAGE Conference and Exhibition 2018.

Bourgoyne Jr., A. T., K. K. Millheim, M. E. Chenevert, and F. S. Young Jr., 1986, Applied drilling engineering: Society of Petroleum Engineers, Inc. SPE Textbook Series.

Bracewell, R. N., 1986, The fourier transform and its applications: McGraw-Hill New York, **31999**.

Breiman, L., 2002, Manual on setting up, using, and understanding random forests v3. 1: Statistics Department University of California Berkeley, CA, USA, **1**.

Brie, A., F. Pampuri, A. Marsala, O. Meazza, et al., 1995, Shear sonic interpretation in gas-bearing sands: Presented at the SPE Annual Technical Conference and Exhibition, Society of Petroleum Engineers.

Bruno, M., et al., 1992, Subsidence-induced well failure: SPE Drilling Engineering, **7**, 148–152.

Bühlmann, P., B. Yu, et al., 2002, Analyzing bagging: The Annals of Statistics, **30**, 927–961.

Buizard, S., A. Bertrand, K. M. Nielsen, S. de Pierrepont, A. Grandi, H. Hoeber, G. Oexnevad, and A. Gresillaud, 2013, Ekofisk life of field seismic-4d processing: Presented at the 75th EAGE Conference & Exhibition incorporating SPE EUROPEC 2013.

Bunting, T., P. Watterson, and M. Vassallo, 2013, Isometrix; isometrically sampled towed-streamer marine seismic data: 13th International Congress of the Brazilian Geophysical Society & EXPOGEF, Rio de Janeiro, Brazil, 26–29 August 2013, Society of Exploration Geophysicists and Brazilian Geophysical Society, 1177–1180.

Butterworth, S., 1930, On the theory of filter amplifiers: Wireless Engineer, **7**, 536–541.

Campbell, K. W., 2009, Estimates of shear-wave q and κ 0 for unconsolidated and semiconsolidated sediments in eastern north america: Bulletin of the Seismological Society of America, **99**, 2365–2392.

Cantillo, J., 2012, Throwing a new light on time-lapse technology, metrics and 4d repeatability with sdr: The Leading Edge, **31**, 405–413.

Carcione, J. M., 2007, Wave fields in real media: Wave propagation in anisotropic, anelastic, porous and electromagnetic media: Elsevier.

Carminatti, M., B. Wolff, L. Gamboa, et al., 2008, New exploratory frontiers in brazil: Presented at the 19th World Petroleum Congress, World Petroleum Congress.

Carter, A. J., V. A. Torres Caceres, K. Duffaut, and A. Stovas, 2020, Velocity-attenuation model from check-shot drift trends in north sea well data: Geophysics, **85**, D65–D74.

Casagrande, A., 1944, Shear failure of anisotropic materials: Proc. Boston Soc. Civ. Engineers, **31**, 74–87.

C&C Reservoirs, 2020, DAKS - Digital Analog Knowledge System.

Chambers, K., J. Kendall, and O. Barkved, 2010, Investigation of induced microseismicity at valhall using the life of field seismic array: The Leading Edge, **29**, 290–295.

Cheng, C. H., M. N. Toksöz, and M. E. Willis, 1982, Determination of in situ attenuation from full waveform acoustic logs: Journal of Geophysical Research: Solid Earth, **87**, 5477–5484.

Cheng, P., and G. F. Margrave, 2013, Estimation of q: a comparison of different computational methods: CSPG/CSEG/CWLS GeoConvention, **12**, 2–5.

Claerbout, J. F., 1985, Imaging the earth's interior: Blackwell scientific publications Oxford, **1**.

Coburn, T. C., 2000, Geostatistics for natural resources evaluation.

Cooley, J. W., and J. W. Tukey, 1965, An algorithm for the machine calculation of complex fourier series: Mathematics of computation, **19**, 297–301.

Costa, A., E. Poiate, C. Amaral, A. Pereira, L. Martha, M. Gattass, and D. Roehl, 2011, Geomechanics applied to the well design through salt layers in brazil: A history of success, *in* Multiscale and Multiphysics Processes in Geomechanics: Springer, 165–168.

Cressie, N., 1990, The origins of kriging: Mathematical geology, **22**, 239–252.

Curie, P., 1894, Sur la symétrie dans les phénomènes physiques, symétrie d'un champ électrique et d'un champ magnétique: Journal de physique théorique et appliquée, **3**, 393–415.

Cypriano, L., Z. Yu, D. Ferreira, B. Huard, R. Pereira, F. Jouno, A. Khalil, E. N. A. Urasaki, N. M. S. M. da Cruz, A. Yin, D. Clarke, and C. C. Jesus, 2019, Obn for pre-salt imaging and reservoir monitoring – potential and road ahead: Presented at the 16th International Congress of the Brazilian Geophysical Society & EXPOGEF 2019, Rio de Janeiro, Rio de Janeiro, Brazil.

De Ridder, S., B. Biondi, and R. Clapp, 2014, Time-lapse seismic noise correlation tomography at valhall: Geophysical Research Letters, **41**, 6116–6122.

de Ridder, S. A., and B. L. Biondi, 2015, Ambient seismic noise tomography at ekofisk: Geophysics, **80**, B167–B176.

Dheeru, D., and E. Karra Taniskidou, 2017, UCI machine learning repository.

Dias, R., F. Borges, C. Ushirobira, C. Carbonari, B. P. Dias, and A. Bulcão, 2020, Seismic modeling to mitigate risk in well location-a case study in brazilian pre-salt: 82nd EAGE Annual Conference & Exhibition, European Association of

Geoscientists & Engineers, 1–5.

Dias, R., J. Fonseca, A. Bulcão, B. Dias, L. Teixeira, A. Maul, and F. Borges, 2019, Salt stratification and least square migration to improve pre-salt reservoir images: Santos basin, brazilian offshore example: Presented at the Second EAGE/PESGB Workshop on Velocities.

Doornhof, D., T. G. Kristiansen, N. B. Nagel, P. D. Pattillo, and C. Sayers, 2006, Compaction and subsidence: Oilfield review, **18**, 50–68.

Duda, R. O., and P. E. Hart, 1973, Pattern classification and scene analysis: A Wiley-Interscience Publication, New York: Wiley, 1973.

Duffaut, K., and M. Landrø, 2007, V_p/V_s ratio versus differential stress and rock consolidation - A comparison between rock models and time-lapse AVO data: Geophysics, **72**, C81 – C94.

Ebaid, H., K. Wang, M. Seixas, G. Kumar, G. Brew, and T. Mashiotta, 2017, Practical example of data integration in a prm environment, bc-10, brazil: First EAGE Workshop on Practical Reservoir Monitoring, European Association of Geoscientists & Engineers, cp–505.

Eiken, O., M. Zumberge, and G. Sasagawa, 2000, Gravity monitoring of offshore gas reservoirs, *in* SEG Technical Program Expanded Abstracts 2000: Society of Exploration Geophysicists, 431–434.

Eissa, E., and A. Kazi, 1988, Relation between static and dynamic young's moduli of rocks: International Journal of Rock Mechanics and Mining Sciences & Geomechanics Abstracts, **25**, 479 – 482.

Emerick, A. A., and A. C. Reynolds, 2012, History matching time-lapse seismic data using the ensemble kalman filter with multiple data assimilations: Computational Geosciences, **16**, 639–659.

Eshelby, J. D., 1957, The determination of the elastic field of an ellipsoidal inclusion, and related problems: Proc. R. Soc. Lond. A, **241**, 376–396.

Ewing, W. M., W. S. Jardetzky, F. Press, and A. Beiser, 1957, Elastic waves in layered media: PhT, **10**, 27.

Fakcharoenphol, P., S. Charoenwongsa, H. Kazemi, Y.-S. Wu, et al., 2013, The effect of water-induced stress to enhance hydrocarbon recovery in shale reservoirs: SPE Journal, **18**, 897–909.

Fatti, J. L., G. C. Smith, P. J. Vail, P. J. Strauss, and P. R. Levitt, 1994a, Detection of gas in sandstone reservoirs using avo analysis: A 3-d seismic case history using the geostack technique: Geophysics, **59**, 1362–1376.

Fatti, J. L., P. J. Vail, G. C. Smith, P. J. Strauss, and P. R. Levitt, 1994b, Detection of gas in sandstone reservoirs using AvO analysis: A 3-D seismic case history using the geostack technique: Geophysics, **59**, 1362–1376.

Favretto-Anres, N., and J.-P. Sessarego, 1999, Identification of shear wave parameters of viscoelastic solids by laboratory measurements of stoneley-scholte

waves: Acta Acustica United with Acustica, **85**, 505–516.

Fisher, F., and V. Simmons, 1977, Sound absorption in sea water: The Journal of the Acoustical Society of America, **62**, 558–564.

Fjær, E., R. M. Holt, A. Raaen, R. Risnes, and P. Horsrud, 2008, Petroleum related rock mechanics: Elsevier, **53**.

Flom, P. L., and D. L. Cassell, 2007, Stopping stepwise: Why stepwise and similar selection methods are bad, and what you should use: Presented at the North-East SAS Users Group Inc 20th Annual Conference: 11-14th November 2007; Baltimore, Maryland.

Fonseca, J., L. Teixeira, A. Maul, P. Barros, F. Borges, J. Boechat, and M. González, 2018, Modelling geological layers into new velocity models for seismic migration process-a brazilian pre-salt case: Presented at the First EAGE/PESGB Workshop on Velocities.

Foster, D. J., and C. C. Mosher, 1992, Suppression of multiple reflections using the radon transform: Geophysics, **57**, 386–395.

Fridleifsson, I. B., R. Bertani, E. Huenges, J. W. Lund, A. Ragnarsson, L. Rybach, et al., 2008, The possible role and contribution of geothermal energy to the mitigation of climate change: IPCC scoping meeting on renewable energy sources, proceedings, Luebeck, Germany, Citeseer, 59–80.

Futterman, W. I., 1962, Dispersive body waves: Journal of Geophysical research, **67**, 5279–5291.

Gaarenstroom, L., R. Tromp, A. Brandenburg, et al., 1993, Overpressures in the central north sea: implications for trap integrity and drilling safety: Geological Society, London, Petroleum Geology Conference series, Geological Society of London, 1305–1313.

Galperin, E. I., 1985, Vertical seismic profiling and its exploration potential: D. Reidel Publishing Company.

Gardner, G., L. Gardner, and A. Gregory, 1974, Formation velocity and density—the diagnostic basics for stratigraphic traps: Geophysics, **39**, 770–780.

Gassmann, F., 1951, Elastic waves through a packing of spheres: Geophysics, **16**, 673–685. (Errata in GEO-17-2-0399; Errata in GEO-18-1-0269).

Geertsma, J., 1973, A basic theory of subsidence due to reservoir compaction: the homogeneous case: Verhandelingen Kon. Ned. Geol. Mijnbouwk. Gen, **28**, 43–62.

Graebner, M., 1992a, Plane-wave reflection and transmission coefficients for a transversely isotropic solid: Geophysics, **57**, 1512–1519.

———, 1992b, Plane-wave reflection and transmission coefficients for a transversely isotropic solid (short note): Geophysics, **57**, 1512–1519.

Grasso, J. R., 1992, Mechanics of seismic instabilities induced by the recovery of hydrocarbons: pure and applied geophysics, **139**, 507–534.

Greenberg, M., and J. Castagna, 1992, Shear-wave velocity estimation in porous rocks: theoretical formulation, preliminary verification and applications1: Geophysical prospecting, **40**, 195–209.

Grude, S., M. Landrø, and J. Dvorkin, 2014, Pressure effects caused by CO_2 injection in the Tubåen Fm., the Snøhvit field: International Journal of Greenhouse Gas Control, **27**, 178 – 187.

Hampson, D., 1986, Inverse velocity stacking for multiple elimination, *in* SEG Technical Program Expanded Abstracts 1986: Society of Exploration Geophysicists, 422–424.

Han, F.-X., J.-G. Sun, and K. Wang, 2012, The influence of sea water velocity variation on seismic traveltimes, ray paths, and amplitude: Applied Geophysics, **9**, 319–325.

Hashin, Z., and S. Shtrikman, 1963, A variational approach to the theory of the elastic behaviour of multiphase materials: Journal of the Mechanics and Physics of Solids, **11**, 127–140.

Hatchell, P., and S. Bourne, 2005, Rocks under strain: Strain-induced time-lapse time shifts are observed for depleting reservoirs: The Leading Edge, **24**, 1222–1225.

Hatchell, P., H. Ruiz, A. Libak, B. Nolan, and R. Agersborg, 2019, Precise depth and subsidence measurements during deepwater obn surveys, *in* SEG Technical Program Expanded Abstracts 2019: Society of Exploration Geophysicists, 162–166.

Healy, J., W. Rubey, D. Griggs, and C. Raleigh, 1968, The denver earthquakes: Science, **161**, 1301–1310.

Hermansen, H., G. Landa, J. Sylte, and L. Thomas, 2000, Experiences after 10 years of waterflooding the ekofisk field, norway: Journal of Petroleum Science and Engineering, **26**, 11 – 18.

Hicks, G. J., 2002, Arbitrary source and receiver positioning in finite-difference schemes using kaiser windowed sinc functions: Geophysics, **67**, 156–165.

Hovem, J. M., 2012, Marine acoustics: The physics of sound in underwater environments: Peninsula publishing Los Altos, CA.

Hubbert, M. K., and W. W. Rubey, 1960, Role of fluid pressure in mechanics of overthrust faulting: Bull. Geol. Soc. Am, **71**, 617–628.

Hudson, J., 1980, Overall properties of a cracked solid: Mathematical Proceedings of the Cambridge Philosophical Society, Cambridge University Press, 371–384.

Ide, J. M., 1936, Comparison of statically and dynamically determined young's modulus of rocks: Proceedings of the National Academy of Sciences, **22**, 81–92.

Ikelle, L. T., and L. Amundsen, 2005, Introduction to petroleum seismology: Society of Exploration Geophysicists.

Jerkins, A. E., H. A. Shiddiqi, T. Kværna, S. J. Gibbons, J. Schweitzer, L. Ottemöller, and H. Bungum, 2020, The 30 june 2017 north sea earthquake: location, characteristics, and context: Bulletin of the Seismological Society of America, **110**, 937–952.

Johnston, D., 2013, Practical applications of time-lapse seismic data: Society of Exploration Geophysicists.

Jones, T., and A. Nur, 1983, Velocity and attenuation in sandstone at elevated temperatures and pressures: Geophysical Research Letters, **10**, 140–143.

Karelitz, M., 1938, Oil pad bearings and driving gears of 200 inch telescope: Mechanical Engineering, **60**, 541.

Karsli, H., and Y. Bayrak, 2008, Ground-roll attenuation based on wiener filtering and benefits of time-frequency imaging: The Leading Edge, **27**, 206–209.

Ketcham, S. A., R. J. Greenfield, M. L. Moran, and T. S. Anderson, 2001, Soil attenuation in seismic simulations: Implications for vehicle tracking: Technical report, ENGINEER RESEARCH AND DEVELOPMENT CENTER HANOVER NH COLD REGIONS RESEARCH ....

Kibblewhite, A. C., 1989, Attenuation of sound in marine sediments: A review with emphasis on new low-frequency data: The Journal of the Acoustical Society of America, **86**, 716–738.

King, M. S., 1983, Static and dynamic elastic properties of igneous and metamorphic rocks from the canadian shield.

Kiyashchenko, D., A. Mateeva, Y. Duan, D. Johnson, J. Pugh, A. Geisslinger, and J. Lopez, 2020a, Frequent 4d monitoring with das 3d vsp in deep water to reveal injected water-sweep dynamics: The Leading Edge, **39**, 471–479.

Kiyashchenko, D., W.-F. Wong, D. Cherief, D. Clarke, Y. Duan, and P. Hatchell, 2020b, Unlocking seismic monitoring of stiff reservoirs with 4d obn: a case study from brazil pre-salt, *in* SEG Technical Program Expanded Abstracts 2020: Society of Exploration Geophysicists, 3759–3763.

Kommedal, J. H., O. I. Barkved, and D. J. Howe, 2004, Initial experience operating a permanent 4c seabed array for reservoir monitoring at valhall, *in* SEG Technical Program Expanded Abstracts 2004: Society of Exploration Geophysicists, 2239–2242.

Kragh, E., and P. Christie, 2002, Seismic repeatability, normalized rms, and predictability: The Leading Edge, **21**, 640–647.

Ku, H., 1966, Notes on the use of propagation of error formulas: Journal of Research of the National Bureau of Standards, **70**.

Landau, L., and E. Lifshitz, 1987, Fluid mechanics. volume 6 of course of theoretical physics, 2nd english ed. translated from the russian by jb sykes, wh reid.

Landrø, M., 1999, Repeatability issues of 3-d vsp data: Geophysics, **64**, 1673–1679.

———, 2001, Discrimination between pressure and fluid saturation changes from time-lapse seismic data: Geophysics, **66**, 836–844.

Landrø, M., P. Digranes, and L. Strønen, 2001, Mapping reservoir pressure and saturation changes using seismic methods-possibilities and limitations: First break, **19**, 671–684.

Landrø, M., and P. Hatchell, 2012, Normal modes in seismic data—revisited: Geophysics, **77**, W27–W40.

Landrø, M., S. Kodaira, T. Fujiwara, T. No, W. Weibull, and B. Arntsen, 2019, Time lapse seismic analysis of the tohoku-oki 2011 earthquake: International Journal of Greenhouse Gas Control, **82**, 98–116.

Landrø, M., O. A. Solheim, E. Hilde, B. O. Ekren, and L. K. Stronen, 1999, The gullfaks 4d seismic study: Petroleum Geoscience, **5**, 213–226.

Landrø, M., and J. Stammeijer, 2004, Quantitative estimation of compaction and velocity changes using 4d impedance and traveltime changes: Geophysics, **69**, 949–957.

Landrø, M., D. Wehner, and F. Borges, 2018, How variations of the formation shear modulus around boreholes could be estimated from the tube wave: AGU Fall Meeting Abstracts, S51F–0398.

Le Diagon, F., Y. Abbas, T. Bunting, J. dos Santos, C. Montana, A. de Oliveira, G. de Lima, L. Balancin, G. Basta Silva, F. Borges, et al., 2014, Finite difference modeling to evaluate the improvements associated with a multicomponent towed streamer measurement in espirito santo basin offshore brazil, *in* SEG Technical Program Expanded Abstracts 2014: Society of Exploration Geophysicists, 3287–3291.

Lecerf, D., J. Burren, E. Hodges, and C. Barros, 2015, Repeatability measure for broadband 4d seismic, *in* SEG Technical Program Expanded Abstracts 2015: Society of Exploration Geophysicists, 5483–5487.

Levenberg, K., 1944, A method for the solution of certain non-linear problems in least squares: Quarterly of applied mathematics, **2**, 164–168.

L'Heureux, J. S., and M. Long, 2016, Correlations between shear wave velocity and geotechnical parameters in Norwegian clays: Proceedings of the 17th Nordic Geotechnical Meeting.

L'Heureux, J. S., M. Long, M. Vanneste, G. Sauvin, L. Hansen, U. Polom, I. Lecomte, J. Dehls, and N. Janbu, 2013, On the prediction of settlement from high-resolution shear-wave reflection seismic data: The Trondheim harbour case study, mid Norway: Engineering Geology, **167**, 72 – 83.

Lin, Y., and Y. Jeon, 2006, Random forests and adaptive nearest neighbors: Journal of the American Statistical Association, **101**, 578–590.

Long, M., and S. Donohue, 2007, In situ shear wave velocity from multichannel analysis of surface waves (MASW) tests at eight Norwegian research sites:

Canadian Geotechnical Journal, **44**, 533 – 544.

MacBeth, C., M.-D. Mangriotis, and H. Amini, 2019, Post-stack 4d seismic time-shifts: Interpretation and evaluation: Geophysical Prospecting, **67**, 3–31.

MacKay, S., J. Fried, and C. Carvill, 2003, The impact of water-velocity variations on deepwater seismic data: The Leading Edge, **22**, 344–350.

Marzetta, T. L., and M. Schoenberg, 1985, Tube waves in cased boreholes: 55th Annual International Meeting, SEG, Expanded Abstract, 34 – 36.

Mateeva, A., J. Lopez, J. Mestayer, P. Wills, B. Cox, D. Kiyashchenko, Z. Yang, W. Berlang, R. Detomo, and S. Grandi, 2013, Distributed acoustic sensing for reservoir monitoring with vsp: The Leading Edge, **32**, 1278–1283.

Matheron, G., 1963, Principles of geostatistics: Economic Geology, **58**, 1246.

Matter, J. M., M. Stute, S. Ó. Snæbjörnsdottir, E. H. Oelkers, S. R. Gislason, E. S. Aradottir, B. Sigfusson, I. Gunnarsson, H. Sigurdardottir, E. Gunnlaugsson, G. Axelsson, H. A. Alfredsson, D. Wolff-Boenisch, K. Mesfin, D. Fernandez de la Reguera Taya, J. Hall, K. Dideriksen, and W. S. Broecker, 2016, Rapid carbon mineralization for permanent disposal of anthropogenic carbon dioxide emissions: Science, **352**, 1312 – 1314.

Maul, A., A. Bulcão, R. Dias, B. Pereira-Dias, L. Teixeira, F. Borges, M. González, C. Guizan, and M. Cetale, 2021, Benefits of inserting salt stratification to detail velocity model prior to least-squares reverse-time migration: Journal of Applied Geophysics, 104469.

Maul, A. R., M. A. C. Santos, C. G. Silva, L. M. T. da Silva, M. d. L. Á. G. Farias, J. S. da Fonseca, R. de Melo Dias, J. B. T. Boechat, F. A. de Souto Borges, L. F. Fernandes, et al., 2019a, Improving pre-salt reservoirs seismic images when considering the stratified evaporites insertion in the initial model for the velocity updating processes prior to the seismic migration: Brazilian Journal of Geophysics, **37**, 235–247.

Maul, A. R., M. A. C. Santos, C. G. Silva, M. d. L. Á. G. Farias, J. S. da Fonseca, F. A. de Souto Borges, and C. E. B. de Salles Abreu, 2019b, Evaporitic velocity modeling uncertainties and variabilities: Implications for pre-salt projects in the santos basin, brazil: Brazilian Journal of Geophysics, **37**, 175–186.

Mavko, G., T. Mukerji, and J. Dvorkin, 2009a, The rock physics handbook: Tools for seismic analysis of porous media, 2nd ed.: Cambridge University Press.

———, 2009b, Rphtools, https://pangea.stanford.edu/departments/geophysics/, last accessed 19 july 2017.

Mello, V., M. Santos, R. Penna, J. Rosseto, and C. Deplante, 2019, 4d petroelastic modeling for a brazilian pre-salt field: What to expect from interpretation?: 81st EAGE Conference and Exhibition 2019, European Association of Geoscientists & Engineers, 1–5.

Meredith, J., M. Toksöz, and C. Cheng, 1993, Secondary shear waves from source

boreholes: Geophysical prospecting, **41**, 287–312.

Mindlin, R. D., 1949, Compliance of elastic bodies in contact: J. Appl. Mech., **16**, 259–268.

Mitchell, P., R. Paez, D. Johnston, G. Mohler, and C. da Cunha Neto, 2009, *in* 4D seismic in deep water at the Dikanza field, offshore Angola, West Africa: 3924–3928.

Mondol, N. H., J. Jahren, K. Bjørlykke, and I. Brevik, 2008, Elastic properties of clay minerals: The Leading Edge, **27**, 758–770.

Mordret, A., M. Landès, N. Shapiro, S. Singh, and P. Roux, 2014, Ambient noise surface wave tomography to determine the shallow shear velocity structure at valhall: depth inversion with a neighbourhood algorithm: Geophysical Journal International, **198**, 1514–1525.

Motz, E., D. Canny, and E. Evans, 1998, Ultrasonic velocity and attenuation measurements in high density drilling muds: Presented at the SPWLA 39th Annual Logging Symposium, OnePetro.

Müller, T. M., B. Gurevich, and M. Lebedev, 2010, Seismic wave attenuation and dispersion resulting from wave-induced flow in porous rocks—a review: Geophysics, **75**, 75A147–75A164.

Müller, T. M., and P. N. Sahay, 2016, Biot coefficient is distinct from effective pressure coefficient: Geophysics, **81**, L27–L33.

Murphy III, W. F., 1982, Effects of partial water saturation on attenuation in massilon sandstone and vycor porous glass: The Journal of the Acoustical Society of America, **71**, 1458–1468.

———, 1984, Acoustic measures of partial gas saturation in tight sandstones: Journal of Geophysical Research: Solid Earth, **89**, 11549–11559.

Nagel, N., 2001, Compaction and subsidence issues within the petroleum industry: From wilmington to ekofisk and beyond: Physics and Chemistry of the Earth, Part A: Solid Earth and Geodesy, **26**, 3–14.

Nagel, N., K. Strachan, et al., 1998, Implementation of cuttings reinjection at the ekofisk field: Presented at the SPE/ISRM Rock Mechanics in Petroleum Engineering, Society of Petroleum Engineers.

Nagel, N. B., 1998, Ekofisk field overburden modelling: Society of Petroleum Engineers.

Noll, A. M., and M. R. Schroeder, 1964, Short-time “cepstrum" pitch detection: The Journal of the Acoustical Society of America, **36**, 1030–1030.

Norris, A. N., 1990, The speed of a tube wave: Journal of the Acoustical Society of America, **87**, 414 – 417.

Ofstad, K., 1980, Npd paper no. 25: Norwegian Petroleum Directorate. (Appendex 2).

Okada, Y., 1985, Surface deformation due to shear and tensile faults in a half-

space: Bulletin of the seismological society of America, **75**, 1135–1154.

Oppenheim, A. V., and R. W. Schafer, 2004, From frequency to quefrency: a history of the cepstrum: IEEE Signal Processing Magazine, **21**, 95–106.

Orange, A., K. Key, and S. Constable, 2009, The feasibility of reservoir monitoring using time-lapse marine csem: Geophysics, **74**, F21–F29.

Osborne, M. J., and R. E. Swarbrick, 1997, Mechanisms for generating overpressure in sedimentary basins: A reevaluation: AAPG bulletin, **81**, 1023–1041.

Ostrander, W. J., 1984, Plane-wave reflection coefficients for gas sands at nonnormal angles-of-incidence: Geophysics, **49**, 1637–1648.

Ottemöller, L., H. Nielsen, K. Atakan, J. Braunmiller, and J. Havskov, 2005, The 7 may 2001 induced seismic event in the ekofisk oil field, north sea: Journal of Geophysical Research: Solid Earth, **110**.

Oye, V., K. Iranpour, T. Kværna, S. Gibbons, L. Vedvik, and H. Nielsen, 2014, Migration-based location method applied to a perforation shot using lofs data at the ekofisk field, norway: 76th EAGE Conference and Exhibition 2014, European Association of Geoscientists & Engineers, 1–5.

Park, C. B., R. D. Miller, and J. Xia, 1998, Imaging dispersion curves of surface waves on multi-channel record, *in* SEG Technical Program Expanded Abstracts 1998: Society of Exploration Geophysicists, 1377–1380.

Pattillo, P., T. Kristiansen, G. Sund, R. Kjelstadli, et al., 1998, Reservoir compaction and seafloor subsidence at valhall: Presented at the SPE/ISRM Rock Mechanics in Petroleum Engineering, Society of Petroleum Engineers.

Pebesma, E. J., 2006, The role of external variables and gis databases in geostatistical analysis: Transactions in GIS, **10**, 615–632.

Pedenaud, P., C. Hurtevent, and S. Baraka-Lokmane, 2012, Industrial experience in sea water desulfation: Presented at the SPE International Conference on Oilfield Scale, Society of Petroleum Engineers.

Pereira-Dias, B., A. Bulcão, D. S. Filho, R. Dias, F. Duarte, and F. Loureiro, 2017, Elastic least-squares reverse time migration in the image domain, *in* SEG Technical Program Expanded Abstracts 2017: Society of Exploration Geophysicists, 4353–4357.

Petersen, D. P., and D. Middleton, 1962, Sampling and reconstruction of wavenumber-limited functions in n-dimensional euclidean spaces: Information and control, **5**, 279–323.

Pilz, M., and S. Parolai, 2017, Shear wave velocity versus quality factor: results from seismic noise recordings: Geophysical Journal International, **210**, 660–670.

Porsani, M. J., M. G. Silva, P. E. Melo, and B. Ursin, 2009, Ground-roll attenuation based on svd filtering, *in* SEG Technical Program Expanded Abstracts 2009: Society of Exploration Geophysicists, 3381–3385.

Prioul, R., A. Bakulin, and V. Bakulin, 2004, Nonlinear rock physics model for estimation of 3D subsurface stress in anisotropic formations: Theory and laboratory verification: Geophysics, **69**, 415–425.

Prioul, R., and T. Lebrat, 2004, Calibration of velocity-stress relationships under hydrostatic stress for their use under non-hydrostatic stress conditions: 74th Ann. Internat. Mtg., Soc. of Expl. Geophys., 1698–1701.

Probert, T., R. van Dok, and J. Gaiser, 2004, Time-lapse shear wave splitting analysis at ekofisk field, north sea: Presented at the 66th EAGE Conference & Exhibition.

Radon, J., 1986, On the determination of functions from their integral values along certain manifolds: IEEE transactions on medical imaging, **5**, 170–176.

Raileanu, L. E., and K. Stoffel, 2004, Theoretical comparison between the gini index and information gain criteria: Annals of Mathematics and Artificial Intelligence, **41**, 77–93.

Raji, W., and A. Rietbrock, 2013, Attenuation (1/q) estimation in reflection seismic records: Journal of Geophysics and Engineering, **10**, 045012.

Raknes, E. B., and B. Arntsen, 2015, A numerical study of 3d elastic time-lapse full-waveform inversion using multicomponent seismic data: Geophysics, **80**, R303–R315.

Rasolofosaon, P., 1998, Stress-induced seismic anisotropy revisited: Revue de l'Institut Français du Pétrole, **53**, 679–692.

Rayleigh, L., 1885, On waves propagated along the plane surface of an elastic solid: Proceedings of the London Mathematical Society, **1**, 4–11.

Rentsch, H., M. Mes, et al., 1988, Measurement of ekofisk subsidence: Presented at the Offshore Technology Conference, Offshore Technology Conference.

Reuss, A., 1929, Berechnung der fließgrenze von mischkristallen auf grund der plastizitätsbedingung für einkristalle.: ZAMM-Journal of Applied Mathematics and Mechanics/Zeitschrift für Angewandte Mathematik und Mechanik, **9**, 49–58.

Roche, M., et al., 2007, Corrosion management: A key issue in pipeline integrity: Presented at the International Petroleum Technology Conference, International Petroleum Technology Conference.

Rosa, A. L. R., 2018, The seismic signal and its meaning.

Røste, T., O. P. Dybvik, and O. K. Søreide, 2015, Overburden 4d time shifts induced by reservoir compaction at snorre field: The Leading Edge, **34**, 1366–1374.

Røste, T., A. Stovas, and M. Landrø, 2005, Estimation of layer thickness and velocity changes using 4d prestack seismic data: Presented at the 67th Annual Conference and Exhibition, Extended Abstracts, C010, EAGE.

Ruger, A., 1997, P-wave reflection coefficients for transversely isotropic models

with vertical and horizontal axis of symmetry: Geophysics, **62**, 713–722.
Sayers, C., 1981, Ultrasonic velocity dispersion in porous materials: Journal of Physics D: Applied Physics, **14**, 413.
Sayers, C. M., 2002, Stress-dependent elastic anisotropy of sandstones: Geophysical prospecting, **50**, 85–95.
Schoenberg, M., and J. Douma, 1988, Elastic wave propagation in media with parallel fractures and aligned cracks: Geophysical prospecting, **36**, 571–590.
Schoenberg, M., and C. M. Sayers, 1995, Seismic anisotropy of fractured rock: Geophysics, **60**, 204–211.
Scholte, J., 1942, On the stoneley wave equation: Proceedings of the Koninklijke Nederlandse Akademie van Wetenschappen, **45**, 20–25.
———, 1947, The range of existence of rayleigh and stoneley waves: Geophysical Journal International, **5**, 120–126.
Schoonbeek, J., et al., 1976, Land subsidence as a result of natural gas extraction in the province of groningen: Presented at the SPE European Spring Meeting, Society of Petroleum Engineers.
Schuster, G. T., 2017, Seismic inversion: Society of Exploration Geophysicists.
Settari, A., F. Mourits, et al., 1998, A coupled reservoir and geomechanical simulation system: Spe Journal, **3**, 219–226.
Shannon, C. E., 1948a, A mathematical theory of communication: Bell system technical journal, **27**, 379–423.
———, 1948b, A mathematical theory of communication: The Bell System Technical Journal, **27**, 379–423.
Sheng, J., 2014, Critical review of low-salinity waterflooding: Journal of Petroleum Science and Engineering, **120**, 216–224.
Sheriff, R. E., and L. P. Geldart, 1995, Exploration seismology: Cambridge university press.
Shotton, J., A. Fitzgibbon, M. Cook, T. Sharp, M. Finocchio, R. Moore, A. Kipman, and A. Blake, 2011, Real-time human pose recognition in parts from single depth images: CVPR 2011, 1297–1304.
Shuey, R. T., 1985, A simplification of the Zoeppritz-equations: Geophysics, **50**, 609–614. (Errata in GEO-50-9-1522).
Sibson, R. H., 1985, A note on fault reactivation: Journal of Structural Geology, **7**, 751–754.
Simao, N. M., 2009, Seismicity of the mid-atlantic ridge in the momar area at a regional scale, observed by autonomous hydrophone arrays: PhD thesis, Université de Bretagne occidentale-Brest.
Skrettingland, K., T. Holt, M. T. Tweheyo, I. Skjevrak, et al., 2011, Snorre low-salinity-water injection–coreflooding experiments and single-well field pilot: SPE Reservoir Evaluation & Engineering, **14**, 182–192.

Smith, G. C., and P. M. Gidlow, 1987, Weighted stacking for rock property estimation and detection of gas: Geophys. Prosp., **35**, 993–1014.

Stainsby, S., and M. Worthington, 1985, Q estimation from vertical seismic profile data and anomalous variations in the central north sea: Geophysics, **50**, 615–626.

Stammeijer, J., and P. Hatchell, 2014, Standards in 4d feasibility and interpretation: The Leading Edge, **33**, 134–140.

Stevens, J. L., and S. M. Day, 1986, Shear velocity logging in slow formations using the stoneley wave: Geophysics, **51**, 137–147.

Stoneley, R., 1924, Elastic waves at the surface of separation of two solids: Proc. R. Soc. Lond. A, **106**, 416–428.

Storvoll, V., K. Bjørlykke, and N. H. Mondol, 2005, Velocity-depth trends in mesozoic and cenozoic sediments from the norwegian shelf: AAPG bulletin, **89**, 359–381.

Stovas, A., and M. Landro, 2002, Fluid-Pressure Discrimination in Anisotropic Reservoir Rocks - a Sensitivity Study: 64th Mtg., Eur. Assn. Geosci. Eng., P318.

Strobl, C., J. Malley, and G. Tutz, 2009, An introduction to recursive partitioning: rationale, application, and characteristics of classification and regression trees, bagging, and random forests.: Psychological methods, **14**, 323.

Sulak, A., J. Danielsen, et al., 1988, Reservoir aspects of ekofisk subsidence: Presented at the Offshore Technology Conference, Offshore Technology Conference.

Sulak, R., L. Thomas, R. Boade, et al., 1991, 3d reservoir simulation of ekofisk compaction drive (includes associated papers 24317 and 24400): Journal of Petroleum Technology, **43**, 1–272.

Sylte, J., L. Thomas, D. Rhett, D. Bruning, N. Nagel, et al., 1999, Water induced compaction in the ekofisk field: Presented at the SPE Annual Technical Conference and Exhibition, Society of Petroleum Engineers.

Tarantola, A., 1986, A strategy for nonlinear elastic inversion of seismic reflection data: Geophysics, **51**, 1893–1903.

Teixeira, L., and W. M. Lupinacci, 2019, Elastic properties of rock salt in the santos basin: Relations and spatial predictions: Journal of Petroleum Science and Engineering, **180**, 215–230.

Teixeira, L., J. Nunes, A. Maul, J. Fonseca, P. Barros, and F. Borges, 2018, Seismic-based salt characterisation for geomechanical modelling of a presalt reservoir: Presented at the 80th EAGE Conference and Exhibition 2018.

Tenghamn, R., and P. E. Dhelie, 2009, Geostreamer–increasing the signal-to-noise ratio using a dual-sensor towed streamer: First Break, **27**, 45–51.

Tertyshnikov, K., and R. Pevzner, 2020, 3c vsp with das-an obvious approach: First EAGE Workshop on Fibre Optic Sensing, European Association of Geoscient-

ists & Engineers, 1–4.

Teufel, L. W., and H. E. Farrell, 1990, In situ stress and natural fracture distribution in the ekofisk field, north sea: Technical report, Sandia National Labs., Albuquerque, NM (USA).

Thedy, E., P. Dariva, W. Ramos Filho, P. Maciel Jr, F. Silva, and I. Zorzanelli, 2015, First results on reservoir monitoring in jubarte prm-offshore brazil: Presented at the Third EAGE Workshop on Permanent Reservoir Monitoring 2015.

Thedy, E., R. Filho, W. Johann, S. Seth, S. Souza, and P. Murray, 2013, Jubarte permanent reservoir monitoring–installation and first results: 13th International Congress of the Brazilian Geophysical Society & EXPOGEF, Rio de Janeiro, Brazil, 26–29 August 2013, Society of Exploration Geophysicists and Brazilian Geophysical Society, 918–920.

Thomsen, L., 1986, Weak elastic anisotropy: Geophysics, **51**, 1954–1966. (Discussion in GEO-53-04-0558-0560 with reply by author).

———, 1987, Elastic anisotropy due to aligned cracks, *in* SEG Technical Program Expanded Abstracts 1987: Society of Exploration Geophysicists, 857–857.

———, 1995, Elastic anisotropy due to aligned cracks in porous rock: Geophysical Prospecting, **43**, 805–829.

Thomson, W. T., 1950, Transmission of elastic waves through a stratified solid medium: Journal of applied Physics, **21**, 89–93.

Tikhonov, A., A. Leonov, and A. Yagola, 1998, Nonlinear ill-posed problems (volume 1): Applied Mathematics and Mathematical Computation, **1**.

Toksöz, M., D. H. Johnston, and A. Timur, 1979, Attenuation of seismic waves in dry and saturated rocks: I. laboratory measurements: Geophysics, **44**, 681–690.

Van Den Bark, E., and O. D. Thomas, 1981, Ekofisk: first of the giant oil fields in western europe: AAPG Bulletin, **65**, 2341–2363.

Van Gestel, J.-P., J. H. Kommedal, O. I. Barkved, I. Mundal, R. Bakke, and K. D. Best, 2008, Continuous seismic surveillance of valhall field: The Leading Edge, **27**, 1616–1621.

Van Oort, E., J. Gradishar, G. Ugueto, K. Cowan, K. Barton, J. Dudley, et al., 2003, Accessing deep reservoirs by drilling severely depleted formations: Presented at the SPE/IADC Drilling Conference, Society of Petroleum Engineers.

Vanorio, T., A. Nur, and Y. Ebert, 2011a, Rock physics analysis and time-lapse rock imaging of geochemical effects due to the injection of co 2 into reservoir rocks: Geophysics, **76**, O23–O33.

———, 2011b, Rock physics analysis and time-lapse rock imaging of geochemical effects due to the injection of CO_2 into reservoir rocks: Geophysics, **76**, O23 – O33.

Vesnaver, A. L., F. Accaino, G. Bohm, G. Madrussani, J. Pajchel, G. Rossi, and G. D. Moro, 2003, Time-lapse tomography: Geophysics, **68**, 815–823.

Vialle, S., and T. Vanorio, 2011, Laboratory measurements of elastic properties of carbonate rocks during injection of reactive CO_2-saturated water: Geophysical Research Letters, **38**, L01302.

Vudovich, A., L. Chin, D. Morgan, et al., 1988, Casing deformation in ekofisk: Presented at the Offshore Technology Conference, Offshore Technology Conference.

Wales, D. J., and J. P. Doye, 1997, Global optimization by basin-hopping and the lowest energy structures of lennard-jones clusters containing up to 110 atoms: The Journal of Physical Chemistry A, **101**, 5111–5116.

Walton, K., 1987, The effective elastic moduli of a random packing of spheres: Journal of the Mechanics and Physics of Solids, **35**, 213–226.

Wang, K., P. Hatchell, C. Udengaard, K. Craft, and S. Dunn, 2012, Direct measurement of water velocity and tidal variations in marine seismic acquisition, *in* SEG Technical Program Expanded Abstracts 2012: Society of Exploration Geophysicists, 1–5.

Wanniarachchi, W., P. Ranjith, M. Perera, T. Rathnaweera, Q. Lyu, and B. Mahanta, 2017, Assessment of dynamic material properties of intact rocks using seismic wave attenuation: an experimental study: Royal Society open science, **4**, 170896.

Wapenaar, K., F. Broggini, E. Slob, and R. Snieder, 2013, Three-dimensional single-sided marchenko inverse scattering, data-driven focusing, green's function retrieval, and their mutual relations: Physical Review Letters, **110**, 084301.

Webb, K., C. Black, H. Al-Ajeel, et al., 2003, Low salinity oil recovery-log-inject-log: Presented at the Middle East Oil Show, Society of Petroleum Engineers.

Wehner, D., 2019, Experimental studies of the acoustic signal generated by marine seismic sources: PhD thesis, NTNU.

Wehner, D., F. Borges, and M. Landrø, 2021, Tube-wave monitoring as a method to detect shear modulus changes around boreholes: A case study: Geophysics, **86**, B193–B207.

Wehner, D., Y. Liu, and M. Landrø, 2017, Estimate the shear wave velocity close to wells from tube waves–an experimental study: Presented at the Fourth Sustainable Earth Sciences Conference.

White, J. E., 1965, Seismic waves: Radiation, transmission, and attenuation: McGraw-Hill Book Company. International Series in the Earth Sciences.

White, R., 1992, The accuracy of estimating q from seismic data: Geophysics, **57**, 1508–1511.

Winkler, K., and A. Nur, 1979, Pore fluids and seismic attenuation in rocks: Geophysical Research Letters, **6**, 1–4.

Zarembo, V., and M. Fedorov, 1975, Density of sodium-chloride solutions in temperature-range 25-350 degrees c at pressures up to 1000 kg-cm2: JOURNAL

OF APPLIED CHEMISTRY OF THE USSR, **48**, 2021–2024.

Zemanek Jr, J., and I. Rudnick, 1961, Attenuation and dispersion of elastic waves in a cylindrical bar: The Journal of the Acoustical Society of America, **33**, 1283–1288.

Zheng, T.-y., Z.-x. Yao, and P.-c. Liu, 1995, The 14 november 1986 taiwan earthquake-an event with isotropic component: Physics of the Earth and Planetary Interiors, **91**, 285–298.

Ziatdinov, S., A. Bakulin, B. Kashtan, S. Golovnina, and V. Korneev, 2005, Tube waves in producing wells with tubing and casing, *in* SEG Technical Program Expanded Abstracts 2005: Society of Exploration Geophysicists, 340–343.

Zoback, M. D., 2010, Reservoir geomechanics: Cambridge University Press.

Zoback, M. L., 1992, First-and second-order patterns of stress in the lithosphere: The world stress map project: Journal of Geophysical Research: Solid Earth, **97**, 11703–11728.

Zoeppritz, K., 1919, On the reflection and propagation of seismic waves at discontinuities: Erdbebenwellen VII B, 66–84.

ISBN 978-82-326-6251-7 (printed ver.)
ISBN 978-82-326-6876-2 (electronic ver.)
ISSN 1503-8181 (printed ver.)
ISSN 2703-8084 (online ver.)

NTNU

Norwegian University of
Science and Technology